INTERLAYER EXCHANGE COUPLING AND COLOSSAL MAGNETORESISTANCE IN TRANSITION METAL OXIDE BASED THIN FILM SUPERLATTICES

A Thesis Submitted
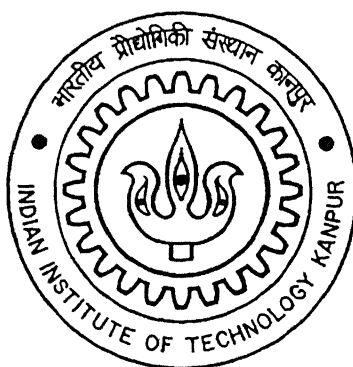
in Partial Fulfillment of the Requirements

for the Degree of

Doctor of Philosophy

by

Prahallad Padhan

to the

DEPARTMENT OF PHYSICS
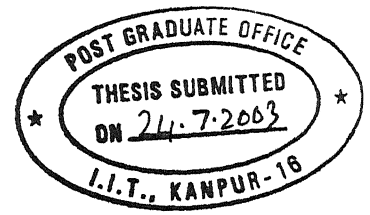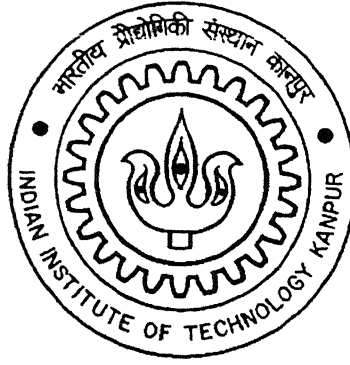## INDIAN INSTITUTE OF TECHNOLOGY KANPUR
JULY, 2003

TH
PHY/2003/D
P13ι
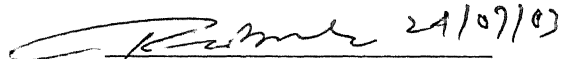
CERTIFICATE

It is certified that the work contained in this thesis entitled *"Interlayer exchange coupling and colossal magnetoresistance in transition metal oxide based thin film superlattices"*, by *Prahallad Padhan*, has been carried out under my supervision and that this work has not been submitted elsewhere for any degree.

24/07/03

Dr. R. C. Budhani

Professor

Department of Physics

Indian Institute of Technology

Kanpur

July, 2003

synopsis

Title :   Interlayer exchange coupling and colossal magnetoresistance in transition metal oxide based thin film superlattices.

Name of the student	:	Prahallad Padhan
Registration number	:	9610976
Degree for which submitted	:	Doctor of Philosophy
Department	:	Physics
Thesis Supervisor	:	Prof. R. C. Budhani
Month and Year of submission	:	June 2003

Magnetic thin films, thin film heterostructures and superlattices have generated tremendous technological and scientific interest in recent years. Fascinating effects such as giant magnetoresistance, oscillatory exchange coupling, tunneling magnetoresistance and magnetocrystalline anisotropy have been discovered in such artificial structures. These effects find applications in a variety of technologies such

as magnetic data storage, magnetic memories, magnetic sensors etc. The field of magnetic thin films is also being enriched by the discovery of new materials such as half metallic ferromagnets, layered perovskites and dilute magnetic semiconductors. In this thesis we focus on interlayer exchange coupling (IEC) and giant magnetoresistance (GMR) in thin film multilayers of transition metal oxides.

While the phenomena of IEC and GMR have been studied extensively in the case of $3d$ - transition metal based superlattices such as $Fe - Cr$, studies of the effects of artificially introduced periodicity on transport and magnetization in oxide-based multilayers is an emerging field of research. This thesis focuses on two types of superlattices of the ferromagnetic manganite $La_{0.7}Ca_{0.3}MnO_3$ ($LCMO$). In one case the spacer thin films are of $LaNiO_3$ (LNO) which is a metallic and non-magnetic perovskite with good lattice match with $LCMO$. The spacer material in the second multilayer system is $Er_{0.7}Sr_{0.3}MnO_3$ ($ESMO$) which has paramagnetic and insulating ground state.

In chapter 1 of the thesis, we review some basic aspects of transport and magnetism in $3d$ - transition metal-based superlattices. This is followed by a summary of some general properties of the mixed valence manganites and recent research on magnetic ordering and magnetotransport in a variety of manganite based thin film heterostructures and multilayers.

Chapter 2 describes the methodology used to prepare laser ablation targets and fabrication of thin films and multilayers using pulsed laser deposition. This is followed by a description of instrumentation developed and used to study the structural and physical properties of thin films and multilayers.

Chapter 3 presents detailed studies of thickness dependence of the resistivity and magnetoresistance in thin films of $La_{0.7}Ca_{0.3}MnO_3$. The structural and physical properties of thin films of the perovskite manganites depend sensitively on deposition parameters, crystallinity, strain and thickness. We have monitored the change in lattice parameter due to lattice mismatch induced strain and thicknesses using $X-$ray diffraction. These changes in the structure affect resistivity and magnetoresistance

of the films. We note that at lower thickness the resistivity of the films is highly sensitive to the substrate induced stress and roughness. These factors manifest themselves as enhanced residual resistivity, suppressed T_C and insulating behavior at low temperatures. We also note that the overall quality of films is better on $SrTiO_3$ substrate. It improves further, if a TiO_2 terminated surface is realized through suitable etching.

Chapter *4* deals with the characterization of thin films of $LaNiO_3$ and $Er_{0.7}Sr_{0.3}MnO_3$ used as spacer layers in the superlattices. The nicolate is a paramagnetic metal while $Er_{0.7}Sr_{0.3}MnO_3$ is a paramagnetic insulator. These compounds show negligible change in resistance in the presence of a magnetic field. We compare the resistivity of ultra - thin films of $LaNiO_3$ deposited on $LaAlO_3$ with $SrTiO_3$ and $La_{0.7}Ca_{0.3}MnO_3$ buffer layers.

Chapter *5* describes the crystallographic structure, and the temperature and magnetic field dependent resistivity of $LCMO/LNO$ superlattices grown on $LaAlO_3$ and $SrTiO_3$ substrates as a function of spacer layer thickness. The normal-to-the-plane lattice parameter of the superlattices deposited on $LaAlO_3$ approaches the bulk value as the spacer layer thickness increases. While on $SrTiO_3$ it shows a negligible variation. The electron transport in superlattices with the spacer layer thickness $\leq$ *4 unit cell* is characterized by a thermally activated resistivity and a large magnetoresistance at low temperatures. As the spacer layer thickness increases above *four unit cell*, the thermally activated behavior is suppressed. A parallel resistor model, which explicitly takes into account the interfacial disorder in each unit of the superlattice, correctly reproduces the broad features of the resistivity curves. The field dependent resistivity for samples with lower spacer layer at lowest temperatures show a magnetorelaxor - type of behavior.

In chapter *6* we present the changes in magnetization and magnetotransport properties as the magnetic layer thickness is increased to *20 u.c.*. Here the electronic transport shows a transition from the transport behavior of the ferromagnetic layer to that of the non-magnetic spacer layer as the spacer layer thickness increases from *1 u.c.* to *10 u.c.*. The saturation field and remnant magnetization show antiferromagnetic

interlayer coupling for $n \approx 2$ followed by an overdamped oscillatory behavior with period of ~ 4 u.c. with the increasing spacer layer thickness. The low temperature magnetoresistance of the antiferromagnetically - coupled superlattices is characterized by a steep increase up to a critical field, whereas in the ferromagnetically coupled samples the magnetoresistance rises monotonically.

In chapter 7 we examine the perpendicular-to-plane magnetoresistance of the LCMO/LNO superlattices by sandwiching them between two $YBa_2Cu_3O_7$ electrodes. The perpendicular-to-plane magnetoresistance in the temperature window of 20 K to 80 K is larger by a factor ~ 15 compared to the magnetoresistance parallel to film plane.

In chapter 8 we report electrical and magnetic behavior of LCMO/ESMO superlattices. The magnetoresistance at the lowest temperatures rises with the increase in spacer layer thickness, and approaches ~ 100 % in samples with 10 u.c. thick spacer layer. At the lowest temperatures the magnetoresistance also shows a steep increase up to a critical field which shifts to the higher values with the increasing spacer layer thickness. These samples also show a giant loss of magnetic moment per Mn site in $La_{0.7}Ca_{0.3}MnO_3$, as the spacer layer thickness is increased. This phenomenon is a signature of spin frustration at interlayer. In these samples the zero-field-cooled hysteresis loop is symmetric around the zero field and field-cooled hysteresis loop shifted towards the negative fields.

In chapter 9 we present the summary of the work and identify scope for further research.

Acknowledgements

Pre-doctoral requirements and thesis research are the unbroken structure of PhD program in IITK. The pre-doctoral period, is the indelible part of my PhD program because of the following two reasons; (*i*) on several occasions the physicist have shown how they make the academic status of a student, and (*ii*) without my concern DPGC members have decided my research project and that was developed the worst part of my PhD program. I was at the rim to leave IITK. Before coming to final decision I have met to a physicist who can make the good academic record of a student, this thesis is an example.

All of the work described in this thesis grew from the inspirations and suggestions of Professor Ramesh Chandra Budhani. Under his supervision I have gained experience in design and fabrication of cryogenic experiment. I am fortunate to work with him with broadening opportunities. I would like to express my deep and sincere gratitude to Professor Budhani.

I would like to thank R. P. S. M. Lobo of Laboratoire de Physique du Solide, Ecole Suprieure de Physique et Chime Industrielles de la Ville de Paris, CNRS UPR 5, 75231 Paris Cedex 5, France for measuring magnetization.

I am very grateful to Profs. Alak Kumar Majumdar, Vishwas N. Kulkarni, K. P. Rajeev, V. Subrahmanyam for their suggestions and advices at several occasions.

I sincerely thank to all post doc fellows, research scholars, research assistants and M.Sc. students of my laboratory who made possible and successful outcomes of this research project.

I express my thanks to the people of physics office, physics workshop, central workshop, glass-blowing center, and liquid helium plant and liquid nitrogen plant for their vital support at several occasions to make the project successful.

Finally I would like to thank my parent, sisters and brother for raising me in an environment where creativity and a love for education were encouraged. I would especially like to thanks for the efforts of my family during the self-finance stage of my doctoral program.
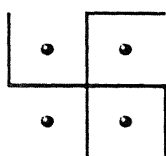
Prahallad Padhan

To

  My Parents

List of Publications

- Prahallad Padhan and R. C. Budhani.
  Perpendicular-to-plane magnetoresistance in $La_{0.7}Ca_{0.3}MnO_3/LaNiO_3$ superlattices: The effects of interfacial disorder and spin diffusion on charge transport.
  (Communicated)

- Prahallad Padhan, R. C. Budhani and R. Lobo
  Overdamped interlayer exchange coupling and disorder dominated magnetoresistance in $La_{0.7}Ca_{0.3}MnO_3/LaNiO_3$ superlattices.
  (Europhysics Lett. in Press)

- Prahallad Padhan and R. C. Budhani
  Interfacial disorder driven metal-insulator transition and enhanced low temperature magneto resistance in $La_{0.7}Ca_{0.3}MnO_3/LaNiO_3$ superlattices.
  Phys. Rev. B 67, 024414 (2003)

- Navneet K. Pandey, Prahallad Padhan and R. C. Budhani
  Percolative transport in the vicinity of charge - order ferromagnetic transition in a hole-doped manganites.
  PRAMANA - journal of physics, 58, 1075 (2002)

- R. C. Budhani, N. K. Pandey, P. Padhan, S. Srivastava and R. Lobo
  Electric and magnetic field driven non-linear charge transport and magnetic ordering in epitaxial thin films of $PrCaSrMnO_3$.
  Phys. Rev. B 65, 14429 (2002)

- P. Padhan, N. K. Pandey, S. Srivastava, R. K. Rakshit, V. N. Kulkarni and R. C. Budhani
  Transition from double exchange ferromagnetic metal to hysteretic insulator mimicking charge-ordering effects in ultra thin films of a perovskite manganite.
  Solid State Commun. 117, 27 (2001)

- S. Srivastava, N. K. Pandey, P. Padhan and R. C. Budhani
  Current switching effects induced by electric and magnetic fields in Sr-substituted in $PrCaMnO$ films.
  Phys. Rev. B 62, 13868 (2000)

Contents

List of Figures

Chapter 1

Introduction

1.1 Introduction

Magnetic thin films, thin film heterostructures and superlattices have generated tremendous technological and scientific interest in recent years. Fascinating effects such as giant magnetoresistance, oscillatory exchange coupling, tunneling magnetoresistance and magnetocrystalline anisotropy have been discovered in such artificial structures. These effects find applications in a variety of technologies such as magnetic data storage, magnetic memories, magnetic sensors etc. The field of magnetic thin films is also being enriched by the discovery of new materials such as half metallic ferromagnets, layered perovskites and dilute magnetic semiconductors. In this thesis we focus on interlayer exchange coupling (IEC) and giant magnetoresistance (GMR) in thin film multilayers of transition metal oxides.

Interlayer exchange coupling is an interaction between two ferromagnetic (FM) layers separated by a non-magnetic spacer layer that, for small external field, causes the layer magnetization to align either ferromagnetically or antiferromagnetically. P. Gruenberg et al. [1] showed, for the first time, evidence of antiferromagnetic (AF) coupling of Fe layers across Cr spacer layers by means of light scattering from spin waves. The interlayer exchange coupling was also reported in *1986* in layered structures of dysprosium [2] and gadolinium [3] separated by yttrium spacer

and for iron [1] film separated by chromium spacer. Exchange coupling in super-lattice structures consisting of alternate ferromagnetic and antiferromagnetic layers has also been studied theoretically. The field of magnetotransport and interlayer magnetic coupling received renewed interest with the discovery of giant magnetoresistance in Fe/Cr multilayers. A careful investigation of interlayer exchange coupling and magnetoresistance (MR) was carried out by Parkins et al. [4] in $Fe/Cr/Fe$ and $Co/Ru/Co$ multilayers. The interlayer exchange coupling in these systems showed a remarkable oscillatory behavior with the increasing spacer layer thickness. The MR in $Fe/Cr/Fe$ and $Co/Ru/Co$ systems also shows oscillations with the increasing spacer layer thickness and the period of oscillations matches with the period of the IEC [4]. A large negative magnetoresistance when IEC is antiferromagnetic indicates ease in spin diffusion through the spacer as magnetization vectors of the neighboring ferromagnetic layers are made parallel by the external magnetic field. It is now believed that antiferromagnetic interlayer exchange coupling is not a necessary requirement for large magnetoresistance. The magnetoresistance is large even when the magnetizations of each layer originate randomly with a net zero spontaneous moment of the multilayer. The fundamental spin - polarized transport in multilayers involves: (i) spin - dependent mean free path, (ii) spin - dependent transmissivity at the ferromagnet - nonmagnet interfaces, (iii) differential rates of scattering both within the ferromagnetic layers and at the ferromagnetic - nonmagnetic interfaces for electrons with spin along and opposite to the local magnetization, (iv) rate of loss of spin memory in the ferromagnetic layers, nonmagnetic layers and at their interfaces and (v) rate of mixing of spin polarized currents. The role of interfaces and how the metallurgical and magnetic disorder affects magnetoresistance is still an active field of research in the case of metallic superlattices.

In this chapter we present a brief overview of the theoretical and experimental investigations of transition metal superlattices and the superlattice structures consisting of metal oxides. This chapter also presents a summary of the structural and physical properties of the manganese based perovskite oxides. Finally we present the motivation for undertaking this study followed by the outline of each chapter of the thesis.

1.2   Transition metal superlattices

1.2.1   The mechanism of oscillatory exchange coupling

There are several theoretical approaches to explain the oscillatory nature of interlayer exchange coupling in $3d$ - transition metal based magnetic multilayers. Total energy calculations and model calculations are two principal theoretical approaches. There are several model calculations such as: (i) the quantum well theory (QWT) of Edwards et al. [5], (ii) an extension of Ruderman - Kittel - Kasuya - Yosida ($RKKY$) theory adapted to the multilayer geometry by Bruno and Charppert [6], (iii) the free electron model [7], (iv) the hole confinement model [8] and (v) Anderson (or sd – mixing) model [9, 10]. These models relate the oscillation periods, in the limit of large spacer thicknesses, to the Fermi surface parameters of the bulk spacer material.

In the quantum well theory of Edwards [5], the ferromagnetic layers form the barriers and the non-magnetic layer forms the well of this quantum well system. An interplay between magnetic and electric degrees of freedom occurs because the barrier height is spin independent. The interference between the disturbances in the electron density in the nonmagnetic spacer, arising from the coupling to the two ferromagnetic layers, is treated exactly in the QWT.

In the $RKKY$ formalism, localized magnetic moments in a metal can interact magnetically with the conduction electrons. This interaction propagates between different magnetic sites via these electrons. In *1954* Ruderman and Kittel [11] proposed the coupling between two nuclear spins via their hyperfine contact interaction with the conduction electrons. Kasuya and Yosida [12] developed and extended similar coupling between two localized d - electrons via their mutual coupling to the conduction electrons. The mechanism has become known as the $RKKY$ theory. When it is adapted to magnetic multilayers, the periods in oscillation are associated with the wave vectors perpendicular to the layer linking two points of the Fermi surface with antiparallel velocities. The $RKKY$ theory involves exchange coupling between the bulk magnetic moment of the magnetic layers and the spin of the conduction electrons in the interlayer, and correctly predicts an oscillatory interlayer coupling.
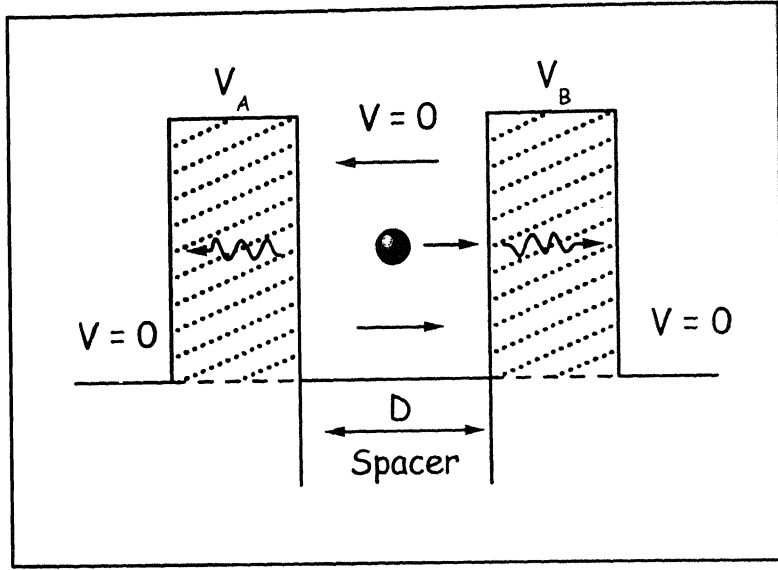
Figure 1.1: Schematic representation of the sandwich system.

Bruno [13] has explained the oscillation in interlayer exchange coupling by taking into account spin - dependent reflectivity of Bloch waves (i.e. itinerant electrons) at the paramagnet - ferromagnet interfaces. He has calculated the interlayer exchange coupling for a sandwich of two ferromagnetic films separated by a *PM* metal film. The simple one dimensional representation of this sandwiched system is shown in the Fig. *1.1*. It consists of a spacer layer of width '*D*' and potential zero, sandwiched between two potential perturbations '*A*' and '*B*' with potential heights V_A and V_B respectively. Outside the perturbation the potential is zero. For positive potential perturbation it represents barriers while for negative potential perturbation it represents potential wells. The conduction electrons in the spacer layer are represented by Bloch waves of momentum $\vec{k_i}$. The Bloch wave of momentum $k_\perp$ (> 0) undergoes reflection on reaching the paramagnetic - ferromagnetic interface. The reflection coefficient can be written as $r_B = |\vec{r_B}| e^{i\Phi_B}$. This wave of momentum $\vec{k_r}$ ($k_\perp < 0$) undergoes further reflection at the interface A with reflection coefficient $r_A = |\vec{r_A}| e^{i\Phi_A}$. The interference between these reflected waves in the non - magnetic spacer leads

to oscillation in the electronic density. The phase shift of the wave function after a complete round trip in the spacer is $\Delta\Phi = 2k_\perp D + \Phi_A + \Phi_B$. The density of states in the spacer will increase for constructive interference ($\Delta\Phi = 2n\pi$) and will decrease for destructive interference ($\Delta\Phi = (2n+1)\pi$). Thus the change of density of states due to interferences, $\Delta n(\epsilon)$ should vary like $cos(\Delta\Phi)$ and should be proportional to the strength of reflections on A and B i.e. $|\vec{r_A} \cdot \vec{r_B}|$, to the spacer width D, to the density of states per unit length and energy $\frac{2}{\pi}\frac{dk_\perp}{d\varepsilon}$. Thus the expression for the change in the density of states is [13],

$$\Delta N \approx \frac{2}{\pi} Im \left(r_A \ r_B e^{2ik_\perp D} \right),\tag{1.1}$$

where the factor 2 accounts for the spin degeneracy. The energy derivative of the reflection coefficients has been neglected compared to the energy derivative of the exponential factor. It is valid when the reflection coefficients are small, so that higher order terms may be neglected. On the other hand if $|r_A| = |r_B| = 1$, the interferences lead to bound states and the wave vector $k_\perp$ is quantized; the bound states occur when the interferences are constructive i.e. when $\Delta\Phi = 2n\pi$. As 'D' increases the bound states move towards lower energy and the integrated density of states jump each time a bound state has energy ϵ. The expression for change in the integral density of states due to quantum interference is [13],

$$\Delta N \approx -\frac{2}{\pi} Im \ ln(1 - r_A \ r_B e^{2ik_\perp D}),\tag{1.2}$$

when $|\vec{r_A} \cdot \vec{r_B}|$ is small, this expression reduces to Eq. (1.1).

Bruno [13] has estimated the change in energy due to quantum interferences in the spacer at $T = 0$. Thus the energy change due to quantum interferences is;

$$\Delta E = - \int_{-\infty}^{\varepsilon_F} \Delta N(\varepsilon)\, d\varepsilon$$

$$\Delta E = \frac{2}{\pi} Im \int_{-\infty}^{\varepsilon_F} ln(1 - r_A \ r_B e^{2ik_\perp D}) \ d\varepsilon.$$

For small confinement, this becomes

$$\Delta E = - \frac{2}{\pi} Im \int_{-\infty}^{\varepsilon_F} r_A \ r_B e^{2ik_\perp D} \ d\varepsilon.\tag{1.3}$$

ΔE is the coupling energy between the layers A and B. Since the potential depends on the coordinate in the direction normal to the layers, the coupling energy for a three dimensional system is

$$\Delta E \approx -\frac{1}{2\pi^3} \, Im \int d^2 \vec{k_\parallel} \int_{-\infty}^{\varepsilon_F} r_A \, r_B \, e^{2ik_\perp D} \, d\varepsilon. \qquad (1.4)$$

The reflection coefficient at the paramagnet - ferromagnet interfaces depends on the direction of the electron spin with respect to the direction of the magnetization in the ferromagnet. The exchange coupling energy per unit area at $T = 0$ is $E_{AB} = \Delta E_F - \Delta E_{AF}$, where ΔE_F and ΔE_{AF} are energies due to the interferences when the magnetization vectors of the FM layers are aligned ferromagnetic and antiferromagnetic respectively.

$$E_{AB} = -\frac{1}{\pi^3} \, Im \int d^2 \vec{k_\parallel} \int_{-\infty}^{\varepsilon_F} \Delta r_A \, \Delta r_B \, e^{2ik_\perp D} \, d\varepsilon, \qquad (1.5)$$

where $\Delta r = \frac{r^\uparrow - r^\downarrow}{2}$ is the spin asymmetry of the reflection coefficient with $r^\uparrow$ and $r^\downarrow$ being the spin-up and spin-down reflection coefficients respectively. The variation of exchange coupling energy with the spacer thickness depends on the spacer material (via $k_\perp$) whereas the strength and phase are determined by the spin asymmetry of the reflection coefficient at the ferromagnetic - paramagnetic interfaces. When the magnetization vectors of the magnetic layers are at angle θ, the exchange coupling $E_{AB}(\theta)$ is proportional to $cos(\theta)$. The expression for $E_{AB}(\theta)$ has been expanded in powers of $cos(\theta)$ as;

$$E_{AB}(\theta) = J_0 + J_1 \, cos(\theta) + J_2 \, cos^2(\theta) + \cdots \cdots \cdots, \qquad (1.6)$$

where J_0 is the nonmagnetic coupling constant, J_1 the Heisenberg coupling constant and J_2 the biquadratic coupling constant. Bruno [13] has given the expression for J_1 using a simple free electron model for a semi - infinite magnetic layer in the limit of large spacer thickness. The leading contribution for J_1 is,

$$J_1 = \frac{\hbar^2 k_F^2}{4 \pi^2 \, m \, D^2} \, Im \left(\Delta r_\infty^2 \, e^{2ik_F D} \right), \qquad (1.7)$$

where $k_F = \sqrt{2m(\varepsilon_F - U)}$ for $\varepsilon_F > U$ and $k_F = i\sqrt{2m(U - \varepsilon_F)}$ for $\varepsilon_F < U$. Here ε_F and U are the Fermi energy and potential of the spacer layer respectively. The thickness dependence of coupling is driven by the factor $e^{2ik_F D}$; thus the coupling oscillates for a metallic spacer (k_F- real) thickness and decays exponentially for an insulating spacer (k_F- imaginary) as its thickness is increased.

These calculations are for flat interfaces, whereas real samples always have misfit dislocations due to lattice mismatch of a layer with the underlying layer and surface roughness because of imperfect growth modes. To incorporate roughness at the interfaces, Bruno and coworkers have taken into account fluctuations in the spacer layer thickness. They observe attenuation of oscillations with increasing roughness and disorder [14]. Wang et al. [9] have calculated the magnetic coupling of two iron layers separated by a chromium layer taking into account the roughness of the interfaces. They have considered a system where the chromium is in the paramagnetic state with two rough planes of iron embedded in its surface. Yafet [15] has successfully explained the interlayer exchange coupling in Gd/Y superlattices using this configuration.

1.2.2   The mechanism of giant magnetoresistance

The GMR effect is observed as a response to currents flowing either in-the-planes (CIP) or perpendicular-to-the-planes (CPP) of the superlattices. The advantage in CPP geometry is that all carriers contributing to current are forced to pass through the interfaces as well as the bulk. This makes the current distribution uniform and permits application of a series resistance model in which contribution from individual constituent and the interfaces are summed. This CPP measurement is, however, quite non-trivial because of the extremely small resistance of the metallic samples. In the CIP configuration the dimensions are macroscopic and $four - probe$ measurement techniques are used. In contrast, CPP measurements are usually carried out with $two - probe$ using sophisticated techniques to measure the small resistance. There are several methods to measure $CPP - GMR$. Because of the very small layer thickness, these fall into two major categories: (i) use of very sensitive techniques to measure small resistance, and (ii), increase the resistance by reducing the area through which current flows. In the case of $3d$ - transition metal based superlattice

CPP resistance has been measured by lithographic patterning of multilayers in the form of columns of small cross sectional area [16]. In order to increase the resistance to a measurable value, several hundred alternate layers of constituents are deposited. However, stacking of such large number of units makes the interfaces increasingly disordered. The *CPP* resistance and *MR* have also been measured by sandwiching the superlattice between two thin - film electrodes of niobium in their superconducting state [17]. While this method allows measurements of *CPP* magnetoresistance of thin film multilayers, its applicability is limited due to the low critical temperature ($\sim$ *9.2 K*) and upper critical field ($\sim$ *1 KGauss*) of *Nb*. The *GMR* of *3d* - transition metal based magnetic multilayer in *CPP* – geometry is described by the two current series resistor model. In this model, the resistance of a multilayer is obtained by dividing the current into independent spin-up and spin-down contributions and calculating the resistance each current encounters in both the parallel and anti-parallel states. To calculate the *GMR* one adds up the resistance contributions in series for each current channel and combine them as two overall resistors in parallel. When the resistances from both the parallel and antiparallel magnetic states are known, a simple calculation of the specific resistance ΔR_S = *Area* $\times$ (*R(Antiparallel)* − *R(Parallel)*). This theory has two forms based on the relative size of the spin diffusion length and layer thickness [18, 19].

Several mechanisms have been proposed to understand the *GMR* in transition metal based artificially layered materials. The main mechanism for the phenomenon is considered to be spin - dependent scattering of charge carriers at the interfaces. Spin - dependent scattering has been postulated to be a dominant resistance mechanism in bulk ferromagnets since the work of Mott [20]. In the presence of a magnetic field, the spin-flip process can not easily invert a given spin orientation. Considering only parallel and antiparallel orientations, the total current can be viewed as consisting of two components flowing in parallel, one with spin-up (parallel to magnetization) and the other with spin-down (antiparallel to magnetization). Electrical resistivity is proportional to electron scattering rates. If scattering rates for spin-up and spin-down electrons are different then the resistivity of the two kinds of currents will be different. This is the basis of Mott's two currents model. Conduction electrons with spin parallel

to the layer magnetization are scattered weakly close to the layer, carrying current more effectively and leading to low resistance, and those with spin antiparallel to the magnetization are scattered strongly, leading to high resistance. The other physical mechanism to describe GMR is based on the quantum well theory and the reflectivity of the itinerant electrons at the interfaces. The quantum well states and especially the formation of interface states in magnetic superlattice give rise to strong interface scattering, which leads to large GMR amplitudes.

Fuchs [21] and Sondheirmer [22] have given a theoretical model for resistivity of thin film due to surface roughness. Carcia and Suna [23] have extended this approach to multilayers. Using this quasiclassical approach with the spin - dependent scattering at the interfaces as well as in the bulk, Camley and coworkers [24] have analyzed the large magnetoresistance of iron - chromium multilayers. The interface roughness is assumed to act as the source of spin - dependent scattering. This approach reproduces the general trends of transport as a function of temperature, thickness and number of interlayers. Camley et al. [24] have also shown that the resistivity of multilayers increases as magnetization of the ferromagnetic layer rotates from parallel to antiparallel alignment. Levy and Zhang [25] have used a quantum approach to determine electrical transport in multilayers. They have considered surface roughness scattering from an array of interfaces, by making the scattering spin - dependent. The bulk and interface scattering are treated by introducing bulk and interface scattering potentials. This model agrees with the magnetoresistance data on the iron - chromium system. Xing and coworkers [26] have proposed that the strong spin - dependent scattering also comes from the spin-split density of states for majority and minority spin d - band in the magnetic layers and occurs both in the bulk and at the interfaces. These models are for the multilayers with the current parallel to the layers.

Mark Johnson [27] has given a formalism for magnetoresistance based on spin transport by conduction electrons across the interfaces of magnetic and nonmagnetic layers of a sandwich structure. His model consists of two - single domain ferromagnetic metal films (f_1 and f_2) of thickness d_f separated by a nonmagnetic metal film (P) of thickness d_P as shown in the inset of Fig. 1.2. The spin diffusion length (i.e. the

average distance that a conduction electron diffuses before the direction of its spin is changed) is given as; $\delta_i (i = f, P) = (2 D_i T_{2i})^{0.5}$, where D_i is the conduction electron diffusion constant and T_{2i} the spin relaxation time. In his calculation, the thickness of the nonmagnetic spacer layer is less than the spin diffusion length ($d_P < \delta_i$), and the magnetization of the magnetic layers are constrained to lie in the film plane. The magnetization of f_1 points up, while the magnetization of f_2 is considered in up as well as down configuration. The density of states of the films at zero temperature and zero current is shown in the upper part of Fig. 1.2. The Stoner model based density of states is shown for the ferromagnetic layers and the nonmagnetic metal film is depicted with parabolic sub-bands. When the current is zero, the Fermi level of the magnetic and nonmagnetic metal at the interfaces are aligned. When a steady state current I is applied through the films from f_1 to f_2, charge transport involves only electrons near E_F, and in f_1 only electrons in the up-spin sub-band are available for transport. If there is no spin flipping, the total current that passes across the interface is sum of the charge current (I_e) and I_M the current due to magnetization ($I = I_q + I_M$), where $I_M = \frac{1}{ek_B T} I_e$, 'e' is the charge of the electron and K_B is the Boltzman constant. In the steady state the up-spin sub-band of the paramagnetic spacer gains population and the down-spin sub-band adjusts in order to maintain charge neutrality. The up-spin sub-band chemical potential is raised above its equilibrium value and this causes a nonequilibrium magnetization $\widetilde{M} = \beta \, \Delta n$, where Δn is the difference in number density of carriers between up-spin and down-spin sub-bands. The rise of up-spin chemical potential in the paramagnetic spacer will have a back effect on f_1, raising its chemical potential. If the magnetization of f_2 is parallel to that of f_1 then its chemical potential will also rise to align with that of the up-spin band of the spacer. There is no voltage drop across the sandwich in this configuration. The density of states of these films in this configuration is shown in the lower part of Fig. 1.2. If the magnetization of f_2 is antiparallel to that of f_1, then its chemical potential will align with that of the down-spin sub-band of the spacer. The chemical potential of f_2 is lowered with respect to the equilibrium and a voltage drop takes place across the sandwich. This voltage is linear with current and is identified as a spin-coupled resistance (R_S).
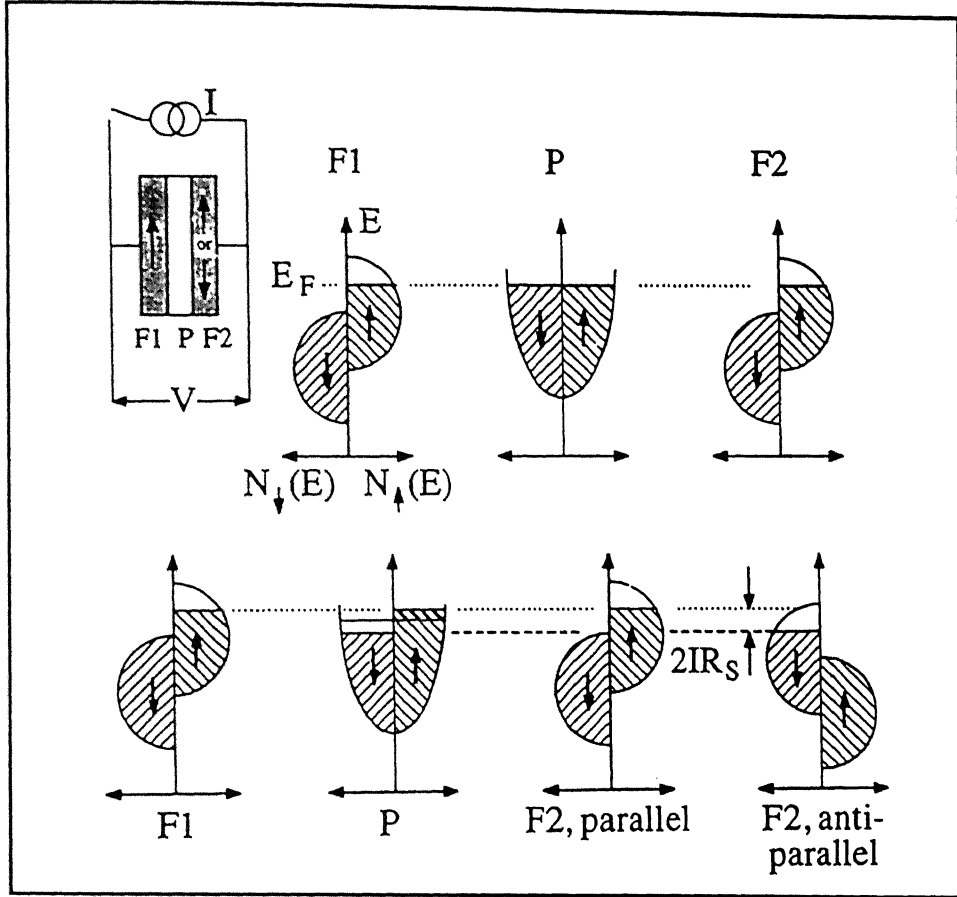
Figure 1.2: Model of density of states of two ferromagnetic films in interfacial contact with a paramagnetic film. Top: In equilibrium the Fermi levels align. Bottom : When a current is driven through the sandwich the voltage drop across the trilayers depends on the orientations of the magnetization of the ferromagnetic films. Inset : Configuration of the measurement and the sandwich structure. (Figure reproduced from [27].)

Johnson [27] has calculated the resistance for a multilayer composed of n bilayers of ferromagnetic metal with bulk conductivity σ_f and nonmagnetic metal with bulk conductivity σ_P which form an interface with conductance G. For the parallel configuration of the magnetization of f_1 and f_2 the resistance per bilayer is $R' = \left(\frac{d_f}{\sigma_f}\right) + \left(\frac{d_P}{\sigma_P}\right) + \left(\frac{2}{G}\right)$, whereas for antiparallel configuration the resistance of the bilayer is $R = 2R_S + R'$ and magnetoresistance is given by $MR = \frac{2R_S}{R'}$. If the magnetization of f_1 and f_2 are oriented at an angle θ then the spin couple resistance is

$2R_S sin^2\left(\frac{\theta}{2}\right)$. If $d_P > \delta_P$ then the nonequilibrium magnetization in P will be smaller and R_S will decrease exponentially. Interface resistance is expected to contain contributions from interfacial alloying, scattering from spin - dependent potential step at the interface and scattering from interfacial states. This effect does not appear in the CIP geometry because there is no net charge or spin transport through the interfaces and therefore no spin accumulation.

In the model of Verlet and Fert [18] the current density is proportional to spin - dependent electrochemical potential where the proportionality constant includes contributions from electron reflections by the potential step and from diffuse scattering by disorder at the interfaces. The model assumes incoherent scattering by the successive interfaces. Barnas and Fert [28] have calculated the interfacial resistance for perpendicular transport in magnetic multilayers within the Landauer approach. They have assumed that the spin - dependent interface resistance is due to electron reflections and refractions at an interface potential step between ferromagnetic and nonmagnetic metal as well as the impurities located at the interfaces. Their calculation is based on the interfacial potential steps and the impurity concentration. When the electron scattering at the successive interfaces is incoherent these two contributions are comparable. Barnas et al. [28] have theoretically analyzed the in-plane electronic transport in ultrathin metallic magnetic structures composed of two ferromagnetic films separated by a nonmagnetic metallic spacer. They have considered the role of quantum size effects and interface roughness on magnetoresistance. Within the one-band model, they have predicted two different oscillation periods in the resistivity and magnetoresistance as a function of the spacer thickness. It is also shown that the spin - dependent scattering due to interface roughness can enhance or reduce the magnetoresistance generated by the spin - dependent scattering at impurities or other defects inside the films. Zhang and Levy [29] have also derived the conductivity of multilayers for the CPP geometry. Their treatment is based on the Kubo formalism. They have compared the CIP and CPP conductivities and magnetoresistances. For mean-free-paths much larger than the thickness of a multilayer, the CIP and CPP conductivities are the same. This is to be expected because the inhomogeneities of the system do not show up in this limit. They have determined different parameters (spin

- independent mean free paths in the bulk, mean free path due to interface scattering and the spin - dependent scattering ratio at the interfaces and in the iron layers), which best fit the experimental data of Ref. *30* for the *CIP* magnetoresistance. They have calculated *CIP* and *CPP* magnetoresistance for iron - chromium multilayer using the same set of parameters. The *CPP* magnetoresistance is larger and decreases much more slowly, as the thickness of the layers (various thickness of *Cr* (*Fe*) layer for fixed *Fe* (*Cr*) layer thickness) increases. Ioth et al. [*31*] have presented the cell coherent potential approximation method for the origin of *CIP* and *CPP* magnetoresistance in magnetic multilayers. They have treated the randomness at the interfaces and layered structure simultaneously. The *CPP* magnetoresistance is larger than the *CIP* magnetoresistance in this case also.

There are many experimental studies which deal with correlation between giant magnetoresistance and interface roughness. Parkin [*32*] has measured the *MR* of magnetic - nonmagnetic multilayers in which a thin magnetic layer of different ferromagnetic material is present at the interfaces. These samples show enhanced magnetoresistance. The magnitude of the *MR* depends on the magnetic nature of the material at the interfaces. He has suggested that the giant magnetoresistance arises from spin - dependent scattering from magnetic impurities localized at the interfaces. Baumgart et al. [*33*] have made similar structures by depositing a thin layer of a variety of elements (*V, Mn, Ge, Ir* and *Al*) at the interfaces of iron - chromium multilayers. They conclude that the total number of spin - dependent scattering centers at the interface, not the details of the interface structure, dominates the magnetoresistance properties. Schuller and coworkers [*34*] have studied the transport properties of iron - chromium multilayers by introducing roughness at the interfaces through changes in the deposition parameters and annealing. The samples annealed at moderate temperature show less correlated interface roughness and slight interdiffusion. This increases the resistivity and magnetoresistance. Schuller et al. [*34*] note that in cobalt - copper multilayers annealing leads to a decrease in the magnetoresistance in contrast to the increase on annealing seen in iron - chromium multilayers. Belien et al. [*35*] have studied the influence of interface roughness on giant magnetoresistance of polycrystalline *Fe/Cr* superlattices grown by molecular beam epitaxy (*MBE*)

on polycrystalline substrates. X − ray diffraction spectra, combined with resistivity data, show that a moderate atomic step density at the interfaces can enhance the magnetoresistance, whereas interdiffusion and interface roughness strongly suppress the magnetoresistance.

1.3   Transition metal perovskite oxide superlattices

The discovery of *GMR* and oscillatory exchange coupling in transition metal based multilayers have prompted researchers to look for similar effects in thin film multilayers of transition metal compounds. Multilayers of magnetic oxides such as the hole-doped manganites, ruthenates, and Fe_3O_4, separated by spacer layers of diverse conductivities and magnetic properties, have been tried [36-44]. However, unlike the case of elemental superlattices, measurements of electron transport and magnetic ordering in these systems have generally yielded mixed results. For example, Gong *et al.* [36] have studied the *MR* of $La_{0.67}Ca_{0.33}MnO_3$ and $SrRuO_3$ superlattices as a function of $SrRuO_3$ spacer thickness. Both $La_{0.67}Ca_{0.33}MnO_3$ and $SrRuO_3$ are ferromagnetic metals below their Curie temperatures of $\sim$ *250 K* and $\sim$ *145 K*, respectively. No oscillatory behavior of magnetoresistance is seen as the $SrRuO_3$ spacer thickness is increased from one unit cell (*u.c.*) to *16 u.c.*. However, the saturation field of these superlattices shows non-monotonic behavior. Gong *et al.* [36] attributed it to rotation of the magnetic easy axis on the plane of the multilayer. Orozco *et al.* [37] have reported oscillatory magnetic coupling in multilayers of the ferromagnetic semiconductor Fe_3O_4 and metallic *TiN*. Nikolaev and co-workers [38] have measured the magnetoresistance and magnetic coupling in superlattices of $La_{2/3}Ba_{1/3}MnO_3$ and $LaNiO_3$ (*LNO*). The hole-doped manganite $La_{2/3}Ba_{1/3}MnO_3$ is ferromagnetic with a metal - like conductivity below $T_C \sim$ *340 K*, [45] and the ~~nicolate~~ *LNO* is a metallic paramagnet down to *4.2 K* [46]. In superlattices consisting of a fixed $La_{2/3}Ba_{1/3}MnO_3$ layer thickness ($\sim$ *12 u.c.*), Nikolaev *et al.* [38] observe oscillatory exchange coupling as the *LNO* thickness is varied from *3 u.c.* to *10 u.c.*. While these authors also observe a positive magnetoresistance in antifer-

romagnetically coupled superlattices at *5 K*, oscillations in magnetoresistance that commensurate with the magnetic coupling (Ref. *4*) are not seen. Venimadhav *et al.* [*47*] also reported electrical and magnetic properties of the superlattices consisting of a ferromagnetic manganite ($La_{0.6}Pb_{0.4}MnO_3$) and a metallic but nonsuperconducting cuprate $La_4BaCu_5O_{13+x}$. They observed a monotonic behavior of the Curie temperature and saturation field in these multilayers as the cuprate layer thickness is increased from *1 u.c.* to *8 u.c.*, while keeping the thickness of the manganite fixed at *10 u.c.*. Interestingly, these samples exhibit semiconductor - like resistivity (*negative* $d\rho/dT$) down to *4.2 K*, although thin films of individual oxides are metallic below *300 K*. However, to our best knowledge, similar measurements of resistivity over a broad temperature range in systems where oscillatory coupling is observed are not available. It is certainly of interest to know if the resistivity of such systems is also insulating at low temperatures. The semiconductor - like behavior observed by Venimadhav *et al.* [*47*] suggests disordered interfaces in these thin - film multilayers. A sufficiently disordered interface can suppress the metal - like transport in individual constituents. This disorder can be of magnetic as well as structural origin. The magnetic and structural inhomogeneities at the interfaces can dominate the contribution of fundamental processes such as the Ruderman-Kittel-Kasuya-Yosida interaction and spin - polarized tunneling to magnetic coupling [*48*] and transport in these artificial structures. It is also important to point out that the materials used in such systems are compounds with inherent complexities of narrow bands, short mean free path and electron correlations. These factors may restrict the fundamental processes that are responsible for *GMR* and *IEC* in transition metal - based superlattices. In the following, we provide a brief review of the magnetization and transport in a special class of hole doped transition metal oxides. There are *Mn* – based perovskites. These systems will be the fundamental building block of our superlattices.

1.3.1   Manganese perovskite oxides

The carrier doped perovskite manganites have the general formula $A_{1-x}A'_xMnO_3$, where A is a rare earth and A' an alkaline earth atom. The physical properties of these compounds depend on the choice of the elements A, A' which deter-

mines the average A – site ionic radius and the dopant concentration x. The Mn atoms in the carrier doped manganite have charge states Mn^{3+} and Mn^{4+}. The octahedral crystal field of oxygen ions allows the d – orbital electronic configuration of $t_{2g}^3 \, e_g^1$ and $t_{2g}^3 \, e_g^0$ type for the Mn^{3+} and Mn^{4+} ions. Within a certain range of dopant concentration and average A – site ionic radius, these compounds exhibit large decrease in resistance near the Curie temperature in the presence of a magnetic field. Such large negative magnetoresistance is called the colossal magnetoresistance (CMR). Besides the CMR effect, mixed-valence manganites can exhibit various magnetic, structural, and electronic phase transitions, leading to a complex physical behavior. Manganites are part of a larger class of transition metal oxides with perovskite structure, which include among others high – temperature superconducting copper oxides. All these materials are strongly correlated electron systems in which the electron – electron interaction plays a dominant role. Depending on the choice of the element A and A' mixed – valence manganites form two diametrically opposite but equally fascinating ground states. The ferromagnetic and metallic ground state in $La_{1-x}Ca_xMnO_3$, for example, was studied in the 1950s using transport, magnetization and neutron scattering measurements [49, 50]. Zener [51] has proposed a microscopic theory of ferromagnetism and metallicity in these compounds. His double exchange model (DE) has been refined for dopant concentration, hybridization and spin canted states. Recent studies reveal that the electron transport in the paramagnetic insulating and ferromagnetic metallic states of these compounds is influenced greatly by the propensity of the e_g electron to polarize the lattice and the t_{2g} spins in its vicinity [52]. These studies indicate that the charge carriers in the paramagnetic state are small lattice polarons dressed with a magnetic cloud. The current transport in the paramagnetic state occurs by thermally activated hopping of these polarons. Experimental evidence for the existence of dynamic lattice distortions and the formation of ferromagnetic droplets of size ~ 10 $\mathring{A}$ in the PM state [53, 54] support this polaronic picture. Measurements with techniques which probe the local environment of the Mn ions, such as extended X – ray absorption fine structure ($EXAFS$) [55], suggest that some vestige of the Jahn-Teller lattice distortions remain in the ferromagnetic state as well.

Mixed valence manganites for certain choices of A and A' at half filling ($x = 0.5$), undergoes a Charge Ordering (CO) transition in which Mn^{3+} and Mn^{4+} ions form two interpenetrating pseudo-cubic sublattices [56, 57]. The sublattice structure precludes a charge transfer as it would be self - destructive. The charge ordered state undergoes orbital and antiferromagnetic spin ordering of the CE – type at still lower temperatures. However, for x less than half filling, the antiferromagnetic ordering in the charge ordered state of $Pr_{1-x}Ca_xMnO_3$ is followed by the growth of nanometer size ferromagnetic regions at lower temperatures. These regions have been variedly called as droplets, clusters or stripes [58]. The current transport in the droplet phase is a fascinating field of research as it is susceptible to nucleation, growth and coalescence under external perturbations such as strong magnetic field or pressure [59], X – ray [60], electric field [61] and intense photon flux [62]. In the following sections we discuss some critical properties of these systems in detail.

1.3.1.1 Perovskite Structure

Most of the stoichiometric ABO_3 perovskites exhibit a distortion of the cubic structure. The structure of $AMnO_3$ manganite is shown in the Fig. 1.3. The basic structure of $AMnO_3$ manganite is usually orthorhombic. Here the lattice distortion is caused by deformation of the MnO_6 octahedra arising from the Jahn-Teller effect that is inherent to the high-spin ($S = 2$) Mn^{3+} with double degeneracy of the e_g - orbitals. Another source of distortion in these structures is purely geometric. It comes from the differences in size of the A and Mn ions. The cation size induced lattice distortion is expressed interms of Goldschmit factor: $t = \dfrac{(\langle r_A \rangle + \langle r_O \rangle)}{\sqrt{2} \times (\langle r_{Mn} \rangle + \langle r_O \rangle)}$ with r_A, r_{Mn} and r_O are the ionic radius of A – site element, manganese and oxygen respectively. The tolerance factor 't' is unity for a perfect cubic perovskite. It decreases when the ionic radius of A – site is too small to fill the space at the cube center. This makes the oxygen move towards the center. The $Mn - O - Mn$ bond is bent and the angle becomes smaller than $180°$. This bond angle distortion decreases the overlap between the orbitals and narrows the energy band. If the A – cation size is large, tolerance factor increases and the space available for Mn – ion in its MnO_6 is large.
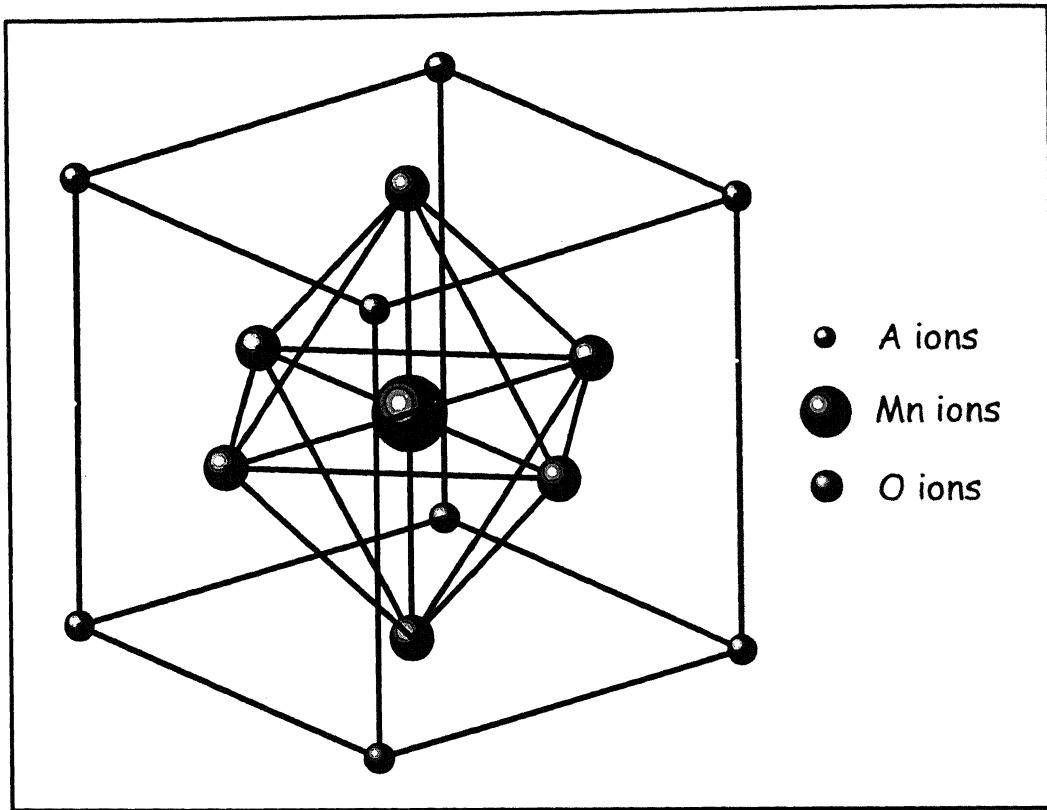
Figure 1.3: Schematic representation of $AMnO_3$ perovskite manganite structure.

1.3.1.2   Electronic structure

Atomic orbitals in a solid form bands due to their overlap and the periodic potential of the lattice. The overlap of orbitals of neighboring atoms determines the strength and direction of the binding forces between the atoms. The valence electrons in the s and p bands are weakly bound to the atomic core, and interact strongly with neighboring atoms. Such electrons are shared equally by all the like atoms and described by band model. When interatomic interactions are weak and the electrons are tightly bound to atomic cores the system is described by the localized electron theory. Localized electrons are characterized by a large value of the energy (U) required to transfer a valence electron from one site to an occupied orbital on another equivalent site, and a small bandwidth (W). In insulating transition metal

oxide (Mott - Hubbard insulator or charge transfer insulator) the Fermi level falls in a gap in the one electron density of states when the electron correlations are such that $U >> W$. In some transition metal oxide the charge transfer gap may go to zero and the compounds become metal. The gap is not sharp when $U \sim W$, there is a possibility of strong electron correlation [63]. In the transition metal compounds, d - electrons are localized, being described by ligand field theory. In manganites the bandwidth is basically determined from the overlap of d - orbitals of two adjacent Mn atoms through the bridging oxygen atom. The overlap is determined by the indirect transfer d - orbitals of Mn site through ligand p - orbital. Because of this indirect transfer, the d - bandwidth becomes, in general, even narrower. The Mn – ions in the manganites are surrounded by six oxygen atoms, which give rise to an electric field, and quenches the orbital angular momentum of the Mn – ions. This octahedral environment of ligands leads to a difference in the energy of t_{2g} and e_g levels such that the t_{2g} level lies lower than the e_g level. The crystal field splitting between t_{2g} and e_g levels is $\sim$ 1.5 eV in Mn^{3+} [64]. Substitutions of some of the A – site trivalent ions by a divalent ion lead to mixed valency in the form of Mn^{3+} and Mn^{4+} ions. The energy required to flip a d - electron spin in a Mn – ion is about $\sim$ 2 eV, which is larger than the crystal field splitting in Mn^{3+}. Due to this strong intra-atomic Hund's coupling all d - electron spins of Mn^{3+} and Mn^{4+} are aligned parallel leading to electronic configuration Mn^{3+} : $t_{2g}^3 e_g^1$ and Mn^{4+} : $t_{2g}^3 e_g^0$, with spin only moment $4\mu_B$ and $3\mu_B$ respectively. The partial filling of t_{2g} or e_g orbitals generally leads again to degeneracy of the ground state. The partial degeneracy of the $3d$ - orbitals can be further lifted by a volume - conserving distortion of the MnO_6 octahedra. The symmetry of the cubic crystal field is hereby lowered in such a way that the center of gravity of the t_{2g} levels and the center of gravity of the e_g levels remain unchanged. Therefore Mn^{3+} can lower its ground state energy by a spontaneous local distortion since the raised elastic energy during this process is compensated by the lowering of the Coulomb energy of the e_g electron. This is called the Jahn-Teller distortion. Mn^{3+} is a Jahn-Teller distorted ion and can lower its energy in proportion to the distortion. The Jahn-Teller effect is illustrated in Fig. 1.4 for a tetragonal elongation of the MnO_6 octahedron in the z – direction. In that case, the $d_{3z^2-r^2}$ orbital is energetically more favorable

than the $d_{x^2-y^2}$ orbital, and the degeneracy of the t_{2g} states is also partially lifted. The Jahn-Teller splitting of the e_g levels in Mn^{3+} is typically about $2\delta_{JT} \cong 1\ eV$ [64]. The Jahn-Teller distortions can be randomly oriented along the crystalline axes of the material, but in certain manganites a preferential occupation of the e_g orbitals can exist throughout the whole sample. This is called the cooperative Jahn-Teller effect [65].
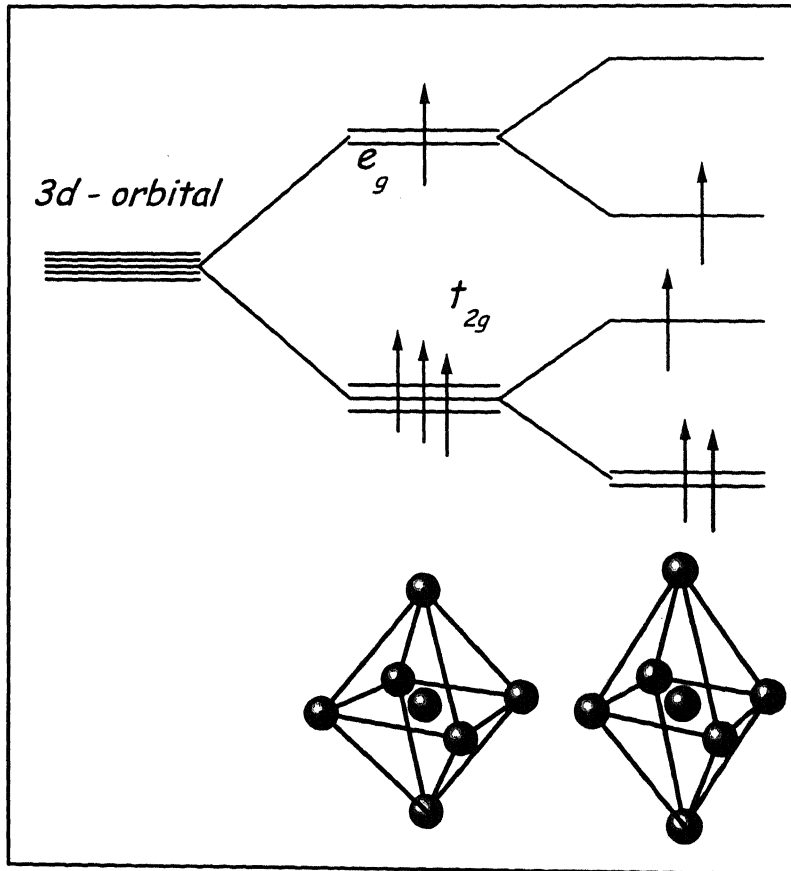
Figure 1.4: Schematic representation of crystal field splitting of five folds degenerate atomic $3d$ orbitals into three fold t_{2g} and two fold e_g levels. The further splitting due to John-Teller distortion is also shown in the figure.

1.3.1.3 The magnetic state

Magnetism in the manganese perovskite oxides is very complex due to the interaction between the atomic moments. This interaction gives rise to complex mag-

netic ordering and cooperative magnetic moments. The spins of two nearest atomic sites can correlate their orientation either due to a direct exchange or an indirect exchange. The direct exchange between moments of two atoms occurs when the overlap region of charge density contribute to both the atoms in accordance to Pauli exclusion principle. The direct exchange coupling is strong but decreases rapidly with the increasing interatomic distance. Indirect exchange occurs between localized magnetic moments through an intermediary nonmagnetic ion or through itinerant electrons. The indirect exchange through the itinerant electrons occurs in metals and the $RKKY$ coupling is an example of this. Indirect exchange through the nonmagnetic ion is called superexchange, this occurs in insulator. In the following, we identify some important magnetic interactions which lead to rich magnetic phases in these materials.

1.3.1.3.1 Superexchange

The superexchange interaction arises between two neighboring Mn ions through the bridging O^{2-} ion. Two of the valence electrons of O^{2-} overlap with available lowest energy $3d$ - orbitals of the Mn ions. Due to the strong Hund coupling in Mn, and due to the fact that the $3d$ - shells are less than half-filled in both Mn^{3+} and Mn^{4+}, these electrons occupy empty $3d$ - orbitals. Since the valence electrons of O^{2-} have opposite spins due to the Pauli exclusion principle, the superexchange interaction leads to antiferromagnetism. Anderson, Goodenough and Kanamori have given a set of rules governing the sign and magnitude of the superexchange. This exchange interaction influenced by the characteristic distortions of the perovskite structure, leads to variety of magnetic ordering such as the A, B, C, E, G and CE – types. The B – type ordering is ferromagnetic, but all other types of ordering are antiferromagnetic.

1.3.1.3.2 Double exchange

The celebrated double exchange theory of ferromagnetism and metallicity in manganite compounds given by Zener [51] envisaged transfer of the lone e_g electron on Mn^{3+} ions, which is strongly Hund coupled to the onsite t_{2g} spins $(S = \frac{3}{2})$, to the neighboring Mn^{4+} ions through the bridging oxygen atom. The different interactions

leading to the coupling between two neighboring Mn – ions in the Zener system is shown in Fig. *1.5*. The Hund's rule in each individual ion or atom drive the system into a configuration where the unpaired spins are aligned to lower the energy. In the Zener hopping process the spin of the conduction electrons remains unchanged as they move from ion to ion (the electron hopping maintain the z – projection of the spin). This is possible when the net spin of the incomplete d - shells are all parallel-otherwise, an up-spin electron can land on a down-spin ion and pay energy proportional to the Hund coupling. The conduction electrons lower their kinetic energy if the t_{2g} spins of manganese, are fully polarized. The kinetic energy is regulated by hopping amplitude
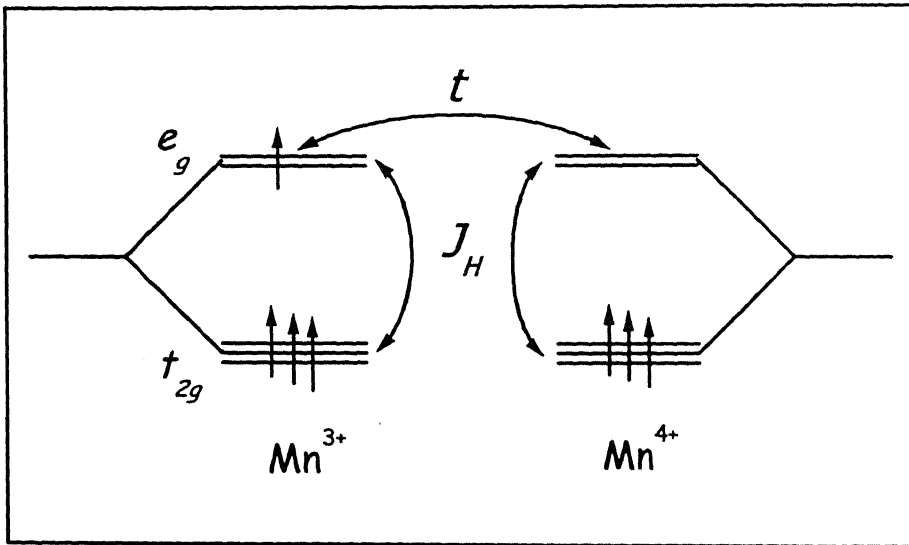
Figure 1.5: Schematic representation of different coupling between Mn^{3+} and Mn^{4+} ions. In the figure J_H is the Hund coupling and t is the hopping parameter.

usually denoted by 't'. The d - shell spins are then indirectly coupled via an interaction mediated by the conduction electrons. The double exchange mechanism was generalized by Anderson and Hasegawa who considered a pair of neighboring Mn ions with random spin directions [66]. The effective hopping integral when an electron jumping between two Mn – ions with spins S_i and S_j oriented at angle θ_{ij} is; $t_{eff} = t_0 \cos\left(\frac{\theta_{ij}}{2}\right)$, with t_0 the normal transfer integral when all spins are aligned. The hopping probability is therefore largest when the spins are aligned parallel and becomes zero when they

are aligned antiparallel. Quantum mechanical treatment of the effective hopping was also studied by Anderson and Hasegawa [66], Kubo and Ohata [67] and Cieplak [68]. de Gennes [69] has proposed the spin-canted state, as the possible stable state obtained by doping an antiferromagnetic state with holes or electrons. This spin-canted idea i.e. coexistence of ferromagnetic and antiferromagnetic features (the spin-canted state has a net moment, coexisting with a staggered distribution of spins perpendicular to that net moment) has been extensively used to describe experimental results in under doped manganites.

1.3.1.4 Electron transport in hole doped manganites

The double exchange theory can only be used to explain the transport properties of manganites qualitatively [70]. It overestimates the Curie temperature of most manganites, it underestimates the resistivity values in the paramagnetic phase by several orders, it can not describe the large magnetoresistance and it cannot account for the existence of orbital ordering and charge ordering in several compounds. Kubo and Ohata [67] have calculated the dependence of Curie temperature on the charge - carrier bandwidth in a double exchange system, and the dependence of the bandwidth on temperature. Their theory predicts a phase transition which is some what different from the behavior expected for a $3D$ Heisenberg ferromagnet. Furukawa [71] have used the Kondo lattice model for double exchange systems and conformed the linear dependence of Curie temperature on the bandwidth. Millis et al. [52, 72] were the first to identify the significance of electron - phonon coupling. They argued that strong interplay between electron - phonon coupling, charge localization and Hund coupling generates a unique ferromagnetic metallic phase in these systems.

The strong electron - phonon coupling in manganites is mainly caused by the Jahn-Teller effect. The $J - T$ effect causes local distortions of the crystal structure in which some of the $Mn - O$ bonds become shorter and others longer. This breaks the local cubic symmetry and splits the degeneracy of the e_g levels. By occupying the orbital with the lowest energy, the e_g electron becomes effectively self-trapped to form together with the surrounding deformed lattice a quasi-particle called lattice polaron or Jahn-Teller polaron. The large value of electron - phonon coupling in

the manganites with dopant concentration below 0.2 indicates that the static $J - T$ effect plays a key role. Millis et al. [72] have argued that a dynamical $J - T$ effect may persist at higher dopant concentration, without leading to long - range order but producing important fluctuations that localize electrons by splitting the degenerate e_g levels at a given MnO_6 octahedron. Their calculations predict localization of charge carriers by Jahn-Teller distortions around and above T_C. At temperature below T_C, the effective electron - phonon coupling becomes smaller than the critical value, leading to a relaxation of the lattice and an enhancement of the conductivity. In this theory both Jahn-Teller coupling and DE are needed to explain the properties in the various magnetic phases. This leads to the prediction of lower, more correct T_C values, and can explain the high resistivity and large magnetoresistance effect of manganites. However, the formalism of Mills et al. [72] does not consider orbital or charge ordering. Roder et al. [73] have incorporated Jahn-Teller coupling into DE model with quantum phonons, treating the localized spins in the mean field approximation and the polaron formation with the Lang-Firsov variational approximation. Their calculations indicate that these polarons appear as localized lattice distortions with a spin polarization around the position of the charge carrier, having a coherence length of the order of two unit cells. These quasi-particles can therefore be called magneto-elastic polarons, since they are associated with spin clusters and essentially form small metallic islands in a paramagnetic lattice [73].

Electron transport in the paramagnetic state of the hole doped manganites has been studied in detail. The resistivity in this regime has been fitted to a purely activated law, small polaron hopping theory and Mott's variable range hopping model. Holstein [74] have studied the formation and transport properties of small - lattice polarons in strong electron - phonon coupled systems, in which charge carriers are self-localized in the energetically favorable lattice distortion. If the carrier together with its lattice distortion is comparable in size to the cell parameter, it is called a small polaron. When the charge-carrier motion is faster than the lattice vibrations, the polaron is said to be in the adiabatic limit. In this limit the electrical resistivity is activated and is given by,

$$\rho \propto T \times exp(\frac{W_P}{K_B T}).\tag{1.8}$$

There are several reports of the evidence of small polaron behavior over an extended temperature range in the transport measurements on polycrystalline ceramic samples, single crystals and thin films. There is also direct evidence for small polaron formation in the distribution of $Mn - O$ bond lengths contained in the pair distribution function [75]. The thermopower favors polaron hopping in the paramagnetic state. Alternatively, the presence of magnetic disorder and the intrinsic variation of the Coulomb potential due to random distribution of A - site (A^{3+} and A^{2+}) ions in the lattice lead to the formation of mobility edges. The fluctuating Coulomb potential in manganites may be caused by substitution or vacancies on the A or B site. At high temperatures, carriers are excited from the Fermi energy to the mobility edges, giving an activated behavior. At low temperature, when the available phonon energy is small one has nearest neighbor hopping followed by variable range hopping. This view is also compatible with the small polaron picture, since variable range hopping of small polaron also leads to $ln(\rho) \propto T^{-\frac{1}{4}}$ [64, 76]. For highly correlated electron systems a small gap appears at the E_F and the hopping law is then $ln(\rho) \propto T^{-\frac{1}{2}}$ at temperature below the correlation gap [64, 77]. Although Jahn-Teller polarons are an essential part of the electronic transport in manganites at high temperatures, they cannot provide a complete picture of the metal-to-insulator transition [64, 78]. Furthermore, there are indications for the existence of manganite compounds like $La_{2/3}Sr_{1/3}MnO_3$ in which polaron formation does not take place, so that the carrier localization in these compounds cannot be due to self-trapping at all [79].

Coey et al. [64] have argued a non-polaronic localization of charge carriers. Such localization can result from both magnetic disorder (random spin alignment) and non-magnetic disorder (static potential disorder). The random substitution of dopant ions for A - site causes local potential fluctuations. While the different ionic size of the cations generate lattice distortions, lead to local variations in the amplitude of the hopping transport between the manganese ions. Furthermore, any clustering of dopants in the otherwise randomly doped lattice introduces local fluctuations in the

carrier density. Besides these non-magnetic effects, also magnetic disorder in the sense of DE spin disorder can lead to localization of carrier states. In this case, transport of charge carriers will probably take place by spin - dependent hopping between the localized states. Wagner et al. [80] have proposed a spin - dependent hopping model to describe the field dependent carrier transport in the paramagnetic state. They have suggested that the localized carriers in the paramagnetic state, spin polarized their environment to form small magnetic clusters. The charge transport occurs via hopping of charge carriers between magnetic quasi-particles with spin J. The carriers themselves are delocalized within the spin clusters, but they encounter a magnetic barrier when they cross the boundary between adjacent clusters. The hopping barrier depends on the misorientation between the local magnetization vectors. The total energy barrier is reduced when the spins become aligned, and has a maximum value when the spins are antiparallel and hopping is forbidden in terms of the double exchange mechanism. In many ways these arguments are similar to those used by Abeles et al. [81] to explain transport in $SiO_2 - Ni$ films.

1.3.1.5   Charge ordered state at half filling

Goodenough [56] has explained many of the features of $La_{1-x}Ca_xMnO_3$ observed in neutron scattering by Wollan and Kohler [50]. His approach was based on semicovalent exchange. According to semicovalent exchange, both antiferromagnetic and ferromagnetic coupling among the Mn − ions can be effectively generated, depending on the orientation of the orbitals. Analyzing various possibilities for the orbital directions, Goodenough has proposed A − and CE − type phases for manganites. Coulomb interactions and oxygen played important role to generate Hund - like rules and to produce covalent bond respectively. The lattice distortions are also quite relevant in deciding which of the many possible states has minimum energy. The charge/orbital - ordering becomes more stable when the band filling coincides with a rational number for the periodicity of the crystal lattice. The charge, spin and orbital ordering are basically described at half-filling. The robustness of charge/orbital - ordering depends on the bandwidth. In the reduced bandwidth system such as $R_{0.5}Ca_{0.5} MnO_3$ ($R = Pr, Nd, Sm..$) no ferromagnetic or metallic state is realized

[82]. At carrier concentration 0.5 the compound shows real space ordering of Mn^{3+} and Mn^{4+} ions on the (001) plane, while the e_g orbital shows the 1 × 2 superlattice on the same (001) plane. The change in the lattice parameter at the charge ordered transition temperature results in an elongation of the orthorhombic $a-$ and $b-$ axes and contraction in the $c-$ axis [83]. Generally, a decrease in magnetization and increase in resistance is observed below the charge ordered transition [84, 85]. The charge ordered state melts on application of external perturbation such as magnetic field and electric field. The magnetic field at which the charge/orbital - ordered state melts, varies from system to system for example in $Nd_{0.5}Sr_{0.5}MnO_3$, $Pr_{0.5}Ca_{0.5}MnO_3$ and $Sm_{0.5}Ca_{0.5}MnO_3$ the melting fields is 11, 27 and 50 tesla respectively [82]. There have been several theoretical studies to understand the charge/orbital - ordered state in manganites. Mishra et al. [86] have derived polaronic charge ordered state whose properties depend on the magnitude of coupling in the framework of dynamical mean field theory. Stojkovic et al. [87] have predicted a re-entrant transition on cooling from a charge ordered state to a homogeneous (metallic) state using both on-site and nearest neighbor Coulomb repulsion in the extended Hubbard model. Such re-entrant transitions, where in the melting of the charge ordered state occurs on decreasing the temperature, have been observed in the manganites. Phase separation in the manganites has been a subject of few theoretical investigations [88]. Generally, phase separation involves formation of ferromagnetic clusters in the background of an anti-ferromagnetic phase.

1.3.2 MR & IEC in perovskite oxide superlattices

Several multilayer systems synthesized using transition metal oxides have been investigated. These include systems where the hole doped manganites, ruthenates and Fe_3O_4 are used as the magnetic layers and non-magnetic oxides of diverse conductivities as spacers. For example, Gong et al. [36] have studied the structure, magnetization and magnetotransport of superlattices consisting of metallic ferromagnets $La_{0.67}Ca_{0.33}MnO_3$ and $SrRuO_3$ (SRO) grown by pulsed leaser deposition (PLD) method. These samples show enhanced magnetoresistance at low temperatures. They have attributed this enhancement to additional spin - dependent scattering center

near the interfaces due to disorder. Nikolaev and coworkers [36, 89, 90] have studied oxide - based magnetic multilayers and heterostructures grown by ozone assisted molecular beam epitaxy method. They have measured magnetization and the low temperature magnetoresistance in multilayers and heterostructures of ferromagnetic $La_{2/3}Ba_{1/3}MnO_3$ (LBMO) and paramagnetic LNO grown on (001) oriented $SrTiO_3$ (STO). The multilayers are sandwiched between $50\mathring{A}$ thick LNO layers and are characterized by the reflection high energy electron diffraction (RHEED) and X - ray diffraction. The multilayers with lower spacer layer thickness ($11.5\ \mathring{A}$ and $15.3\ \mathring{A}$) show the signature of antiferromagnetic coupling. These multilayers show a small ($< 0.2\ \%$) hysteretic, positive low-field magnetoresistance. They have suggested that the positive magnetoresistance is due to the small mean free path in the manganites. They have calculated the interlayer exchange coupling for a superlattice with $15\ \mathring{A}$ spacer layer using the relation $J = H_{Sat}M_{Sat}t_{FM}$, where H_{Sat}, M_{Sat} and t_{FM} are saturation field, saturation magnetization and magnetic layer thickness respectively. The saturation field of the sample starts to grow and saturation magnetic moment falls with the increasing temperature [89]. The interlayer exchange coupling in these multilayers shows an oscillatory behavior as a function of the spacer layer thickness. To explain this oscillatory interlayer exchange coupling, Nikolaev et al. have used the RKKY model. Calculation based on the Fermi surface parameters of LNO compared well with the experimental data. This group has also measured field dependent magnetoresistance of the multilayers at $55\ K$. The samples with antiferromagnetic interlayer coupling show low-field positive magnetoresistance while the samples with ferromagnetic coupling show negative magnetoresistance. These authors have suggested that this behavior originates from the variation of the electronic structure of the system due to the change in the magnetic configuration.

Izumi et al. [42, 91, 92] have studied the structural, magnetic and magneto-transport properties of some manganites based superlattices grown by PLD method. Their superlattices consist of metallic ferromagnetic $La_{0.6}Sr_{0.4}MnO_3$ as the magnetic layer and three different nonmagnetic spacer layers. These are; metallic antiferromagnet $La_{0.45}Sr_{0.55}MnO_3$ [91], insulating antiferromagnet $La_{0.6}Sr_{0.4}FeO_3$ (LSFO) [42] and insulating diamagnet $SrTiO_3$ [92]. The compound $La_{0.6}Sr_{0.4}MnO_3$ is metallic

below the Curie temperature $T_C \sim 340$ K and $La_{0.45}Sr_{0.55}MnO_3$ shows a metallic behavior with the Neel temperature of ~ 230 K. The samples with thinner spacer layers show large magnetoresistance at low temperatures. Izumi et al. have interpreted this behavior in terms of the magnetic field induced alignment of canted spins at the interfaces. The magnetic transition temperature and ferromagnetic volume fraction of superlattices with $LSFO$ spacer layers, reduce as the spacer layer thickness is increased from 2 $u.c.$ to 5 $u.c.$. The resistivity and magnetoresistance of these samples at low temperatures show opposite trend. These authors have suggested that the antiferromagnetic spin arrangement in the $LSFO$ layers modifies the ferromagnetic spin arrangement of the $La_{0.6}Sr_{0.4}MnO_3$ layers via a frustrated magnetic interaction at the interfaces. The effective strength of antiferromagnetic interaction caused by the $LSFO$ layer seems to depend on its thickness. In the case of superlattices with STO spacers, the resistivity shows a clear crossover from insulating to a metallic state when the STO layer thickness reduced from 5 $u.c.$. This recovery of conductivity at lower thicknesses of STO has been argued to be due to electron hopping and hybridization effects through the STO layers. These samples also show suppressed magnetization and large magnetoresistance at low temperatures.

Venimadhav et al. [47, 93] have studied electrical and magnetic properties of two different classes of manganite based superlattices grown on (001) oriented $LaAlO_3$ (LAO) by PLD method. One class of superlattices consisting of ferromagnetic $La_{0.67}Ca_{0.33}MnO_3$ and insulating $LaMnO_3$, $Pr_{0.7}Ca_{0.3}MnO_3$ ($PCMO$) and $Nd_{0.5}Ca_{0.5}MnO_3$ ($NCMO$). While the samples with $PCMO$ and $NCMO$ spacers show enhanced magnetoresistance, such effects are not seen in superlattices with $LaMnO_3$ spacer layers. Venimadhav et al. have also fabricated superlattice consisting of ferromagnetic $La_{0.6}Pb_{0.4}MnO_3$ ($LPMO$: $T_C \sim 320$ K) and a metallic but non-superconducting cuprate $La_4BaCu_5O_{13+x}$. The ferromagnetic layer thickness (10 $u.c.$) is fixed while the thickness of the nonmagnetic layer varies form 1 $u.c.$ to 8 $u.c.$. The Curie temperature, saturation field and magnetoresistance of these samples decreases as the spacer layer thickness increases. The authors have suggested canting of the spin structure near the interface as the mechanism for reduced magnetization and lower T_C. Sahana et al. [94] have measured X − ray diffraction in-

tensity, susceptibility and magnetoresistance of the superlattices consisting of $LPMO$ and $La_{0.85}MnO_{3-\delta}$. The compound $La_{0.85}MnO_{3-\delta}$ shows insulating behavior with a paramagnetic to antiferromagnetic transition. These superlattices show enhanced magnetoresistance near the transition temperature of $LPMO$.

Panagiotopoulos et al [40, 95] have studied superlattices consisting of ferromagnetic $La_{2/3}Ca_{1/3}MnO_3$ and antiferromagnetic $La_{1/3}Ca_{2/3}MnO_3$ grown on (001) oriented LAO by PLD method. They have fabricated three different series of multilayer on $40\ nm$ thick antiferromagnetic buffer layer: these are; (i) equal thickness of magnetic and antiferromagnetic layers forming superlattice period 2, 5, 8, 10, 20 and $32\ nm$, (ii) ferromagnetic layer thickness $(3\ nm)$ is fixed and antiferromagnetic layer thickness varies $(1.5, 3, 4.5$ and $6\ nm)$, and (iii), antiferromagnetic layer thickness $(3\ nm)$ is fixed and ferromagnetic layer thickness varies $(1.5, 3, 4.5$ and $6\ nm)$. These samples are characterized by low angle as well as high angle $X-$ray diffraction. Magnetic measurements of these samples show exchange biasing behavior at low temperatures. Exchange bias behavior is also observed in the sputtered deposited superlattices consisting of charge ordered insulator $La_{1/4}Ca_{3/4}MnO_3$ $(T_{CO} \sim 180\ K)$ and metallic ferromagnet $La_{2/3}Sr_{1/3}MnO_3$ $(T_C \sim 330\ K)$ [96].

H. Li and coworkers [44] have measured resistivity and magnetoresistance of superlattices consisting of $La_{2/3}Ca_{1/3}MnO_3$ and the antiferromagnetic insulator $Pr_{2/3}Ca_{1/3}MnO_3$. In these samples the magnetic layer thickness is fixed at $100\ \mathring{A}$ and nonmagnetic layer thickness varies in steps of 5, 10, 20, 30 and $100\ \mathring{A}$. The superlattices were grown on (110) oriented $NdGaO_3$ substrate by facing target sputtering technique. A sharp transition and enhanced low field magnetoresistance near T_C is observed in these samples. Li et al. have interpreted this behavior in terms of the inhomogeneities in manganites involving ferromagnetic and antiferromagnetic domains. Yafeng Lu et al. [97] have studied structure, cross-sectional morphology and transport properties of superlattices consisting of $La_{2/3}Ba_{1/3}MnO_3$ and $SrTiO_3$. These superlattices were grown on (001) STO and (001) $NdGaO_3$ substrates by the laser molecular beam epitaxy method. The T_C of $LBMO$ is reduced in these superlattices also there is enhancement in magnetoresistance. The authors attribute these observations to a strong biaxial distortion due to lattice mismatch between the constituents.

A correlation is seen between the strain and metal - insulator transition temperature. Dorr et al. [98] have studied the microstructure, coercive field and magnetotransport in superlattices consisting of $La_{0.7}Sr_{0.3}MnO_3$ and $SrTiO_3$ as a function of STO layer thickness. These multilayers were grown on (001) STO substrates by PLD in off-axis geometry. $X - ray$ diffraction and transmission electron microscopy studies confirm a well-defined superlattice structure, coherent growth, and fairly smooth interfaces of these samples. For $La_{0.7}Sr_{0.3}MnO_3$ thickness below 3 nm, a drop in Curie temperature and a strong enhancement in coercive field have been seen. The current-in-plane transport shows a transition from metallic to insulating behavior at magnetic layer thickness $\sim$ 2.3 nm.

Jo et al. [41] have measured the electrical transport properties of multilayers consisting of $La_{0.7}Ca_{0.3}MnO_3$ and $SrTiO_3$ grown on (001) STO by PLD method. The spacer layer thickness in this series was kept constant at 7 nm where as the $LCMO$ was varied. The metallic behavior of $LCMO$ in these samples was suppressed as the magnetic layer thickness was reduced from 25 nm to 2.5 nm. Correspondingly there is a drop in the magnetic moment per Mn ion. These samples with higher magnetic layer thickness show enhanced magnetoresistance at low temperatures. Jo et al. have suggested that this behavior originates from magnetic inhomogeneities along the growth direction and magnetically disordered interfaces. Kwon et al. [43] have also measured transport properties of superlattices consisting of $La_{0.7}Ca_{0.3}MnO_3$ and $SrTiO_3$ grown on (001) oriented LAO by PLD method. These superlattices show enhanced magnetoresistance and broad magnetoresistance transition. T. Kawai and coworkers [99] have studied magnetic and transport properties of a series of superlattices grown on (001), (110) and (111) STO substrates by laser molecular beam epitaxy. The superlattices consisting of ferromagnetic $La(Sr)MnO_3$ and antiferromagnetic $LaFeO_3$ are studied as a function of magnetic and spacer layer thickness. These samples show reduced ferromagnetism when the ferromagnetic layer thickness is smaller than the antiferromagnetic layer thickness, and bulk-like ferromagnetism when the ferromagnetic layer thickness is larger than the antiferromagnetic layer thickness. The samples with individual magnetic and antiferromagnetic layer thickness $\leq$ 2 $u.c.$ show $\sim$ 35 $\%$ magnetoresistance near the transition temperature. They have attributed this behavior to

spin frustration in *FM* layers caused by the neighboring antiferromagnetic layers. The superlattices with ferromagnetic $La_{1-\delta}MnO_3$ and antiferromagnetic $LaFeO_3$ were grown on *(111)* oriented $SrTiO_3$ show ferromagnetic (or ferrimagnetic) behavior and a reduced magnetization as the stacking periodicity of the superlattices is decreased. The samples grown on *(001)* or *(110)* oriented substrates show spin frustration effect at the interfaces. Kawai et al. have also made superlattices with layers of $La_{1-\delta}MnO_3$ and $LaMO_3$ where $M = Ni, Co, Fe$ and Cr. The samples with $M = Fe$ and Cr have a reduced T_C where as the T_C is enhanced for $M = Ni$ and Co. This variation of transition temperature has been explained in the framework of molecular field theory. Most importantly, the superlattices consisting of antiferromagnetic layers of $LaCrO_3$ and $LaFeO_3$ deposited on *(111)* *STO* show ferromagnetic behavior consistent with the Kanamori - Goodenough rules.

1.4   Motivation for the present work

The phenomena of *IEC* and *GMR* have been studied extensively in the case of *3d* - transition metal based superlattices such as *Fe − Cr*, studies of the effects of artificially introduced periodicity on transport and magnetization in oxide - based multilayers is an emerging field of research. This thesis focuses on two types of superlattices of the ferromagnetic manganite $La_{0.7}Ca_{0.3}MnO_3$. In one case the spacer thin films are of $LaNiO_3$ which is a metallic and non-magnetic perovskite with good lattice match with *LCMO*. The spacer material in the second multilayer system is $Er_{0.7}Sr_{0.3}MnO_3$ (*ESMO*) which has paramagnetic and insulating ground state.

In chapter *1* of the thesis, we review some basic aspects of transport and magnetism in *3d* - transition metal based superlattices. This is followed by a summary of some general properties of the mixed - valence manganites and recent research on magnetic ordering and magnetotransport in variety of manganite based thin film heterostructures and multilayers.

Chapter *2* describes the methodology used to prepare laser ablation targets and fabrication of thin films and multilayers using pulsed laser deposition. This is followed by a description of instrumentation developed and used to study the structural and physical properties of thin films and multilayers.

Chapter 3 presents detailed studies of thickness dependence of the resistivity and magnetoresistance in thin films of $La_{0.7}Ca_{0.3}MnO_3$. The structural and physical properties of thin films of the perovskite manganites depend sensitively on deposition parameters, crystallinity, strain and thickness. We have monitored the change in lattice parameter due to lattice mismatch induced strain and thicknesses using $X-$ ray diffraction. These changes in the structure affect resistivity and magnetoresistance of the films. We note that at lower thickness the resistivity of the films is highly sensitive to the substrate induced stress and roughness. These factors manifest themselves as enhanced residual resistivity, suppressed T_C and insulating behavior at low temperatures. We also note that the overall quality of films is better on $SrTiO_3$ substrate. It improves further, if a TiO_2 terminated surface is realized through suitable etching.

Chapter 4 deals with the characterization of thin films of $LaNiO_3$ and $Er_{0.7}Sr_{0.3}MnO_3$ used as spacer layers in the superlattices. The nicolate is a paramagnetic metal while $Er_{0.7}Sr_{0.3}MnO_3$ is a paramagnetic insulator. These compounds show negligible change in resistance in the presence of a magnetic field. We compare the resistivity of ultra - thin films of $LaNiO_3$ deposited on $LaAlO_3$ with $SrTiO_3$ and $La_{0.7}Ca_{0.3}MnO_3$ buffer layers.

Chapter 5 describes the crystallographic structure, and the temperature and magnetic field dependent resistivity of $LCMO/LNO$ superlattices grown on $LaAlO_3$ and $SrTiO_3$ substrates as a function of spacer layer thickness. The normal-to-the-plane lattice parameter of the superlattices deposited on $LaAlO_3$ approaches the bulk value as the spacer layer thickness increases, while on $SrTiO_3$ it shows a negligible variation. The electron transport in superlattices with the spacer layer thickness ≤ 4 *unit cell* is characterized by a thermally activated resistivity and a large *MR* at low temperatures. As the spacer layer thickness increases above *four unit cell* the thermally activated behavior is suppressed. A parallel resistor model, which explicitly takes into account the interfacial disorder in each unit of the superlattice, correctly reproduces the broad features of the resistivity curves. The field dependent resistivity for samples with lower spacer layer at lowest temperatures show a magnetorelaxor - type of behavior.

In chapter *6* we present the changes in magnetization and magnetotransport properties as the magnetic layer thickness is increased to *20 u.c.*. Here the electronic transport shows a transition from the transport behavior of the ferromagnetic layer to that of the non-magnetic spacer layer as the spacer layer thickness increases from *1 u.c.* to *10 u.c.*. The saturation field and remnant magnetization show antiferromagnetic interlayer coupling for $n \approx 2$ followed by an overdamped oscillatory behavior with period of $\sim$ *4 u.c.* with the increasing spacer layer thickness. The low temperature magnetoresistance of the antiferromagnetically - coupled superlattices is characterized by a steep increase up to a critical field, whereas in the ferromagnetically coupled samples the magnetoresistance rises monotonically.

In chapter *7* we examine the perpendicular-to-plane magnetoresistance of *LCMO/LNO* superlattices by sandwiching them between two $YBa_2Cu_3O_7$ (*YBCO*) electrodes. The perpendicular-to-plane magnetoresistance in the temperature window of *20 K* to *80 K* is larger by a factor $\sim$ *15* compared to the magnetoresistance parallel to film plane.

In chapter *8* we report electrical and magnetic behavior of *LCMO/ESMO* superlattices. The magnetoresistance at the lowest temperatures rises with the increase in spacer layer thickness, and approaches $\sim$ *100 %* in the sample with *10 u.c.* thick spacer layer. At the lowest temperatures the magnetoresistance also shows a steep increase up to a critical field, which shifts to the higher values with the increasing spacer layer thickness. These samples also show a giant loss of magnetic moment per *Mn* site in $La_{0.7}Ca_{0.3}MnO_3$, as the spacer layer thickness is increased. This phenomenon is a signature of spin frustration at interlayer. In these samples the *ZFC* hysteresis loop is symmetric around the zero field and *FC* hysteresis loop shifted towards the negative fields.

In chapter *9* we present the summary of the work and identify scope for further research.

Chapter 2

Sample fabrication and characterization methods

2.1 Introduction

There are several techniques, with certain advantages and disadvantages, to fabricate thin films and multilayers. Pulsed laser deposition method is one of the widely used thin film fabrication processes to deposit transition metal oxides. Ceramic targets synthesized by the solid - state reaction method are commonly used for laser ablation. There are several parameters which critically affect the quality of films. Any deviation in these parameters of deposition can create defects, formation of dead layer, loss of stoichiometry and metastable phases in the thin film. In general, the objective is to have films which show the properties similar to that of a bulk single crystal. This requires characterization of the films by a large number of diagnostic tools.

In this chapter, we give a brief overview of preparation of stoichiometric bulk ceramic targets using the solid - state reaction method. This is followed by a brief description of instrumentation of pulsed laser deposition method used for the fabrication of thin films. Then the buffered *HF* procedure used to improve the surface

roughness of the substrate. We discuss the use of atomic force microscopy technique used for measurements of surface topography and X – ray diffraction used to study crystal structure and epitaxial growth of thin films. Here we also describe the design and fabrication of a dipstick cryostat and a superconducting magnet and the procedures used to measure temperature dependent electronic transport in the presence of a magnetic field. Finally, we give a brief description for the procedure used to measure the temperature and field dependent magnetization.

2.2   Target preparation

Targets for laser ablation were prepared by the standard solid - state reaction method from oxides and carbonates of relevant metals. These oxides and carbonates were taken in stoichiometric proportions to achieve the desired composition, and mixed thoroughly to achieve homogeneity. After grinding the mixture for a period of *2 hrs*, it was calcined at *1150 °C* for *15 hrs*. During this process, the carbonates dissociate into oxides of respective metals and CO_2 escapes into the atmosphere. For easy escape of CO_2 and moisture, calcination is preferable in the powder form. The grinding and calcination processes were repeated three times following the same steps. The calcined mixture was finally palletized in the form of a *2 cm* diameter disc and sintered at high temperature for *10 hrs*. Two sintering temperatures were used; for the manganites and ~~nicolate~~ nickelate we used *1400 °C*, where as $YBa_2Cu_2O_3$ targets were sintered at *970 °C*.

The process of pelletization introduces strain, plastic flow and reduction of pore size of the powder. The pelletization was done under *40 KPa* pressure using a hydraulic press. Sometimes crack introduced by inhomogeneous compression tend to grow during sintering for reason of stress relief. During sintering the fine particles of the compound agglomerate when heated at a suitable temperature. This agglomeration is accompanied usually by a decrease in the porosity and an increase in density. In traditional ceramic processing the typical sintering temperature is three quarter of the melting temperature expressed in the absolute scale. In general, five different transport processes have been considered as contributing to the observed configu-

rational change during sintering. These are, viscous flow, plastic flow, evaporation condensation, volume diffusion and surface diffusion.

2.3   Thin film fabrication

Thin films and multilayer structures can be synthesized, in principle, by any thin film deposition technique. Physical vapor deposition (PVD) has been employed extensively for this purpose. Some examples of PVD techniques are; Thermal evaporation, electron beam heating, dc or rf sputtering, ion beam sputtering and pulsed laser deposition (PLD). Although PLD method was first used as early as 1968, it gained popularity only after the discovery of high T_C superconductivity in copper oxide based perovskites. The physical processes in PLD include coupling of electromagnetic radiation with condensed matter (target), production of nascent plasma of the target material and finally its expansion away from the target and condensation of the gaseous species on the substrate. The technique of pulsed laser deposition has several advantages for thin film growth, some of them are;

1. The energy source (Laser) for production of atomic and molecular species is outside the vacuum chamber. This provides a much greater degree of flexibility in material use and geometrical arrangement of substrate, heater etc.

2. Almost any solid material can be ablated. The kinetic energies of the ablated species lie mainly in a range that promotes surface mobility on the substrate.

3. Very precise control over growth rate can be achieved by tuning the pulsed energy and repetition rate.

4. Film stoichiometry close to the target can be realized. Since the time scale of ablation is so fast that the concepts of congruent melting and evaporation do not apply. All constituents of the target are deposited at the same rate.

5. The ability to produce species with electronic states far from chemical equilibrium has the potential to produce novel or metastable materials that would be unattainable under thermal conditions.

The *PLD* technique also has the following disadvantages.

1. Ejection of nano and microscale clusters from the target during ablation. However, a considerable degree of success has been achieved in recent years in controlling the particulate matter.

2. Formation of crystallographic defects in the film by bombardment of high kinetic energy atoms and molecules.

3. Inhomogeneous flux and angular energy distribution within the ablation plume, which can lead to thickness variation and non-stoichiometry.

2.3.1   Excimer laser

A schematic diagram of thin film growth by the pulsed laser ablation is shown in the Fig. *2.1*. We have used a commercial excimer laser *Lumonics' PM – 800* for *PLD*. The excimer is a gas laser system, which emits radiation in the *UV* region. The excimer molecules are formed in a gaseous mixture of halogen (F_2) and rare gas (Kr) in a background buffer gas (Ne) at several atmospheric pressure. The gases are normally supplied from separate high pressure gas cylinders. The laser is operated with a gas mixture at *4700 mbar*. The system can achieve pulse repetition rates up to *20 hertz* with energies $\sim$ *650 mJ / pulse*. The laser head is first evacuated, and then recommended quantities of F_2 and Kr are introduced, followed by the addition of *Ne* gas to the required operating pressure. The entire procedure is generally carried out automatically by the laser's microprocessor control. The number of laser pulses, pulse repetition rate, pulse energy and the operation of the laser are controlled by the microprocessor. Energy is pumped into the gas mixture through avalanche electric discharge excitation. The discharge creates ionic and electronically excited species that react chemically and produce excimer molecules. Once the excimer is formed, the lasing action takes place between the bound upper electronic state and a repulsive or weakly bound ground state. As the ground state is repulsive, the excimer molecule can dissociate rapidly and the ratio of upper state lifetime to lower state lifetime is high. This makes the excimer the perfect laser medium because population inversion and therefore high gain are so easily achieved.
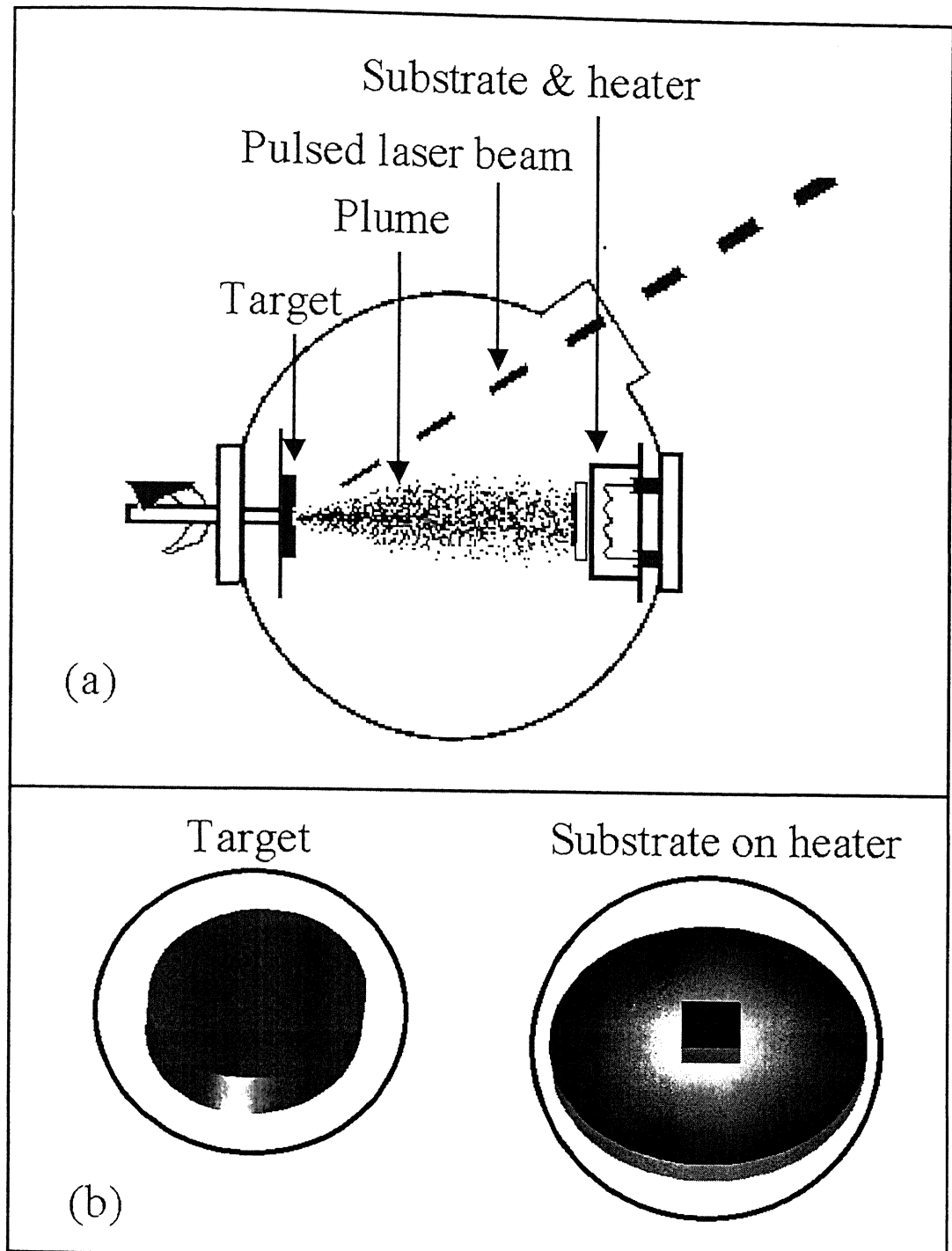
Schematic

Figure 2.1: Panel (a) represents the shcematic diagram of the deposition chamber during film deposition. A bulk target used for ablation and a substrate mounted on a heater block are shown in panel(b).

2.3.2   Deposition Chamber

We have used a custom made, all - stainless steel vacuum chamber for *PLD*. The chamber is evacuated with mechanical and oil diffusion pumps to a base pressure of $\sim 5 \times 10^{-6}$ *Torr*. To eliminate back streaming of oil vapors, the chamber is equipped with a liquid nitrogen trap. The chamber also has provision for inletting desired gas through a mass flow controller and a quartz window for the entry of the laser beam. Further, the chamber is equipped with a multi - target carousal and substrate heater capable of reaching $\sim 800\,^{\circ}C$ in oxygen environment.

2.3.3   Substrate surface and epitaxy

A layer-by-layer epitaxial growth is essential for synthesis of high quality superlattices. For a given lattice misfit $((a - b) / b)$ where a and b are lattice parameters of the film and substrate respectively, the incommensurate structure $(a \neq b)$ is stabilized by strong addatom - addatom coupling compared to the addatom - substrate interaction. If the later is stronger, the commensurate $(a = b)$ structure is stable. In this case we say there is epitaxy. In general, if lattice misfit $((a - b) / b)$ is within $1 - 2\,\%$ film growth takes place in layer-by-layer mode accommodating the difference $(a - b)$ through expansion or contraction of the in-plane lattice parameter. At larger thicknesses, the compressive or tensile strain is relieved through production of lattice defects. However, if lattice misfit is significantly large, an island - type growth starts at the beginning of the deposition. The nature of substrate largely controls the film growth morphology, defect structures and level of stress. For heteroepitaxial growth, the choice of the substrate depends on several factors of which the most important are the compatibility of lattice parameter, an atomically smooth surface, match between thermal coefficient of expansion with the deposit and chemical and physical inertness.

The substrates commonly used for epitaxial growth of manganites are (001) cut single crystal wafers of $SrTiO_3$ (STO) and $LaAlO_3$ (LAO). Commercially available wafers are prepared by mechanochemical polishing with an alkaline solution containing suspension of silica particles. Kawasaki et al. [100] have shown that the surfaces of such wafers have small corrugation of *0.2 to 0.8 nm* diameter. The (001) direction

of STO consists of alternating stacks of SrO and TiO_2 atomic planes. Kawasaki et al. suggested that if one of the two atomic planes is dissolved in a wet solution, then it is possible to prepare an atomically smooth surface terminated by undissolved atomic plane. They have shown that a buffered HF (BHF) solution with $pH = 4.5$ selectively dissolve the SrO planes to form an atomically smooth surface terminated by the TiO_2 planes.

We have used BHF treatment of our STO substrates. After the treatment, substrates were glued on the heater block using silver paint. Temperature of the heater block was monitored with a Chromel - Alumel thermocouple. The heater is mounted in front of the target at a desired distance. Since the uniformity of the layer thickness depends on the source to substrate distance, we have optimized this separation carefully.

2.3.4   Deposition of thin films and Superlattices

Bulk ceramic targets of the desired stoichiometry were glued on aluminum holders with silver epoxy. The target holder assembly consisting of a rotating stage can hold six targets at a time. The polished surface of the target was adjusted with respect to the laser focal point to achieve the desire fluence. The pulses of energy ($\sim$ 300 mj) were focused on the target to realize an areal energy density of $\sim$ 3 J/cm^2. To remove possible contamination from the target, predeposition laser ablation was carried out while keeping a shutter in front of the substrates. The deposition of films and superlattices was carried out at 400 $mTorr$ partial pressure of oxygen, while the laser repetition rate and substrate temperature were held at 10 $hertz$ and $750\,^\circ C$ respectively. The deposition rate per laser pulse from different targets was calibrated by measuring the thickness of several films. For fabrication of multilayers, target of the constituent compounds were brought in front of the laser beam for a precalibrated duration. After completion of the run, deposition chamber was backfilled with oxygen to atmospheric pressure, and the samples were cooled to room temperature at the rate of $5\,^\circ C/min$.

2.4   Structural and physical characterization methods

2.4.1   Stoichiometry and Surface morphology

The stoichiometry, epitaxial quality and surface morphology are important aspects in the growth of superlattices or heterostructures. We have studied these factors with the use of different characterization techniques. Rutherford backscattering is a powerful technique to measure stoichiometry and thickness. These measurements were performed at the van de Graaff laboratory of our institute using $1.4 - 1.6\ MeV\ He^+$ ions. A surface barrier detector was placed at $150°$ with respect to the incident beam to detect the scattered ions. The Rutherford backscattering spectra were analyzed using the $RUMP$ simulation code [101]. We have examined the surface morphology of thin films using atomic force microscopy (AFM). These measurements were performed at the nano - imaging laboratory of $I.I.T.\ KANPUR$ using a commercial microscope (Molecular Imaging $USA : PicoSPM - 4$) with $AFMA$ scanner. The film surface was monitored in magnetic AC mode with a magnetic coated cantilever (force constant $2.8\ N/m$ and resonance frequency $75\ KHz$) using $PicoSCAN - 4$ software.

2.4.2   Structural characterization

Physical properties of thin films and superlattices depend sensitively on their crystallinity, strain, roughness and crystallographic structure. Characterization of the structure therefore becomes a prerequisite to understand various physical properties. $X -$ ray diffraction is the most powerful technique for structure determination of macroscopic specimen. Techniques based on electron diffraction and imaging are useful but do not give a global picture of the structure. $X -$ ray diffraction offers high intrinsic accuracy due to the accurate knowledge of wavelength and layer diffraction angles. Also, in this case the specimen may stay in air and is not exposed to damaging radiation nor excessive heat transfer.

In a standard $X -$ ray experiment in the Bragg geometry, radiation of wavelength λ is diffracted from the equally spaced atomic planes. The path difference between the diffracted $X -$ rays from two adjacent planes is $2d\ sin\theta$, where d is their

separation and θ the angle between incident beam and plane - normal. The radiation diffracted from the adjacent plane will be completely in phase if the path difference is equal to a hole number n of the wavelength. The mathematical condition for diffraction is therefore $2d\,sin\theta = n\lambda$. This relation was first formulated by W. L. Bragg, and is known as Bragg law. The angle between the diffracted and transmitted radiation is 2θ. This is known as diffraction angle and it is this angle, rather than θ, which is usually measured experimentally.

We have used a commercial diffractometer (Rich. Seifert model no. $XRD3000P$) to study thin film epitaxy of single layer and superstructure of epitaxial multilayers. The diffractometer consists of a radiation source and radiation detector on the circumference of a vertical circle of radius R. The source here is a sealed $X-$ ray tube generator. It contains a tungsten filament, which emits electrons, and a polished metal target made of Cu. $X-$ rays are produced from the target surface on electron bombardment. The radiation from an $X-$ ray tube consist of continuous bremstrahlung spectrum superimposed with the characteristic peaks of the target element. A few micron thick homogeneous and pin-hole free $Ni-$ foil, which has its $K-$ absorption edge between $K\widehat{\alpha}$ and $K\widehat{\beta}$ lines of the target, is used as a filter for $K\widehat{\beta}$ lines. The thin film sample stage is at the center of the circle. While the sample position is fixed, a stepper motor assembly provides for the rotation of radiation source and detector. The goniometer is capable of maintaining and changing vertical 2θ or $\theta-\theta$ positions with an angular position of $120\ degree$. The operation and control of the diffractometer and recording of the counter output are performed through computer control software.

The diffraction profile from an ideal superlattice is a superposition of the diffracted radiation from three sources. It consists of Bragg diffraction maxima from the atomic planes of the constituents and multiple satellite peaks on both sides of these maxima. The position of the multiple satellite peaks of structurally coherence superlattice is determine by the relation $[102]$: $2\frac{sin\theta}{\lambda_x} = \frac{1}{d} \pm \frac{n}{\Lambda}$, where θ is angle at the peak position, n is the integer that labels the order of the satellite around the fundamental Bragg peak, λ_x is the $X-$ ray wavelength, Λ is the superlattice period (modulation wavelength) and $\bar{d} = \frac{\Lambda}{n}$, where N is the number of atomic planes of the constituent

in one period of the superlattice. Modulation wavelength can be expressed in terms

of the angular position of two successive satellite peaks: $\Lambda = \dfrac{\lambda_x}{2 \times (sin\theta_i + sin\theta_{i+1})}$,

where θ_i and θ_{i+1} are the angular position of the ith and $(i + 1)th$ satellite peaks.

Using this relation the value of Λ can be determined from any order of successive

satellite peaks have well - defined intensity.

2.4.3　Transport measurements

Measurements of resistivity and magnetoresistance were carried out in a liquid

helium storage dewar. The dewar neck is chosen to be as narrow as possible in order

to minimize the entry of thermal radiation into the helium bath. At the same time

the neck is wide enough to allow the user ample room to insert the experiment.

The neck of our *50 liters* liquid helium storage dewar is *2 inches* in diameter and it

houses a superconducting solenoid. The physical size of the solenoid is limited by the

neck of the storage dewar. It also limits the space inside the solenoid to accommodate

insertable dipstick cryostat for experiment. The magnet form is an aluminum mandrel.

It has *25* layers with *330 turns/layer* of *0.33 nm* diameter *Nb – Ti* multifilamentary

superconducting wire. A sketch of the superconducting magnet assembly is shown in

Fig. *2.2*.

A schematic diagram of the dipstick cryostat designed for use in the super-

conducting solenoid is shown in Fig. *2.3*. This cryostat could produce a wide range

of temperatures with good temperature control. A resistance (Lake shore Cernox

sensor) is used for temperature measurement and control in conjunction with a con-

stantan wire heater. Six twisted pairs of copper wire provide electrical connections.

The vacuum pumping line of the cryostat is made of thin wall stainless steel tube,

because of its high strength, small heat capacity and poor thermal conductivity. A

brass head designed as the holder of a vacuum - sealed multipin connector, has a bel-

low sealed vacuum valve. The brass head is hard soldered to one end of the stainless

steel pipe. A resistance heater is wound on an oxygen free high conductivity (*OFHC*)

copper rod at the free end of the stainless steel pipe. A horizontal *OFHC* copper

plate soft soldered on an *OFHC* copper screw head is screwed at the other end of the

OFHC copper rod. A flange is hard solder on the stainless steel pipe at a suitable
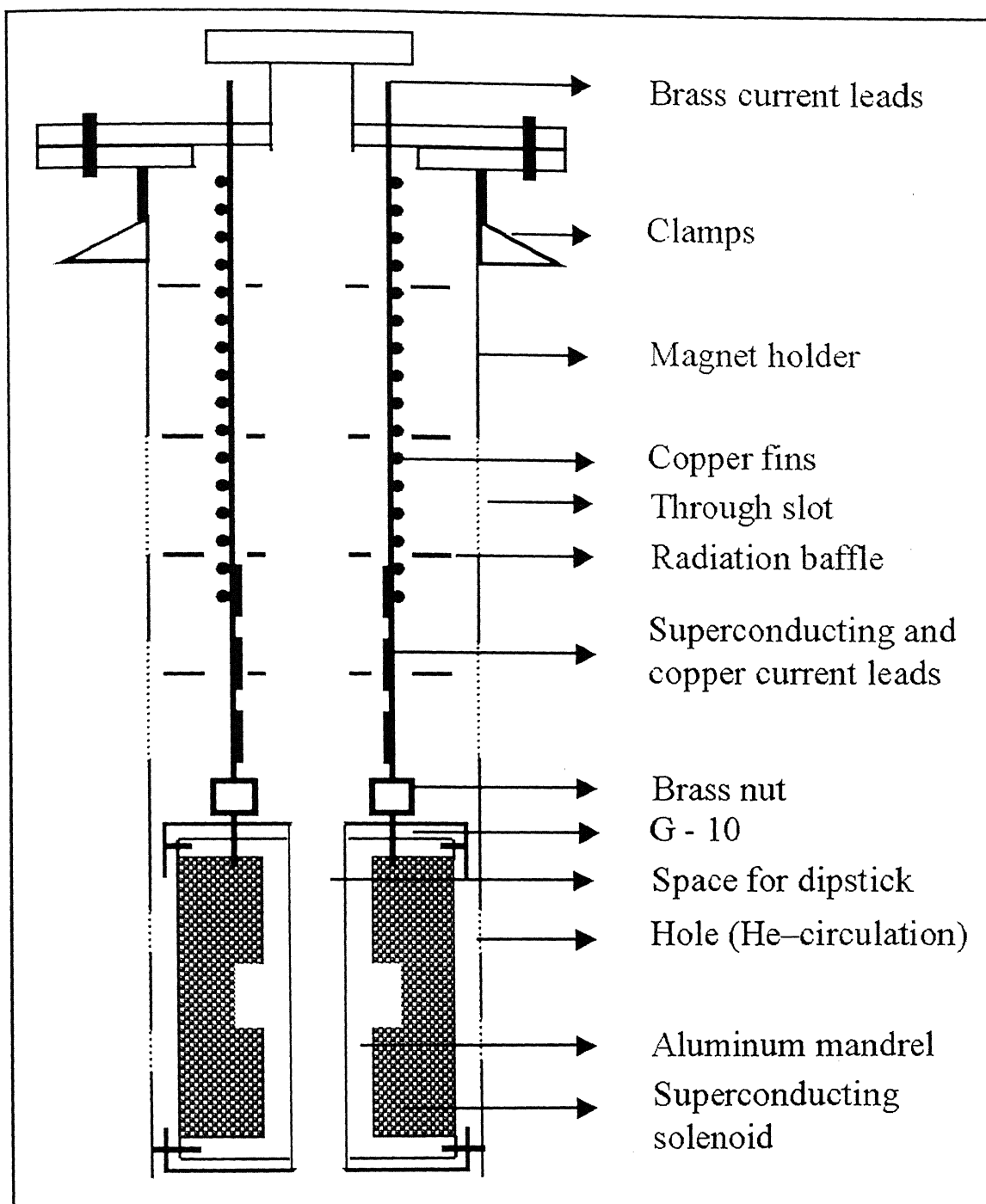
Figure 2.2: Schematic view of insertable superconducting solenoid assembly.

1. Dip stick probe

Inside cane

2. Heater on a copper rod
3. Flat copper plate
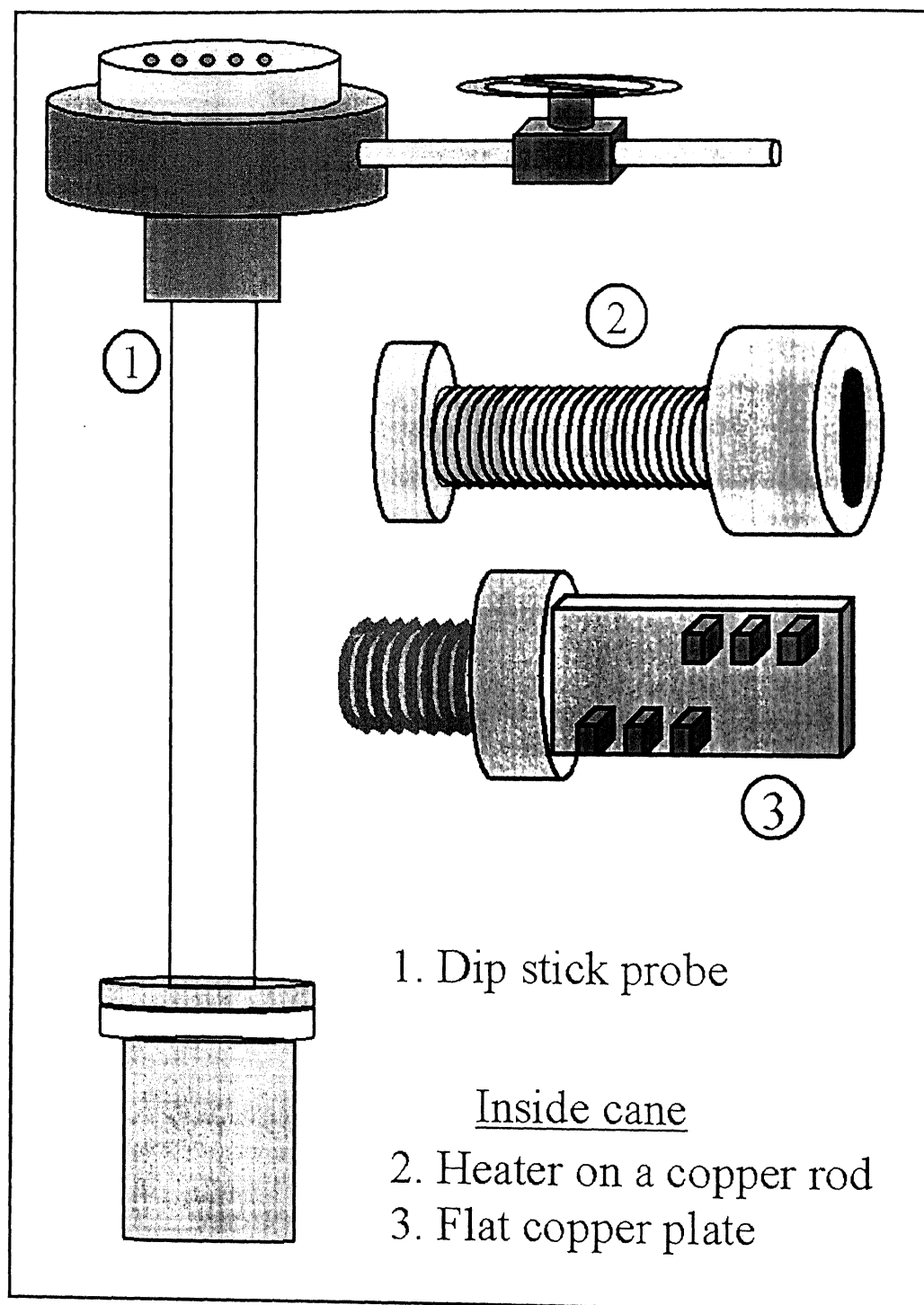
Figure 2.3: Schematic diagram of insertable dipstick probe used for transport measurements.

position to provide screw tight vacuum fitting to the stainless steel vacuum can with indium *'O'* ring. All instrumentation leads were wrapped around the stainless steel pipe below the brass flange to provide heat sink. The resistance thermometer was mounted on the reverse side of the *OFHC* copper plate, whose front face holds the sample. Silver pads were evaporated on the sample for making electrical contacts. The pumping line is also used to admit exchange gas (helium gas) to cool the sample from the room temperature to *4.2 K*. We have used a *Keithley 224* programmable current source to apply current to the sample and the voltage developed across the sample was measured with a *HP 34420A nano volt/micro ohm meter*. The sample temperature was monitored by using a *Lake Shore 331* temperature controller. A *HP 6012B DC* power supply was used to supply constant *dc* current to the super-conducting solenoid. All these instruments were controlled through *GPIB* interface. Measurements of resistivity and magnetoresistance were carried out in constant field as well as constant temperature modes. The magnetic field was scanned from zero to *+ 4 tesla* followed by cyclic sweep between *+ 4 tesla* to *− 4 tesla*. For some samples the cyclic sweeps between *+ 4 tesla* to *− 4 tesla* of the in-plane magnetic field were repeated. We have also used constant voltage methods. A fixed or variable voltage was impressed on the sample and the current was monitored, by measuring the voltage drop across a metal film resistor. This was the preferred method of measurement for current-voltage (*I − V*) characteristic and the electric field dependent *R vs. T* curves in the temperature range *20 K − 300 K*. The constant voltage measurements were performed using a *CTI* closed cycle helium refrigerator.

2.4.4 Magnetization

The magnetization measurements were performed using a superconducting quantum interference device (*SQUID*) magnetometer at Laboratoire de physique du solide, Ecole Superieure de physique Chime Industrielles de la Ville de Paris, *CNRS UPR 5, 75231* Paris Cedex *5*, France. Some measurements were also performed at the new *SQUID* laboratory of Indian Institute of Technology, Kanpur (India) using *Quantum Designed MPMS* system. The change in the spontaneous magnetization with temperature was measured in a low in-plane magnetic field. Both zero-field-cool

(*ZFC*) and field-cooled (*FC*) measurements were performed. In the first case, the sample is first cooled down to *4.2 K, a 50 Gauss* external magnetic field is applied along the (*100*) direction and magnetization is measured on heating the sample upto room temperature. In other case, a *50 Gauss* external magnetic field is applied along the (*100*) direction at room temperature, the sample is cooled down to *4.2 K* and the field-cooled magnetization is measured on heating the sample to room temperature. We have also measured the $M - H$ loops with an in-plane field at *10 K*. In this case the sample is first cooled to *10 K* and then the spontaneous magnetization is recorded on scanning the magnetic field from zero to + *5 tesla* followed by a cyclic sweep between + *5 tesla* to − *5 tesla*. These measurements were carried out for two orientations ((*010*) and (*100*)) of the in-plane magnetic field.

2.5   Conclusions

We have made stoichiometric ceramic targets of $La_{0.7}Ca_{0.3}MnO_3$, $LaNiO_3$, $Er_{0.7}Sr_{0.3}MnO_3$ and $YBa_2Cu_3O_7$ using solid - state reaction method. Thin films and multilayers were grown on (*001*) oriented polished single crystal *LAO* and *STO* by pulsed laser deposition technique. To achieve atomically flat surface we have given a buffered *HF* treatment to the substrates before deposition of thin films and multilayers. The stoichiometry, surface morphology and structure of the films were compared from the scans of the Rutherford backscattering, atomic force microscopy and $X -$ ray respectively. The transport measurements on the films and multilayers were performed in magnetic field (*0* to *4 tesla*) and electric field (*0* to *6000 V/cm*) in the temperature range of *4.2 K* to *360 K*. Measurements of magnetic moment were performed using a *SQUID* based magnetometer (*MPMS Quantum Designed USA*).

Chapter 3

Physical properties of thin films of magnetic character

=============================

3.1 Introduction

The A − site carrier doped ABO_3 perovskites with Mn at the B − site show a rich electronic, magnetic and structural phase diagram originating from the interplay between lattice, charge, magnetic and orbital degrees of freedom. Most of these features have a close bearing on the average A − site ionic radius $\langle r_A \rangle$ and the dopant concentration x. Out of all Mn − based ABO_3 perovskites, $La_{1-x}Ca_xMnO_3$ is the most extensively studied system. Jonker and van Santen [49] have studied the transport and magnetization of this compound as a function of Ca concentration. Wollen and Koehler [50] were the first to study crystallographic and magnetic structure of this system. For $x = 0$, the end member $LaMnO_3$ contains only Mn^{3+} ions, which arrange themselves in the A − type antiferromagnetic structure. Its resistivity shows thermally activated behavior in the entire temperature range with activation energy ranging from $0.1\ eV$ to $0.36\ eV$ [103]. For $x < 0.17$, the compound is antiferromagnetic and its resistivity is thermally activated. In the dopant range of $0.17 < x < 0.5$ a ferromagnetic phase is formed where the moments are close to the expected spin

only value $(4 - x)\mu_B$ per formula unit. The resistivity in this composition range on cooling below room temperature shows a transition from a thermally activated to a metallic - like behavior. For $x = 0.5$ the system shows transition from ferromagnetic to antiferromagnetic state accompanied by charge ordering. For x above 0.5, it is antiferromagnetic and show insulator - like resistivity. The end member $CaMnO_3$ contains only Mn^{4+}, whose t_{2g} spins are arranged into a G – type antiferromagnetic structure. The physical properties of $LCMO$ depend on the Mn_{La-Ca} environment, the $Mn - O - Mn$ bond angle and $Mn - O$ bond length. For compound with $x \sim 0.3$, the Curie temperature is $\sim 250\ K$ with a saturation magnetization slightly less than the expected spin only value of $\sim 3.7\ \mu_B$. The room temperature resistivity of the $x = 0.3$ compound varies from $\sim 1\ m\Omega\ cm$ to $\sim 50\ m\Omega\ cm$. The resistivity of this compound near T_C shows a significant drop in presence of a magnetic field [104]. The transition temperature and magnetoresistance also varies with external perturbations such as magnetic field [105] and pressure [106].

While these effects are observed in equilibrium structures synthesized in the form of single crystals and bulk ceramics where the stereography of MnO_6 octahedra is not affected by the method of preparation, in thin films grown on a substrate, the magnetotransport can be significantly different due to the substrate induced stresses. Substrate induced stress can controlled by a proper choice of substrate, thickness of film and the deposition parameters. The stress is also found to affect the microstructure of the films. Atomic force microscopy pictures of the surface of $La_{0.66}Ca_{0.34}MnO_3$ show a highly ordered grain pattern induced by strain [107]. Lebedev et al. [108] have studied the microstructure in $La_{1-x}Ca_xMnO_3$ films deposited on STO. Close to the interface, both the film and the substrate are elastically strained in opposite direction in such a way that the interface is perfectly coherent. While the upper part of the film shows a domain structure. The in-plane lattice parameter of thin films of $LCMO$ near the substrate therefore depends on the nature of lattice mismatch between the film and the substrate [109]. The three dimensional strain state and crystallographic domain structure of $La_{0.8}Ca_{0.2}MnO_3$ have been studied as a function of lattice mismatch using normal and grazing-incidence X – ray diffraction techniques [110]. Both the in-plane and out-of-plane lattice parameters of $LCMO$

films vary with film thickness. Jacob et al. [111] have measured the c − axis lattice parameter of $LCMO$ of several thicknesses deposited on STO. The lattice parameter increases with the increase in film thickness. Miniotas et al. [112] have evaluated the $Mn - O$ and $Mn - Mn$ bond distances in $La_{1-x}Ca_x MnO_3$ films deposited on STO and LAO. The $Mn - O$ bond length was found to be fixed, independent of substrate type, while the $Mn - Mn$ distance varied. The physical properties of $LCMO$ such as insulator-to-metal transition temperature, magnetoresistance [113, 114], coercive field [115] and microstructure [116] are strongly dependent on the film thickness. The zero-field resistivity of $LCMO$ deposited on different substrates decreases with the increase in film thickness, while the transition temperature increases and saturates to bulk value for thicker film [117]. The magnetoresistance is lager for the film with lower transition temperature. Jin et al. [114] have measured the magnetoresistance of $LCMO$ film deposited on LAO with different thicknesses. They have seen a maximum magnetoresistance (~ 99.92 % at $77\ K$) for the film thickness of $\sim 1000\ \AA$. Enhanced low field magnetoresistance has been reported and attributed to the spin - dependent scattering of polarized electrons at the grain boundary [118]. An ultra thin ($\sim 6\ nm$) $La_{0.67}Ca_{0.33}MnO_3$ film deposited on STO is ferromagnetic $T_C \sim 150\ K$ but remains insulating [119]. This behavior is explained by the coexistence of two different phases, a metallic ferromagnet (in the highly strained region) and an insulating antiferromagnet (in the low-strain region). Fath et al. [120] have studied the phase inhomogeneities in thin film of $LCMO$ using the scanning tunneling microscopy. The phase separation is observed below the Curie temperature where different structures of metallic and more insulating areas coexist and are field dependent. This suggests that the insulator-to-metal transition at T_C should be viewed as a percolation of metallic ferromagnetic domains. Ziese and coworkers [113] have measured magnetization and resistance of $La_{0.7}Ca_{0.3}MnO_3$ deposited on various substrates with different thickness. On decreasing the film thickness, saturation magnetization remains unchanged down to $\sim 4\ nm$ while the Curie temperature shows a small drop. The coercive field of the samples with thickness in the range $\sim 9\ nm$ to $\sim 300\ nm$ shows linear temperature dependence. They have deduced an electrically dead layer of thickness ($\approx 11\ nm$) at the substrate interfaces.

This chapter describes structural and physical characterization of single layer *LCMO* films of various thicknesses. Our *X* − ray study confirms an opposite nature of lattice mismatch of *LCMO* to the lattice parameter of *LAO* and *STO*. Our studies also indicate the presence of a tetragonal distortion of *LCMO* near the substrate - film interface. The systematic variations of room temperature resistivity and transition temperature with sample thickness suggest variation of lattice structure with film thickness. The magnetoresistance rises below the transition temperature as film thickness decreases. On lowering the film thickness, the transition temperature shifts towards the low temperatures and the resistivity become thermally activated. The samples with thickness ($\leq$ *50 u.c.*) deposited on *LAO* show thermally activated behavior on cooling below room temperature down to *4.2 K*. This critical thickness below which no metal - like resistivity is seen is smaller for the films deposited on *STO* as compared to the film deposited on *LAO*. The critical thickness of the films on *STO* is highly influenced by the surface roughness of the substrate.

3.2   Results

3.2.1   Rutherford Backscattering, X − ray diffraction and Atomic Force Microscopy

The achievement of stoichiometry and epitaxial growth are essential for fabrication of superlattices. We have performed Rutherford backscattering experiment using *1.4 MeV He$^+$* ions to establish the stoichiometry of our films. A typical Rutherford backscattering spectrum is shown in the Fig. *3.1*. The *RUMP* simulation curve (solid line) fits well to the experimental data. The simulated curve gives the elemental ratio of the film (the ratio between *La* and *Ca* as *0.7 : 0.3* with an error $\pm$ *0.02*), and film thickness ($\sim$ *600 Å*). Physical properties of thin films fabricated by any deposition technique depend on their thickness, microstructure and growth morphology, in addition to electronic structure. The equilibrium growth morphology depends on deposition parameters and the nature of substrate on which the film is being deposited. To compare the structure of *LCMO* films deposited on different substrates with the structure of bulk samples, we have taken powder *X* − ray diffraction
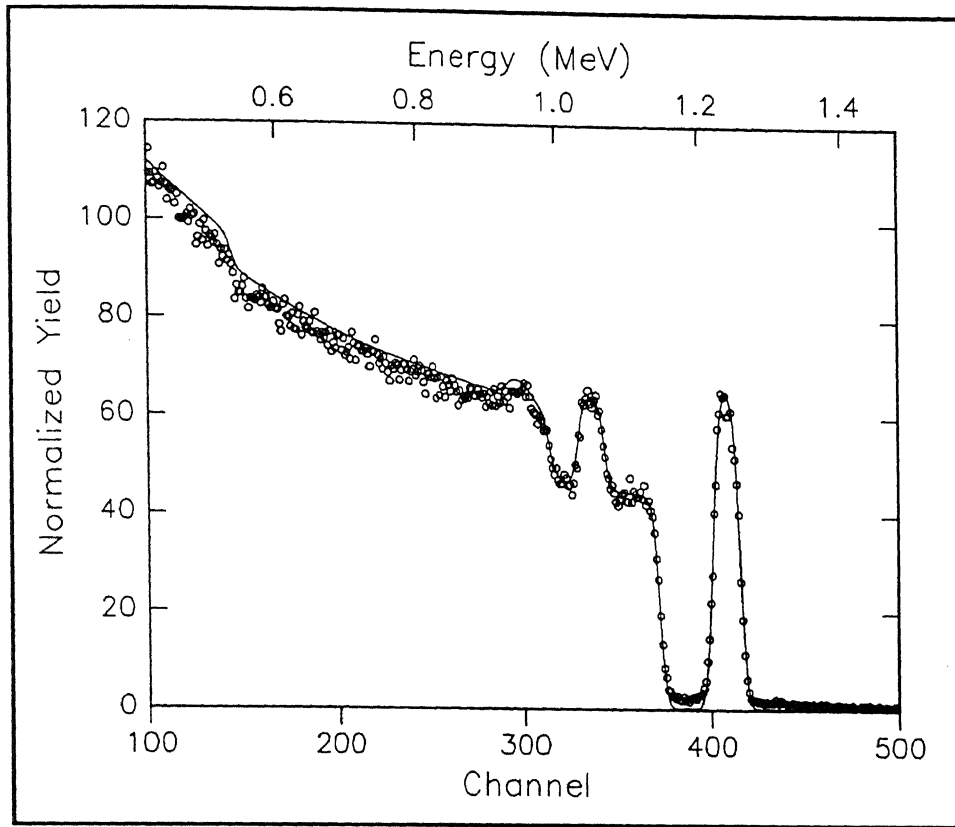
Figure 3.1: Rutherford backscattering spectrum of He^+ from the film and substrate. The sample is a $\sim$ *600 Å* thick *LCMO* film deposited on (*001*) oriented *STO*. The solid line is the *RUMP* simulated data.

scans of *LCMO* samples prepared using solid state reaction method. The ($\theta - 2\theta$) *X* – ray diffraction profile from a powdered sample of bulk *LCMO* is shown in Fig. *3.2* (curve *a*). All diffraction lines in the profile correspond to the pseudo-cubic perovskite structure of *LCMO* with the lattice parameter *a = 3.86 Å*. The pseudo-cubic *LAO* substrate has a smaller (*3.792 Å*) and the cubic *STO* has a larger (*3.905 Å*) lattice constant than *LCMO* at room temperature. The substrate induced stress in *LCMO* is tensile (*a* is expanded in the in-plane and compressed in the out-of-plane) on *STO* and compressive (*a* is compressed in the in-plane and expanded in the out-of-plane) on *LAO*. X–ray diffraction profiles of the *LCMO* films grown on (*001*) oriented *LAO* and on (*001*) oriented *STO* are shown in Fig. *3.2*
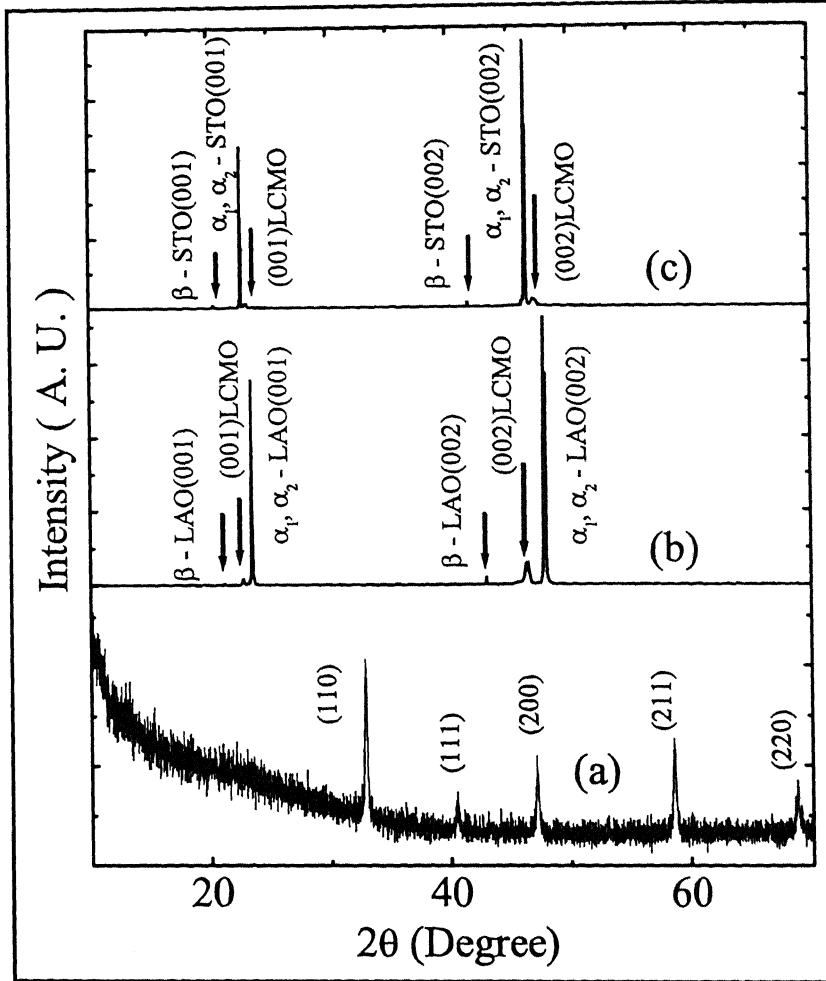
Figure 3.2: X − ray (θ − 2θ) scans for $LCMO$ powder sample (curve a) and $LCMO$ films deposited on (001) oriented LAO (curve b) and STO (curve c). In curve (a) the diffraction lines are indicated by their corresponding pseudo-cubic (hkl) values. Curve (b) and (c) show (001) and (002) reflections of the substrate and the $LCMO$ film due to $K\widehat{\alpha}$ and $K\widehat{\beta}$ excitations.

(curve b and c respectively). The presence of only ($00l$) fundamental Bragg peaks of the $LCMO$ due to Cu − $K\widehat{\alpha}$ and $K\widehat{\beta}$ excitations along with the ($00l$) peaks of the substrate, indicate strong texture and epitaxial growth of the films along the pseudo-cubic ($00l$) direction. The (001) reflection from the $LCMO$ film located next to the (001) reflection of LAO and STO substrates is shown in Fig. 3.3. The position of this peak depends on the film thickness, and it approaches the bulk value when the

thickness exceeds $\sim$ *1000 Å*. The variation of the lattice parameter of *LCMO* deposited on *LAO* is also shown in the inset of Fig. *3.3*. It is evident from this figure that a stress - relaxed bulk - like structure is realized once the film thickness exceeds $\sim$ *1000 Å*. The morphology of epitaxially grown *LCMO* thin film was examined by atomic force microscopy (*AFM*) at room temperature. A typical *AFM* picture over an area of *10 μm* × *10 μm* of a $\sim$ *100 u.c.* thick *LCMO* film grown on (*001*) *LAO* is shown in Fig. *3.4*. The rms surface roughness of our films as measured by *AFM* is *0.20 nm - 0.25 nm*.
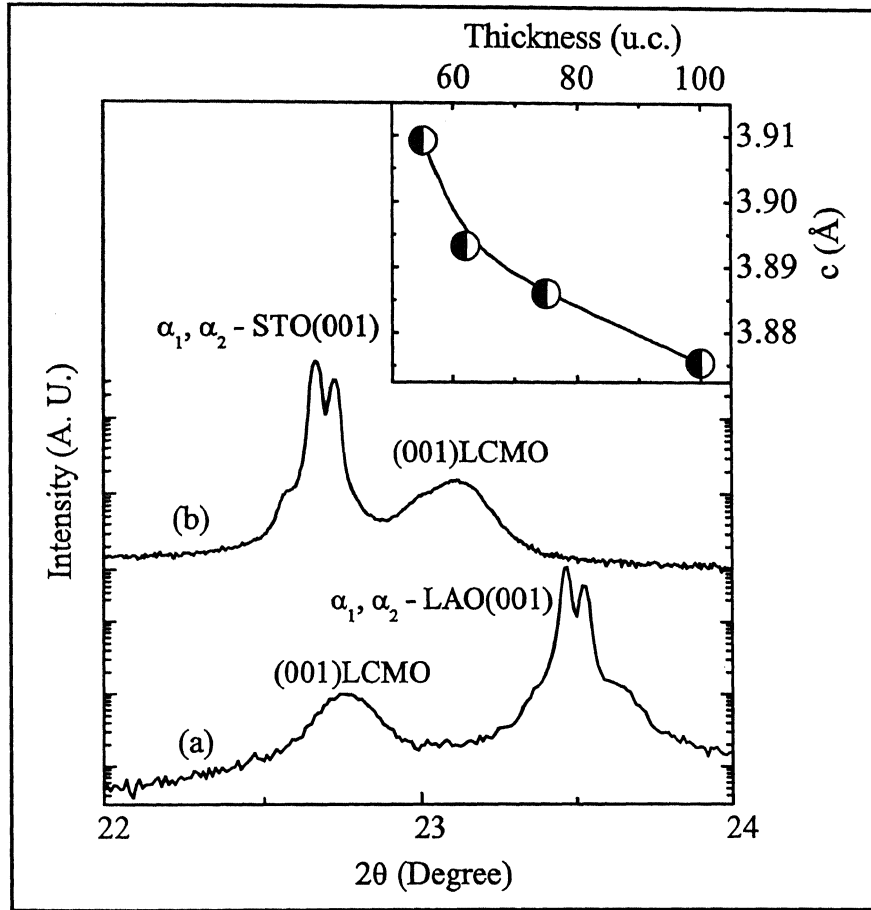
Figure 3.3: Diffracted X - ray intensity around the (*001*) peak of *LCMO* films deposited on *LAO* and *STO* (curve a and b respectively). Figure also shows the (*001*) reflected intensity of substrate due to $K\widehat{\alpha}_1$ and $K\widehat{\alpha}_2$ excitations. Inset shows the pseudo-cubic c - axis lattice parameter of *LCMO* films deposited on *LAO* with different thicknesses.
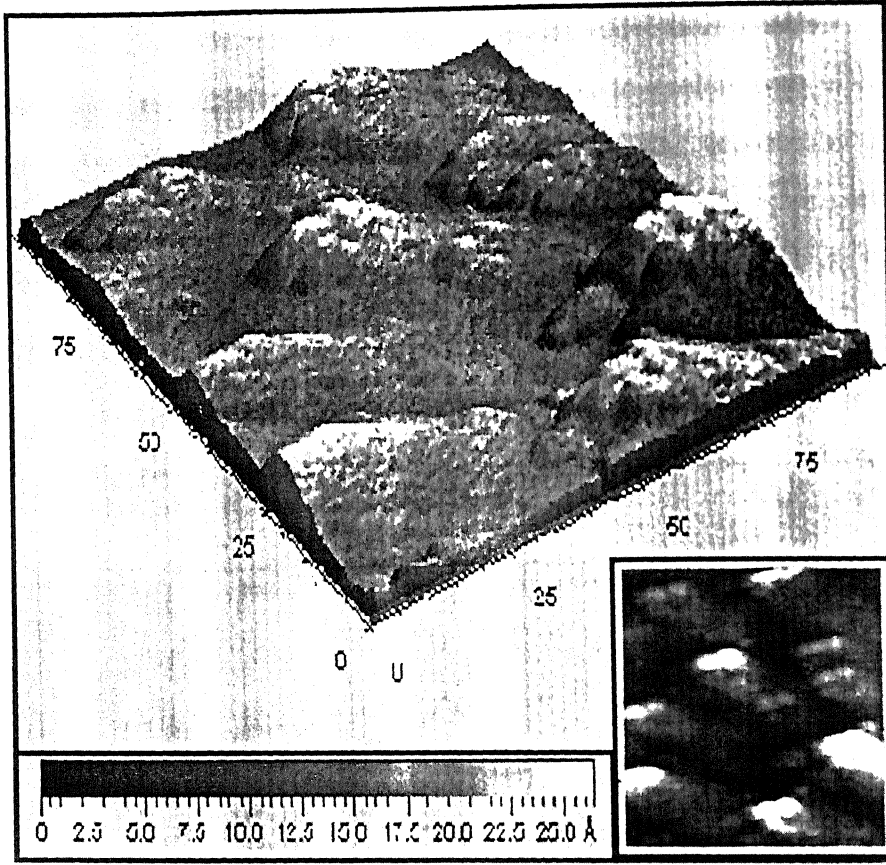
Figure 3.4: *AFM* picture of (*001*) surface of ∼ *100 u.c.* thick *LCMO* film deposited on (*001*) oriented *LAO*.

3.2.2　Electronic transport: Effect of electric and magnetic fields

Fig. *3.5*(a) shows the resistivity ($\rho(H, T)$) of a ∼ *85 u.c.* thick *LCMO* film grown on (*001*) oriented *LAO* substrate. The zero-field resistivity of the film on cooling below room temperature first shows a thermally activated behavior, followed by metallic conduction below a temperature T_P at which it is maximum. These are characteristic features of the resistivity of a hole-doped manganite where the double exchange leads to a metallic and ferromagnetic state below a critical temperature. In the presence of an in-plane magnetic field, a significant drop in resistivity in the
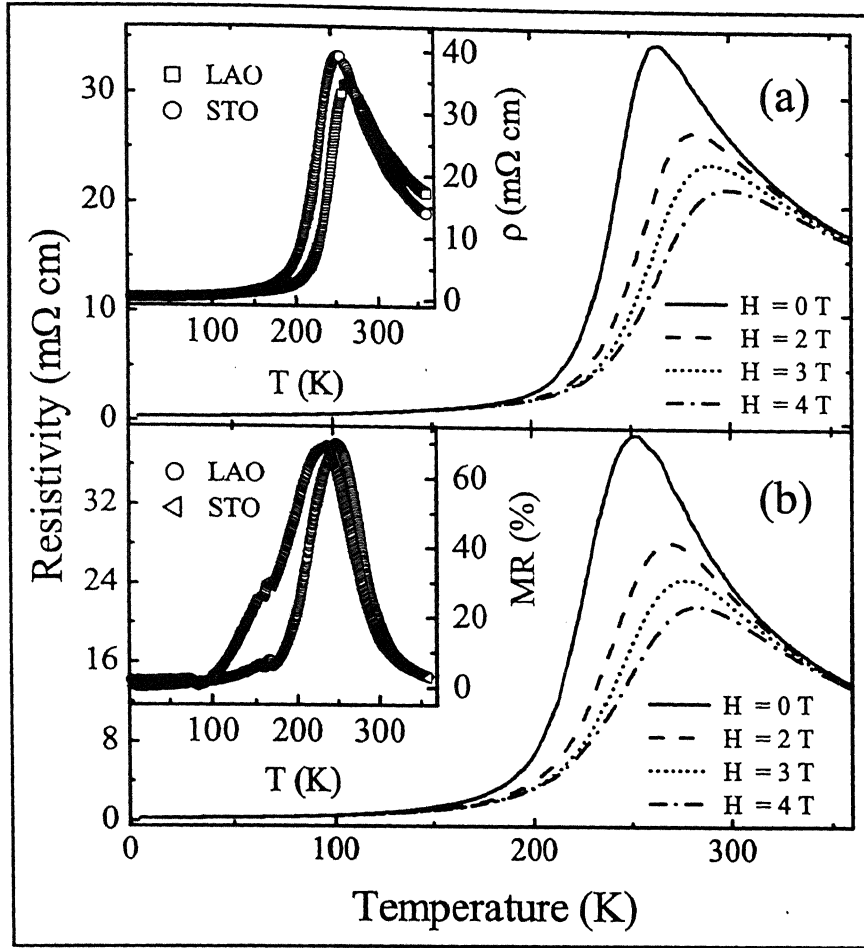
Figure 3.5: Temperature dependent resistivity of ~ 85 u.c. thick LCMO film deposited on (001) oriented (a) LAO and (b) STO. Inset of panel (a) and panel (b) show the zero-field resistivity and magnetoresistance in 4 tesla field respectively of these two films at different temperatures.

vicinity of T_P occurs and also the critical temperature increases with the field. Quite similar features in the $\rho(H, T)$ of ~ 85 u.c. thick LCMO film grown under identical condition in the same run on (001) oriented STO substrate are seen (Fig. 3.5(b)). The inset of Fig. 3.5(a) compares the temperature dependent zero-field resistivity of these two films. The peak in resistivity, which corresponds to the onset of ferromagnetic state on cooling, is at 263 K and 252 K for films on LAO and STO respectively. This temperature is close to the reported Curie temperature of the bulk LCMO. The temperature dependence of magnetoresistance $\frac{\Delta\rho}{\rho} = \frac{(\rho(0,\ T) - \rho(H,\ T))}{\rho(0,\ T)}$ at 4 tesla

of these two films is shown in the inset of Fig. $3.5(b)$. The general trend of the magnetoresistance and its peak value ($\sim$ 70 $\%$) on the two types of substrates are similar.
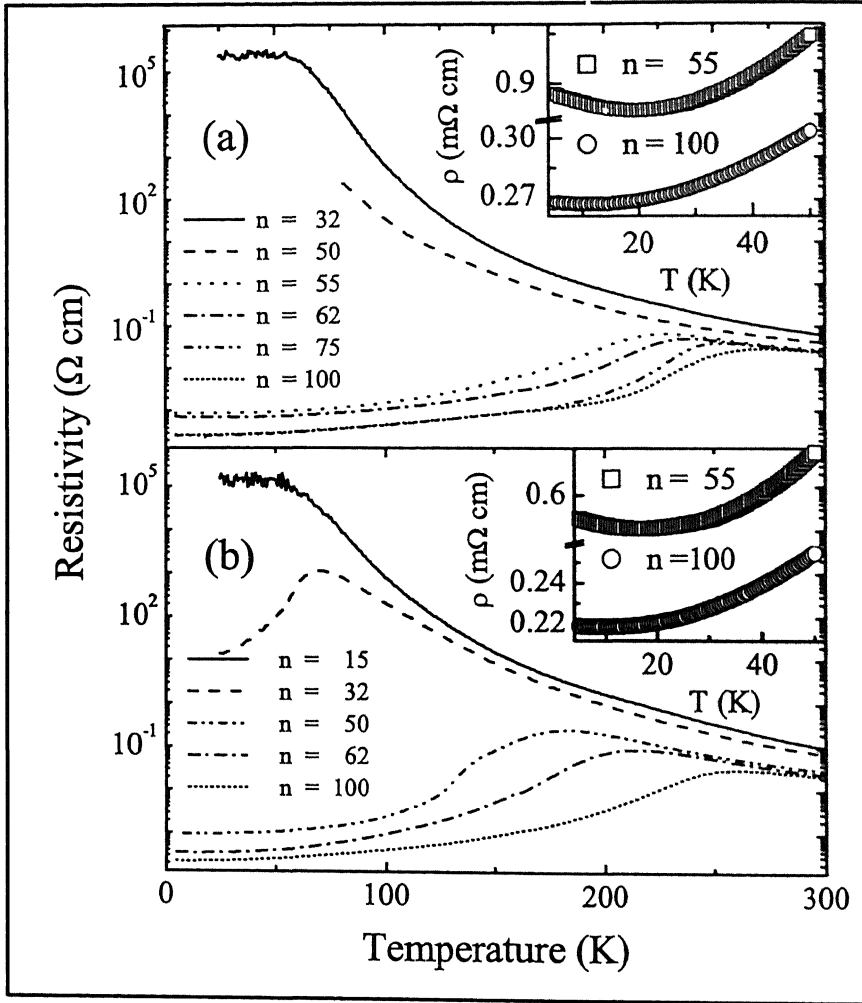
Figure 3.6: Panel (a) shows zero-field electrical resistivity of $LCMO$ films of different thicknesses deposited on (001) oriented LAO. Film thickness is written in the units of pseudo-cubic lattice parameter a = 3.86 $\mathring{A}$. The inset shows the resistivity of the $\sim$ 55 $u.c.$ and $\sim$ 100 $u.c.$ thick films on LAO at lower temperatures. Zero-field resistivity of $LCMO$ of different thicknesses deposited on (001) oriented STO is shown in the lower panel (b). The inset shows the resistivity of the $\sim$ 55 $u.c.$ and $\sim$ 100 $u.c.$ thick films on STO at lower temperatures.
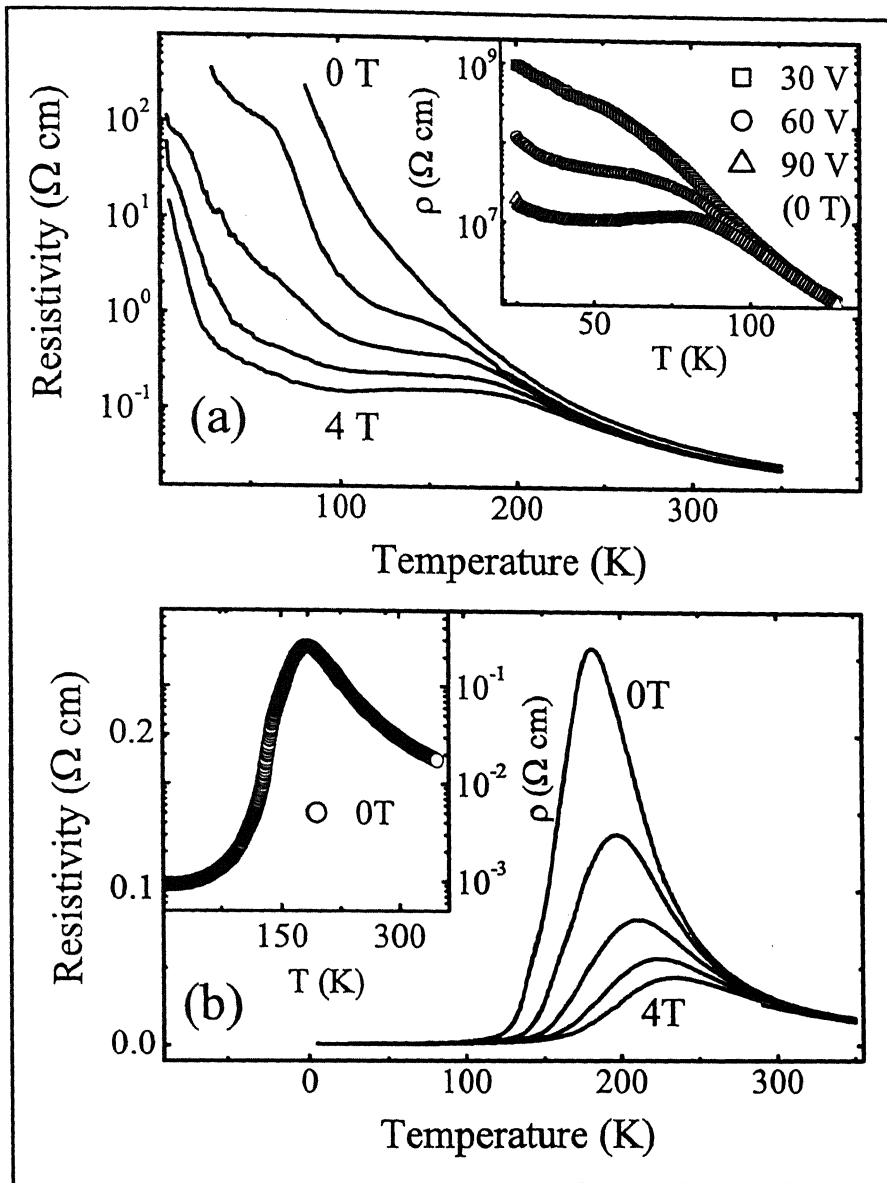
Figure 3.7: (a) Temperature dependent electrical resistivity of a ~ *50 u.c.* thick *LCMO* film deposited on *(001)* oriented *LAO* in presence of *0, 1, 2, 3* and *4 tesla* magnetic field applied parallel to the constant in-plane current. Inset shows the resistivity of the same film measured in a constant voltage mode. The electric fields used are *2000, 4000* and *6000 V/cm* for curves from the top to bottom respectively. (b) Temperature dependent electrical resistivity of a ~ *50 u.c.* thick *LCMO* film deposited on *(001)* oriented *STO* in presence of *0, 1, 2, 3* and *4 tesla* magnetic field applied parallel to the constant in-plane current. Inset shows the zero-field resistivity plotted on a semilog scale to highlight the metallic behavior.

Transport properties of $LCMO$ films on (001) oriented LAO and STO show a remarkable change with the film thickness. The $\rho(0, T)$ of $LCMO$ films of various thicknesses deposited on (001) oriented LAO substrate is shown in Fig. $3.6(a)$. We note that the temperature range over which thermally activated behavior is observed in $\rho(0, T)$ of ~ 100 u.c. thick film increases and the peak temperature T_P shifts to the lower temperatures with the decrease in film thickness. The magnitude of the resistivity also increases with the decrease in film thickness, and becomes very high below a certain thickness. In such films, the metallic state at the lowest temperatures disappears and the resistivity shows a thermally activated behavior over the entire temperature range between 300 K and 4.2 K. At intermediate thicknesses (~ 55 u.c. to ~ 100 u.c.), the metallic resistivity below T_P disappear at the lowest temperatures ($\leq 300 K$) and the resistivity shows a $\sim log\ (1/T)$ divergence. The inset of Fig. $3.6(a)$ shows the low temperature part of resistivity of ~ 55 u.c. to ~ 100 u.c. thick films. Fig. $3.6(b)$ shows the thickness dependent $\rho(0, T)$ of $LCMO$ on (001) oriented STO. The critical thickness of the $LCMO$ film on STO above which a low temperature metallic state develops is smaller than that of the $LCMO$ film on LAO. The low temperature behavior of resistivity of the $LCMO$ films on STO is shown in Fig. $3.6(b)$ (inset).

We now discuss the metal-to-insulator transition seen in these films with decreasing thickness in some detail. Fig. $3.7(a)$, show the resistivity of a ~ 50 u.c. thick film deposited on (001) oriented LAO substrate. In zero - magnetic field the resistivity measured in a constant current mode shows a thermally activated behavior on cooling below room temperature. For $T \leq 90$ K, the resistance of the sample becomes comparable to the input impedance of the voltmeter (~ 1 $G\Omega$). However, in the presence of a magnetic field the resistance at lower temperatures shows a large drop. At 4 tesla field for example, the resistivity is first thermally activated down to ~ 200 K. This is followed by a shoulder and then a shallow minimum at $T \sim 100$ K. On cooling the sample below ~ 50 K, a thermally activated behavior sets in again. At ~ 100 K the resistivity drops by ~ 4 orders of magnitude on application of 4 tesla field. The overall temperature and field dependence of the resistivity of this film on
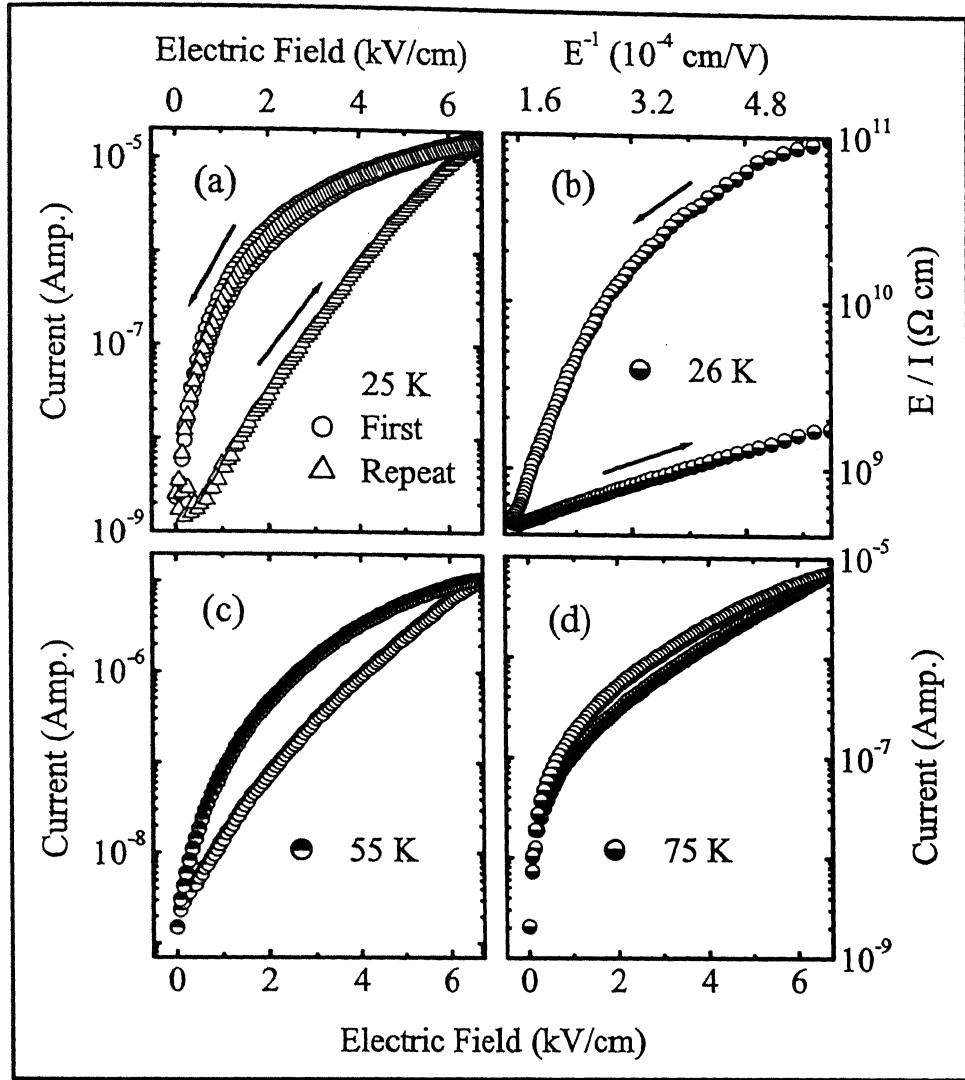
Figure 3.8: $I - V$ characteristic of a $\sim$ *50 u.c.* thick film deposited on *(001)* oriented *LAO* at different temperatures: (*a*) at *25 K*, both the first and repeat scan are shown to highlight the hysteretic behavior in the first scan; (*b*) *25 K* data plotted to illustrate the *exp(1/E)* dependence of the resistance; (*c*) and (*d*) $I - V$ curves at *55 K* and *75 K*, respectively.

LAO is similar to that of a charge ordered manganite such as $Pr_{0.7}Ca_{0.3}MnO_3$ [*61*, *62*]. Since large changes in the electrical resistance of *PCMO* in the *CO* − state can also be triggered through application of electric field [*61*, *121*], we have examined the electric field dependence of the resistivity in these ultra thin films. In the inset of Fig. *3.7(a)* we show the resistivity of this film measured in a constant voltage mode.

Even at the lowest voltage ($E = 2000$ V/cm), the thermally activated behavior of resistivity becomes less pronounced at ~ 60 K. At the highest field (6000 V/cm), we in fact see a metallic behavior in the temperature window of 30 K to 85 K. From a comparison of Fig. $3.7(a)$ and its inset, it is clear that the electric and magnetic fields have similar effect on the charge transport. The resistivity of a ~ 50 u.c. thick LCMO film deposited on STO along with ~ 50 u.c. film on LAO is shown in the Fig. $3.7(b)$. This film has a distinct peak (T_P), its overall value is much larger than that of the thicker film shown in Fig. $3.6(b)$. Further, the onset of the ferromagnetic state in this case is lowered to ~ 180 K. However, as seen in the inset of Fig. $3.7(b)$, the resistivity remains metallic down to ~ 20 K. In the presence of a 4 tesla magnetic field, the magnetoresistance of this film is ~ 85 % near T_P.

The drop in resistance on application of an electric field as seen in the inset of Fig. $3.7(a)$, must also reflect in the $I - V$ characteristics of the sample. In Fig. 3.8 we show the $I - V$ characteristics of the ~ 50 u.c. film on LAO at some selected temperatures. For each of these measurements, the sample was first cooled to the desired temperature in zero electric field and then the field was scanned at a constant rate from zero to a maximum value followed by a reversed scan to zero-field. As evident in the figure, the current transport is highly nonlinear in electric field. On field reversal however, the behavior is hysteretic with current following the Ohm's law. Subsequent field scans at the same temperature and at higher temperatures do not reveal the hysteresis. The behavior remains Ohmic in both directions of the field scan. The hysteretic state is, however, recovered if the sample is warmed up to ~ 180 K and then cooled to the temperature of measurement. Further, the current transport at $T \geq 80$ K is fully reversible irrespective of the sample history. Unlike the behavior of the $I - V's$ in a charge ordered manganite where one sees sharp, step - like increase in current at a particular voltage, here the sample resistance goes smoothly as $exp(1/E)$ with the electric field (see Fig. 3.8, panel b). Films deposited on untreated STO also succumb to this type of unusual transport provided their thickness is sufficiently small.

3.2.2.1   Effect of substrate surface roughness

In Fig. *3.9* we show the electrical resistivity of a $\sim$ *32 u.c.* thick film of *LCMO* deposited on *BHF* – treated and – untreated *STO* and *LAO* substrates. Since the resistance of some of these films at low temperatures was $\geq$ *10^8* Ω these measurements had to be done in a constant electric field mode. For the film on *BHF* – *STO*, the *I* – *V* response was Ohmic and reversible over the entire temperature range. The resistivity of this sample goes through a peak at $\sim$ *90 K* followed by a metallic behavior down to the lowest temperature of measurement. Film of the same thickness but on untreated *STO* has a much higher resistivity and the T_P is shifted to lower temperature by $\sim$ *20 K*. Moreover, the *I* – *V* characteristics of this film at
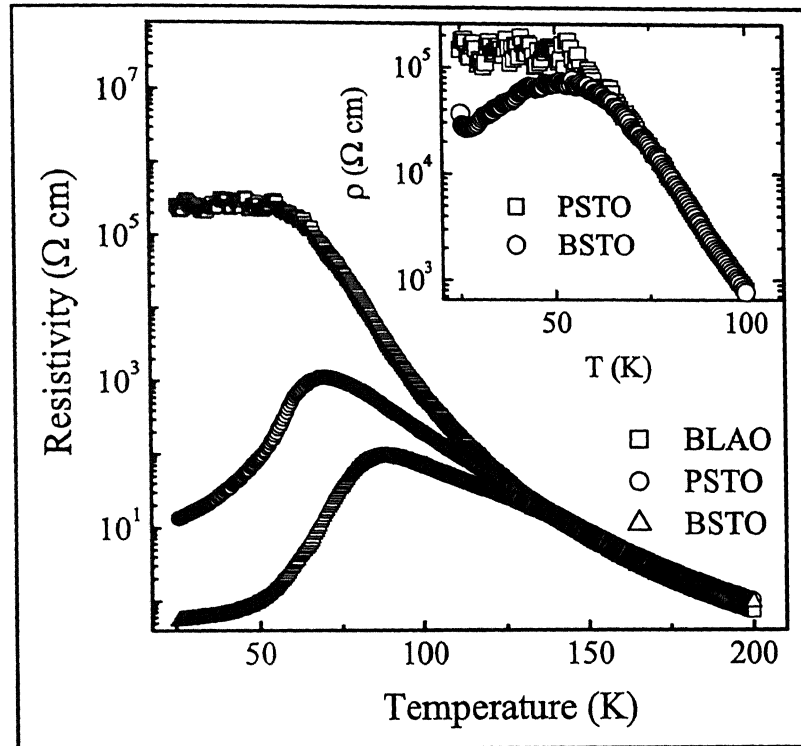
Figure 3.9: Comparison of the zero-field electrical resistivity of $\sim$ *32 u.c.* film on *BHF* – treated *STO* (*B* – *STO*), *BHF* – treated *LAO* (*B* – *LAO*) and untreated *STO* (*P* – *STO*). Inset shows the resistivity of $\sim$ *15 u.c.* films deposited on treated and untreated *STO* substrates. The film on *BHF* – *STO* clearly shows a metallic behavior at low temperature.

$T \leq 70\ K$ were highly nonlinear and hysteretic just as in the case of the film on LAO (Fig. *3.8*). The behavior of the film on BHF treated LAO deposited along with the films on STO, is characterized by a thermally activated resistivity down to $\sim 65\ K$. Below this temperature not much current flows through the sample even when the electric field is increased to *6000 V/cm*. In the inset of Fig. *3.9*, we compare the resistivity of a $\sim 15\ u.c.$ thick film on $BHF - STO$ and untreated STO. Once again, the film on treated substrate shows a T_P and a metallic behavior at $T < T_P$ although its resistivity over the entire range of temperature is much higher than the resistivity of the $\sim 32\ u.c.$ film on $BHF - STO$. The $\sim 15\ u.c.$ film on untreated STO, on the other hand, is highly insulating. From these observations two conclusions can be drawn immediately: one, the film on STO, have better metallic behavior; and two, the buffer HF treatment significantly improves the film quality. The most important aspect of transport in these ultra thin films, however, is the mechanism responsible for the loss of metallic character and the dependence of transport on the strength of the driving force, and its hysteretic character.

3.2.3   Magnetization

For $x \sim 0.3$, the Curie temperature of bulk $LCMO$ in this concentration range is $\sim 250\ K$ with a saturation magnetization slightly less than the expected spin only value of $\sim 3.7\ \mu_B$ *per Mn* atom. The moment is also reduced in non-stoichiometric, cation deficient composition with $x \sim 0.3$. The compounds with a spontaneous magnetization considerably less than the spin only moment, exhibit characteristic differences in field-cooled and zero-field-cooled magnetization and a coercivity which increases rapidly at low temperatures [122]. The temperature dependence of zero-field-cool and field-cool magnetization of $\sim 100\ u.c.$ thick $LCMO$ film deposited on (*001*) LAO is shown in the Fig. *3.10(a)*. In order to compare the Curie temperature observed in resistivity measurement of $\sim 100\ u.c.$ film, $\rho(T)$ is included in the Fig. *3.10(a)*. The ZFC and FC magnetization was measured in presence of *10 Gauss* magnetic field applied along the (*100*) direction of the film. The ZFC magnetization increases slowly with temperature on heating above *5 K* and becomes maximum at $\sim 220\ K$. Between *220 K* to *260 K*, the magnetization drops
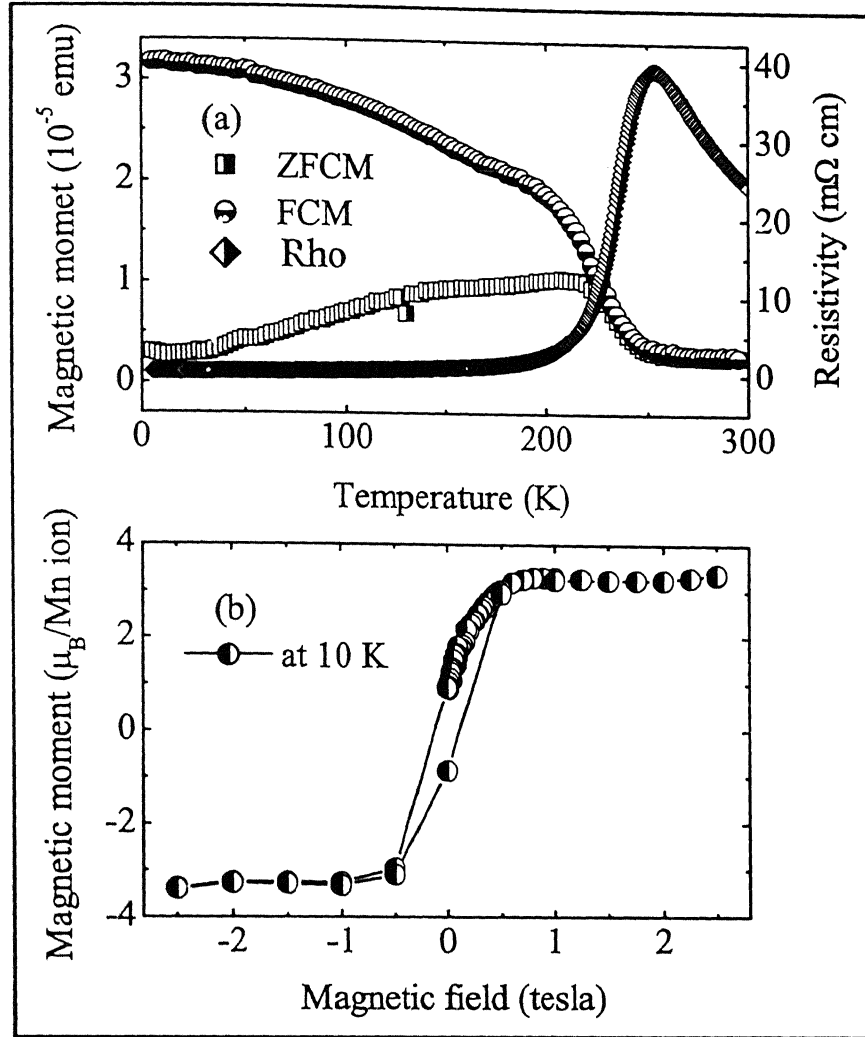
Figure 3.10: Panel (a) shows temperature dependent zero-field-cool (ZFC), field-cool (FC) magnetization and resistivity of a ~ 100 u.c. thick $LCMO$ film deposited on (001) oriented LAO. Panel (b) shows the hysteresis loop of the same film.

rapidly and above $260\ K$ its value becomes negligibly small. The FC magnetization decreases slowly and then rapidly with temperature on heating above $5\ K$ and the magnetization is very small above $260\ K$. Near the paramagnetic to ferromagnetic transition temperature, the magnetization is related to the temperature by simple power law $\frac{M}{M_0} = \alpha \left(1 - \frac{T}{T_c}\right)^\beta$, where M_0 is the saturation magnetization at $T = 0$, T_C is the Curie temperature and the critical exponent β is a sensitive indicator of the dimensionality of the system. The low field saturation magnetization is $\sim 0.35\ u_B$.

The value of $\beta = 0.33$ is similar to that of a standard Heisenberg - type spin-spin coupling. The temperature dependent FC magnetization was fitted with the above relation for $\beta = 0.33$. The value of α and T_C obtained from the fitting are 1.04 and $\sim 247\ K$ respectively. The zero-field-cool hysteresis loop of the same film measured at $10\ K$ is shown in Fig. $3.10(b)$. The saturation magnetic moment obtained by extrapolating to the zero-field is $3.64\ \mu_B$. The high-field saturation magnetization is close to that expected for high spin manganese in octahedral coordination. For spin only moment, $\mu = gS\mu_B$, with $g = 2$, the magnetic moment of $LCMO$ for $x = 0.3$ is;

$\mu = 2\ \mu_B\ ((0.7 \times 2\ (from\ Mn^{3+})) + (0.3 \times 3/2\ (from\ Mn^{4+}))) = 3.7\ \mu_B$.

3.3   Discussion

Electronic properties of ultra thin epitaxial films are influenced by the nature of the substrate, which largely controls the film growth morphology, defect structure and the level of stress. In general, if the difference Δa between the lattice parameters of the film and substrate is within ~ 2 percent, film growth takes place in a layer by layer mode accommodating the difference Δa through expansion or contraction of the in-plane lattice parameter. At larger thicknesses, the compressive or tensile state is relieved through production of lattice defects. However, if the difference in the lattice parameters is significantly larger, an island type growth starts at the beginning of film deposition [123]. The lattice parameter of bulk $La_{0.7}Ca_{0.3}MnO_3$ is $3.86\ \mathring{A}$ whereas for the cubic crystals of STO and LAO it is $3.905\ \mathring{A}$ and $3.792\ \mathring{A}$ respectively leading to $\Delta a = -\ 0.045\ \mathring{A}$ and $+\ 0.068\ \mathring{A}$ between the $LCMO$ and the substrates. It is, therefore, expected that the films of $LCMO$ on STO will be under tensile stress whereas the state of stress will be compressive in film deposited on LAO. The stress due to the in-plane lattice mismatch leads to a compressed and expanded out-of-plane lattice parameter of the films of $LCMO$ on STO and LAO respectively. The out-of-plane lattice parameter calculated from the $X - ray$ diffraction profile shown in Fig. 3.3 is smaller than that of the bulk value for the film on STO and larger for the film on LAO. The substrate induced stress is, however, gradually relived with the increasing film thickness. This is evident from the behavior of the lattice

parameter which approaches the bulk value once the thickness exceeds ~ 1000 Å. The inset of Fig. 3.3, shows the gradual decreases of out-of-plane lattice parameter of the $LCMO$ on LAO towards the bulk value with the increase in film thickness. Further, the extent of lattice deformation in films on LAO is expected to be larger due the higher value of Δa.

In $La_{0.7}Ca_{0.3}MnO_3$ the spin disorder and strong electron - phonon scattering result in the localization of e_g electrons, and hence an insulating behavior at $T > T_C$. As the temperature is lowered and spin fluctuations decrease, the combined itinerant/local - moment system lowers its total energy by aligning the spins ferromagnetically and allowing the itinerant electrons to gain kinetic energy. The increase in mobility of itinerant e_g electrons favors the double exchange and leads to the metallic state. The characteristic features of electronic transport of thick $LCMO$ film, with the exception of the residual resistivity and T_P, are independent of the substrate and magnetic field. The application of magnetic field also causes local ordering of magnetic spins in the paramagnetic insulating state and hence the peak in resistivity shifts to higher temperatures. Cao et al. [124] explained this phenomenon in terms of formation of clusters or domains. In the presence of an in-plane magnetic field, we also observed a large drop in resistivity near T_P and a shift of T_P to higher temperatures. The difference in magnitude of resistivity of $LCMO$ films deposited on STO and LAO substrate can be attributed to the nature of correlation between the magnetic clusters and localization of e_g electrons when the substrate induced distortion in the films is of opposite nature. The high value of T_P observed in the $LCMO$ film deposited on LAO [see Fig. $3.5(a)$ (inset)] is attributed to the compressive stress, which favors deloclization of e_g electrons due to orbital overlap. This behavior is consistent with the variation of T_P of the bulk $LCMO$ under hydrostatic pressure [106, 125] and the reported substrate dependent T_P of $LCMO$ [126]. While the magnetoresistance in the vicinity of T_P is the same for both films, it differs significantly at other temperatures. A comparison of magnetoresistance of $LCMO$ deposited on LAO and STO indicate the presence of more spin fluctuations in the $LCMO$ on STO.
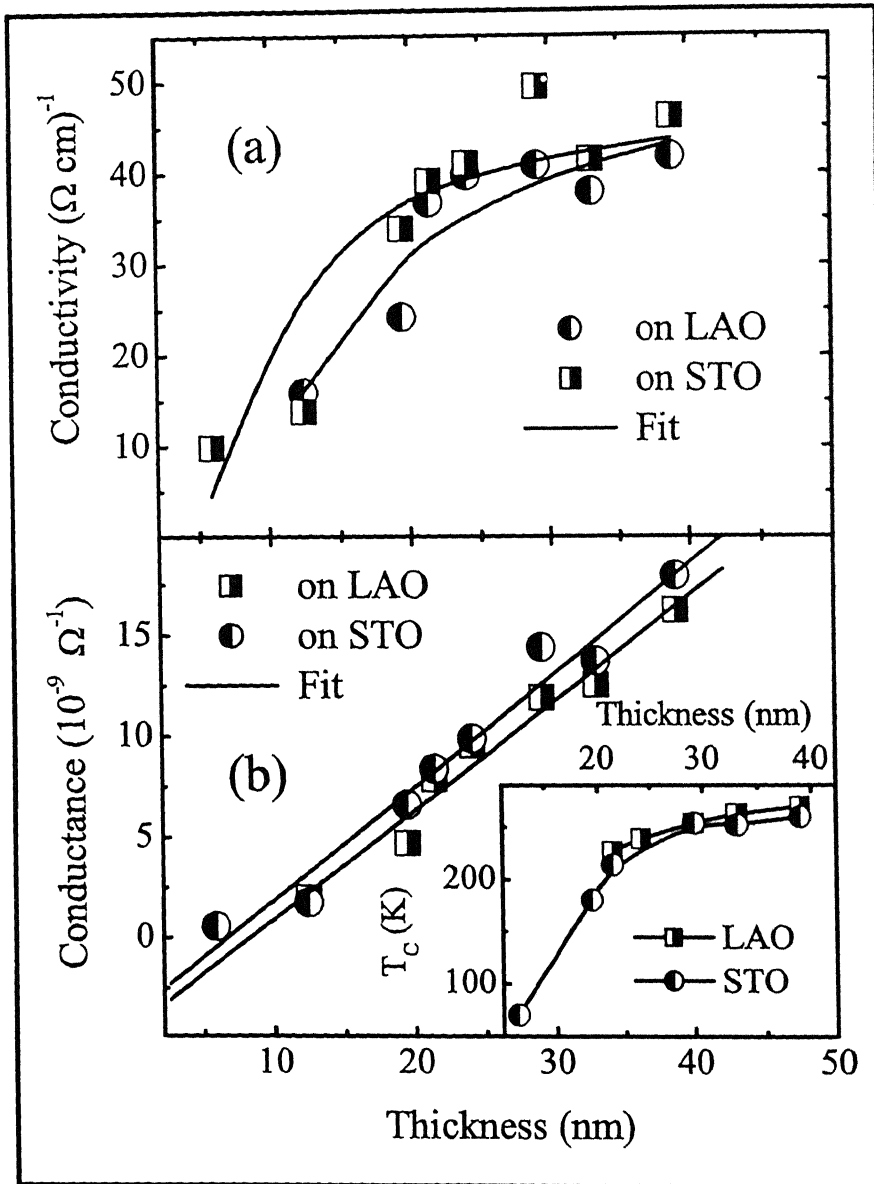
Figure 3.11: (a) Zero-field room temperature conductivity of $LCMO$ film grown on (001) oriented LAO and STO with different thicknesses. The solid curve is the fit to the data using simple parallel resistor model. (b) Zero-field conductance of these samples at room temperature. The solid line is the fit to the data (see text for detail). Inset of panel (b) is the plot of metal insulator transition temperature for different film thicknesses.

The thickness of these films strongly affects electronic transport and magnetism. The characteristic features of the temperature dependent resistivity of bulk $LCMO$ change dramatically as a function of film thickness. The variation of zero-field room temperature conductivity with the thickness of $LCMO$ films deposited on (001) oriented LAO and STO is shown in Fig. $3.11\,(a)$. These data have been fitted with a simple parallel resistor model assuming the film as combination of a conducting layer of $LCMO$ and a insulating layer due to the substrate induced structural disorder with very small conductivity. Assuming the disordered layer conductivity to be zero, the conductivity of the film is approximated to $\sigma \approx \sigma_B\,(t\,/\,(t-t_D))$, where σ_B is the bulk conductivity of $LCMO$ and t_D the thickness of the substrate induced disordered interface layer. The conductance (σt) in metals displays size-effects due to surface and interface scattering that is classically treated within Fuchs-Sondheimer theory [21, 22]. The expression for the conductance in terms of film thickness t is

$$\sigma t = (\sigma_B t)\left[1 - \frac{3l_B}{2t} + (3l_B + 2t)\int_{1}^{\infty}\left(x^{-3} - x^{-5}\right)\,e^{-\frac{dx}{l_B}}\,dx\right], \qquad (3.1)$$

where σ_B is the conductivity and l_B is the mean free path of the bulk material. In the limit of thick and thin films, the conductance can be approximated as;

$$\sigma t = \sigma_B\left(t - \frac{3l_B}{8}\right), \qquad\qquad 3l_B << t, \qquad\qquad (3.2)$$

$$\sigma t = \sigma_B\left(t - \frac{3t^2}{4l_B}\right)\,ln\left(\frac{l_B}{t}\right), \qquad 3l_B >> t\,(3l_B - 2t). \qquad (3.3)$$

The carrier concentration of bulk $LCMO$ below $100\,K$ is $\sim 5.2 \times 10^{-27}\,m^{-3}$ [127], using this, the estimated mean free path is $\sim 1.7\,nm$. In the paramagnetic state, if a mean free path can be defined, it will certainly be less than this value. Most of our films satisfy the condition $l_B << t$ so eq. (3.2) is valid. This equation indicates a linear dependence of conductance with the film thickness. This is shown in Fig. $3.11(b)$. The value of σ_B determined from this analysis is consistent with the measured resistivity of thick $LCMO$ films. The value of σ_B is identical for films on STO and LAO within the uncertainty of these measurements.
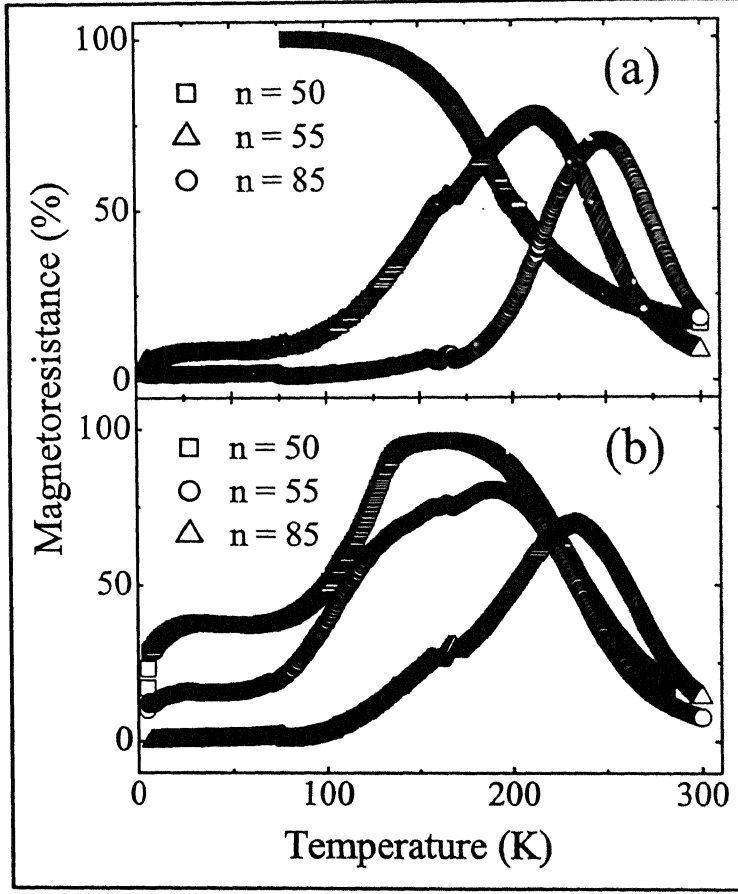
Figure 3.12: Temperature dependent magnetoresistance of *LCMO* films of different thicknesses grown on (*001*) oriented *LAO* (panel a) and *STO* (panel b) with different thicknesses at *4 tesla* in-plane magnetic field.

Chen et al. [*128*] reported that the thickness dependence of T_P mainly results from the strain dependence of the polaronic formation energy though there are also contributions from the electronic bandwidth and the characteristic phonon frequency. The variation of metal - insulator transition temperature (T_P) is shown in the inset of Fig. *3.11(b)*. The T_P decreases with the decrease in film thickness, with nearly identical behavior for *LAO* and *STO* substrates. A marginally higher T_P of *LCMO* on *LAO* indicates that the temperature induced spin disorder is more in the *LCMO* on *STO*.

The resistivity of $LCMO$ with thickness shows a remarkable change in the presence of a magnetic field. The magnetoresistance of $LCMO$ films of thickness 50, 55 and 85 $u.c.$ deposited on LAO and STO substrate is shown in Fig. $3.12(a)$ and Fig. $3.12(b)$ respectively. We note that the temperature where the magnetoresistance is maximum decreases and the magnetoresistance increases as the film thickness is reduced. There are several possible explanations for the sharp increase of magnetoresistance with decreasing film thickness. The lattice distortions in highly strained ultrathin films can enhance electron localization, resulting in a highly resistive state. By applying a high magnetic field, the electrons delocalize as the magnetization increases and hence the resistance is reduced. Several groups [129] have reported an enhanced magnetoresistance in manganite films and bulk materials by introducing structural and spin disorder. The disorder can result in a reduced mobility of the conduction electrons.

To investigate the behavior of temperature dependent resistivity in the paramagnetic state, we have used a simple Arrhenius law, a polaron model and a variable - range hopping model to fit the paramagnetic state resistivity data. Arrhenius law indicates activation energies typically 0.1 eV to 0.2 eV. We have also used the phenomenological polaron hopping expression $\rho = CT \, exp \left(\frac{W_P}{K_B T} \right)$, where C is a constant, W_P is the polaron activation energy and K_B Boltzman constant. Strong exchange coupling between the e_g electrons and local moments is expected to give rise to magnetically self-trapped carriers. These entities are free magnetic polarons (FMP) in contrast to the more common bound magnetic polarons (BMP) where a carrier is trapped by an impurity and the local magnetization is a secondary phenomenon. The lattice distortion (small polaron) leads to the localization of e_g electrons. The localization [130] and self-trapping [69] of e_g electrons contribute to the polaron activation energy. The polaron activation energy of $LCMO$ films changes with the film thickness, nature of the substrate and the magnetic field. The variation of polaron activation energies of $\sim$ 100 $u.c.$ $LCMO$ deposited on (001) oriented LAO and STO with magnetic field is shown in the Fig. $3.13(a)$. The activation energy for the $LCMO$ film on STO is smaller than the film on LAO. This observation is consistent with the observed higher transition temperature of the film on LAO. It appears that the

in-plane compression of the MnO_6 octahedra on LAO leads to the orbital overlap, thereby delocalization of e_g electrons while the in-plane expansion of MnO_6 on STO leads to localization. We attribute the higher polaron activation energy of $LCMO$ film on STO to the localization of the e_g electrons. The polaron activation energy for the films on LAO and STO decreased linearly with external magnetic field. The variation of polaron activation energy with film thickness is shown in Fig. $3.13(b)$. It first decreases with film thickness and then attains saturation for thicker films.
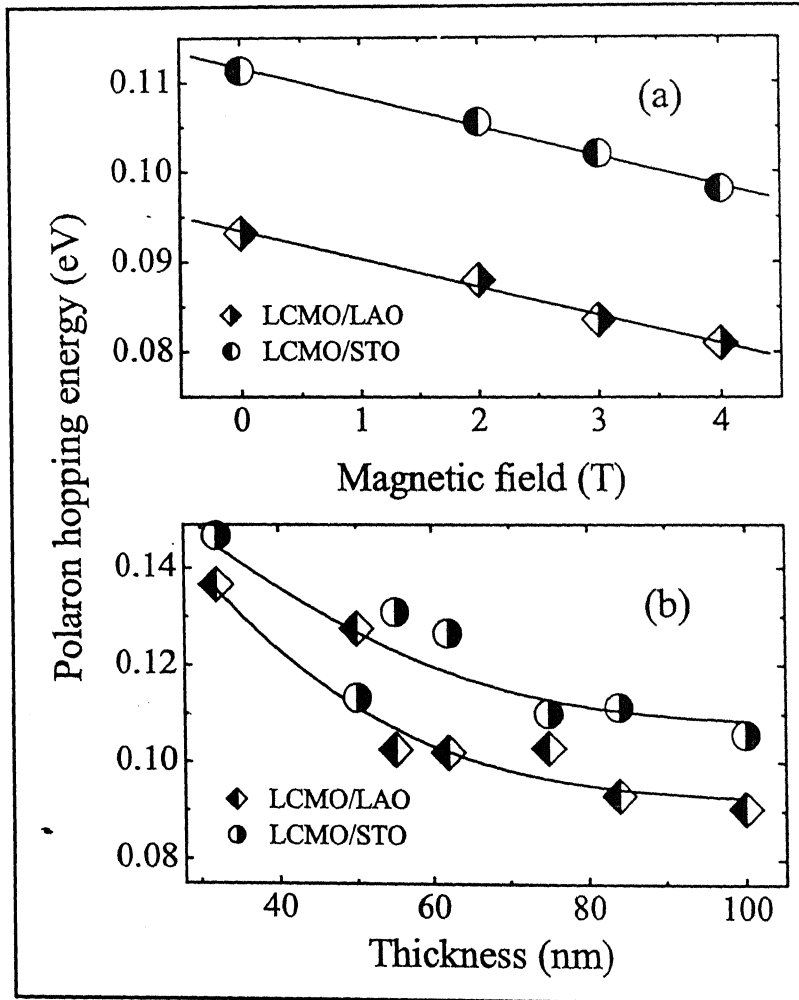
Figure 3.13: (a) Polaron activation energy in paramagnetic insulating state of ~ 100 $u.c$ thick $LCMO$ film grown on (001) oriented LAO and STO at different magnetic fields. (b) Polaron activation energy in paramagnetic insulating state of $LCMO$ films grown on (001) oriented LAO and STO with different thicknesses at zero-field.

We now pay a special attention to the electrical transport in ultra thin films of $LCMO$. The resistivity of these films displays insulating behavior at low temperatures together with a negative magnetoresistance, which is much larger than the colossal magnetoresistance. The physical properties and microstructure of ultrathin films of $La_{0.7}Ca_{0.3}MnO_3$ on STO and LAO substrates have been examined earlier. Zandbergen et al. [119] found that while ~ 80 Å films on (001) STO are ferromagnetic below 160 K, the nature of electrical conduction in these films remains strongly thermally activated down to helium temperatures. These authors, however, have not established the critical thickness above which films behave as a typical double exchange ferromagnet. Based on their high resolution electron microscopy studies, the authors attribute the insulating behavior to lattice mismatch induced in-plane distortion of the structure which traps mobile carriers. Ultra thin films of $LCMO$ on LAO show island type growth. A 150 Å film deposited using pulse laser technique by Biswas et al. [123] shows a behavior similar to that of the 80 Å films on STO [119]. From the results of microscopy, transport and magnetization studies, Biswas et al. suggest a granular structure consisting of ferromagnetic and antiferromagnetic regions for this film. While this model for films on LAO successfully explains the observed low temperature ferromagnetic state of insulating character, many questions remain unanswered in these earlier studies. For example, (i) the critical thickness above which a low temperature metallic state develops is not known, (ii) ultrathin films on STO do not show inhomogeneities and yet they are insulating, (iii) irrespective of the film microstructure, strong magnetic field induces similar metallic character in these films.

Our comparative studies of electrical transport in films deposited on untreated and BHF treated STO and LAO substrates yield some new information about the growth modes and electrical transport in ultra thin films of $LCMO$. First of all, it is evident that the critical thickness below which films on STO become insulating depends on the smoothness of the substrate. Films deposited on BHF treated STO remain metallic down to ~ 20 $u.c.$ thickness. However, in spite of the smoothness of the substrate, the T_P of these films continues to decrease with the decreasing thickness. These observations suggest that the lowering of the T_P and the insulating behavior

are due to the biaxial strain and the inhomogeneous growth regions respectively. On untreated STO, the inhomogeneous regions are likely to be more abundant leading to the insulating behavior at a higher thickness. In the case of LAO substrates, the large Δa leads to island type growth even on atomically smooth surfaces and this is why the BHF treatment does not improve the film quality.

The above picture suggests that ultra thin films of $LCMO$ on LAO and untreated STO can be visualized as consisting of a granular structure where metallic and ferromagnetic domains are separated by nonmagnetic insulating regions. In the case of STO substrates, such regions perhaps nucleate at the polishing related defects, whereas, on LAO the defects as well as island growth are responsible for such regions. While the atomic force microscopy images of the films on LAO clearly indicate the presence of such regions [123], the scanning tunneling microscopy work on STO [120] also suggests the presence of an inhomogeneous distribution of conducting and non conducting regions. Electron transport in such a medium will be dominated by tunneling if the fraction of metallic grains is below the percolation threshold. At the higher concentration of these grains, the conductivity of the sample will be metallic. The tunneling conductance between ferromagnetic grains is dependent on the relative orientation of the magnetization vectors in the grains. As argued by Gittleman et al. [131] in the case of $Ni - SiO_2$ cermet films, the tunneling conductance between two ferromagnetic grains is proportional to the degree of correlation of the magnetic moments of the neighboring grains averaged over all configurations, $\dfrac{\left\langle \vec{\mu_1}\left(\vec{H}\right) \cdot \vec{\mu_2}\left(\vec{H}\right)\right\rangle}{\mu^2}$, where $\vec{\mu_i}$ is the magnetic moment of the ith grain and $|\vec{\mu_i}| = \mu$. The role of applied magnetic field is to orient the moments and thus increase the average $\langle \vec{\mu_1} \cdot \vec{\mu_2}\rangle$. This simple argument shows that a drop in tunneling resistance will occur, as the magnetization vectors of the neighboring grains tend to become parallel under the applied field.

The tunneling resistance between two metallic particles also depends on the strength of the electric field (E) [81]. For a random network of metallic grains it is expected to vary with the electric field as $R \sim R_0 \ exp\left(\frac{E_0}{E}\right)$, where the coefficients R_0 and E_0 are related to the electrostatic charging energy and geometry of the grains. The data shown in Fig. $3.7(a)$ and the behavior of $I - V$ curves in Fig. 3.8 are con-

sistent with this picture. This granular picture is also consistent with the behavior of ZFC and FC magnetization shown in Fig. *3.10*. The $ZFC - FC$ magnetization separates as temperature decreases below the paramagnetic - ferromagnetic transition temperature (T_C). The presence of irreversibility in the $ZFC - FC$ magnetization indicates the presence of short - range spin order. The magnetic behavior differs depending on whether the sample is cooled down with or without a field, which is a characteristic of a spin glass. As is well known, the randomness of the signs of the nearest neighbor coupling (ferromagnetic or antiferromagnetic) is a important prerequisite for a spin glass. At $\sim 10\ K$ as the magnetic field increases, the magnetic ions (Mn^{3+} and Mn^{4+}) align with the field giving rise to a saturation magnetization at $\sim 0.9\ tesla$ field. While this spin and electric field dependent tunneling explains the broad features of our data, the observed hysteretic and history effects in the ($I - V$) curves still need to be understood. Here we hypothesize that the nonconducting intergranular material possesses some elements of charge ordering. Such effects are likely to be introduced by the lattice strain. The strong electric field, in addition to promoting tunneling, also seems to melt these CO regions separating the ferromagnetic clusters. The conducting channels created by the melting remain open even after the electric field is removed. This is why the reverse branch of the $I - V$ curves is Ohmic. Evidence for such permanent changes when the electric field is removed is seen in a large number of CO systems [122, 132]. Experiments on CO systems also show increase in magnetization on application of strong electric field [133]. It is likely that the insulating regions, which constitute the conducting channels under the electric field, also become ferromagnetic. The fact that the virgin state of the samples is recovered only after heating the samples above the FM ordering temperature strongly supports this argument.

3.4   Conclusions

We have studied the structure, surface morphology and stoichiometry of thin films of $La_{0.7}Ca_{0.3}MnO_3$ deposited on (001) LAO and STO by X - ray diffraction, atomic force microscopy and Rutherford back scattering respectively. The critical

thickness required to achieve the bulk lattice parameter of $LCMO$ is smaller on STO than on LAO. We have measured the electric and magnetic - field - dependent charge transport in thin epitaxial films of various thicknesses. At very small thicknesses (< 80 u.c.), the electrical behavior of these films on LAO is significantly affected by the lattice mismatch induced strain and inhomogeneous growth morphologies related to the atomic scale roughness of the substrate. The hysteretic and history dependent insulating behavior seen in the ferromagnetic state of these films suggests coexistence of charge ordered and ferromagnetically ordered regions. We have shown that a special etching procedure, which is known to remove the atomic scale roughness and lead to TiO_2 terminated terraces on STO, results in metallic films even at thickness as low as ~ 15 u.c..

Chapter 4

Physical properties of metallic and insulating spacer films of non-magnetic character

4.1 Paramagnetic metal spacer

4.1.1 Introduction

The nickelates of formula $ANiO_3$ with rare earth element at the A − site, show very interesting changes in their physical properties as the size of the rare - earth element is varied. When A − site is a small cation, they are charge - transfer insulators with a small gap, but when A − site is a large cation these compounds are metals and for intermediate values of $\langle r_A \rangle$, they exhibit insulator-to-metal transition as a function of temperature. The $M - I$ transition is accompanied by electronically induced structural changes involving the $Ni - O - Ni$ angles and $Ni - O$ bond distances. Medarde et al. [134] have proposed a highly covalent $3d^7$ ground state for some of these systems. The $M - I$ transition is caused by opening of a charge - transfer gap. Barman et al. [135] have attributed the $M - I$ transition to a change in the $Ni : 3d - O : 2p$ covalency. The Ni^{3+} in $ANiO_3$ are in the low spin state : $t_{2g}^6 \, e_g^1$ and

order antiferromagnetically, except in $LaNiO_3$, which is a Pauli paramagnet. LNO has a pseudo-cubic structure with a small rhombohedral distortion. Its unit cell (containing two formula units) can be mapped onto a primitive rhombohedral cell with the pseudo-cubic lattice constants $a = 3.83$ Å. Its physical properties are strongly sensitive to oxygen stoichiometry and doping. While $LaNiO_3$ is metallic, $LaNiO_{2.5}$ has Ni^{2+} and is insulating and antiferromagnetic with $T_N = 320$ K. $LaNiO_{2.75}$ is a mixed - valence system (Ni^{2+} / Ni^{3+}) and shows an insulator - metal transition at ~ 75 K, as well as spin localization and magnetic frustration [136]. Gonzalez and coworkers [137] have expressed $LaNiO_{2.5}$ and $LaNiO_{2.75}$ in terms of a homologous series of general formula $La_n Ni_n O_{3n-1}$ with $n = 2$ and 4 respectively. These members consist of $n - 1$ octahedral layers alternating in an ordered way, with one layer NiO_4 square planes along the z - direction of the perovskite structure. $LaNiO_3$ has a tendency to loose oxygen. The reduction in $LaNiO_3$ changes the valence state and O coordination of Ni ions where Ni^{3+} changes to Ni^{2+}. On going from $LaNiO_3$ to $LaNiO_{2.5}$, an enlargement of the cell volume is observed due to the increase in average ionic radius of $Ni(Ni^{3+}$ and $Ni^{2+})$. As the $Ni - O$ distance increases, the electronic transfer integral and bandwidth reduce leading to electronic localization. Gayathri et al. [138] have measured the electronic transport, susceptibility and Hall effect of ~ 2000 Å thick $LaNiO_{3-\delta}$ films deposited on LAO substrate with $\delta = 0, 0.02, 0.08$ and 0.14. They have pointed out that the inconsistency in the value of residual resistivity and resistivity difference ($\rho(300$ K$) - \rho(4.2$ K$))$ in different reports could be due to oxygen non-stoichiometry. These samples show metallic - like thermopower with negative sign and the Hall coefficient has a positive sign. Sagoi et al. [139] have measured the resistivity of LNO films deposited on STO at different substrate temperatures. They observe an increase in the resistivity of the sample as the substrate temperature increases. The lowest resistivity (1.5×10^{-4} Ω cm) is observed at different substrate temperatures of 500 °C and 120 mTorr oxygen pressure. Guo et al. [140] have analyzed the structure and electrical properties of LNO deposited on STO using PLD as a function of substrate temperature and oxygen pressure. The room temperature resistivity of these samples decreases and saturates as the substrate temperature and oxygen pressure increases. The lowest room temperature resistivity

$(5 \times 10^{-5} \ \Omega \ cm)$ is observed at different substrate temperatures of $700 \ ^{\circ}C$ and $35 \ Pa$ oxygen pressure. The sensitivity of LNO to oxygen stoichiometry demands special care during film deposition.

In this section we present preparation, X – ray based characterization and transport measurements on LNO deposited on STO and LAO. The residual resistivity and resistivity difference $(\rho(300 \ K) - \rho(4.2 \ K))$ of our $\sim 72 \ u.c.$ thick LNO films on LAO are $98 \ \mu\Omega \ cm$ and $260 \ \mu\Omega \ cm$ respectively. These parameters for the films on STO are $143 \ \mu\Omega \ cm$ and $248 \ \mu\Omega \ cm$ respectively. A marginally higher value of $\rho(300 \ K)$ and ρ_0 in films deposited on STO is perhaps due to the larger lattice mismatch with STO. A study of ultra thin films of LNO deposited on LAO with different thicknesses of STO buffer layer supports this viewpoint. The good quality films of LNO show a negligibly small magnetoresistance. Further, the field-cooled and zero-field-cooled measurements of magnetization on these films do not show magnetic ordering down to $4.2 \ K$.

4.1.2   Results

4.1.2.1   Rutherford Backscattering and X – ray diffraction

Rutherford backscattering experiments with $1.6MeV \ He^{+}$ ion were performed to compare the stoichiometry and thickness of LNO film deposited on $(001) \ STO$. Fig. 4.1 shows the scattered particle spectrum and the $RUMP$ simulation curve (solid line). The elemental ratio and thickness of the film were calculated from the simulation. Fig. 4.2 shows X – ray diffraction pattern of a bulk powder sample of LNO (curve a), and of a LNO film grown on (001) oriented STO (curve b). While the diffraction pattern of the powder shows all major reflections of the pseudocubic phase, the X – ray profile of the film shows only $(00l)$ Bragg peaks due to $Cu - K\widehat{\alpha}$ and $K\widehat{\beta}$ along with the $(00l)$ reflections of the substrate. Inset of Fig. 4.2 shows the fundamental (001) peak of the LNO film deposited on LAO (curve 1) and STO (curve 2) substrates.
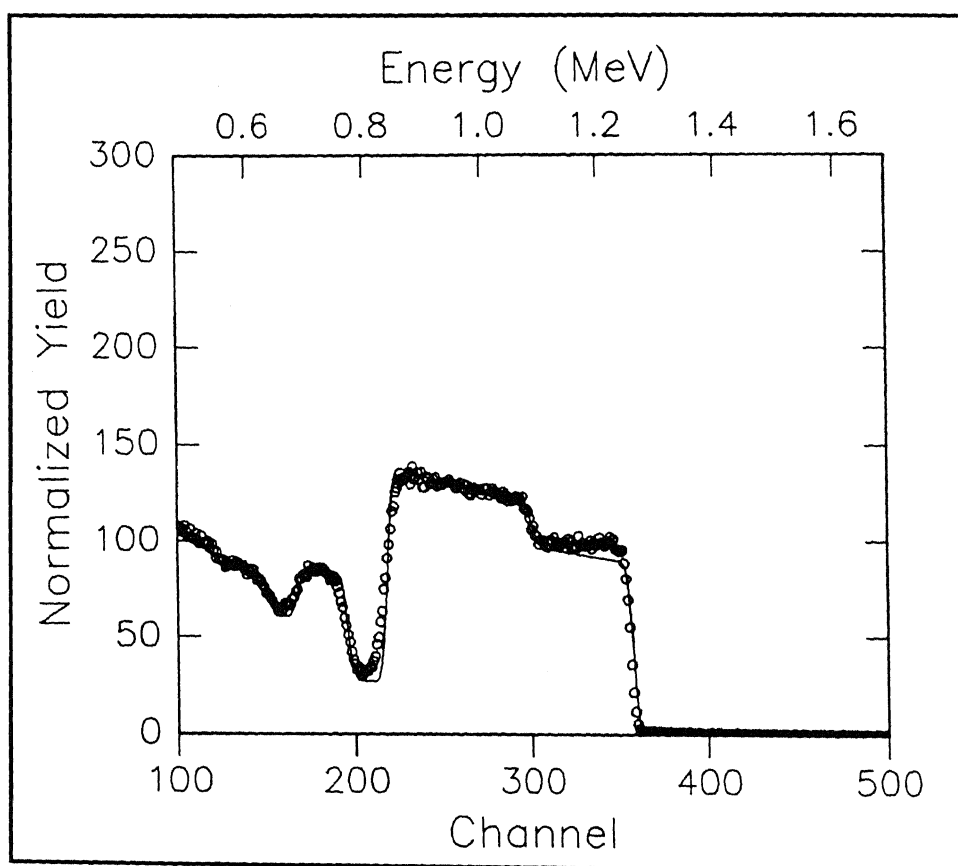
Figure 4.1: Rutherford backscattering spectrum of He^+ ions from thin film and substrate. The sample is *1000 Å* thick *LaNiO₃* film deposited on (*001*) oriented *SrTiO₃*. Solid line is the *RUMP* simulation data.
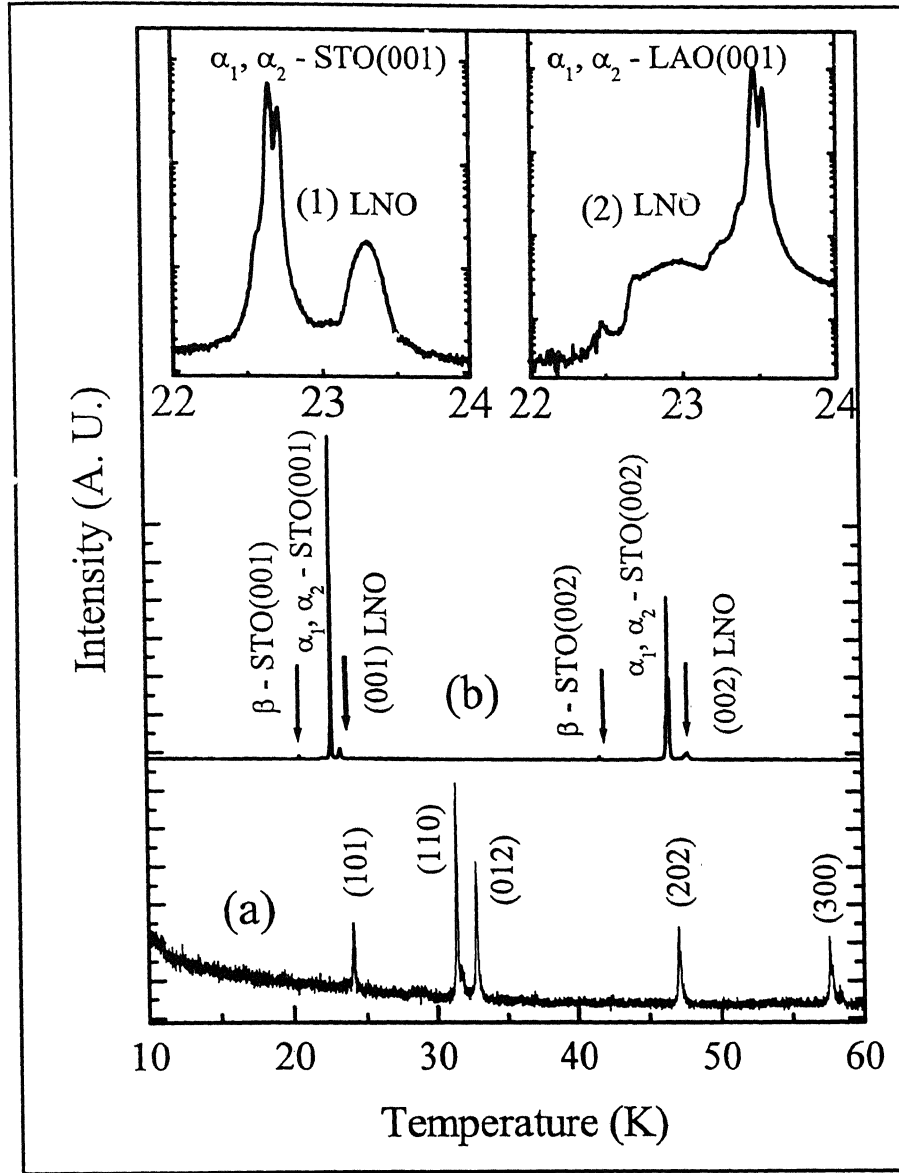
Figure 4.2: X - ray $\theta - 2\theta$ scans for powder sample of bulk of LNO (curve a) and films of ~ 100 $u.c.$ thick LNO deposited on (001) oriented STO (curve b). In curve (a) the diffraction lines are indicated by their corresponding pseudo-cubic (hkl) values. Curve (b) shows (001) and (002) reflection of the film and substrate due to $K\widehat{\alpha}$ and $K\widehat{\beta}$ excitation. Inset (1) and (2) show the reflected X - ray intensity around the (001) peak.

4.1.2.2 Electronic transport

The value of room temperature resistivity and resistivity difference $(\rho(300\ K) - \rho(4.2\ K))$ of bulk LNO samples is different in different reports. Gayathri et al. [138] have suggested that this variation is due to the non-stoichiometry in oxygen concentration. In the case of thin films, lattice mismatch can lead to large changes in the resistivity of LNO. Since the lattice mismatch related strain relaxes as the thin film thickness grows, one expects a change in resistivity with the film thickness. In order to study the effects of film thickness and strain on resistivity, we have deposited several samples on (001) oriented LAO and STO substrates. Fig. $4.3(a)$ shows the zero-field temperature dependent resistivity of $\sim 72\ u.c.$ thick LNO film grown on LAO and $\sim 100\ u.c.$ thick LNO grown on STO. The resistivity of both the films on cooling below room temperature shows metallic behavior down to $4.2\ K$. The film on STO, however, shows a marginally higher resistivity in the entire temperature range. The solid lines are the fit to the data for the relation $\rho = \rho_0 + aT + bT^2$. Table $- 4.1$ shows the residual resistivity (ρ_0), resistivity at $4.2\ K$ and $300\ K$ and their difference for different samples. A comparison of these data with the values given in the literature indicates that our films are stoichiometric. We note an increase in $\rho(300\ K)$ and the appearance of a thermally activated behavior at lower temperatures as the film thickness is reduced. Thin film size effects and lattice mismatch contribute to this effect. The difference in the lattice parameter between STO and LNO is larger as compared to that of LAO and LNO. This clearly increases the resistivity of the films as seen in Fig. $4.3(a)$. In order to address this point further, we have deposited LNO on thin buffer layers of STO. The surface morphology of buffer STO layer on (001) oriented LAO as seen with atomic force microscopy shows smaller surface roughness compare to that of the STO substrate. In Fig. $4.3(b)$ we have shown the zero-field $\rho(T)$ of three $\sim 5\ u.c.$ thick films of LNO deposited on (001) oriented LAO with 0, ~ 6 and $\sim 10\ u.c.$ (curve 3, 2 and 1 respectively) buffer layer of STO. The $\rho(T)$ of these films below room temperature is metallic followed by a thermally activated behavior.
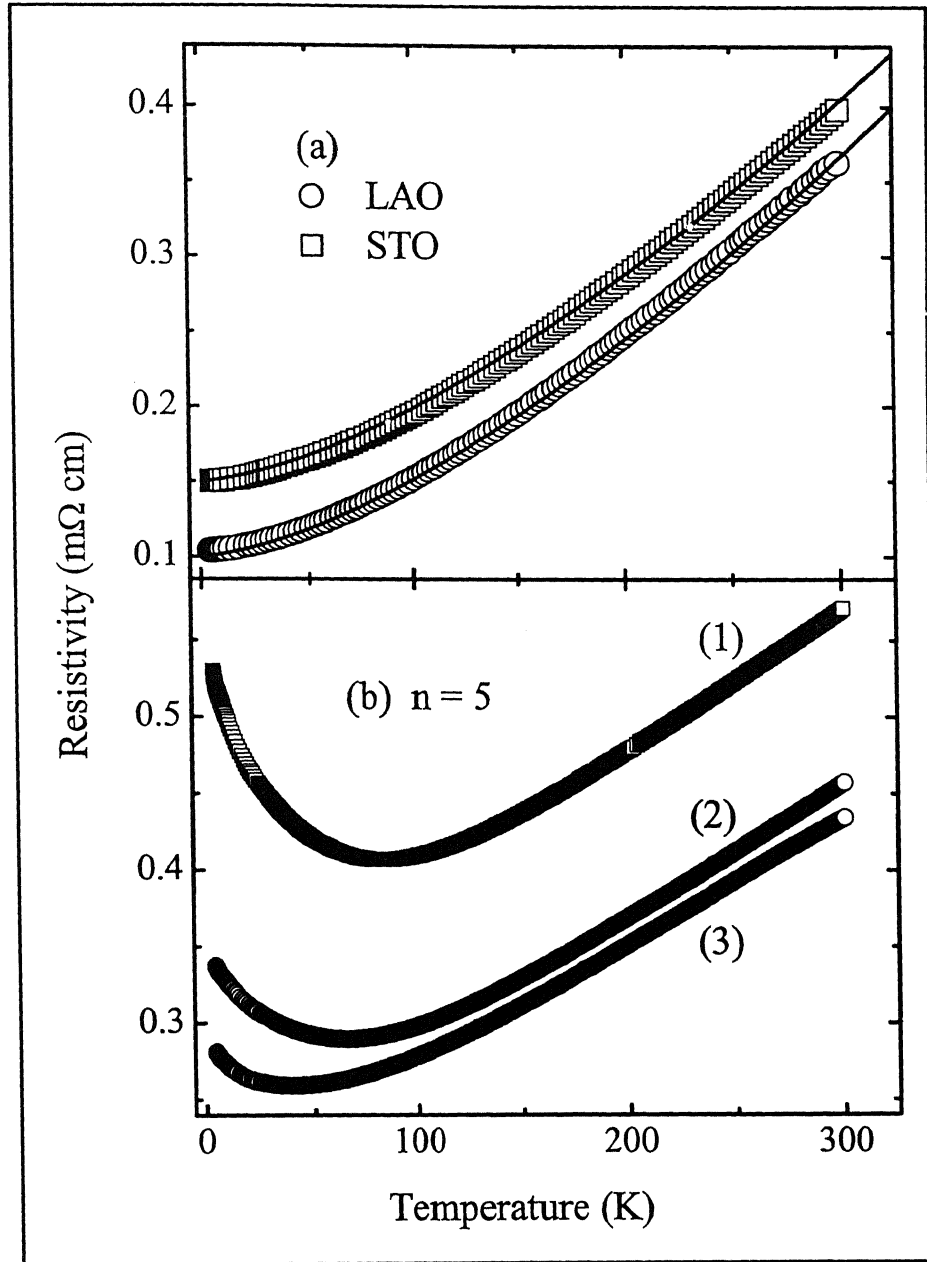
Figure 4.3: Panel (a) shows zero-field resistivity of $\sim$ 72 $u.c.$ thick LNO film deposited on (001) oriented LAO and $\sim$ 100 $u.c.$ thick film deposited on STO. Solid lines are fit to the data for $\rho = \rho + aT + bT^2$. Panel (b) shows the zero-field resistivity of $\sim$ 5 $u.c.$ ultra thin films of LNO deposited on (001) oriented LAO with 0, 6 and 10 $u.c.$ (curve 3, 2 and 1 respectively) buffer layer of STO.

Table 4.1: Electronic transport parameters of various thin films of LNO

Samples	$\rho(300K)$ $(\mu\Omega\ cm)$	$\rho(4.2K)$ $(\mu\Omega\ cm)$	$\Delta\rho$ $(\mu\Omega\ cm)$	ρ_0 $(\mu\Omega\ cm)$
$(100u.c.)LNO/STO$	398	150	248	143
$(72u.c.)LNO/(20u.c.)LCMO/LAO$	364	104	260	98
$(36u.c.)LNO/(20u.c.)LCMO/LAO$	390	107	283	100
$(24u.c.)LNO/(20u.c.)LCMO/LAO$	445	128	317	120
$(12u.c.)LNO/(20u.c.)LCMO/LAO$	1193	564	629	540
$(5u.c.)LNO/LAO$	434	280	154	

Since our objectives are to understand transport in $LCMO/LNO$ superlattices, it is important to understand the behavior of LNO films on $LCMO$ buffer layer. The difference in the lattice parameter of $LCMO$ and LNO is only $\sim 0.03\ \mathring{A}$. In Fig. $4.4(a)$ we show the $\rho(T)$ of four LNO films of various thicknesses grown on (001) oriented LAO with ~ 20 u.c. thick $LCMO$ buffer layer. The $\rho(T)$ of the ~ 20 u.c. thick film of LNO is metallic below room temperature down to $\sim 7\ K$ and then thermally activated. While the $\rho(T)$ of the $\sim 24,\ 36,$ and 72 u.c. LNO films remains metallic below room temperature down to $4.2\ K$. Resistivity of these samples shows linear temperature dependence in the temperature range $50\ K$ to $300\ K$. The change in the absolute value of resistivity at two different temperatures, $50\ K$ and $300\ K$, with the LNO film thickness is shown in the inset of Fig. $4.4(a)$. We have also measured the resistivity of these samples in 4 tesla field aligned parallel to the plane of the film. The $\rho(T)$ in the presence of magnetic field is shown in Fig. $4.4(b)$. The in-field $\rho(T)$ shows a negligible change from its zero-field value. The magnetoresistance of ~ 72 u.c. LNO film grown on (001) LAO with ~ 20 u.c. of $LCMO$ buffer is shown in the inset of Fig. $4.4(b)$.

4.1.2.3 Magnetic susceptibility

Fig. 4.5 shows zero-field-cooled and field-cooled magnetic susceptibility of ~ 500 u.c. thick LNO film deposited on (001) oriented LAO. The field-cooled magnetic susceptibility data can be fitted to the formula $\chi(T) = \chi(0) + aT^2 + CT^{-1}$ where $\chi(0)$ is the temperature independent susceptibility, second term provides the temper-

ature dependent Pauli susceptibility and last term represents the Curie susceptibility. The fitting yields values of $\chi(0)$, a and C as 5.56×10^{-8} emu Gauss^{-1}, $- 2.216 \times 10^{-13}$ emu K^{-2} Gauss^{-1} and 2.579×10^{-7} emu K Gauss^{-1} respectively.
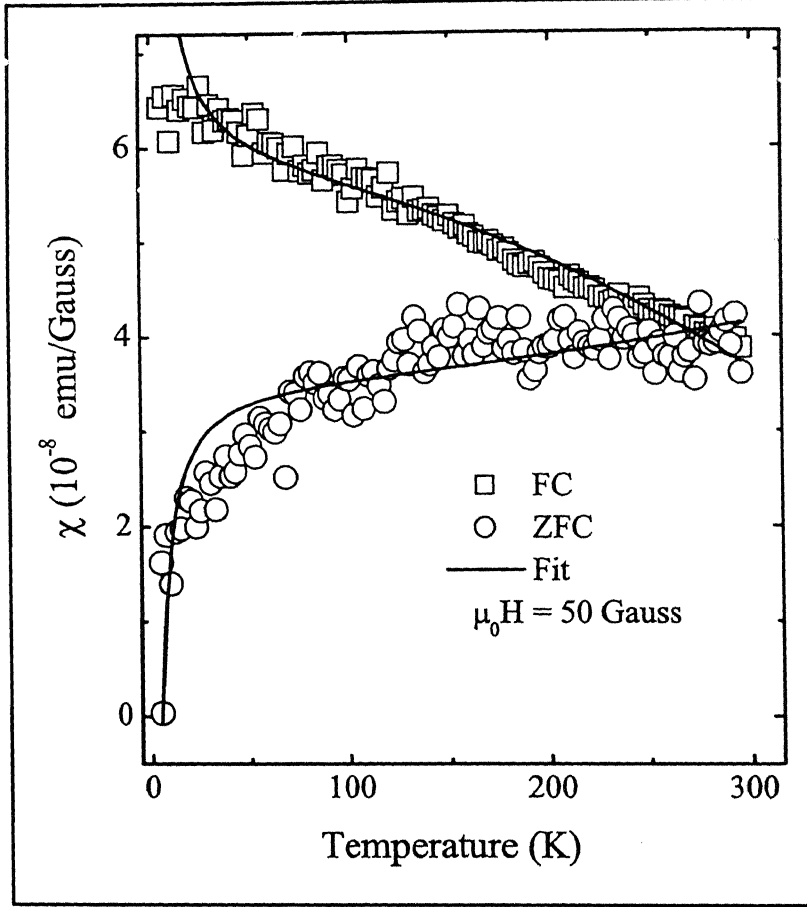
Figure 4.5: Temperature dependent zero-field-cooled, field-cooled susceptibility of ~ 500 u.c. thick LNO film deposited on (001) oriented LAO. The solid line is a fit to the data using relation $\chi = \chi(0) + AT^2 + CT^{-1}$.

4.1.3 Discussion

The pseudo-cubic lattice parameter of LNO, is ~ 3.83 Å. It is smaller by ~ 0.075 Å compared to the lattice parameter of STO and larger by ~ 0.038 Å compared to that of LAO. Clearly, the substrate induced stress is expected to be higher in films deposited on STO. Moreover, on STO the stress is tensile and on LAO it is compressive. This in-plane compression leads to an expansion of the lattice along the

c – axis. In the case of tensile stress the situation is opposite.

The resistivity of the thick LNO films grown on LAO and STO substrates show similar temperature dependence as that of bulk LNO. The observed higher resistivity of LNO films deposited on STO is expected as the LNO films on STO are more distorted than the films on LAO. In general, the physical properties of the $ANiO_3$ perovskites change with the size of the rare-earth, oxygen deficiency, pressure and strain which all contribute to the lattice distortion. Since we cooled our samples from the deposition temperature of $\sim 750~°C$ in $760~Torr$ of oxygen, these films have correct stoichiometry.

The resistivity of LNO with both $T^{1.5}$ and T^2 temperature dependence has been reported. Our data in the temperature range $5~K$ to $300~K$ fit quite well to the relation $\rho = \rho_0 + aT + bT^2$. The large value of residual resistivity shown in the table $- 4.1$ as compared to that of metals may be due to the presence of magnetic ions. The resistivity of LNO derives contributions from electron - phonon and electron - electron scattering effects. Since resistivity above $\sim 100~K$ shows linear dependence we fit the data in the following form;

$$\rho = \rho_0 + a_1 T^2 \qquad \text{if } T << \theta_D$$
$$= \rho_0 + b_1 T \qquad \text{if } T \geq \theta_D$$

Where θ_D is the Debye temperature. Using the relation $\theta_D \approx \frac{\pi^2 b_1}{6 a_1}$ the estimated values of θ_D for the $\sim 72~u.c.$ thick film deposited on LAO and $\sim 100~u.c.$ thick LNO deposited on STO are $293~K$ and $283~K$ respectively.

The resistivity of the ultra thin films of LNO deposited on LAO with STO buffer layer clearly show the effects of substrate induced stress. The resistivity on LAO is small due to the lower value of Δa. When STO buffer layer is deposited, Δa goes from a negative to a large positive value. This seems to increase the resistivity of the films. The thermally activated behavior observed at low temperature in ultra thin film is pronounced when STO buffer is used. Stoichiometric LNO is a charge - transfer metal. Its transport properties are determined by the interplay between the bandwidth and the energy gap of Ni and O bands. This depends on the $Ni - O$ bond distance and the $Ni - O - Ni$ bond angle. The structure of LNO can be envisaged as consisting of alternate planes of LaO and NiO_2. The lattice mismatch of LNO

with (001) oriented LAO may compress the planer $Ni - O$ bonds and expand the out-of-plane $Ni - O$ bonds of the NiO_6 octahedra. The situation will be opposite in the case of LNO films deposited on (001) STO. Huang et al. [141] and Garcia-Munoz et al. [142] have measured the temperature dependent of $A - O$ and $Ni - O$ bond distances in $ANiO_3$. They observe expansion of $Ni - O$ bond on cooling below room temperature. The expansion of $Ni - O$ bond is likely to cause a decrease in electronic transfer parameter 't' and the bandwidth. The decrease in bandwidth will, in turn, promote disorder induced electron localization at low temperatures. This effect of temperature on $Ni - O$ bond length and the large $Ni - O$ in-plane bond length conspire to make the films on STO more insulating at low temperatures. Thin films of LNO deposited on $LCMO$ buffer layers remain metallic down to the lowest temperature. This improved behavior of the films appears to be a result of better lattice match between $LCMO$ and LNO. The resistivity of the LNO films shows negligible variation in the presence of a magnetic field. In Fig. 4.4(b) we show the magnetoresistance of a $\sim$ 72 $u.c.$ thick LNO film. Gayathri et al. [138] have observed positive magnetoresistance (0.9%) for $LaNiO_{3-0.02}$ film while the magnetoresistance is negative for samples with more oxygen deficiency. These results show that the LNO films in the $LCMO/LNO$ superlattices will not contribute directly to any magnetoresistance. Enhanced low temperature susceptibility has been observed in single crystals of LNO [139, 143]. In our sample field-cooled temperature dependence of susceptibility shows weak temperature dependence in the entire temperature range. The large difference in FC and ZFC susceptibility at low temperature indicates presence of localized spin and spin disorder. To interpret the data we have assumed the susceptibility as the combination of pauli susceptibility and Curie susceptibility. The possible contributions to temperature independent susceptibility $\chi(0)$ are core diamagnetism, Pauli temperature independent susceptibility due to conduction electron, diamagnetic orbital contribution due to conduction electron and Van Vleck susceptibility.

4.1.4   Conclusions

We have studied the growth of LNO thin film on (001) LAO and STO substrates using $X - $ ray diffraction and RBS techniques. The resistivity and magnetic

In this section we presents Rutherford backscattering, X – ray based charac-
terization and transport measurements on $Er_{0.7}Sr_{0.3}MnO_3$ deposited on STO and
LAO. The resistance of our $\sim$ *500 u.c.* thick *ESMO* films deposited on *LAO* is very
high ($> 10^9$ Ω) at the low temperature. Further, the field-cooled and zero-field-cooled
measurements of magnetization on the *ESMO* film trace the same path. The film
shows paramagnetic and insulating behavior.

4.2.2 Results

4.2.2.1 Rutherford backscattering and X – ray diffraction
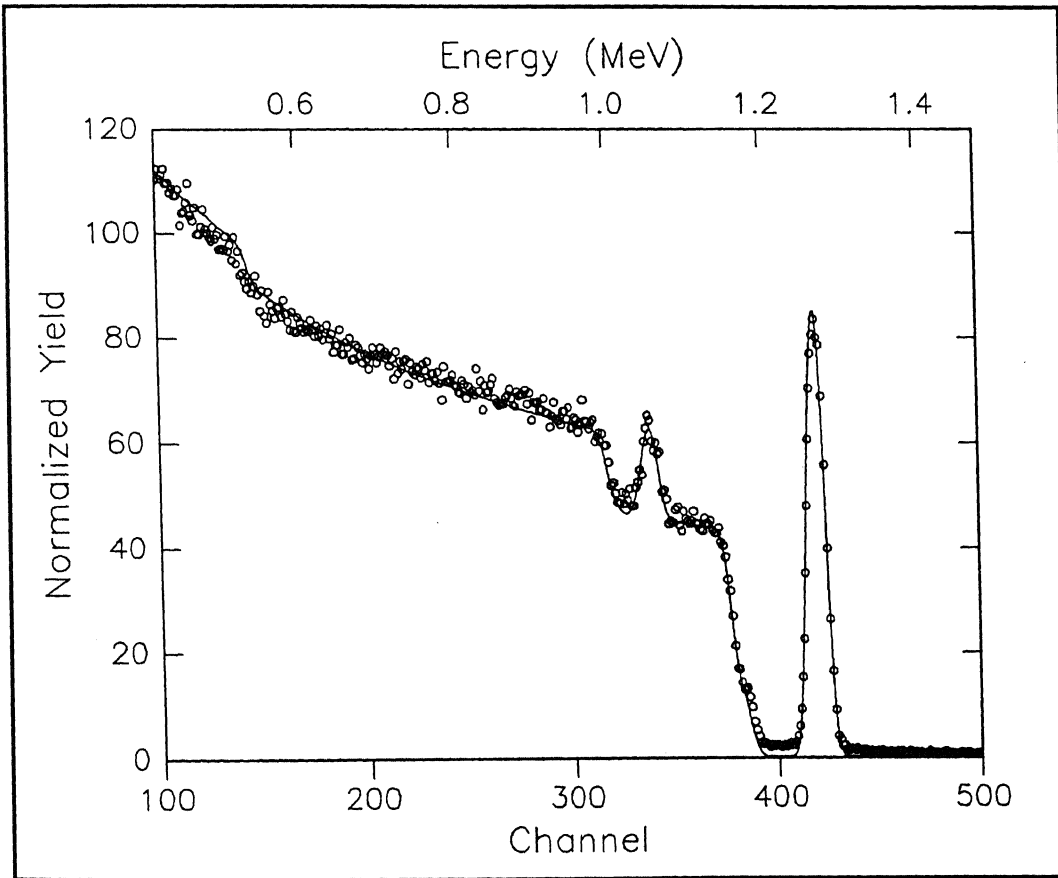
Figure 4.6: Rutherford backscattering spectrum of He^+ ions from thin film and
substrate. The sample is *400 Å* thick $Er_{0.7}Sr_{0.3}MnO_3$ film deposited on (*001*)
oriented $SrTiO_3$. Solid line is the *RUMP* simulation data.

susceptibility of these films have been measured as a function of their thickness. The resistivity of LNO film deposited on STO is higher than of those deposited on LAO in the entire temperature range of $4.2\ K$ to $300\ K$. Ultrathin films of LNO show a thermally activated behavior at temperatures $\leq 30\ K$. This behavior is prominent in the films of LNO deposited on a buffer layer of STO. Our results suggest that lattice mismatch plays a significant role in controlling electron transport in these films. The lattice mismatch effects are, however, suppressed when these film are grown on $20\ u.c.$ thick $LCMO$ buffer. This feature is critical for synthesis of $LCMO/LNO$ superlattices. We further note that LNO films have a negligible magnetoresistance. Therefore, the LNO layers in $LCMO/LNO$ superlattices will not contribute directly to the magnetoresistance.

4.2 Paramagnetic insulator spacer

4.2.1 Introduction

The physical properties of the ABO_3 type mixed valence manganites are regulated by the dopant concentration and the average A − site ionic radius. For a fixed dopant concentration the ground state of the compound depends on the average A − site ionic radius. For example, $La_{0.7}Ca_{0.3}MnO_3$ [49] exhibits a transition from paramagnetic insulating state to ferromagnetic metallic state on cooling, while $Pr_{0.7}Ca_{0.3}MnO_3$ [58, 144] has a charge ordered insulating ground state. The average A − site ionic radii of $LCMO$ and $PCMO$ are $\sim 1.162\ \AA$ and $\sim 1.133\ \AA$ respectively. A smaller average A − site ionic radius ($\sim 1.117\ \AA$) is for the compound $Er_{0.7}Sr_{0.3}MnO_3$. Terai et al. [145] have reported measurements of electronic and magnetic properties of the $Er_{0.5}Sr_{0.5}MnO_3$ ($ErSMO$). The resistivity of $ErSMO$ shows a thermally activated behavior on cooling below room temperature. The resistivity reaches a value of $\sim 10^7\ \Omega\ cm$ at $\sim 80\ K$. There has been no indication of a magnetic ordering (ferromagnetic or antiferromagnetic) in this material over the temperature range of $4.2\ K$ to $300\ K$. Taking note of the insulating behavior and the absence of magnetic ordering, we have chosen $ErSMO$ as the insulating spacer material for our $LCMO$ based magnetic superlattices.
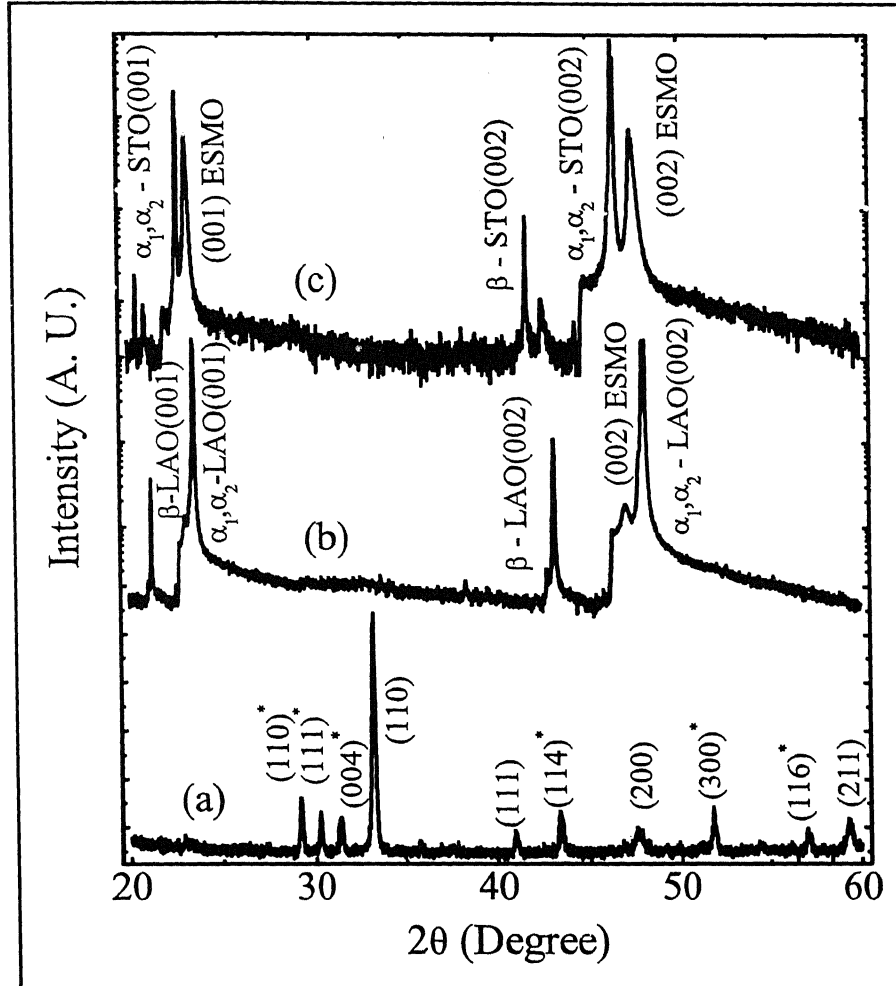
Figure 4.7: X - ray θ - 2θ scans for powder sample of bulk of $ESMO$ (curve a) and films of $\sim$ 500 $u.c.$ thick $ESMO$ deposited on (001) oriented LAO and STO (curve b and c respectively). In curve (a) the diffraction lines are indicated by their corresponding pseudo-cubic (hkl) values and the (hkl) value due to the hexagonal phase of $ErMnO_3$ are marked by the symbol ($*$). Curve (b) and (c) show (001) and (002) reflection of the film and substrate due to $K\widehat{\alpha}$ and $K\widehat{\beta}$ excitation.

Rutherford backscattering experiments with $1.6\mathrm{MeV}$ He^+ ion were performed to compare the stoichiometry and thickness of $ESMO$ film deposited on (001) STO. Fig. 4.6 shows the scattered particle spectrum and the $RUMP$ simulation curve (solid line). The elemental ratio and thickness of the film were calculated from the simulation. The bulk $ErSMO$ shows a mixture of orthorhombic and hexagonal phases [145]. In our sample the dopant concentration is 0.3 and the X - ray diffraction intensity

from the powder sample shows the pseudocubic phase as majority and the hexagonal phase of $ErMnO_3$ as an impurity. However, we have not seen any traces of the hexagonal phase in the thin films of $ESMO$ grown on (001) oriented LAO and STO. The scan of powder sample (curve a) and ~ 500 $u.c.$ thin films of $ESMO$ deposited on (001) oriented LAO and STO (curve b and c) respectively are shown in the Fig. 4.7. The diffraction lines of the powder sample are indicated by the corresponding (hkl) values of pseudocubic phase of $ESMO$ and the hexagonal phase of $ErMnO_3$. The X − ray profile of the thin films of $ESMO$ deposited on (001) oriented LAO and STO show only the (001) fundamental peaks of the pseudocubic structure.

4.2.2.2   Electrical resistivity and magnetoresistance
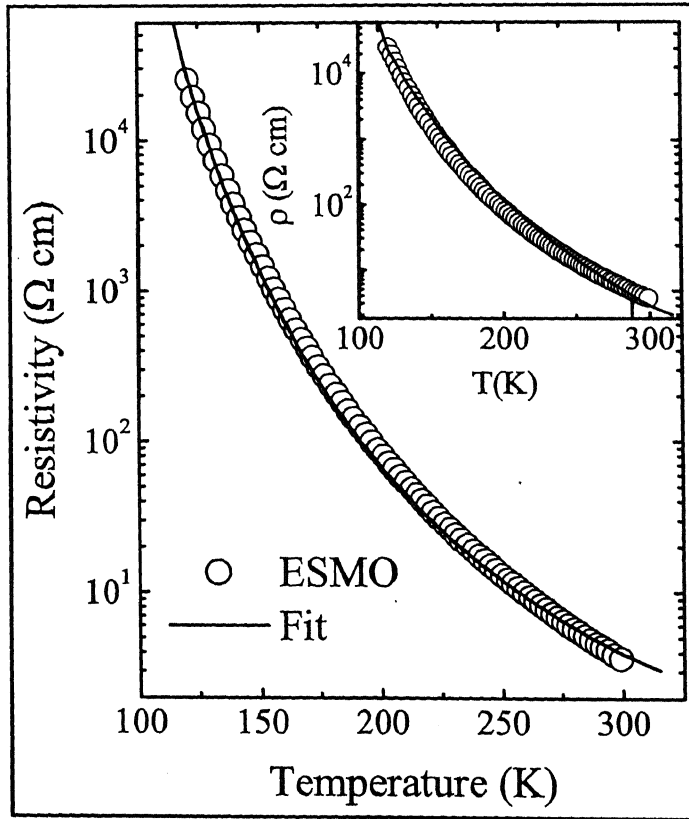
Figure 4.8: Measured and calculated temperature dependent resistivity of ~ 500 $u.c.$ thick $ESMO$ film deposited on (001) oriented LAO at different temperatures. Solid line represents the calculated resistivity using small polaron model. The solid line in the inset is the calculated resistivity using variable range hopping model.

The temperature dependent resistivity of the $\sim$ *500 u.c.* thick film of *ESMO* is shown in the Fig. *4.8*. This sample shows thermally activated behavior on cooling below room temperature down to $\sim$ *120 K*. Below *120 K*, the resistivity becomes so large that a constant current technique of measurement does not work due to the impedance limitations of our voltmeter. The solid line in Fig *4.8* represents the Arrhenius type fit to the data. The *ESMO* film shows a negligibly small change in the $\rho(T)$ in a *4 tesla* field.

4.2.2.3   Magnetic susceptibility
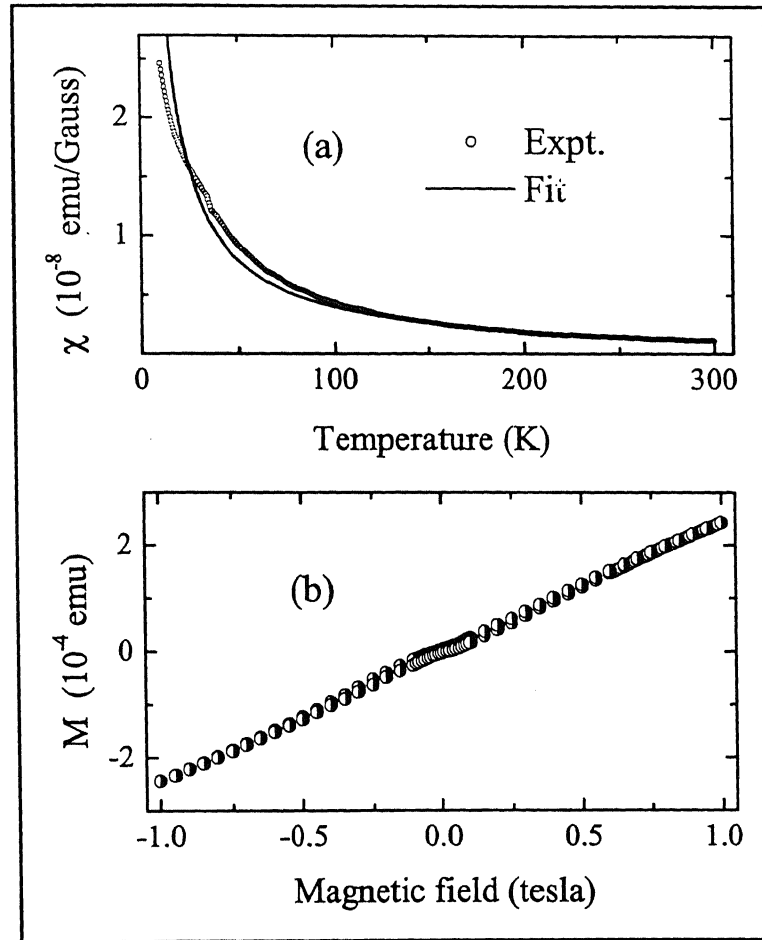
Figure 4.9: Panel (a) field-cooled magnetic susceptibility of $\sim$ *500 u.c.* thick *ESMO* film deposited on (*001*) oriented *LAO* at different temperatures. The solid line is the fit to the data using the relation $\chi = \chi(0) + \chi(T^2) + \chi(T^{-1})$. Magnetic field dependent zero-field-cooled magnetization of this sample is shown in panel (b).

Fig $4.9(a)$ shows the field-cooled magnetic susceptibility of the ~ 500 u.c. thick film of $ESMO$ deposited on (001) oriented LAO. The data were taken at 0.7 tesla in-plane magnetic field. The susceptibility is very small at room temperature and shows weak temperature dependent down to ~ 150 K. As the temperature is reduced below 150 K, the susceptibility increases rapidly down to the lowest temperature. The temperature dependence of the zero-field-cooled magnetic susceptibility is quite similar to that of the field-cooled susceptibility. The solid line in the figure is a fit to the data using the relation $\chi(T) = \chi(0) + aT^2 + CT^{-1}$. The fitting yields the value of $\chi(0)$, a and C as 1.2867×10^{-10} emu Gauss^{-1}, -3.742×10^{-15} emu Gauss^{-1} K^{-2} and 3.887×10^{-7} emu K Gauss^{-1} respectively. Magnetic field dependence of the zero-field-cooled magnetization measured at 10 K is shown in Fig. $4.9(b)$. The magnetization is linear and reversible with magnetic field in both the direction.

4.2.3 Discussion

The pseudo-cubic lattice parameter of $ESMO$, is ~ 3.812 Å. It is smaller by ~ 0.093 Å compared to the lattice parameter of STO and larger by ~ 0.02 Å compared to LAO. The substrate induced stress on the film deposited on STO is tensile and on LAO it is compressive. This in-plane compression leads to an expansion of the lattice along the c – axis. In the case of tensile stress the situation is opposite. Clearly the substrate induced stress is expected to be higher in the case of the film deposited on STO. The average A site ionic radius and dopant concentration has a close bearing on the Mn – O – Mn bond angle and Mn – O bond distance and hence the one electron e_g bandwidth. These two factors control the physical properties of the manganites. The transport properties vary drastically with a small change in the average A – site ionic radius. The compound $Er_{0.7}Sr_{0.3}MnO_3$ has the average A – site ionic radius ~ 1.117 Å which is smaller than that of the $Pr_{1-x}Ca_xMnO_3$ system. The $PCMO$ system shows prominent charge ordering effects, and antiferromagnetic ground state. Even thought the temperature dependent resistivity of $ESMO$ is thermally activated down to lowest temperature just as in the case of $PCMO$ system, its magnetic state is paramagnetic. To understand the transport mechanism in this $ESMO$ compound, we have fitted the measured resistivity using Arrhenius law, small polaron hopping

law and Mott's variable range hopping model. As seen in Fig. *8.4* it is difficult to identify the best fit among them. The energy gap determined from the Arrhenius fit is $\sim$ *0.3 eV* which is closer to the value observed in the spectroscopic measurement of charge ordered compounds [*146, 147*].

4.2.4 Conclusions

We have studied the growth of *ESMO* thin film on (*001*) *LAO* and *STO* substrates using X – ray diffraction. We have also measured the resistivity and magnetic properties of these films. The resistivity of $\sim$ *500 u.c.* thick *ESMO* films shows thermally activated behavior and is very high at temperatures $\leq$ *115 K*. Magnetic susceptibility measurement indicates the presence of paramagnetic nature of *Mn* spin arrangement. The *ESMO* layers in *LCMO/ESMO* superlattices will not contribute directly to the magnetoresistance in superlattices.

Chapter 5

Electron transport in LCMO/LNO superlattices with a fixed LCMO layer thickness of 10 unit cells

5.1 Introduction

The observations of oscillatory magnetic coupling, *GMR* and oscillations in *MR* in *3d* - transition metal based superlattices are now well established [*4, 30, 48*]. It is also established that electrical transport properties of magnetic superlattices depend on the roughness of the interfaces between the layers [*25*]. The interfacial roughness leads to attenuation of oscillations in the exchange coupling [*6, 14*]. An enhanced *MR* at low field and low temperature and oscillations in the magnetic coupling have also been observed in some manganites based superlattices [*36-44*]. However, unlike the case of elemental superlattices, no oscillations in the magnetoresistance of manganites superlattices are seen. The enhanced magnetoresistance observed at low temperatures in $La_{0.7}Ca_{0.33}MnO_3$ and $SrRuO_3$ superlattices by Gong et al [*36*], has been attributed to magnetic non-uniformity near the interfaces. An enhanced magnetoresistance in the superlattices consisting of $La_{0.6}Sr_{0.4}MnO_3$ and $La_{0.6}Sr_{0.4}FeO_3$ at low temperatures observed by Izumi et al. [*42*] also suggest spin frustration at

the interfaces. Jo et al. [41] have suggested the presence of vertically inhomogeneous magnetic structure at the interfaces which may be responsible for enhanced low temperature MR. The structural and magnetic disorder at the interfaces also contribute to the resistivity of the multilayers. Venimadhav et al. [47] have observed an insulator - like behavior in multilayers of $La_{0.6}Pb_{0.4}MnO_3$ and $La_4Ba Cu_5O_{13+x}$.

In this chapter we examine how the temperature dependence of electrical resistivity and magnetoresistance of the ferromagnetic manganite $La_{0.7}Ca_{0.3}MnO_3$ based superlattices change as the thickness of the $LaNiO_3$ spacer layer is varied. In [(10 u.c.) LCMO/(n u.c.) LNO] × 15 superlattices with n taking integral values from 2 to 10, where the cumulative thickness of LCMO and LNO is large enough to see a bulk - like transport, a semiconductor - like resistivity is seen for $n \leq 4$. The superlattices with $n \leq 4$ also show a large negative magnetoresistance at low temperatures. Sample with $n > 5$ are metallic over the entire range of temperatures. A discussion of these features is presented in the light of structural data and the effects of interfacial strain. Our analysis strongly suggests that the magnetic and structural disorders at the interfaces of LCMO and LNO lead to a transition from insulator to metal - like behavior with increasing n, and the large low temperature magnetoresistance seen in sample with $n < 5$. A simple parallel resistor model, where we explicitly incorporate the resistivity of the disordered regions, reproduces the broad features of the $\rho(T)$ curves.

5.2   Results

5.2.1   X – ray diffraction

The epitaxial growth of successive layers of the superlattices depends on deposition parameters, lattice mismatch between the successive layers and the lattice mismatch between the substrate and the bottom layer. X – ray diffraction techniques give reliable information about the growth morphology of the single layer films and superlattices. As described in chapter 2, we have fabricated a series of LCMO/LNO superlattices on LAO and STO substrates. After fabrication of the superlattices, they
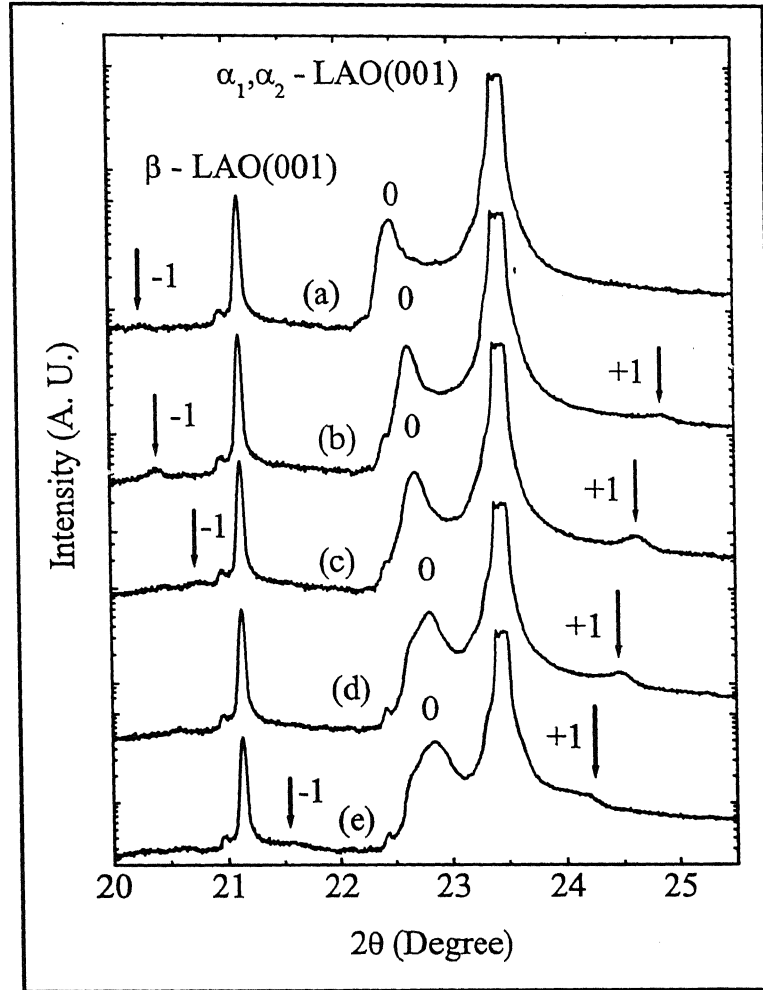
Figure 5.1: X – ray diffraction profiles of superlattices with ~ 10 $u.c.$ of $LCMO$ and 2, 4, 6, 8 and 10 $u.c.$ of spacer layer (LNO) deposited on (001) oriented LAO, curve a, b, c, d and e respectively. The fundamental (001) reflection of the film is marked as '0'. The first order satellites on either side of this reflection are marked as $+$ 1 and $-$ 1. The figure also shows (001) reflection of the substrate due to $K\widehat{\alpha}$ and $K\widehat{\beta}$ excitation.

were characterized extensively using X – ray diffraction. Only the (001) fundamental Bragg diffraction peaks of the substrate and the constituents of the superlattice due to Cu – $K\widehat{\alpha}$ and $K\widehat{\beta}$ excitation are observed. This indicates epitaxial growth along ($00l$) direction of the cubic substrate. The diffracted X – ray intensity around the (001) reflection of the [(10 $u.c.$) $LCMO$/(n $u.c.$) LNO] $\times$ 15 deposited on (001) oriented STO and (001) oriented LAO with $n = 2, 4, 6, 8$ and 10
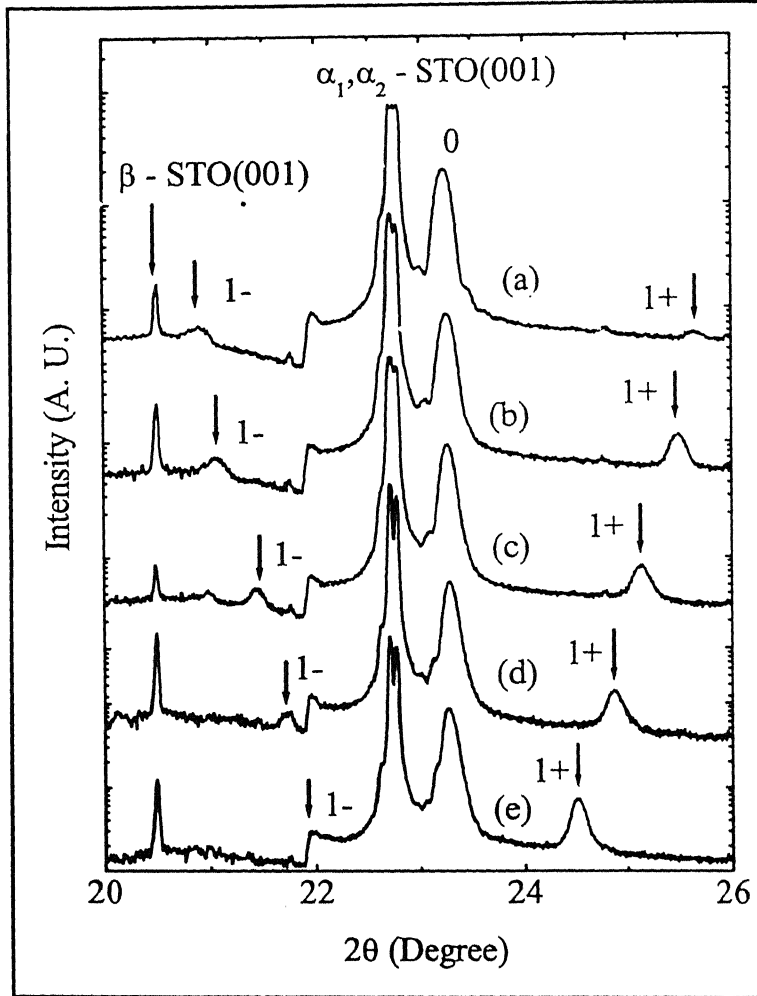
Figure 5.2: X − ray diffraction profiles of superlattices with $\sim$ 10 u.c. of LCMO and
2, 4, 6, 8 and 10 u.c. of spacer layer (LNO) deposited on (001) oriented STO, curve
a, b, c, d and e respectively. The fundamental (001) reflection of the film is marked
as '0'. The first order satellites on either side of this reflection are marked as + 1
and − 1. The figure also shows (001) reflection of the substrate due to $K\hat{\alpha}$ and $K\hat{\beta}$
excitation.

is shown in the Fig. 5.1 and Fig. 5.2 respectively. The presence of two satellite peaks
on either side of the fundamental (001) diffraction clearly shows a modulated structure
[148, 149]. The intensity of the satellite peaks is stronger in the case of superlattices
deposited on STO substrate. The intensity of higher order satellite peaks are not
significant, presumably due to a small electron density difference between LCMO and

LNO. In all superlattices a *10 u.c.* thick *LCMO* is the bottom layer. The lattice parameters '*a*' of *LCMO* and *LNO* in the bulk are *3.86 Å* and *3.83 Å* respectively, where as for the substrate we have $a_{LAO} = 3.792$ Å and $a_{STO} = 3.905$ Å. Clearly, the in-plane lattice parameter of the superlattice is under expansion on *LA⊖* $\overset{S\,TO}{}$ and is in compression on *S⊖* $\overset{LAO}{}$. The variation of the *c* − axis lattice parameter of the superlattices with the spacer layer thickness is shown in Fig. *5.3*. The *c* − axis lattice parameter of the superlattice on *LAO* with (*1 u.c.*) spacer layer is ∼ *3.93 Å* and approaches the bulk value as the thickness increases with *n*. While the *c* − axis lattice parameter of the superlattice on *STO* remains constant. We also notice a distinct broadening of the (*001*) peak as the relative fraction of the *LCMO* and *LNO* unit cells becomes unity.
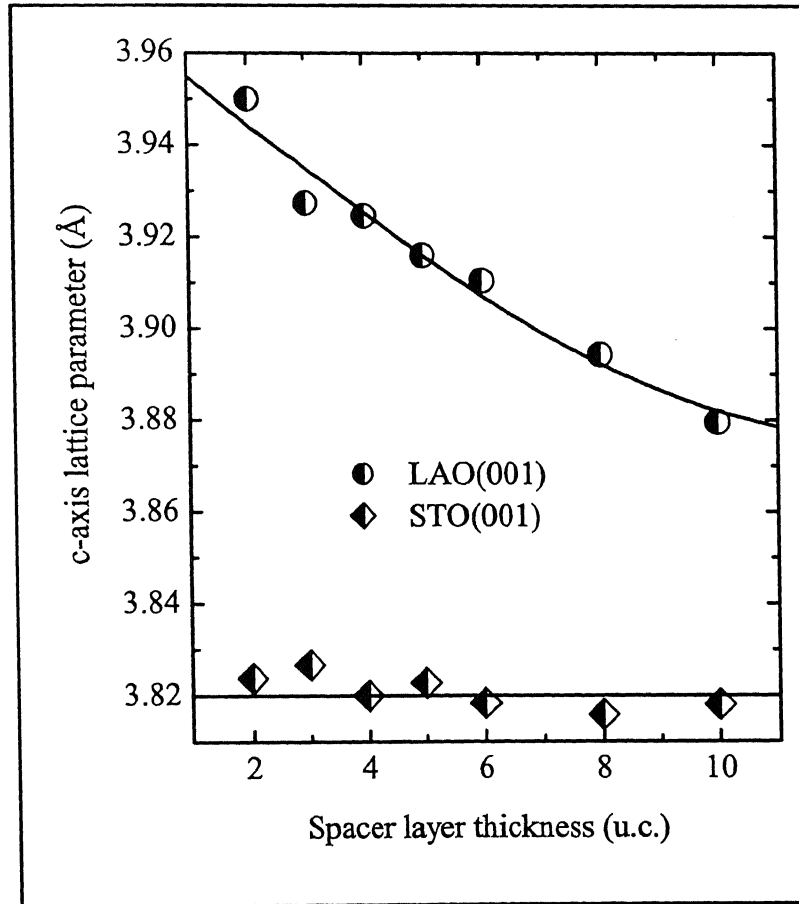
Figure 5.3: *c* − axis lattice parameters of the superlattices grown on (*001*) oriented *LAO* and *STO*.

5.2.2   Electronic transport

The electronic conduction of individual thin films of magnetic layers and the spacer layer of the superlattices are discussed in chapter *3* and *4* respectively. Here, we present results of our measurements on the superlattices. The zero-field $\rho(T)$ of the [(*10 u.c.*) *LCMO*/(*n u.c.*) *LNO*] × *15* superlattices deposited on *LAO* substrate is shown in Fig. *5.4*. For the samples with $n = 2$ and *3*, the resistivity is thermally activated down to ∼ *100 K*. Below this temperature, the resistivity of the superlattices becomes so large that a constant current technique of measurement does not work due to the impedance limitations of our voltmeter. While a similar behavior has been observed in metallic manganites based superlattices, the spacer material in these cases
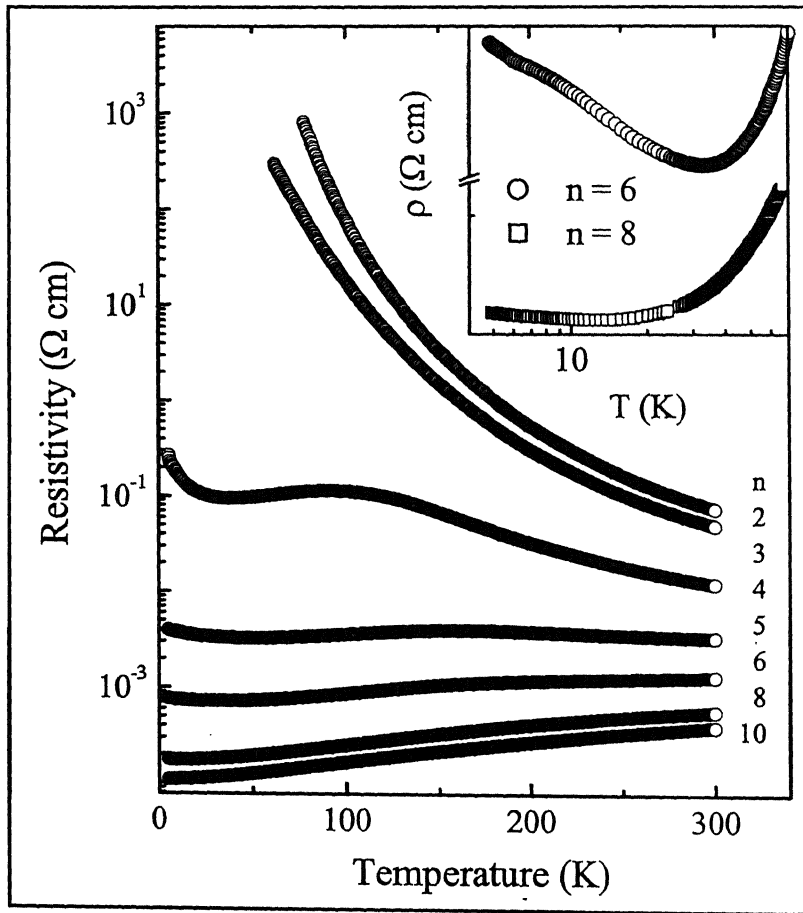
Figure 5.4: Zero-field in-plane electrical resistivity of superlattices grown on (*001*) oriented *LAO* with different spacer layer thicknesses. Inset shows resistivities of samples with $n = 6$ and *8* at lower temperature in log scale.
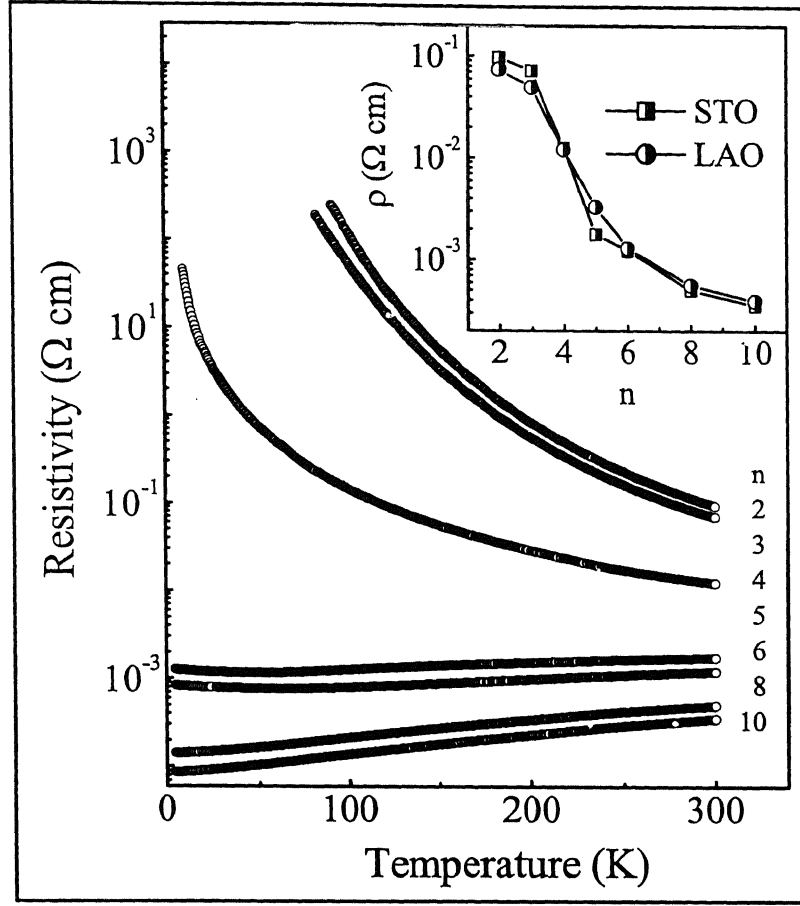
Figure 5.5: Zero-field in-plane electrical resistivity of superlattices grown on (001) oriented STO with different spacer layer thicknesses. Inset shows the room temperature resistivities of samples deposited on LAO and STO with different spacer layer thicknesses.

was an insulator [40-44]. On increasing the LNO layer thickness to 4 $u.c.$, $\rho(T)$ is first thermally activated down to ~ 100 K and then becomes metal - like ($positive$ $d\rho/dT$) in the temperature window of 25 K to 100 K. At $T < 25$ K, $\rho(T)$ is again thermally activated. A qualitatively similar behavior, albeit with a wider metal - like window, is seen for the sample with $n = 5$. The $\rho(T)$ curves remain metallic over the entire temperature range for the sample with $n > 6$. Clearly, an insulator-to-metal transition is seen in these superlattices in the vicinity of $n = 5$. In the inset of Fig. 5.4, we show the low temperature part of the zero-field resistivity of the superlattices with $n = 6$ and 8 deposited on LAO. We have also measured the resistivity of the superlattices

deposited on STO simultaneously with the samples on LAO. The qualitative features of the $\rho(T)$ data for these samples are shown in the Fig. 5.5. In the inset of Fig. 5.5 we show the variation of the room temperature resistivity of the superlattices with different spacer layer thickness. The resistivity of the films on STO is higher by a small fraction. In the inset Fig. 5.7 we show the low temperature part of zero-field resistivity of the superlattices with $n = 6$ and 8 deposited on STO.

5.2.3   Magnetoresistance

Fig. 5.6 shows the resistivity of the superlattices on LAO, measured in 4 tesla field. The in-field resistivity of the sample with $n = 2$ drops significantly from its zero-field value (Fig. 5.4) on application of the field. However, its temperature dependence remains thermally activated down to 4.2 K. The resistivity of the sample with $n = 3$ undergoes a remarkable change on application of the field. In addition to a large negative magnetoresistance, the $\rho(T)$ curve is also metal - like (positive $d\rho/dT$) over a narrow range of temperatures (25 K – 65 K). The drop in resistivity at $\sim$ 65 K suggests onset of magnetic ordering in the $LCMO$ layers of the superlattice. For the sample with $n = 4$, the window of temperature over which a metal - like resistivity is seen widens on application of the field. In the case of the samples with $n > 5$, no appreciable change in the resistivity is seen on application of the field. The resistivity of the superlattices on STO, measured in 4 tesla field is shown in the Fig. 5.7. The qualitative features of in-field resistivity data of the samples are similar to its zero-field $\rho(T)$. In the inset of Fig. 5.6 we show the magnetoresistance ($MR = [(\rho - \rho_H)/\rho] \times 100$ where ρ_H and ρ are in-field and zero-field resistivities of the sample respectively) of superlattices deposited on LAO and STO at 4 tesla field at 100 K with different spacer layer thickness. Magnetoresistance of the superlattices deposited on STO is smaller (the difference is higher at lower spacer layer thicknesses) than the samples deposited on LAO. The MR at 100 K of superlattices on both LAO and STO has a peak at $n = 3$ followed by a rapid drop and then saturation with the increasing n. This clearly indicates the formation of LNO layer for $n > 4$ and the transition from insulator - like to metallic - like behavior of $\rho(T)$.
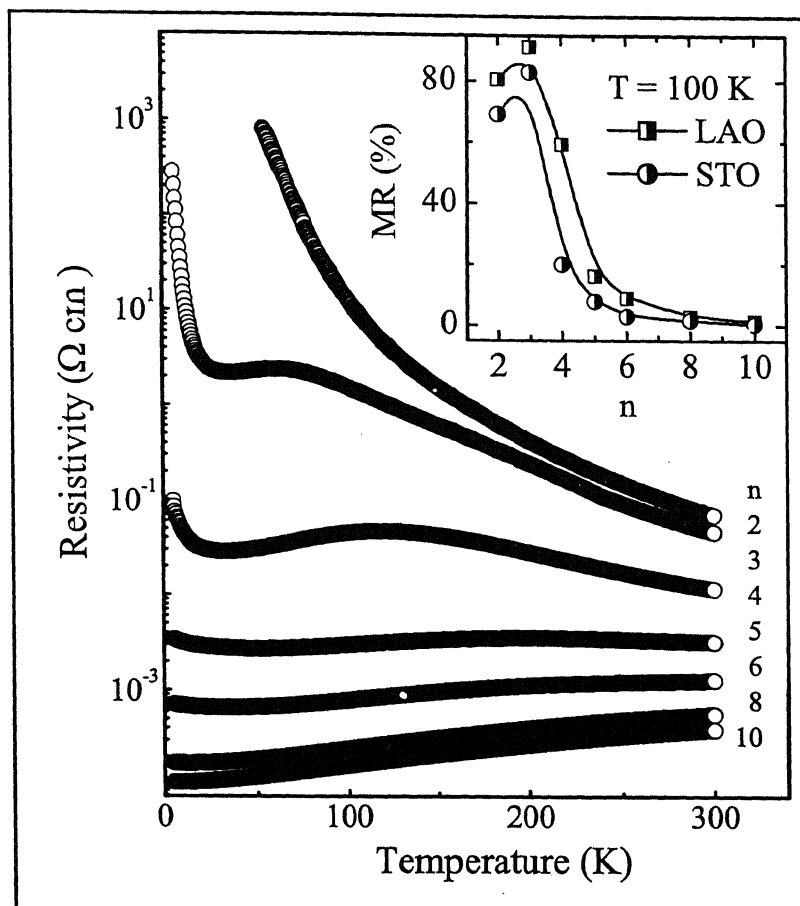
Figure 5.6: In-plane electrical resistivity of superlattices grown on (001) oriented
LAO at 4 tesla magnetic field with different spacer layer thicknesses. Inset shows the
magnetoresistance at 100 K for samples deposited on LAO and STO with different
spacer layer thicknesses.

In Fig. 5.8 we show temperature dependent magnetoresistance of these samples
with different spacer layer thicknesses. The magnetoresistance is measured at 4 tesla
field, and is plotted on a semilog scale. In Fig. $5.8(a)$, we show the magnetoresistance
of superlattices with $n = 2$, 4, 6, 8 and 10. For the superlattice with $n = 2$, MR
increases on cooling below room temperature down to ~ 100 K. Below this temper- .
ature, the magnetoresistance could not be measured because of the large resistance
of the sample. The magnetoresistance of the sample with $n = 4$ also increases on
cooling below room temperature, and saturates at the lowest temperature. In the
case of the superlattice with $n = 5$, we observed a small drop in magnetoresistance
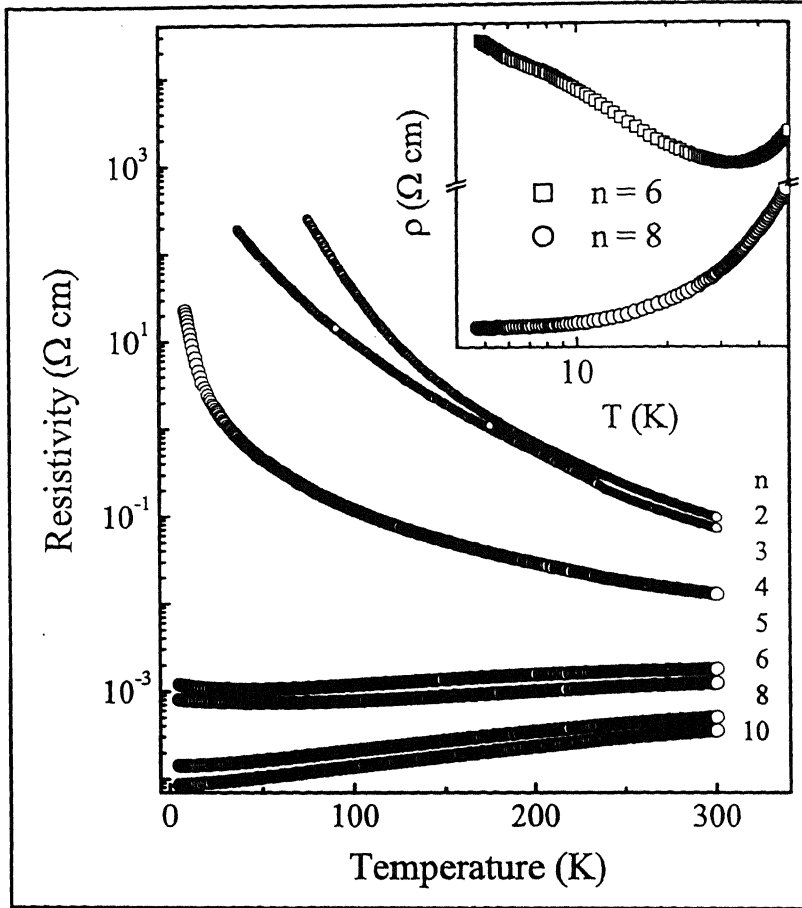
Figure 5.7: In-plane electrical resistivity of superlattices grown on (001) oriented STO at 4 tesla in-plane magnetic field with different spacer layer thicknesses. Inset shows the resistivity of the samples at lower temperature in log scale.

at the lowest temperature. Qualitatively similar behavior without any signature of sharp drop in magnetoresistance at low temperature is seen for the superlattice deposited on STO. The temperature dependent magnetoresistance of the samples with $n = 2, 4, 6, 8$ and 10 deposited on STO is shown in Fig. 5.8(b). The saturation of magnetoresistance at the lowest temperature in samples with $n \leq 5$ is unlike the case of a typical ferromagnetic manganite where the magnetoresistance is maximum near T_C [150]. Also the magnetoresistance is significantly higher in the superlattices.
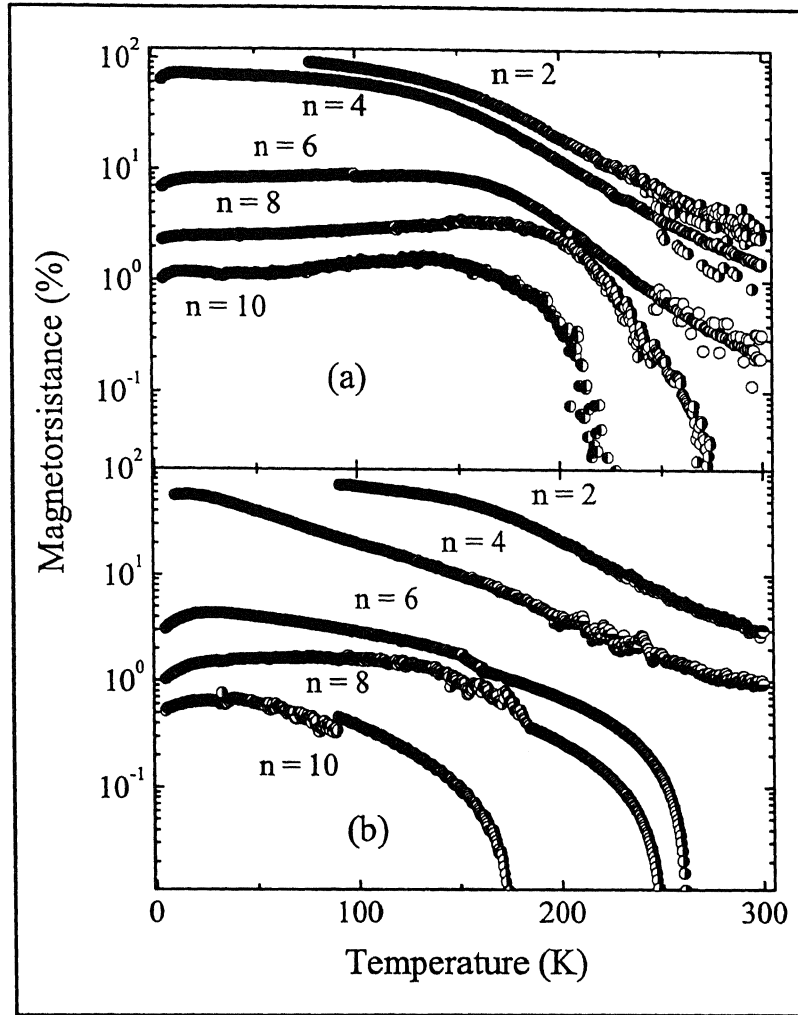
Figure 5.8: Panel (a) shows the magnetoresistance of superlattices with various spacer layer thicknesses grown on (001) oriented LAO at different temperatures. The magnetoresistance of superlattices with various spacers layer thicknesses grown on (001) STO at different temperatures is shown in panel (b).

In Fig. 5.9 we show the behavior of zero-field-cooled MR in samples on LAO with $n = 4$ and 6 as the magnetic field is swept over a complete cycle between $+ 4$ tesla and $- 4$ tesla. As seen in the insets, the magnetoresistance of both samples at $25 \, K$ first increases rapidly and then tends to saturate at the highest field. Absence of hysteresis in these data suggests free rotation of magnetization vectors in each $LCMO$ layers of the superlattice. However, the field dependence of magnetoresistance at temperatures below $\sim 20 \, K$ shows strong hysteretic effects ($5 \, K$ data are shown
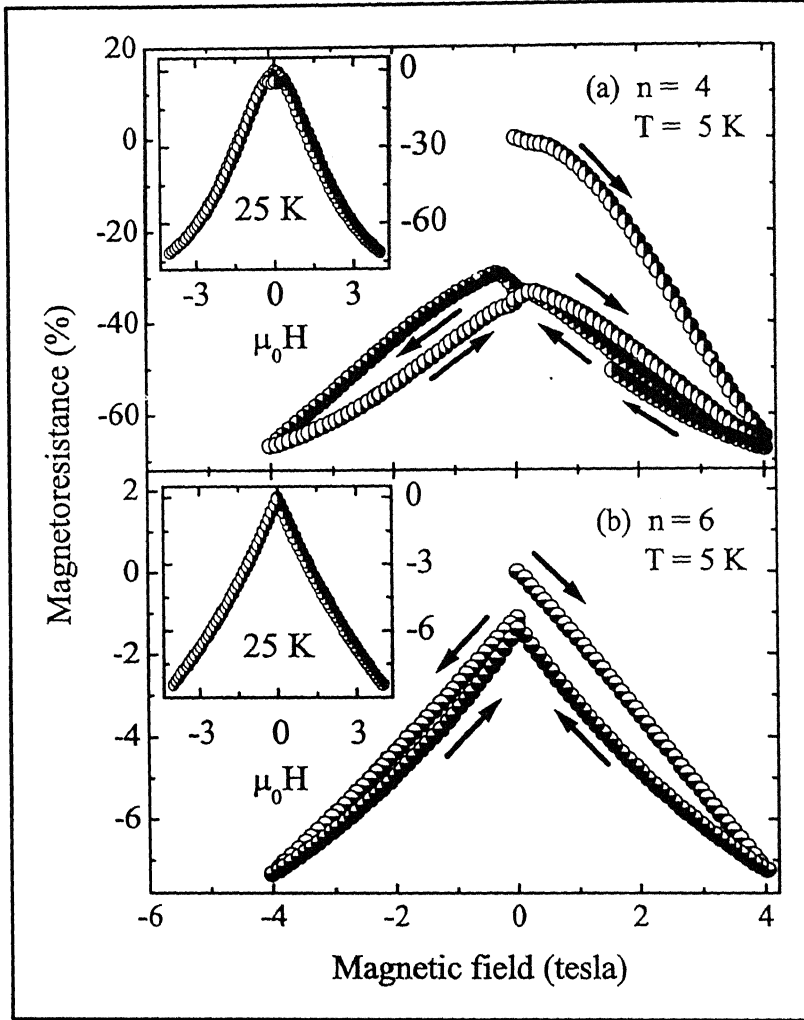
Figure 5.9: (a) Magnetic field dependence of magnetoresistance in $n = 4$ superlattice grown on LAO at $5\ K$. The sample was first zero-field-cooled to $5\ K$ and then the magnetic field was scanned from zero to $+\ 4$ tesla followed by cyclic sweeps between $+\ 4$ tesla and $-\ 4$ tesla. Inset shows field dependence of MR at $25\ K$. (b) $5\ K$ MR of the $n = 6$ superlattice grown on LAO. Field sweep directions are shown by arrows. Inset shows MR at $25\ K$.

in panel (a) and (b) of Fig. 5.9. These low temperature hysteretic effects in ZFC magnetoresistance suggest pinning of $LCMO$ magnetization by the disordered interfacial phase. The magnetoresistance of the sample with $n = 4$ as the magnetic field is swept over five cycle between $+\ 4$ tesla and $-\ 4$ tesla is shown in the Fig. 5.10. In the sample with $n = 4$ we also notice that the magnetoresistance during second

field sweep from $+$ 4 *tesla* to zero field does not trace the path taken during the first sweep. This indicates a week magnetorelaxor - type of behavior seen earlier in $La_{0.5}Ca_{0.5}Mn_{1-x}Cr_xO_3$ films [151].

In Fig. *5.11(a)*, we show the *ZFC* $-$ *MR* of a $n = 4$ sample deposited on *STO* as the magnetic field is swept over a complete cycle between $+$ 4 *tesla* and $-$ 4 *tesla* at *5 K*. The *ZFC* $-$ *MR* of the same sample at *25 K* and *50 K* is plotted in the panel (*b*) and (*c*) respectively. While the *MR* at *50 K* is reversible, the field dependence of magnetoresistance at temperatures below $\sim$ *40 K* shows strong hysteretic effects. The magnetoresistance of the superlattice deposited on *STO* along with those on *LAO* shows subtle differences in magnitude as well as in hysteretic effect.
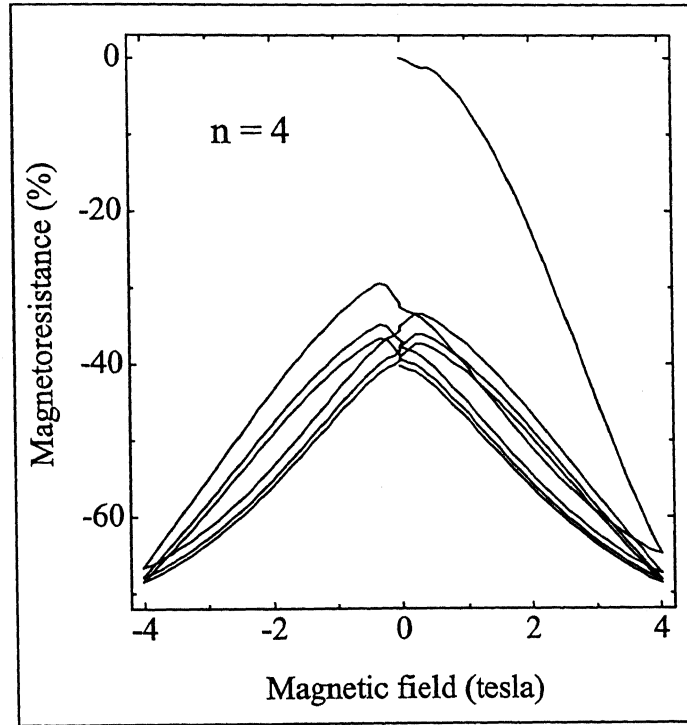
Figure 5.10: Magnetic field dependence of *MR* in $n = 4$ superlattice grown on *LAO* at *5 K*. The sample was first zero-field-cooled to *5 K* and then the magnetic field was scanned from zero to $+$ 4 *tesla* followed by five cyclic sweeps between $+$ 4 *tesla* and $-$ 4 *tesla*.
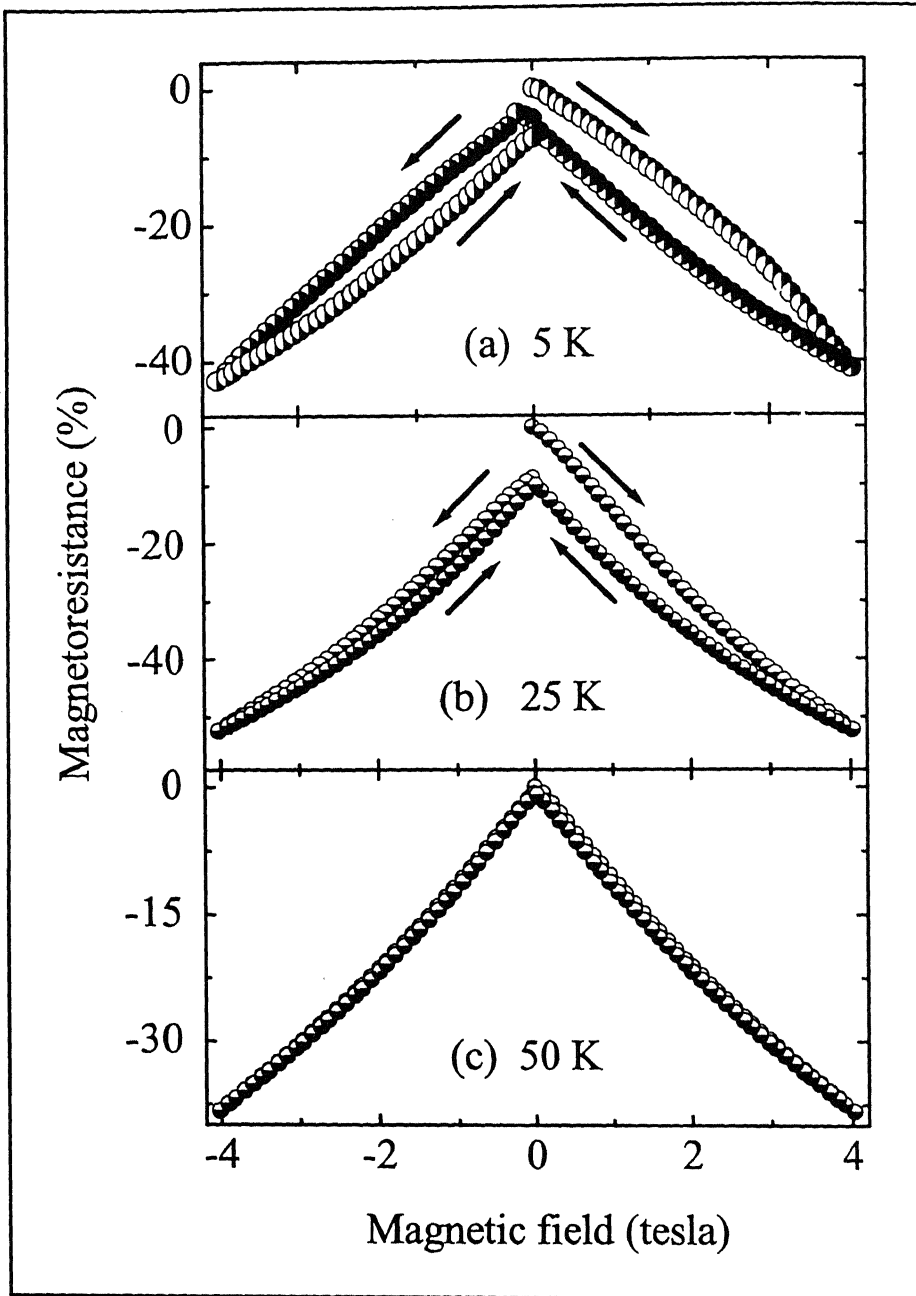
Figure 5.11: Panel (a) shows the magnetic field dependence of magnetoresistance in $n = 4$ superlattice grown on STO at 5 K. The sample was first zero-field-cooled to 5 K and then the magnetic field was scanned from zero to $+$ 4 $tesla$ followed by cyclic sweeps between $+$ 4 $tesla$ and $-$ 4 $tesla$. The MR at 25 K and 50 K of the same superlattice is shown in panel (b) and (c) respectively. Field sweep directions are shown by arrows.

5.3   Discussion

The X – ray diffraction profiles of the multilayers on LAO show a shift of (001) peak towards lower theta as the spacer layer thickness is reduced. This means an expanded out-of-plane lattice parameter. The out-of-plane lattice parameter decreases (peak moves to higher theta values) as the strain starts to relax by the increase in spacer layer thickness. The pseudocubic lattice parameter of LAO ($3.792\ \mathring{A}$) is smaller than the lattice parameter of bulk LCMO ($3.86\ \mathring{A}$) and LNO ($3.83\ \mathring{A}$). For a $\sim 10\ u.c.$ thick $LCMO$ film on LAO, the in-plane lattice parameter is nearly same as the lattice parameter of LAO. This makes the lattice parameter of bulk LNO larger than the in-plane lattice parameter of $\sim 10\ u.c.$ $LCMO$ on LAO. Clearly, LNO film deposited on $10\ u.c.$ $LCMO$ will experience biaxial expansion. The growth of $LCMO$ on LAO and LNO on $LCMO$ leads to a biaxial compressive stress i.e. $\epsilon_{xx} = \epsilon_{yy} < 0$ (ϵ_{xx}, ϵ_{yy} and ϵ_{zz} are the components of compressive strain along the x, y and z axis of the sample respectively). With these strain components and the poission ratio 'ν', the out-of-plane lattice epitaxial strain can be expressed as $\epsilon_{zz} = - \left(2\nu\ /\ (1 - \nu)\right)\epsilon_{xx}$. Assuming $\nu = 0.5$, the in-plane strain on $\sim 250\ u.c.$ thick $LCMO$ film deposited on LAO is $\sim 0.2\ \%$. The in-plane strain on multilayers with $2\ u.c.$ and $10\ u.c.$ thick spacer layer is $\sim 1.2\ \%$ and $\sim 0.2\ \%$ respectively. This shows that the strain in the multilayer start to relax with the increase in spacer layer thickness.

The large room temperature resistivity and its thermally activated nature in superlattices with $n < 4$ is puzzling. The cumulative thickness of $LCMO$ in these samples is well above the threshold for metallic behavior in $LCMO$ films [152]. A comparison with the data for individual films (Fig. $3.5(a)$ and Fig. $4.4(a)$) suggests that $\rho(T)$ of these superlattices should, in fact, have a well-defined peak near the Curie temperature (T_C) and a metal - like behavior below T_C. However, this scenario is applicable only under the assumption that the superlattices have coherent c – axis growth with no interfacial disorder. Two possible mechanisms for the interfacial disorder can be identified. One is of a metallurgical origin where intermixing of the constituent elements of $LCMO$ and LNO takes place at the interface. The ensuing

randomization of the magnetic ions (Mn and Ni) at the interface would also result in a magnetic disorder. The extent of interfacial mixing can be evaluated through analysis of X − ray diffraction data [102, 153] and by making use of high resolution cross-sectional electron microscopy [153, 154]. The interfaces of multicomponent oxides based superlattices such as of the high T_C cuprates and manganites prepared by using magnetron sputtering, PLD and MBE have been studied using these techniques [91, 102, 153, 154]. Further, the layer-by-layer growth of multilayers has also been studied insitu with high and low energy electron diffraction in PLD [91, 155] and MBE [38] processes. These studies suggested that the interfaces of oxide superlattices are relatively sharp. While we have not undertaken a detailed study of interfacial mixing, we expect it to be negligible as our deposition conditions were similar to those used in studies where the interfaces have been analyzed in detail [91, 154, 155]. However, even if the interfaces are ideally terminated, they will always have magnetic disorder. This is because of the changes in the nearest neighbor environment of the magnetic ions at the interfaces and modification in bond angles and bond distances caused by interfacial strain. There are two important consequences of the magnetic disorder. First a local breakdown of the double exchange mechanism [51], which is responsible for metallic conduction in $LCMO$ below T_C and secondly, the disorder can also affect the metallic character of LNO. Noticeably, this cubic perovskite tends to have a charge ordered insulating ground state as the La sites are replaced by ions of smaller radii such as Nd^{3+}, Sm^{3+} etc. [156]. While the thickness of this magnetically and electrically altered interfacial region will decrease as the lattice mismatch is reduced, it is likely to remain non-zero due to magnetic ions even when the lattice parameters of the constituents are identical. Our earlier work on ultrathin films of $LCMO$ [152] indicates that the disorder regions at the film - substrate interfaces is wider in the case of LAO (mismatch $\sim + 1.8\ \%$) than in $LCMO$ films on STO (mismatch $\sim + 1.0\ \%$). In the case of the superlattices, however, the width of the disordered region is decided by the mismatch between $LCMO$ and LNO $\left(\frac{\Delta a}{a} \sim + 0.8\ \%\right)$. This is perhaps the reason why properties of the superlattices on STO and LAO are remarkably similar.
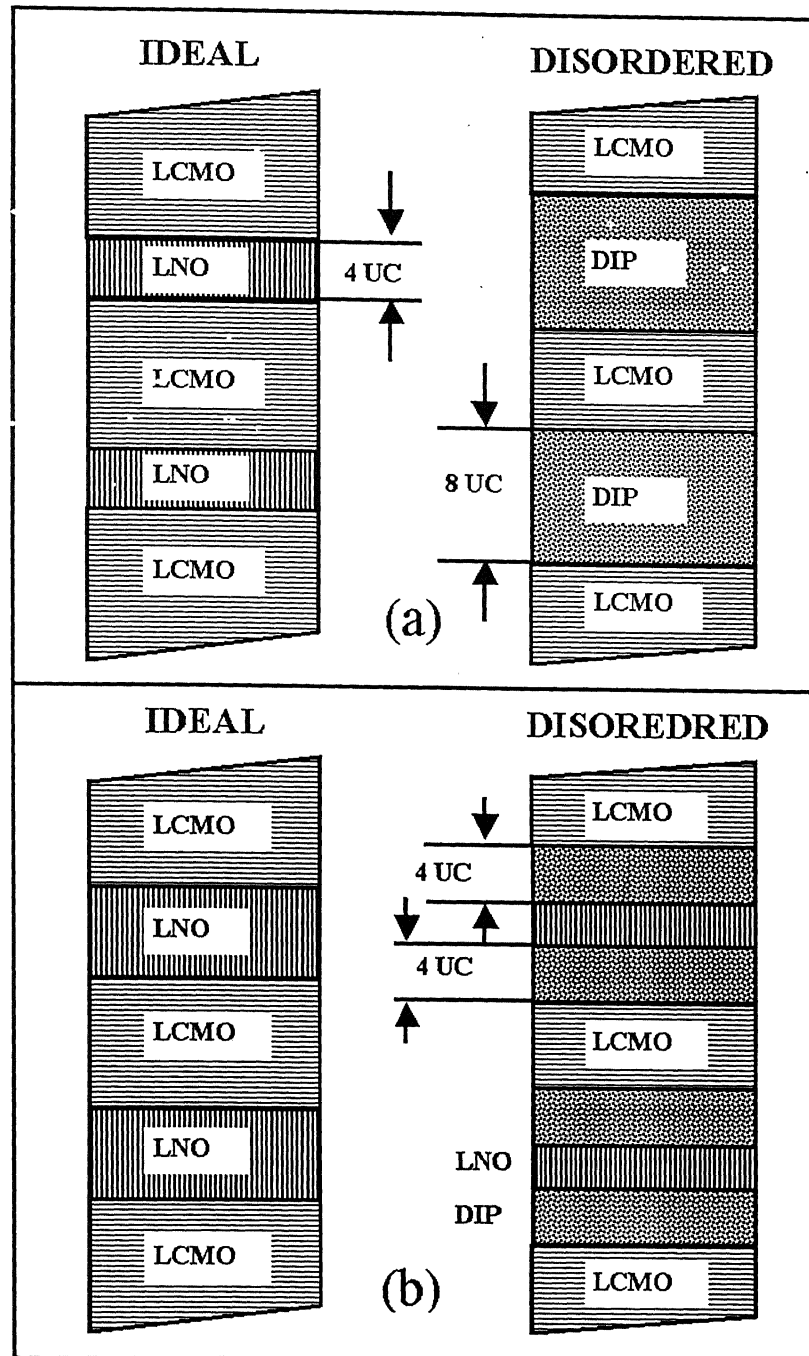
Figure 5.12: (a) A schematic view of the cross section of the superlattice with $n = 4$. Left hand side of the figure shows atomically sharp interfaces. Cross-section of the same superlattice with interfacial disorder is shown on the right. (b) shows the cross-section of superlattices with $n > 4$ is in the clean (left side) and disordered (right side) limits. The disorder is assumed to consume *2 unit cells* of the film on both sides of the interfaces.
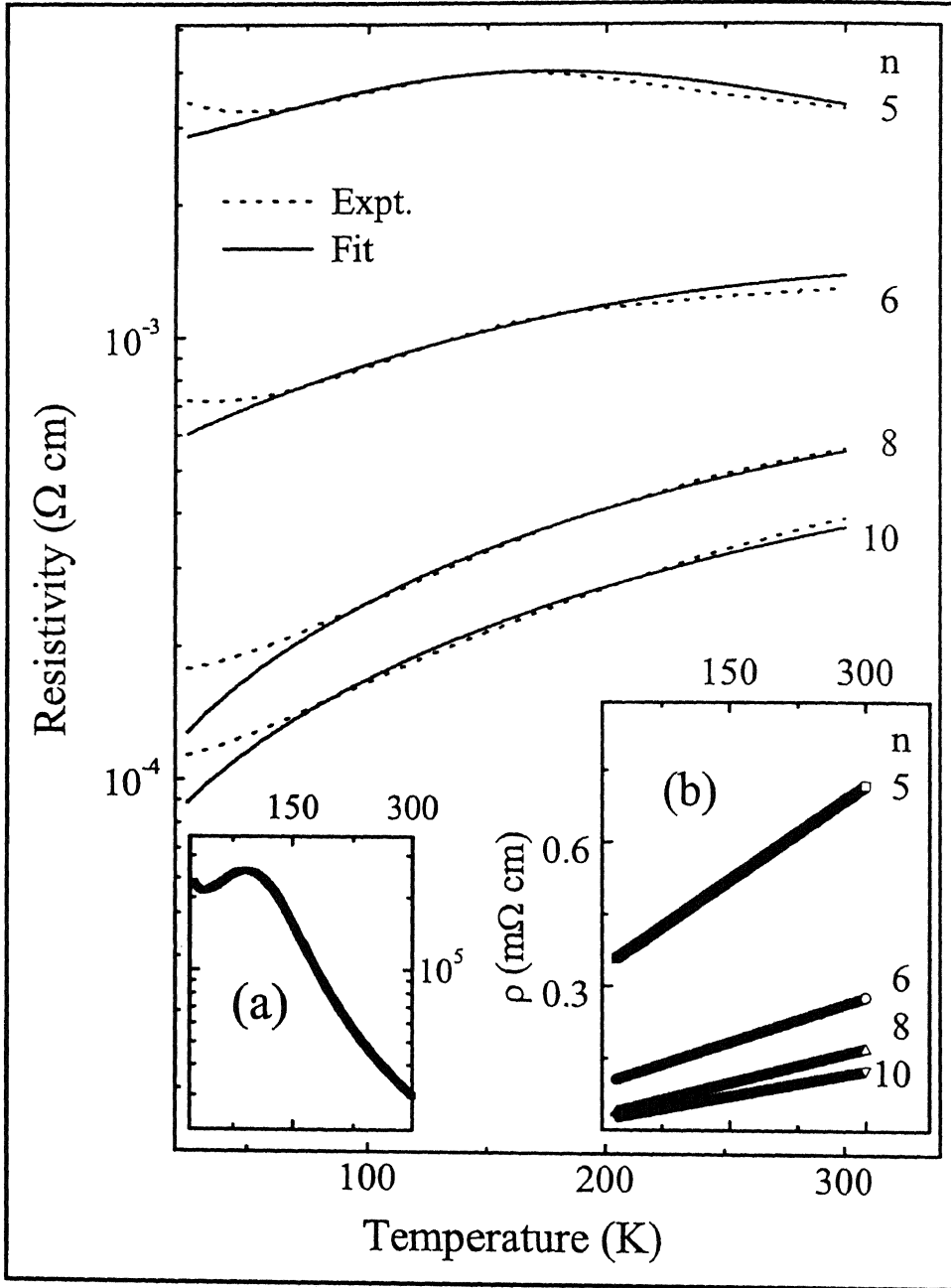
Figure 5.13: The measured and calculated resistivities of the superlattices with $n = 5$, 6, 8 and 10. The calculation is based on a parallel resistor model for a stack of 15 quad layers, each consisting of $LCMO$, LNO and the disordered interfacial phase. The resistivity of the interfacial phases deduced from $\rho(T)$ data of the superlattice with $n = 4$ is plotted in the inset (a). Inset (b) shows the resistivity of LNO layers $(\rho(T) = \rho_0 + \rho_1 T)$ obtained from the best fits (see text for detail).

We have successfully modeled the resistivity of the superlattices by explicitly taking into account the contribution of the interfacial region to total conduction. We first assume that a *2 unit cells* thick *LCMO* and *LNO* on either side of the interface convert to the disordered phase. The superlattice with $n = 4$ then consists of a stack of *15* bilayers of *LCMO* and disordered interfacial phase (*DIP*) as sketched in Fig. *5.12*(*a*). From the measured resistivity of the superlattice with $n = 4$ and the resistivity of *32 u.c.* thick *LCMO* film at various temperatures, wè extract, using a parallel resistor model, the temperature dependence of the resistivity of the *DIP*. The result of this calculation is shown in the inset (*a*) of Fig. *5.13*. Here it is important to point out that the resistivity of the disordered phase has unphysical sign (*negative*) if the $\rho(T)$ of *LCMO* layers is taken to be that of a thicker film (one with a well-defined Curie temperature and *positive* $d\rho/dT$ at $T < T_C$ as shown in Fig. *3.5*(*a*)). Under this model, the superlattices with $n > 4$ consist of *15* identical quad layer units as shown in Fig. *5.12*(*b*). Here, while thickness of *LCMO* and *DIP* remain the same, the *LNO* thickness increases with n. In these periodic quad layer structures it is also reasonable to argue that the resistivities of *LCMO* and *DIP* do not change with n. However, this is certainly not true for the *LNO* as the *LNO* layer thickness increases with n. The data of Fig. *4.4*(*a*) suggest that the resistivity of *LNO* should decrease as n increases. In Fig. *5.13* we show the measured and calculated resistivity of the samples with $n = 4$, *6*, *8* and *10*. Here we have taken the resistivity of *LNO* as $\rho_{LNO}(T) = \rho_0 + \rho_1 T$, with ρ_0 and ρ_1 as temperature independent adjustable parameters. The resistivity of the *DIP* and *LCMO* are the same as used in the calculations for superlattices with $n = 4$. As evident in the figure, the measured and calculated resistivities are in excellent agreement above $\sim$ *75 K*. The disagreement at $T < 75\ K$ is perhaps due to the fact that our calculation does not take into account the upturn in the resistivity of thin *LNO* films at lower temperatures. In the inset (*b*) of Fig. *5.13* we show the calculated $\rho_{LNO}(T)$ for different superlattices. The similarity of these curves with the data on individual films of *LNO* (Fig. *4.4*(*a*)) is noteworthy.

The large negative magnetoresistance at lower temperatures in samples with $n \leq 4$ highlights the sensitivity of electron transport in the disordered interfacial phase

to a magnetic field. While this effect should be present in samples of larger n as well, observing it may be difficult because of the shunting of current paths by the much more conducing LNO layers. The DIP on the $LCMO$ side may consist of pinned t_{2g} spins of the Mn^{3+} and Mn^{4+} ions, which may tend to bias the magnetization of the $LCMO$ layer. Randomly oriented magnetic moments of $LCMO$ layers are likely to inhibit transport of spin - polarized carriers across LCMO - LNO interfaces [18, 27]. At lower temperatures, the depinning of these ionic spins and a concomitant parallel alignment of $LCMO$ moments, may require substantial fields. However, higher temperatures tend to marginalize the pinning. This is perhaps why the magnetoresistance decreases at higher temperatures. The interfacial disorder can also lead to distortion of NiO_6 octahedra in the LNO layers. It is well known that deviations from a perfect cubic symmetry can open up a charge order gap in this rare earth nicolate [156]. Electrical conduction in the resulting antiferromagnetic and insulating state would show a considerable sensitivity to magnetic field.

5.4   Conclusions

We have studied the epitaxy and superstructure in the $LCMO/LNO$ superlattices deposited on (001) oriented STO and LAO by X – ray diffraction. The angular separation between first order satellite peaks becomes wider as the spacer layer thickness decreases from 10 $u.c.$ to 2 $u.c.$.. We have measured the electrical resistivity and magnetoresistance of $LCMO/LNO$ superlattices with different layer thickness over 4.2 K to 300 K temperature range. Superlattices with LNO thickness $<$ 5 $unit$ $cells$ show thermally activated resistivity over the entire temperature range. These samples also show a large magnetoresistance, which grows with decreasing temperature. A parallel resistor model where in the resistance of the disordered interfacial region is considered explicitly, reproduces the broad features of the $\rho(T)$ curves. We attribute the disorder interfacial region to lattice mismatch related strain and truncation of the $3D$ - coordination of magnetic ions at the $LCMO$ – LNO interfaces. A field assisted transport of spin polarized carriers across the interfaces and hopping of e_g electrons between Mn^{3+} and Mn^{4+} ions whose t_{2g} spins are pinned by the interfacial disorder, provide a plausible scenario for the large low temperature magnetoresistance.

Chapter 6

Overdamped oscillatory coupling and magnetoresistance in $(LCMO)_{20}/(LNO)_n$ superlattices

6.1 Introduction

Interlayer exchange coupling and its oscillatory nature in $3d$ - transition metal based magnetic multilayers have been studied extensively in the last decade [4, 48]. In the systems where magnetic layers of Fe, Co or Ni are separated by a non-magnetic simple metal, it is generally recognized that the IEC − interaction is carried by the conduction electrons of the latter [14, 15]. The strength and range of this interaction depends sensitively on the effects of scattering of charge carriers by disorder in the spacer layer and at the spacer - ferromagnet interfaces. In the backdrop of these findings, the recent discovery of overdamped oscillations in IEC of certain multilayers [37, 38] where the constituents are compounds with inherent complexities of narrow bands, short mean free path and electron correlations is quite fascinating.

The nature of IEC in $3d$ - transition metal based superlattices is clearly linked with the behavior of magnetoresistance. The magnetoresistance also shows oscillations with the increasing spacer layer thickness and its period matches with the period of

the IEC [157]. A large negative magnetoresistance when IEC is antiferromagnetic indicates ease in spin diffusion through the spacer as magnetization vectors of the neighboring ferromagnetic layers are made parallel by the external magnetic field. However, limited transport measurements on superlattices made of compounds show no such correlation between the magnetoresistance and interlayer exchange coupling.

This chapter describes extensive measurements of the interlayer exchange coupling, temperature dependent resistivities and Current-in-Plane magnetoresistance in superlattices of the ferromagnetic manganite $La_{0.7}Ca_{0.3}MnO_3$ and a Pauli paramagnet $LaNiO_3$, which remains metallic down to 4.2 K. While the saturation field (H_S) and remnant magnetization (M_r) of these superlattices show an overdamped oscillatory behavior with the increasing LNO layer thickness, the magnetoresistance reveals a remarkable dual character. The magnetoresistance derives contributions from the ease in carrier transmission across interfaces as the magnetization vectors of the adjacent $LCMO$ layers become parallel with field. This effect saturates at $\sim H_S$. The second contribution to magnetoresistance, which is additive, seems to come from field assisted hopping of carriers between localized moments at the interfaces. The manifestations of interfacial disorder in these superlattices are seen in their resistivity as well. The measured resistivity of these periodic structures is much higher than the resistivity inferred from a simple parallel resistor network calculation using bulk resistivities of $LCMO$ and LNO [158]. While in chapter 5 we focussed on electrical transport in $(LCMO)_m/(LNO)_n$ multilayers with $m = 10$ $u.c.$, here we discuss magnetotransport and magnetic ordering in multilayer with a thicker ($m = 20$ $u.c.$) $LCMO$ layers.

6.2   Results

6.2.1   X − ray diffraction

The difference between lattice parameters (Δa) of the substrate and bulk $LCMO$ induces stress in the film at small thickness. The strength of substrate induced stress becomes weaker and the lattice parameter of $LCMO$ film approaches its bulk value as the film thickness increases. In order to study the effects of $LCMO$ layer thickness on the physical properties of superlattices, we have also synthesized samples
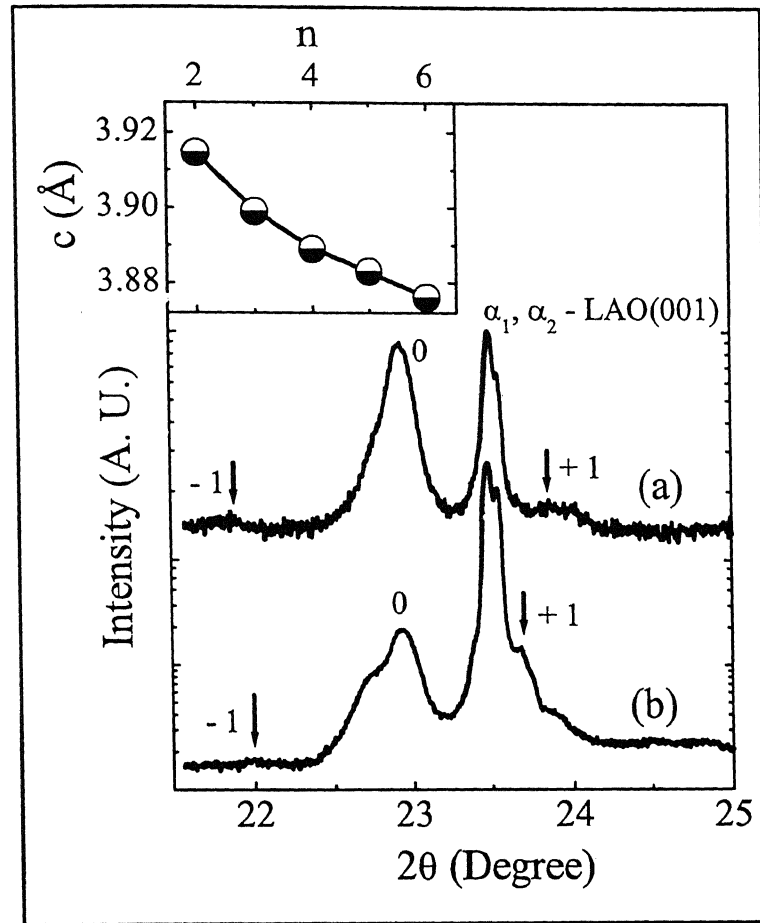
Figure 6.1: X - ray intensity around the (001) reflection of the substrate for the superlattices $(20\ u.c\ LCMO/n\ u.c.\ LNO)$ with $n = 4$ and 6 deposited on (001) oriented LAO (curve a and b respectively). The (001) reflection of the film is marked as '0'. The first order satellites on either side of the reflection are marked as $+\ 1$ and $-\ 1$. Inset shows the c - axis lattice parameter of superlattices as a function of spacer layer thickness.

where the $LCMO$ thickness is $20\ u.c$.. Fig. 6.1 shows X - ray diffraction profiles around (001) reflection for this set of samples. The presence of satellite peaks on either side of the (001) diffraction clearly shows a periodically modulated structure. The negative 'Δa' between LAO and $LCMO$ indicates that the in-plane lattice parameter of the $LCMO$ is under ~~expansion~~ *Compression* while the out-of-plane lattice parameter is under ~~compression~~ *Expansion*. As seen in chapter 5, the out-of-plane lattice parameter of the superlattices deposited on LAO decreases and approach to the bulk value as the spacer

layer thickness increases (Fig. *5.3*). Similar behavior is seen in the superlattices with *20 u.c.* thick *LCMO* deposited on *LAO*. We have plotted in the inset of Fig. *6.1* the *c* − axis lattice parameters of the superlattices with *20 u.c.* thick *LCMO* deposited on *LAO* as a function of spacer layer thickness.

6.2.2   Electronic transport
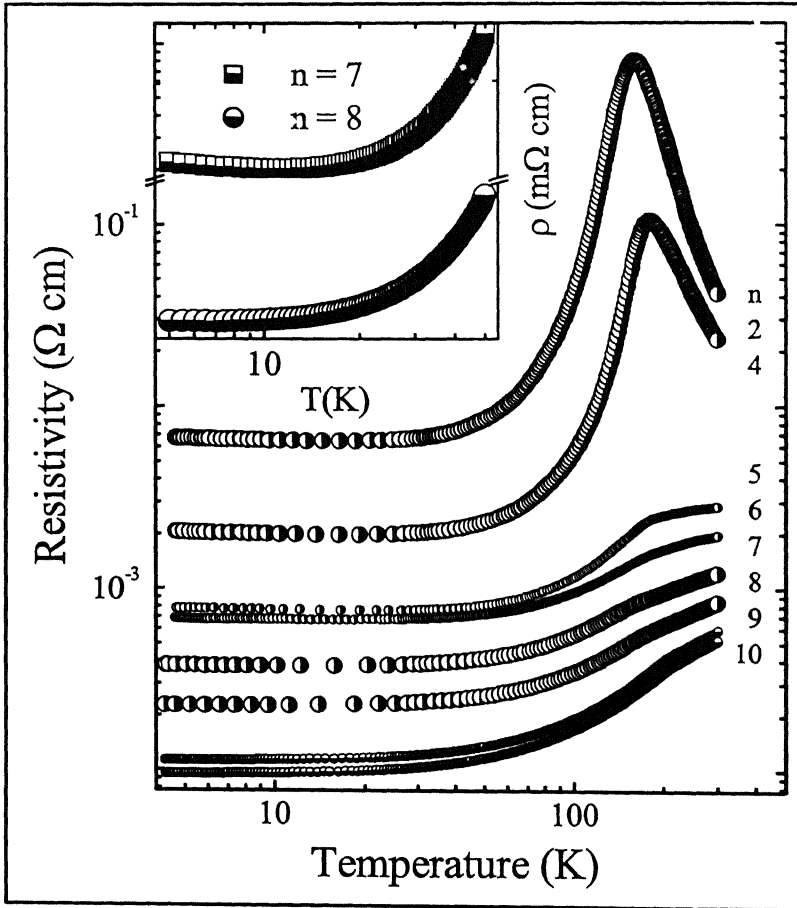
Figure 6.2:   Zero-field, current-in-plane temperature dependent resistivity of *20 u.c LCMO/n u.c. LNO* superlattices deposited on *(001)* oriented *LAO* with different spacer layer thicknesses. Inset shows the low temperature part of resistivity of these superlattices with $n = 7$ and *8* plotted in log scale.

The temperature dependent zero-field resistivity of the *20 u.c.* thick *LCMO* superlattices deposited on *(001)* oriented *LAO* with different spacer layer thicknesses is shown in Fig. *6.2*. The qualitative behavior of $\rho(T)$ for the samples with $n \leq 4$ is

similar to that of a *55 u.c.* thick *LCMO* film (Fig. *3.6*). The $\rho(T)$ of superlattices with $n = 2$ and *4* is thermally activated below room temperature down to a temperature T_P at which the resistivity is maximum. At temperature below T_P resistivity is metal - like (*positive $d\rho/dT$*) down to $\sim 20\ K$ and then again becomes thermally activated. For $n \geq 5$ the samples do not show any peak in resistivity. For superlattices with $n = 5$, *6* and *7*, the $\rho(T)$ below room temperature remains metallic down to *20 K* followed by a thermally activated behavior. For samples with $n \geq 8$ the resistivity remains metallic below room temperature down to *4.2 K*. In the inset of Fig. *6.2* we compare the low temperature behavior of resistivity in sample with $n = 7$ and $n = 8$. In the inset of Fig. *6.3* we show the zero-field resistivity at *5 K* for superlattices deposited on *LAO* as a function of spacer layer thickness. It is maximum for the superlattice with $n = 2$ and it drops as the spacer layer thickness increases.

6.2.3   Magnetoresistance

Fig. *6.3* shows the temperature dependent resistivity of the superlattices in the presence of a *4 tesla* field applied along the direction of the in-plane current. In the presence of magnetic field, the resistivity of these samples drops significantly from its zero-field value and T_P shifted to higher temperatures. The low temperature thermally activated behavior starts below $\sim 25\ K$.

The nature of coupling between the ferromagnetic layers is expected to have a distinct bearing on the magnetoresistance of the superlattices. In Fig. *6.4* we show the magnetoresistance at *4 tesla* of a large number of *LCMO/LNO* samples in the temperature range of *4.2 K* and *300 K*. For all samples, the magnetoresistance rises gradually on cooling below *300 K*, reaches a peak value in the vicinity of the Curie temperature and then drops on further cooling. However, there are many interesting features beneath this broad description of the magnetoresistance. For example; (*i*), The magnetoresistance of samples with thin spacer ($\leq$ *2 u.c.*) is $\sim$ *100 percent* near T_C and it stays high on lowering the temperature. The T_C has been identified with temperature where zero-field resistivity has the peak and it compares well with the T_C deduced from field-cooled magnetization measurement. (*ii*) While the T_C of thick (> *400 Å*) *LCMO* film and *LCMO/LNO* with $n > 8$ *u.c.*, is $\sim$ *220 K*, a significant drop
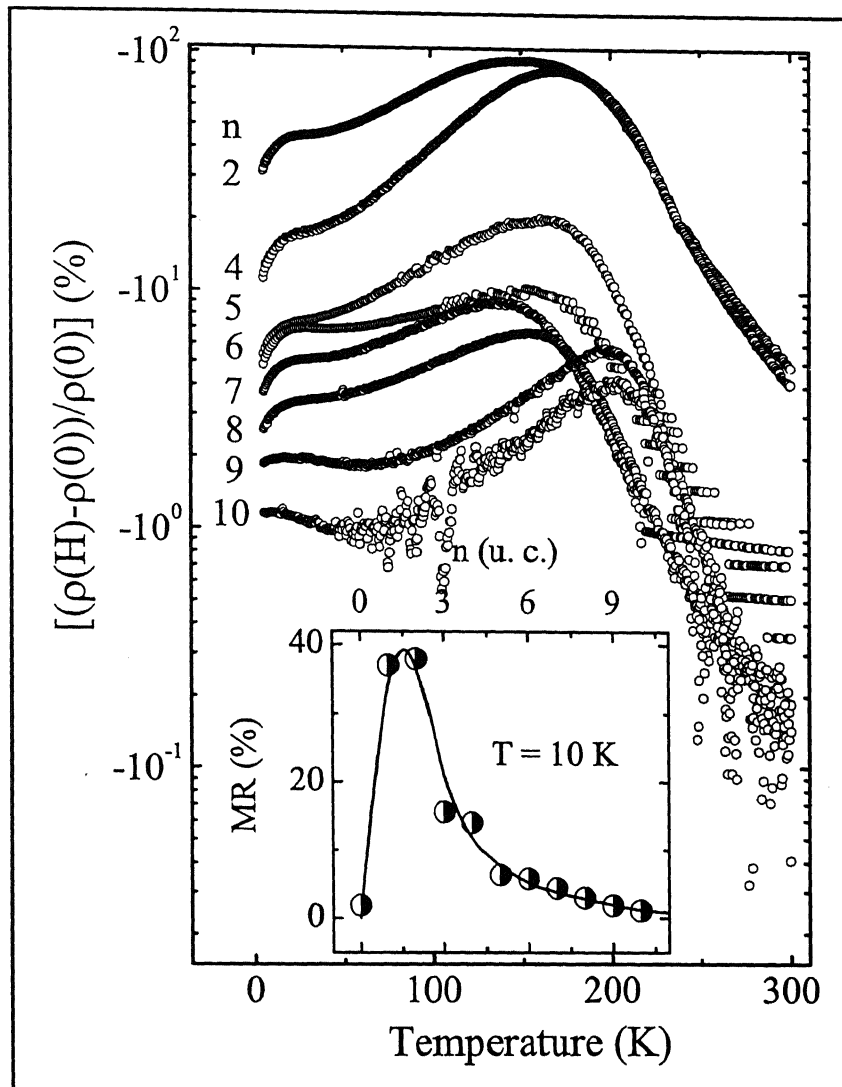
Figure 6.4: Magnetoresistance of *20 u.c* $LCMO/n$ *u.c.* LNO superlattices deposited on *LAO* measured as a function of temperature at *4 tesla*, with the field aligned in a Lorentz force free configuration. Magnetoresistance drops precipitously as the thickness of LNO layer is increased (note the logarithmic scale). Also at $T < 20$ K drop in MR is prominent in samples with thinner LNO layers. Inset shows the MR of different superlattices at *10 K*.
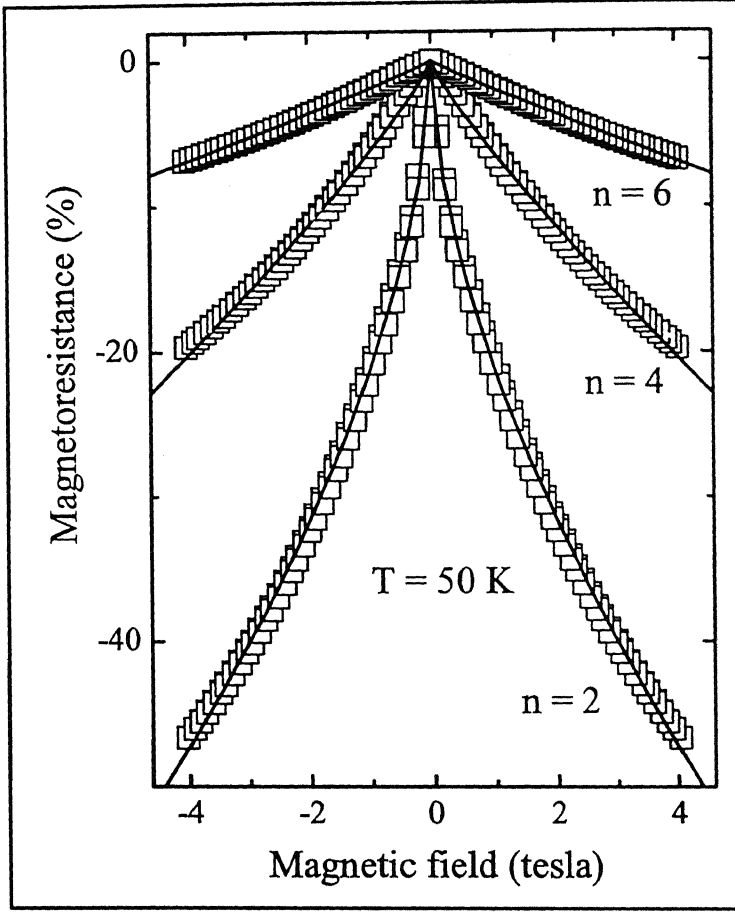
Figure 6.5: Magnetic field dependence of *MR* at *50 K* for three superlattices with *m = 20* and *n = 2, 4* and *6*. Data for a complete field cycle between *+ 4 tesla* and *− 4 tesla* are shown. The *MR* at *50 K* is completely reversible. Solid lines in the figure are fits of the type *MR ∼ H^α*.

In order to address the question whether the *MR* is a consequence of the ease in transport of spin - polarized carriers across the spacer as the moments of the *FM* layers become parallel, in Fig. *6.5* and Fig. *6.6* we show field scans of magnetoresistance for samples with *n = 2, 4* and *6*. In Fig. *6.5*, the *MR* of all three samples at *50 K* is negative even at the lowest field and its magnitude continues to increase with field following a dependence of the type *MR ∼ H^α* where *α = 0.6*, *0.85* and *0.92* for *n = 2, 4* and *6* respectively. The magnetoresistance is also fully reversible at this temperature. A strikingly different behavior of *MR* is seen at *5 K* for sample with *n = 2*, which has antiparallel magnetic coupling between the
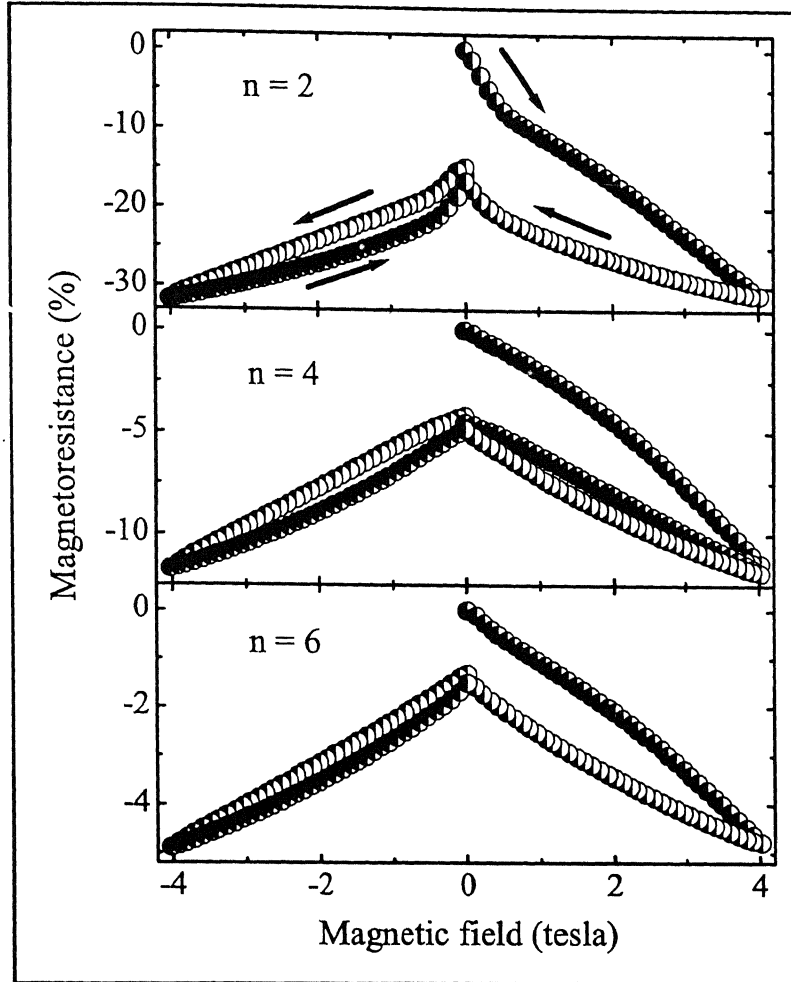
Figure 6.6: Magnetoresistance at *5 K* for three superlattices at different magnetic fields. Data for a complete field cycle between + *4 tesla* and − *4 tesla* for superlattices with *n* = *2* and *4* and a part of second field sweep cycle for superlattice with *n* = *4* are shown. The direction of the magnetic field is marked by arrows for the superlattice with *n* = *2*.

LCMO layers. This characteristic field H_S^* is same as the saturation field till *0.8 tesla* followed by a much slower change. In Fig. *6.6* we show the hysteresis in *MR(H)* of all three samples separately. For samples with *n* = *4* and *6*, the *MR* increases smoothly with field without any signature of a H_S^*. Note that our magnetization data for these samples suggested that the *LCMO* layers are *FM* coupled. The marked change in the behavior of magnetoresistance with increasing field strongly suggests a correlation between the magnetoresistance and magnetic coupling of the sample with

$n = 2$. Another interesting feature of the MR at low temperature ($< 20\ K$) is a pronounced hysteresis. The MR of these samples during second cycle of field sweep from $+ 4$ *tesla* to zero-field does not trace the path taken during the first sweep. This behavior is shown for sample with $n = 4$. Similar irreversibility is also present in MR vs H loops of other samples. A similar irreversibility in MR vs H plots is observed in superlattices with *10 u.c.* thick $LCMO$ layer (Fig. *5.10*).

6.2.4   Magnetization
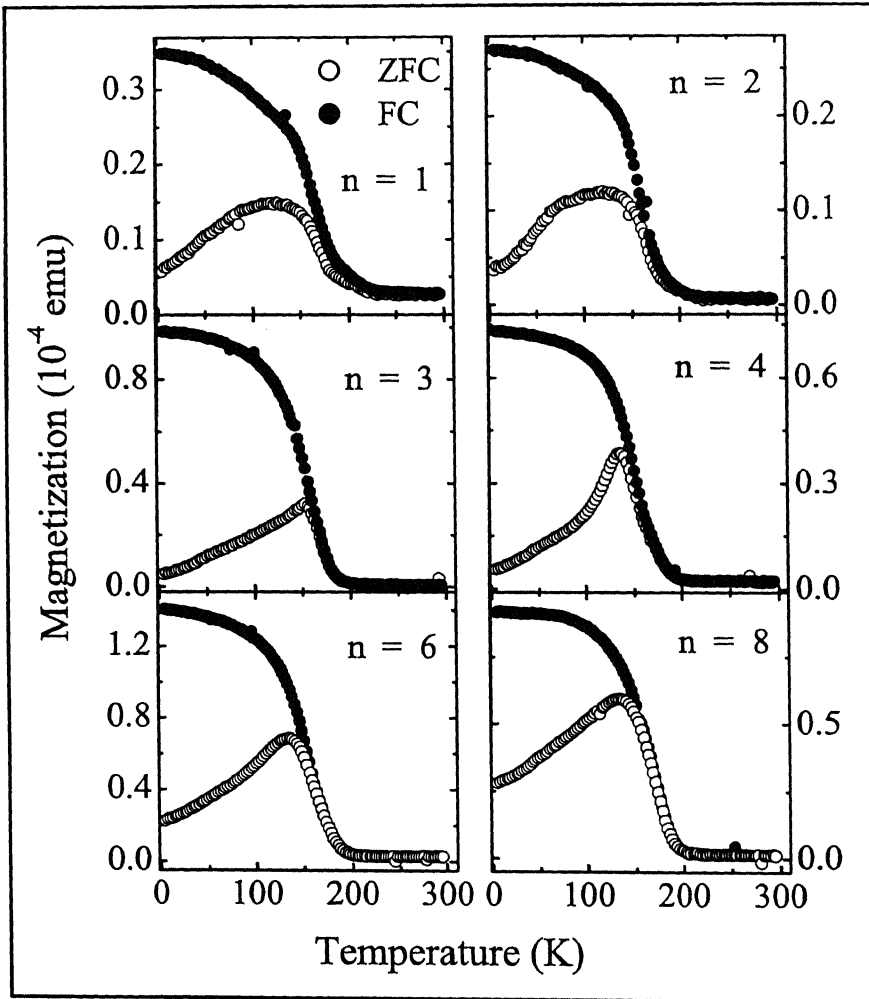
Figure 6.7:   Zero-field-cooled and field-cooled magnetization of superlattices (*20 u.c LCMO/n u.c. LNO*) with $n = 1,\ 2,\ 3,\ 4,\ 6$ and *8* in *50 Gauss* magnetic field aligned along the (*100*) direction of the film.

In Fig. *6.7* we show zero-field-cooled and field-cooled magnetization curves of six samples (with $n \leq 8$) measured in $\sim$ *50 Gauss* field aligned parallel to the plane of the sample. The *ZFC* magnetization of all samples increases slowly with temperature on heating above *5 K* and becomes maximum at temperature T^*. At $T > T^*$, magnetization drops rapidly to a negligibly small value and then remains small above the Curie temperature. The *FC* magnetization at *5 K*, is large. It decreases on heating above *5 K* and merges into the *ZFC* curves at $T > T^*$. A qualitatively similar behavior is seen for the sample with $n \geq 9$. The large difference in *ZFC* and *FC* magnetizations at low temperatures suggests some kind of freezing/frustration of the moments.
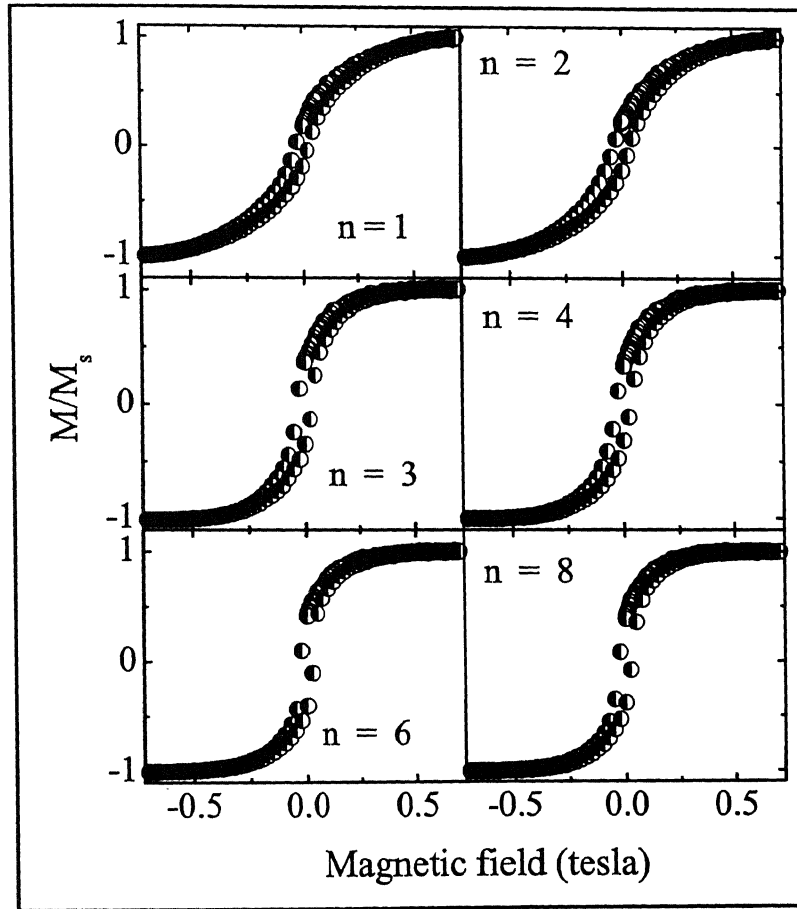
Figure 6.8: Magnetic field dependent normalized magnetic moment $(M_\bullet/M_S)$ of superlattices with $m = 20$ and $n = 1$, *2*, *3*, *4*, *6* and *8* with magnetic field applied along the *(001)* direction of the samples at *10 K*.
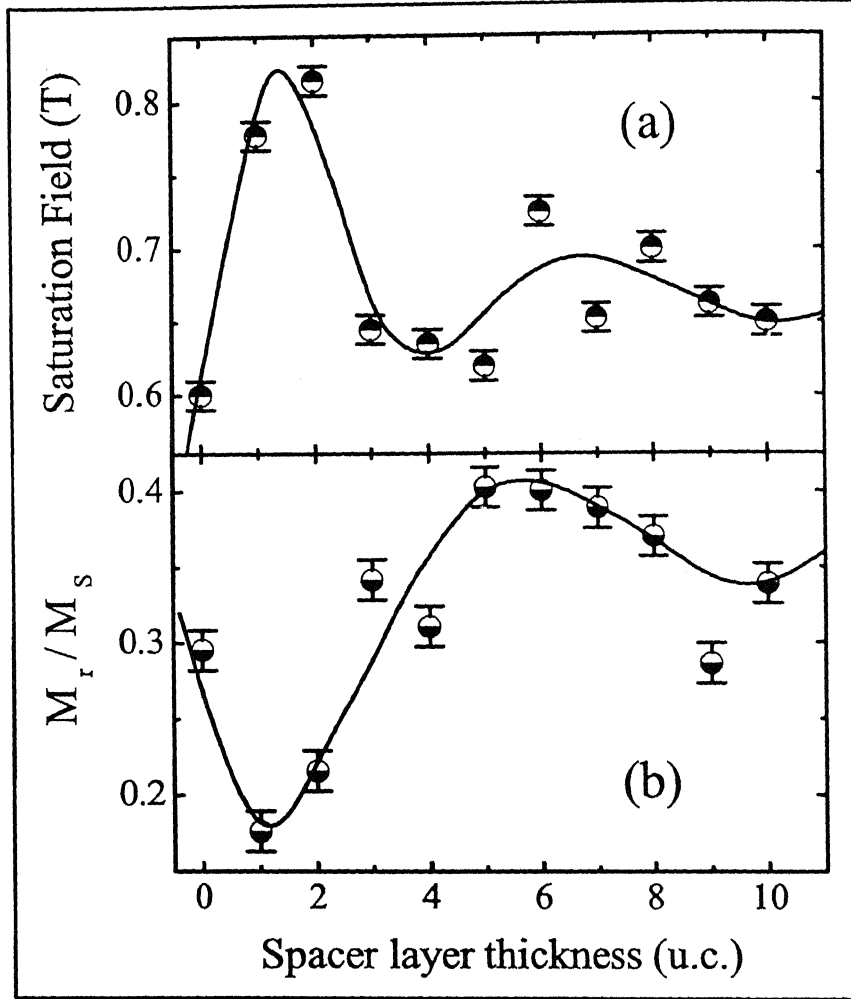
Figure 6.9: Panel (a) shows variation of the saturation field H_S with LNO spacer layer thickness in 20 u.c. LCMO/n u.c. LNO superlattices. The ratio of the remnant and saturation moments (M_r/M_S) for different superlattices is shown in the lower panel (b). Solid lines in the figure are guide to the eye and the significance of error bars is explained in the text. All data were taken at 10 K.

Isothermal measurement of magnetization as a function of applied field (H) is a commonly used method to establish the nature of interlayer coupling. In Fig. 6.8 we show magnetic hysteresis data of the multilayers taken at 10 K. The magnetic field in these measurements was aligned parallel to (001) axis of the substrate. For the sake of clarity, data for only a selected number of superlattices are shown and the magnetization has been normalized with respect to its saturation value. The M_S and H_S have been extracted from the hysteresis loops after taking into account the

weekly diamagnetic response of the substrate. The large saturation field and negligible remnant magnetization (M_r) seen in the case of samples with 1 $u.c.$ and 2 $u.c.$ thick LNO spacer is indicative of antiferromagnetic exchange coupling between the LCMO layers. The antiferromagnetic coupling J_{AF} is directly related to saturation field as $4J_{AF} = H_S M_S t_{FM}$ where M_S and t_{FM} are saturation magnetization of the sample and thickness of the magnetic layer respectively. The sturation field drops when the LNO thickness is increased to 3 $u.c.$ and remains low for the higher values of n. The saturation field and remnant magnetization for all multilayers are shown in Fig. 6.9 where the error bars reflect the variation of H_S and M_r within the step-size of the field used in these measurements. The saturation field for (001) and (010) orientations is the same within the step size. The variation of H_S with the spacer layer thickness shows a peak at $n \sim 2$ followed by a minimum at $n \sim 4$ and then a second broad peak of much lower intensity centered at $n \sim 7$. The remnant magnetization, on the other hand, rises rapidly between $n = 2$ and $n = 4$, reaches a peak value at $n = 6$ and then drops, on a further increase in n.

6.3 Discussion

In the case of superlattices with 10 $u.c.$ thick LCMO layers the interfacial strain starts to relax as the spacer (LNO) layer thickness increases. Similar behavior is observed for the case of 20 $u.c.$ thick LCMO based superlattices. The c – axis lattice parameter of the superlattice with 10 $u.c.$ thick LCMO and 2 $u.c.$ thick LNO is 3.95 $Å$. As the thickness of LCMO increases to 20 $u.c.$, the c – axis lattice parameter becomes 3.915 $Å$. As shown in the inset of Fig. 6.1 the c – axis lattice parameter of the superlattices continue to decrease as the spacer layer thickness increases and becomes 3.876 $Å$ for the superlattices with 6 $u.c.$ thick LNO. A similar behavior of the c – axis lattice parameter is also seen in sample with 10 $u.c.$ thick LCMO layers (see chapter 5). This observation suggests that the disorder interfacial phase (DIP) identified earlier will be same in the superlattices where the magnetic layers are 20 $u.c.$ thick.

It is instructive to compare the behavior of H_S seen in Fig. 6.9 with the data on superlattices of pure metals and compounds. In the case of Fe/Cr, the canonical GMR superlattice for example, a distinct peak is seen in H_S at Cr spacer thickness (d_S) of ~ 10 $\mathring{A}$ followed by a second peak and a third peak like feature at 25 $\mathring{A}$ and 45 $\mathring{A}$ respectively [4]. A similar period has been observed in Fe_3O_4/TiN with much stronger damping of the oscillations at the higher TiN spacer thickness [37]. In the case of $La_{2/3}Ba_{1/3}MnO_3/LaNiO_3$ superlattices, however, a fully developed ferromagnetic coupling is seen for 5 $u.c.$ thick LNO [38]. While this number exceeds our value by ~ 1 $u.c.$ of LNO, the overall features of the data shown in Fig. $6.9(a)$ are similar to what has been observed in the case of $La_{2/3}Ba_{1/3}MnO_3/LaNiO_3$ multilayers. Bruno and Cheppert [14] have shown that in the framework of the Ruderman-Kittel-Kasuya-Yosida exchange coupling, the period of oscillations depends on the Fermi surface parameters of the spacer layer. Since the spacer layers are identical in the two cases, the subtle difference in the position of the first minimum is perhaps due to the difference in the ferromagnetic layers as suggested by Baranas [7] for metallic superlattices. The behavior of remnant magnetization with increasing d_S as shown in the Fig. $6.9(b)$ is consistent with the picture of a change over from antiferromagnetic coupling between the $LCMO$ layers. The large value of M_r (~ 35 % of M_S) for $d_S > 3$ $u.c.$ reflects the squareness of the hysteresis loop, typical of a soft ferromagnet.

In metallic superlattices, a correlation between AF interlayer exchange coupling and large negative magnetoresistance depends on the extent of interfacial disorder. For example in $Fe - Nb$ multilayers [159], while H_S and M_r oscillate with the increasing Nb layer thickness, the magnetoresistance remains small even in the case of the AF coupled samples. Similarly, non-magnetic impurities at interfaces are seen to suppress magnetoresistance without changing the AF coupling [32]. Electron transport and magnetic properties of transition metal oxides are likely to be much more susceptible to interfaces and interfacial disorder due to the covalency of the bonds. Even at a defect-free interface, the truncation of the 3 - dimensional environment of the Mn and Ni ions in the bulk $LCMO$ and LNO respectively can lead to different site spins and overlap integrals for charge transport. The possibility of alloying through
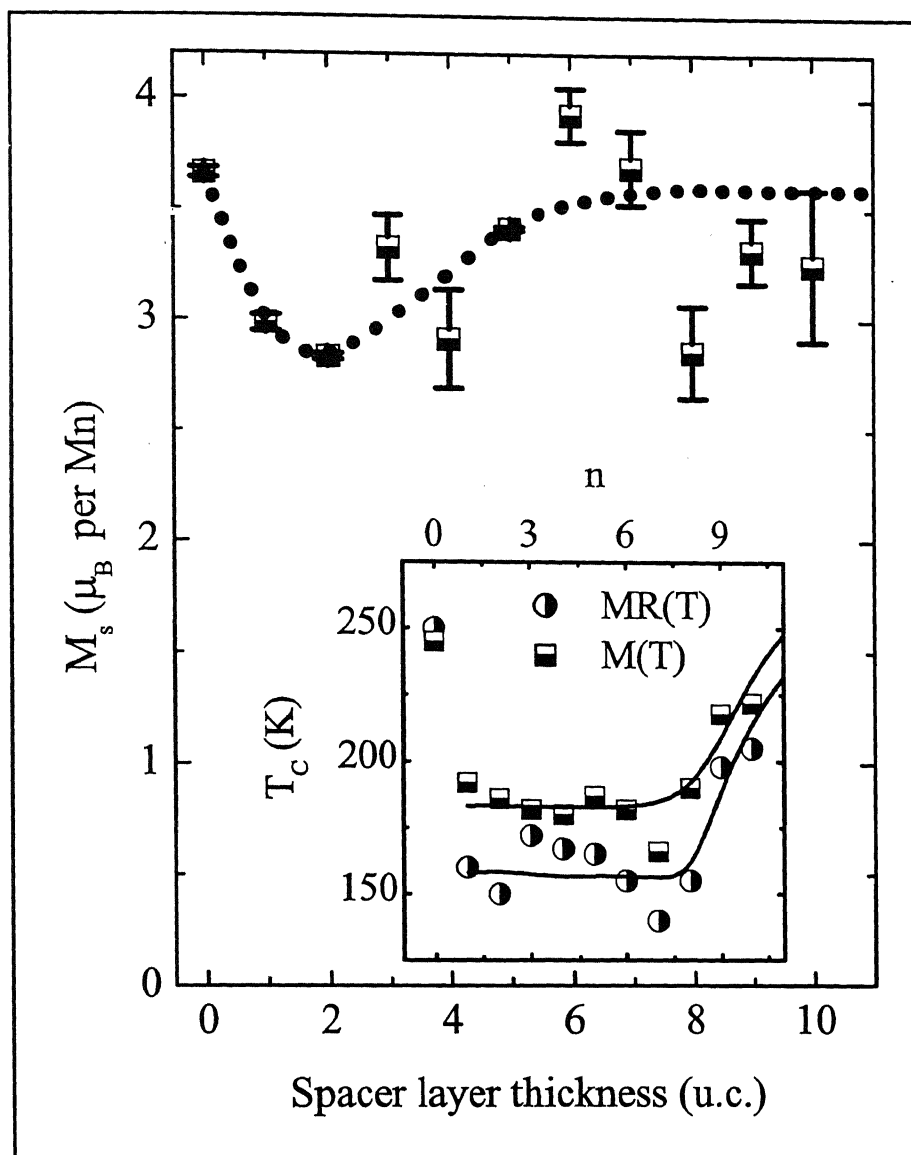
Figure 6.10: *LNO* spacer layer thickness dependence of the saturation moment per *Mn* ion in the superlattices. The dotted line in the figure is a guide to the eye and the error bars reflect the uncertainty in the measurements of sample dimensions. Inset shows the value of transition temperature of superlattice with different spacer layer thicknesses seen in the $MR(T)$ and $FCM(T)$. Solid line in the figure is a guide to the eye.

formation of compound $La_x Ni_{1-x} MnO_3$ and lattice mismatch related strain add to this problem. In our earlier studies of transport in ultrathin films of $LCMO$, LNO and $(LCMO)_m/(LNO)_n$ superlattices ($m = 10$ u.c. and n variable), we have seen clear signatures of a 3 u.c. ~ 4 u.c. thick disordered interfacial phase [158]. Our magnetization measurements also attest to this picture. In Fig. 6.10 we show the variation of saturation magnetization in units of Bohr magneton (μ_B) per Mn ion with LNO thickness. A simple counting of Mn^{4+} and Mn^{3+} spins in the bulk $La_{0.7} Ca_{0.3} MnO_3$ yields an average moment of 3.7 μ_B per Mn site. Measurements of magnetization on a 1000 Å film of $LCMO$ are consistent with this number. In the multilayers with lower LNO spacer layer thickness, the magnetic moment per Mn ion shows a small but distinct drop. We also observe a similar drop in the Curie temperature. However, as n increases beyond 6, the M_S and T_C show steady increase and for the superlattice with $n = 10$, both these quantities reach the bulk value.

For the case of superlattices with 10 u.c. thick $LCMO$ and less than 4 u.c. thick LNO spacer layers, we see large room temperature resistivity, which is thermally activated till the lowest temperature. When the magnetic layer thickness is increased to 20 u.c., the temperature dependence of resistivity in samples with $n < 4$, is similar to that of the resistivity in pure $LCMO$ film. However, as the spacer layer thickness approaches 10 u.c., the behavior of $\rho(T)$ is similar to that of a pure LNO film.

Our modeling of $\rho(T)$ for superlattice with $m = 10$ and n variable strongly suggested that for $n \leq 4$, the LNO layers are completely consumed by the formation of a disordered interfacial phase whose resistivity can be deduced by analyzing the transport in the frame work of a parallel resister network model. Extension of this analysis to present superlattices where the $LCMO$ thickness is 20 u.c., implies that the sample with $n = 4$ will only consist of alternate layers of the DIP and 16 u.c. of $LCMO$. The $\rho(T)$ of the DIP calculated from the resistivity of the $m = 10$, $n = 4$ superlattice is shown in the inset of Fig. 6.11. With this $\rho(T)$, we apply the PRN model to the measured $\rho(T)$ of the sample with $m = 20$ and $n = 4$. A least square fitting procedure allows us to extract $\rho(T)$ of $LCMO$ in the superlattice. These data are also shown in the inset of Fig. 6.11(a) curve (2). The multilayers with $n > 4$
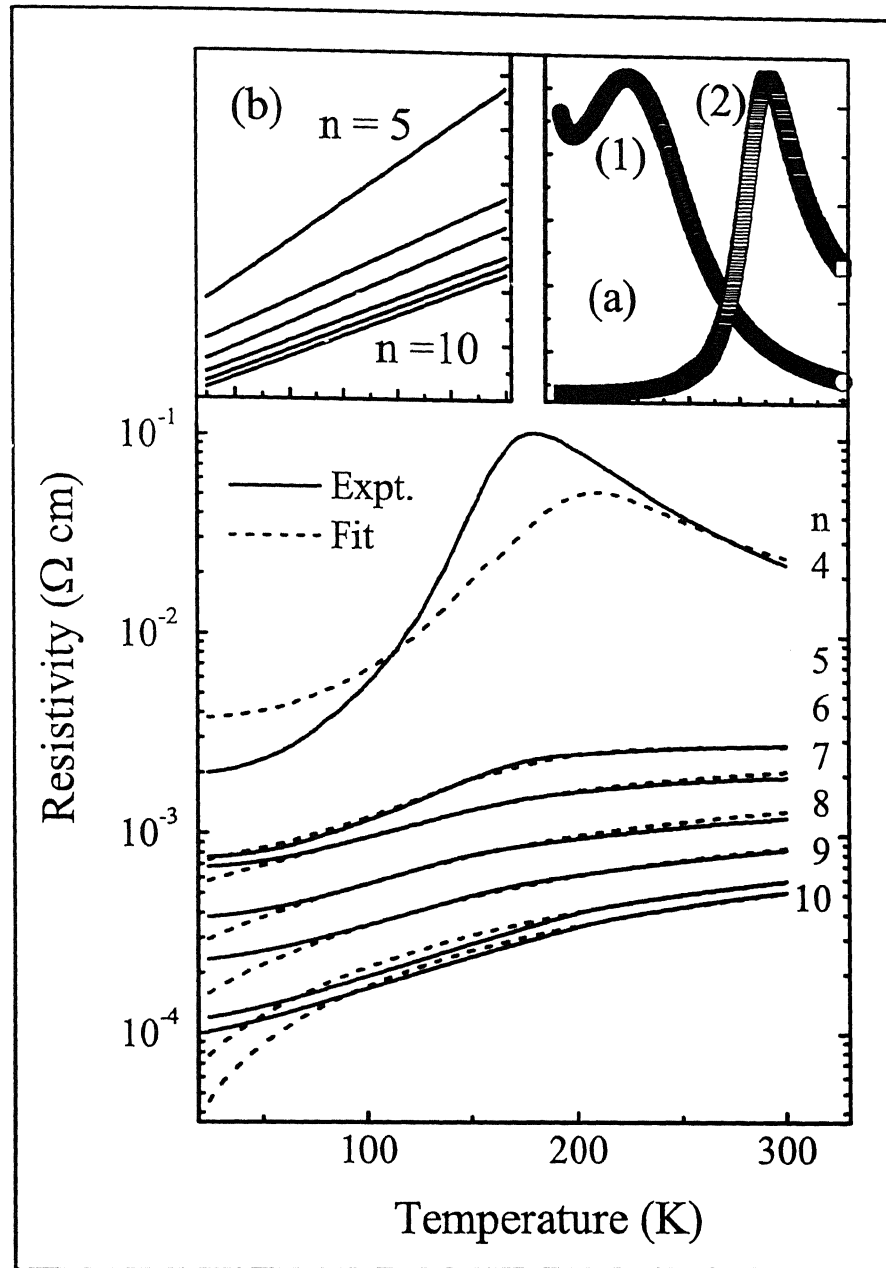
Figure 6.11: The measured and calculated resistivities of the superlattices with $n = 4$, 5, 6, 7, 8, 9 and 10. The calculation is based on the Parallel Resistor Network model for a stack of 15 quad layers, each consisting of $LCMO$, LNO and DIP. The resistivity of DIP deduced from the $\rho(T)$ data of superlattice with $m = 10$ and $n = 4$ (curve 1) and the resistivity of $LCMO$ deduced from the $\rho(T)$ data of superlattice with $m = 20$ and $n = 4$ (curve 2) is shown in the inset (a). Inset (b) shows the resistivity of LNO layers ($\rho(T) = \rho_0 + \rho_1 T$) obtained from the best fits.

in our model consist of a repetitive trilayer structure with a fixed thickness of the DIP and $LCMO$, but with the LNO thickness increasing with n. In Fig. 6.11 we show the PRN model based $\rho(T)$ for multilayer with $n \geq 4$ along with the measured data. The measured and calculated resistivities are in excellent agreement above $\sim 75\ K$. The disagreement at $T < 75\ K$ is perhaps due to the fact that calculation does not take into account the upturn (Fig. $4.4(a)$) in the resistivity of thin LNO films at lower temperature, and the interlayer exchange coupling between the successive magnetic layers. In inset (b) of Fig. 6.11 we show the calculated $\rho(T)$ of LNO for different superlattices. The $\rho(T)$ of LNO varies as $\rho(T) = \rho_0 + \rho_1 T$ with ρ_0 and ρ_1 as temperature independent adjustable parameters.

From our magnetotransport and magnetization data, and studies on ultrathin films of $La_{0.7}Ca_{0.3}MnO_3$ and $LaNiO_3$, a fairly consistent picture of interlayer coupling and magnetotransport emerges in $LCMO/LNO$ superlattices. For LNO layer thickness of $n < 2\ u.c.$, modeling of transport [158] and the behavior of FC/ZFC magnetization suggest a disordered $LCMO/LNO$ interface with thickness $\sim 4\ u.c.$ and frustrated Mn^{3+}, Mn^{4+} and Ni^{3+} spins. We suspect that an $RKKY$ type interaction through this spin - disordered phase causes the AF coupling of the $LCMO$ layers. The steep increase in magnetoresistance of these multilayers up to a critical field H_S^* provides compelling evidence for a correlation between magnetic coupling and transport. The less pronounced but a persistent growth of magnetoresistance with field seen beyond the saturation field is a typical feature of narrow bandwidth manganites and ultrathin films of even wide bandwidth systems such as $LCMO$ and $LSMO$ [82, 120, 160-162]. While in the former it is caused by suppression of charge ordering tendencies in the latter depinning of the interfacial t_{2g} spins by the external field may be responsible for the large negative magnetoresistance. The depinning is arguably a plausible scenario in the present case as well is evident from the sudden drop of the $4\ tesla$ magnetoresistance in samples with $n < 4$ seen at lower temperatures ($T < 20\ K$), where limited thermal energy of the localized spins requires much stronger fields for parallel alignment. The freezing/pinning of spins is also evident in the $ZFC - FC$ magnetization data.

At the higher *LNO* thickness, the *IEC* turns ferromagnetic and the magnetoresistance does not show a steep increase with the field. However, a gradual increase of magnetoresistance up to the maximum field used in these experiments again points towards pinning of the site spins by interfacial disorder. However, this effect is expected to be less remarkable as the *LNO* layers gain their bulk - like conductivity and itinerant electrons facilitate coupling of the localized spins. Some indication of this effect comes from the gain in saturation moment and Curie temperature of the multilayers at the higher *LNO* spacer thickness. Finally, the disorder at the interfaces and in the *LNO* layers is expected to attenuate the oscillatory coupling [*13*, *14*]. The overdamped *IEC* seen in Fig. *6.11* is consistent with this picture of magnetic ordering in interfacial superlattices.

6.4 Conclusions

In summary, we have carried out a systematic study to identify the possible correlation between interlayer magnetic coupling and magnetoresistance in superlattices consisting of two metallic oxides one of which is a double exchange ferromagnet of considerable current interest. We observe overdamped oscillations in the magnetic coupling with the increasing *LNO* spacer layer thickness. While all multilayers show negative magnetoresistance, the effect is particularly large in samples where the *IEC* is antiferromagnetic. These measurements also suggest that interfacial disorder of magnetic and structural origin plays a much greater role in the behavior of magnetoresistance than the nature of interlayer magnetic coupling.

Chapter 7

Current – perpendicular to plane (CPP) magnetoresistance of LCMO/LNO superlattices

7.1 Introduction

The structural and magnetic disorders at the interfaces of thin film superlattices play a critical role in magnetic ordering and magnetoresistance of such heterostructures. While this issue has been addressed at length for $3d$ - transition metal based multilayers [48], recent measurements on similar structures made of magnetic oxides suggest that the interfacial disorder can be equally significant in these systems as well [36, 40-42, 92, 163]. Studies of interfacial disorder and its influence on magnetic coupling and transport are important in the context of the reports of oscillatory exchange coupling (OEC) in Fe_3O_4/TiN [37] and $La_{2/3}Ba_{1/3}MnO_3/LaNiO_3$ [38] superlattices. Bruno and coworkers [13, 14] have shown that scattering of charge carriers by a static disorder in the non-magnetic spacer layers and at the interfaces of the multilayers can suppress the OEC. Such effects are expected to be strong in oxide based systems due to small mean free path of carriers, and the interface roughness resulting from a change in the nearest neighbor environment of the magnetic ions at the interfaces even when there is no metallurgical intermixing of elements

Scattering of charge carriers by the interfacial disorder and its effects on magnetic ordering can be probed with measurements of electrical resistivity. Transport measurements on superlattices are commonly performed in a geometry where the current flows in the plane of the film. For this Current-in-Plane configuration, the effective resistance of the superlattice can be modeled by considering it a parallel combination of resistances of the magnetic and non-magnetic layers, and of the interfacial zones. However, the contribution of interfacial disorder to electron scattering can be measured directly by injecting current through the interfaces. The advantage in this case is that all carriers contributing to current are forced to pass through the interfaces as well as the bulk. This makes the current distribution uniform and permits application of a series resistance model in which contributions from individual metals and interfaces are summed [17]. However, this Current Perpendicular-to-Plane measurement is quite non-trivial because of the extremely small resistance of the metallic samples [16, 17]. In the case of $3d$ - transition metal based superlattices, CPP resistance has been measured by lithographic patterning of multilayers in the form of columns of small cross sectional area [16]. The CPP resistance and magnetoresistance have also been measured by sandwiching the superlattice between two thin - film electrodes of niobium in their superconducting state [17]. The $CPP - MR$ measurements are lacking on oxide - based multilayers except for the tunneling magnetoresistance in junctions made of two magnetic oxides separated by a thin insulator [164].

In this chapter we present measurements of CPP resistance and MR of a magnetic - nonmagnetic superlattice consisting of two metallic compounds. The magnetic layers are of the double exchange ferromagnet $La_{0.7}Ca_{0.6}MnO_3$ and the non-magnetic spacer is $LaNiO_3$. These measurements reveal several interesting aspects of the spin dependent transport such as; (i) a large (~ 80 % at 4 tesla) $CPP - MR$ at temperatures much below the Curie temperature, (ii) a drop in $CPP - MR$ at $T < 20$ K, and (iii), evidence for a disordered interfacial phase which enhances the perpendicular resistance of these structures and seemingly controls the flow of spin - polarized carriers across the interfaces.

7.2 Results

Figure *7.1* shows the resistance of three multilayers measured over *4.2 K* to *300 K* in zero-field and at *4 tesla*. A sketch of the sandwich geometry used for *CPP* resistance measurements is shown in the inset. Since this is essentially a two - terminal measurement, the data in the temperature range where *YBCO* is normal also reflect voltage drop in certain parts of the *YBCO* film, in addition to the resistance of the *YBCO* – superlattice interface and the perpendicular-to-plane (*PP*) – resistance of the superlattice itself. While a correct determination of the current flow patterns and potential distribution on the top and bottom electrodes is quite non-trivial, a linear *T* – dependence of the resistance at *T > 100 K* suggests that it is primarily from the *YBCO* electrodes, with some contribution from planar transport in the superlattice. The normal-state resistance of the sandwich shows a distinct drop with field, which is much larger then the magnetoresistance in *YBCO* [*165*]. The drop in resistance (i.e. difference between zero-field resistance ($R_0(T)$) and in-field resistance ($R_H(T)$)) of the samples at $T > T_C$, when *4 tesla* field is applied, is shown in the Fig. *7.2*. The $R_0(T) - R_H(T)$ of the sample with *8 u.c.* spacer layer in the superlattice, in the normal state of the electrodes has a broad peak centered at $\sim$ *180 K*. This feature is indicative of magnetic ordering in the *LCMO*. The peak in $R_0(T) - R_H(T)$ shifts to a lower temperature as the spacer layer thickness in the superlattice is reduced. This indicates the formation of spin disordered at the interfaces. At $T < T_C$ of *YBCO*, the contribution to measured resistance from transport in *YBCO* and parallel transport in the superlattice disappears, and the geometry truly measures the perpendicular resistance R of the superlattice in series with the resistance of the *YBCO*/superlattice interfaces. In the vicinity of T_C however, *YBCO* has a positive magnetoresistance due to flux flow [*166*] and also possibly due to injection of spin - polarized carriers from the superlattice [*167, 168*]. This leads to broadening of the resistive transition. The field - induced increase in the resistance of *YBCO* in the flux flow regime exceeds the drop in resistance due to the magnetoresistance of the manganite. This causes the zero-field and in-field $R(T)$ curves to cross just below the onset of the transition.
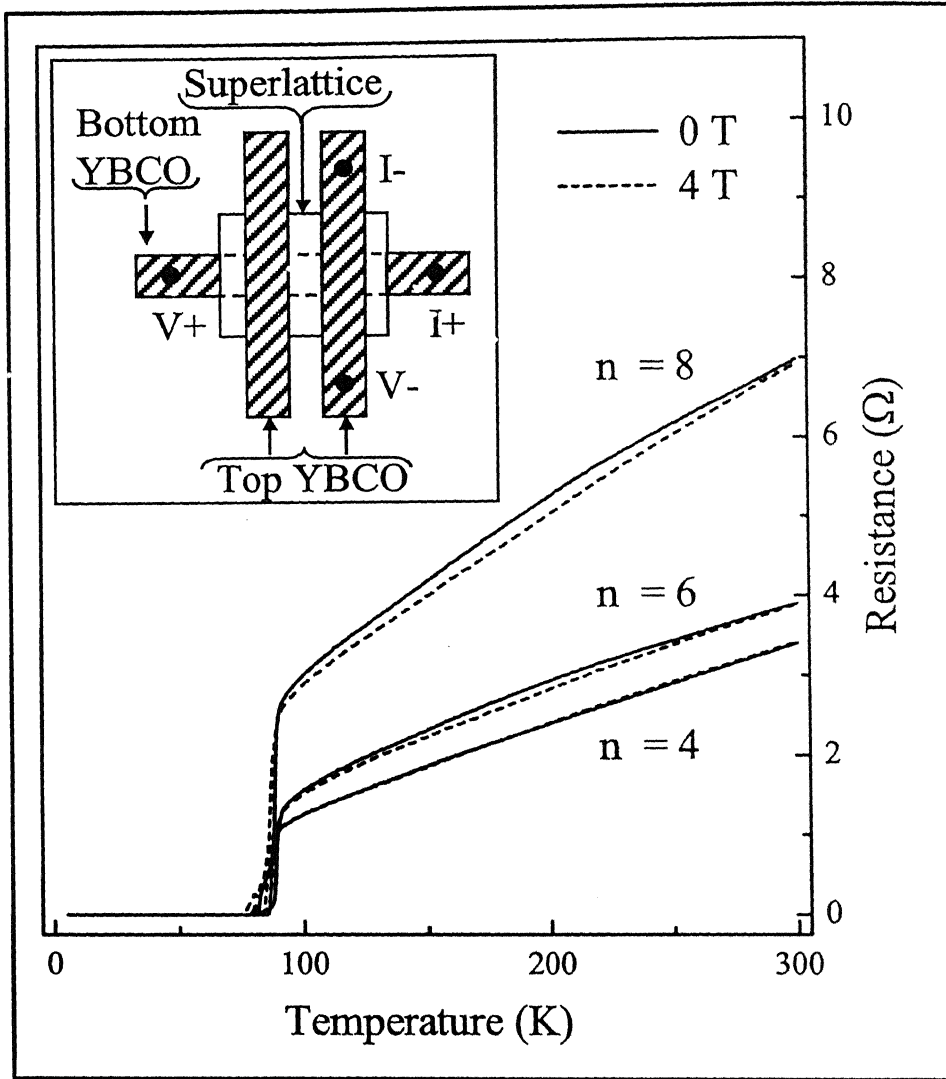
Figure 7.1: Zero-field and in-plane field (4 *tesla*) resistance of the superlattices with $n = 4$, 6 and 8 sandwiched between the *YBCO* electrodes measured in the *CPP* geometry. Inset shows a schematic view of the sandwich geometry used to measure *CPP* – magnetoresistance.

go to zero, the perpendicular resistance of the superlattice decreases with field (negative magnetoresistance of *LCMO* layers). This effect causes the $R(T)$ curves to cross once again. In the Fig. $7.3(a)$ we show the difference between the zero-field and in-field resistances in the transition region of the samples with 6 *u.c.* and 8 *u.c.* thick spacer layers. The two - fold crossing discussed above leads to a pronounced minimum in the $R_0(T) - R_H(T)$ data. This minimum at $\sim 85\ K$ is a measure of the flux flow

resistance. A small but distinct minimum at $T = 79\ K$ seen in the figure suggests the presence of a two - step superconducting transition, which presumably appears because of a low T_C phase of the $YBCO$ in contact with the manganite. The flux flow resistance for the sample with $8\ u.c.$ spacer in the superlattice at various magnetic fields is shown in the Fig. $7.3(b)$. The enhanced difference in zero-field resistance and in-field resistance with the magnetic field is a clear signature of the flux flow.
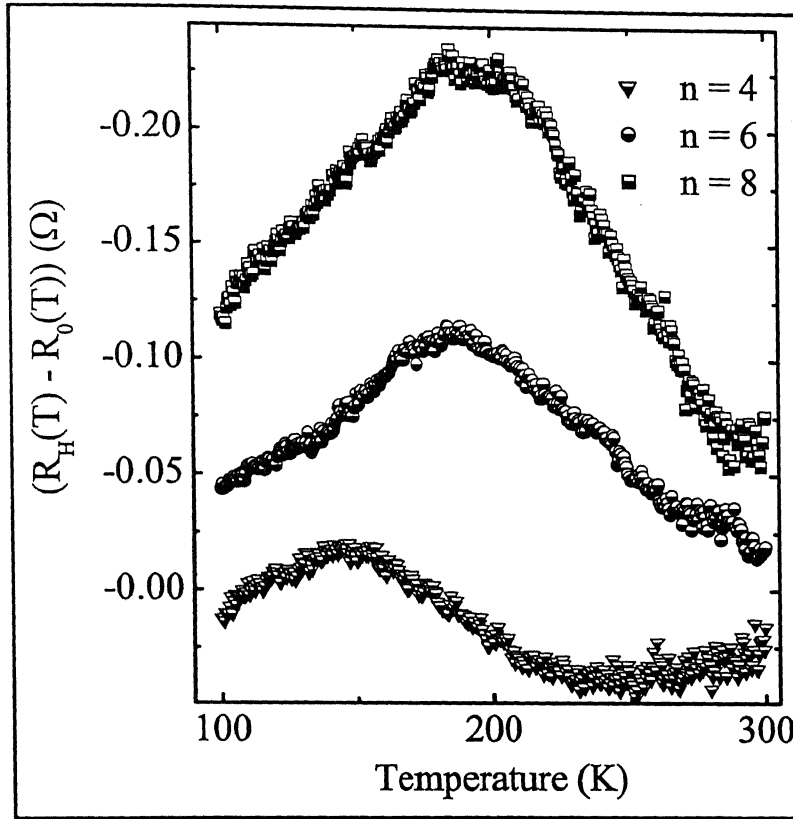
Figure 7.2: The difference in zero-field and in-field resistance of the $n = 4$, 6 and 8 superlattices at 4 tesla in-plane field in the temperature range $100\ K$ to $300\ K$.

At $T < 75\ K$, where the $YBCO$ is fully superconducting the measured resistance is truly the perpendicular R of the multilayer. In the Fig. $7.4(a)$ we show a magnified view of the $R(T)$ curves at zero-field for samples with $6\ u.c.$ and $8\ u.c.$ thick spacer in the superlattice. The resistance of the sample with $8\ u.c.$ spacer in the superlattice at various fields in the temperature range $4.2\ K$ to $75\ K$ is shown in the Fig. $7.4(b)$. There are two noteworthy features of the data shown in Fig. 7.4. First the resistance

at $T > 30$ K remains nearly temperature independent and its value drops linearly with the field. Secondly, the resistance starts diverging at temperatures below ~ 20 K. This effect is stronger at the higher fields.
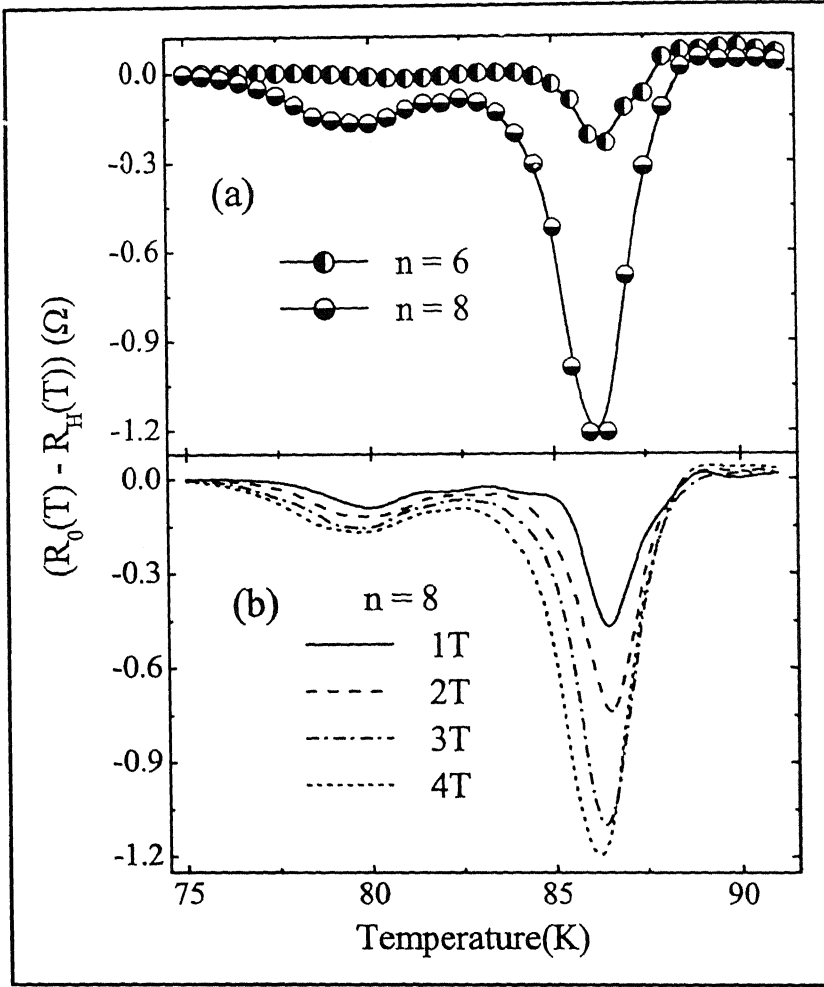
Figure 7.3: Panel (a) shows the difference in zero-field and in-field resistance $(R(0) - R(H))$ of the $n = 6$ and 8 superlattices in the superconducting transition region. Panel (b) shows the $(R(0) - R(H))$ of the $n = 8$ superlattice at several values of magnetic field in the superconducting transition region.

In Fig. 7.5(a) we plot the magnetoresistance of the samples with 6 $u.c.$ and 8 $u.c.$ spacer in the superlattice at 4 $tesla$ in the CPP geometry. In Fig. 7.5(b) we show the $CIP - MR$ at 4 $tesla$ of $n = 6$ and 8 samples prepared in a separate run. The CPP resistance of these structures decreases rapidly with n. This poses experimental difficulties in the measurement of magnetoresistance. However, it is clear from the

figure that the $CPP - MR$ is higher by a factor of $7 \sim 15$ compared to the $CIP - MR$. Moreover, in both CIP and CPP geometries, the magnetoresistance drops at the lowest temperatures. In the case of $3d$ - transition metal based superlattices also the magnetoresistance in the CPP geometry is higher [17, 16], and it tends to reach a saturation value at lower temperatures [16]. The magnetoresistance of sample with 8 $u.c.$ spacer in the superlattice at various fields is shown in the Fig. $7.5(c)$.
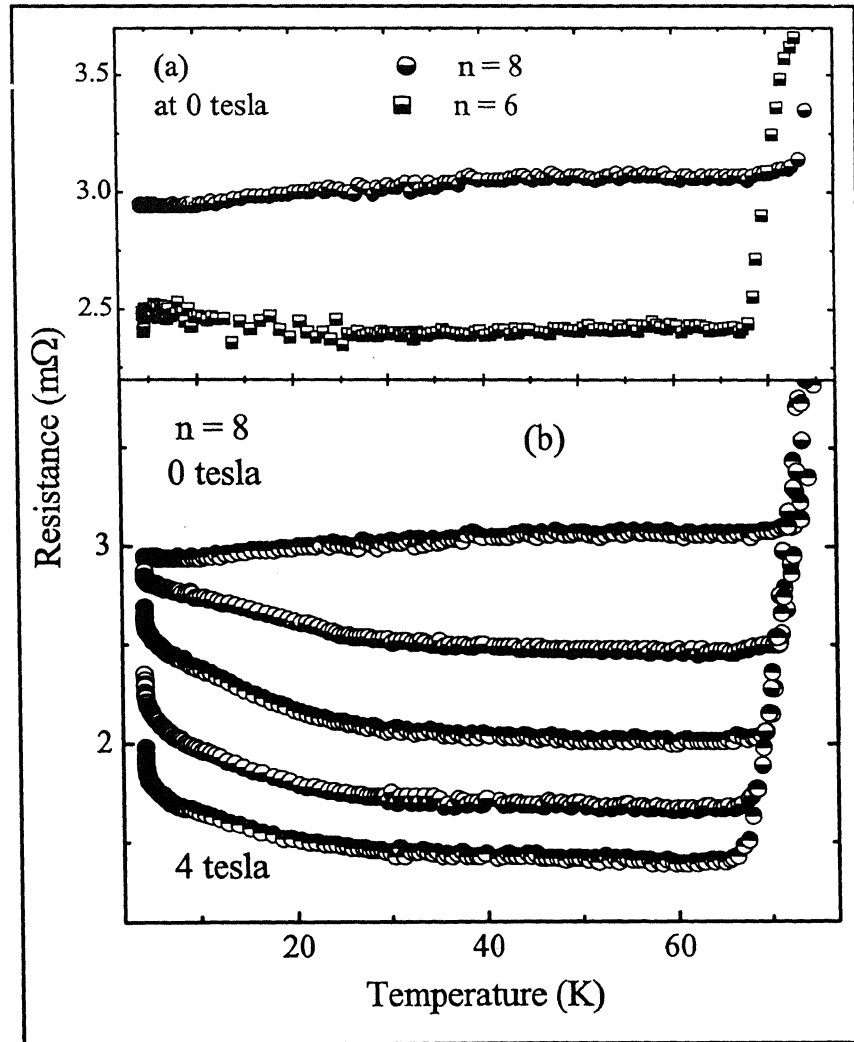
Figure 7.4: Panel (a) shows the current perpendicular-to-plane resistance of the $n = 6$ and 8 superlattices in the temperature range 4.2 K to 80 K measured in zero-field. Panel (b) shows the CPP resistance of the $n = 8$ superlattice at several values $(0, 1, 2, 3,$ and 4 $tesla)$ of the in-plane magnetic field.
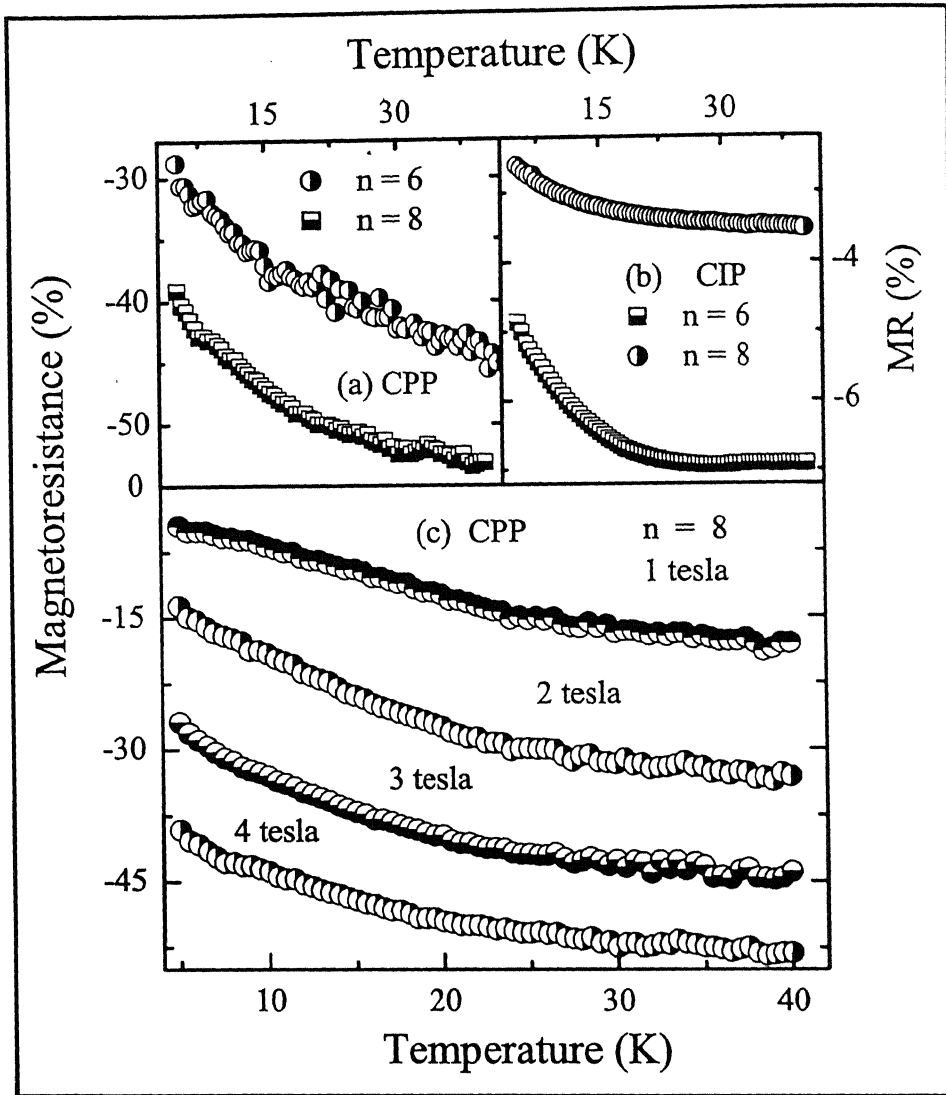
Figure 7.5: Panel (a) shows the magnetoresistance perpendicular-to-plane of the $n = 6$ and 8 superlattices at 4 *tesla* in-plane field in the temperature range $4.2\ K$ to $40\ K$. Panel (b) shows the magnetoresistance parallel-to-plane of the $n = 6$ and 8 superlattices at 4 *tesla* in-plane field. The $CPP – MR$ at several field (0, 1, 2, 3, and 4 *tesla*) is shown in the lower panel (c).

Figure *7.6* shows the $CPP – MR$ of the sample with $8\ u.c.$ spacer superlattice at $5\ K$, $10\ K$ and $40\ K$ as the magnetic field is scanned from 0 to 4 *tesla* in the forward and reverse directions. At $40\ K$, the magnitude of magnetoresistance rises with field, initially linearly, followed by a sublinear dependence. However, it does not saturate at the maximum field of 4 *tesla*. Further, the magnitude of the magnetoresistance

in the field decreasing branch is higher. At the lower temperatures the field-induced drop in resistance is much smaller and it remains linear up to the maximum field. The hysteresis in this case is much more pronounced.
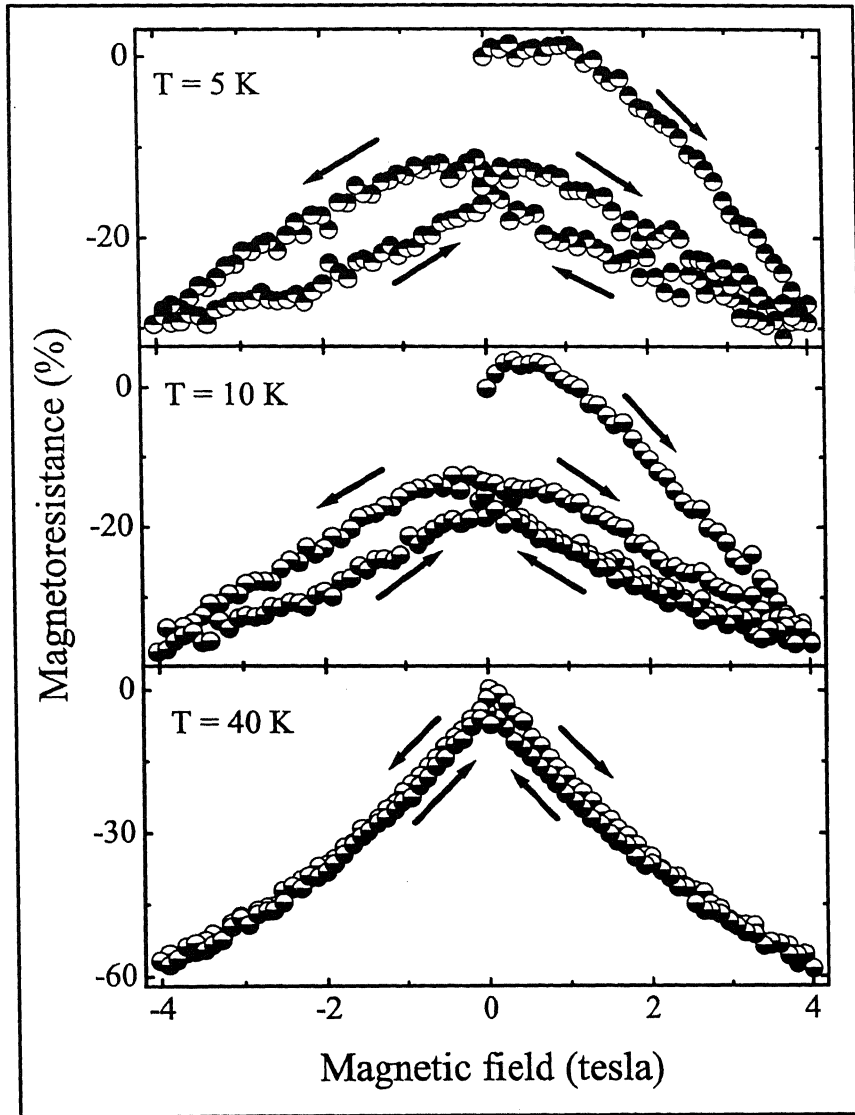
Figure 7.6: Magnetic field dependence of *CPP − MR* of the *n = 8* superlattice at *5 K, 10 K* and *40 K*. Arrows in the figure indicate direction of the field sweep. Zero of the *Y − scale* for the three sets of data is different.

7.3   Discussion

The factors that affect magnetoresistance, the most in magnetic superlattices are the relative orientation of magnetization in successive ferromagnetic layers and the interfacial disorder at the ferromagnet - nonmagnet interfaces. The contribution of the former to $CPP - MR$ has been discussed in detail [13, 14, 18, 27, 48] In general, a parallel alignment of magnetization in the ferromagnetic layers facilitates transport of spin - polarized carriers across interfaces leading to a low magnetoresistance state. Where as, an antiferromagnetic arrangement or an uncorrelated state of net zero - moment of the superlattice enhances scattering of the carriers at the interfaces. The magnetoresistance is large in the latter case. Our measurements of the saturation field in these superlattices reveal an overdamped oscillatory behavior, which peaks at $n = 2$ followed by a minimum at $n = 4$ and a broad maximum centered at $n = 8$. The low magnetoresistance of the $n = 4$ multilayer is consistent with this picture. While the initial increase of magnetoresistance with the magnetic field as seen in Fig. 7.6 can be attributed to field-induced parallel alignment of magnetization in ferromagnetic layers, its non-saturating behavior and the anomalous hysteresis point towards the role of the interfaces.

We have addressed the issue of interfacial disorder through measurements of saturation moment and by modeling the CIP resistance. Our measurements of the CIP magnetoresistance in multilayers consisting of 10 $u.c.$ $LCMO$ and n $u.c.$ LNO strongly suggested that for $n = 4$, the LNO layers are completely consumed by the formation of a Disordered Interfacial Phase (DIP) whose resistivity can be deduced by analyzing the transport in the framework of a Parallel Resistor Network (PRN) model [158]. Extension of this analysis to present multilayers where the $LCMO$ thickness is 20 $u.c.$, implies that the sample with $n = 4$ will only consist of alternate layers of the DIP and 16 $u.c.$ of $LCMO$. The multilayers with $n > 4$ in our model consist of a repetitive trilayer structure with a fixed thickness of the DIP and $LCMO$, but with the LNO thickness increasing with n. We have calculated the perpendicular-to-plane resistance of the samples by adding the resistance of the DIP in a series resistor framework. Two situations have been considered; In one case the interface

is assumed to be disordered, and in the other, the *DIP* phase is not present. Using the calculated resistivities of the *DIP*, *LCMO* and *LNO* the perpendicular resistance of 1×1 mm^2 of the multilayer has been computed. Result of this calculation for $n = 8$ $u.c.$ multilayer is shown in the Fig. 7.7. The perpendicular resistance of the multilayer increases by ~ 2 orders of magnitude when the contribution of the *DIP* is taken into account. Also, the calculated perpendicular-to-plane-resistance of the disordered structure shows an upturn at the lowest temperatures. Our calculated resistance (~ 0.3 $m\Omega$) is in fair agreement with the measured zero-field resistance of ~ 3 $m\Omega$. Note that this calculation does not take into consideration the additive contributions of the spin - polarized nature of transport and scattering of carriers at the *YBCO* – superlattice interfaces.
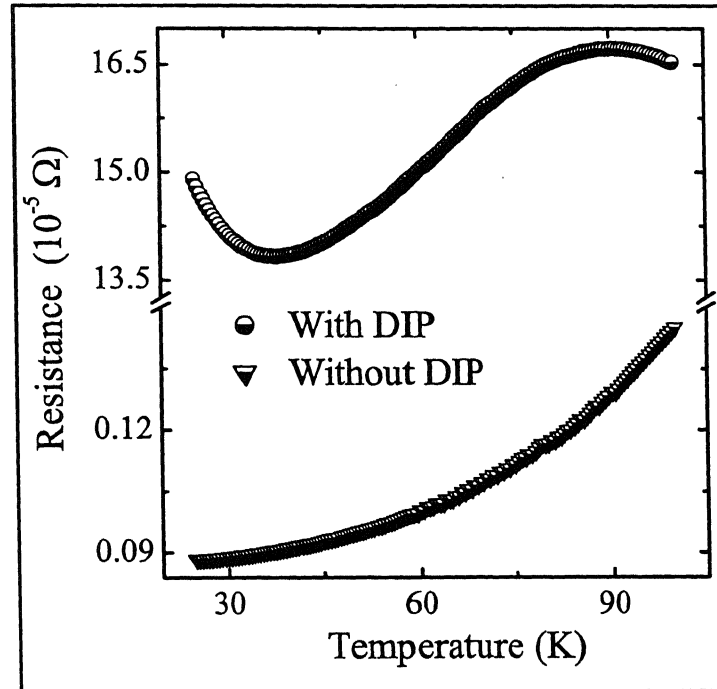
Figure 7.7: The zero-field resistance of the $n = 8$ superlattice calculated by adding the resistance of each layer in series. Two situations are considered, one with disordered interfacial phase and other without the disordered interfacial phase.

The presence of a disordered interfacial phase is also suggested by magnetiza-

of μ_B *per Mn* ion present in the superlattices. A simple counting of the Mn^{3+} and Mn^{4+} spins leads to an average Mn – site spin of *3.7* μ_B in the bulk *LCMO*. Measurements on a *1500 Å* thick *LCMO* film are close to this value. However, in multilayers of lower n, we see a small but distinct suppression of the moment. Correspondingly, there is a lowering of the Curie temperature [169]. The moment tends to recover the bulk value as the *LNO* spacer thickness increases. While such measurements of saturation moment are not available on manganite based superlattices where the spacer is a metallic oxide, a large loss ($\sim$ factor of *3*) of moment has been observed in superlattices such as $La_{0.6}Sr_{0.4}MnO_3/SrTiO_3$ [92] and $La_{0.7}Ca_{0.3}MnO_3/SrTiO_3$ [41] where the spacer is an insulator. A relatively small loss of moment observed in our case is perhaps due to the metallic character of *LNO* where itinerant electrons, particularly at larger thickness of *LNO*, can facilitate ferromagnetic ordering of localized *Mn* moments at the interfaces. The carrier - induced ferromagnetism is seen in many dilute magnetic systems. It is desirable to point out here that ultra thin films of *LCMO* [170] and *LSMO* [162] deposited on *LAO* and *STO* substrates show a considerable loss of moment and an insulating behavior with a large, non-saturating negative magnetoresistance similar to those of charge ordered manganites [57]. From this discussion it is clear that the large non-saturating magnetoresistance and the anomalous hysteresis are due to the formation of a disordered interfacial phase of a complex magnetic character.

7.4   Conclusions

In conclusion, we have measured the *CPP* resistance and magnetoresistance of *LCMO/LNO* superlattices sandwiched between *YBCO* thin film electrodes. A disordered interfacial phase has been identified which enhances the perpendicular-to-plane resistance of these periodic structures. The *DIP* is presumed to cause lowering of the magnetic moment associated with the *Mn* sites in the interfacial regions. Magnetic field dependence of magnetoresistance shows strong hysteretic effects and a non-saturating behavior in field up to *4 tesla*. Our studies highlight interface effects in magnetoresistance of superlattices made of multi-elemental oxides.

Chapter 8

Magnetoresistance and spin frustration in $(LCMO)_{20}/(ESMO)_n$ superlattices

8.1   Introduction

In this chapter we describe how the temperature and magnetic field dependence of resistivity and magnetization of magnetic - nonmagnetic perovskite manganite based superlattices change, when the non-magnetic spacer is an insulator. The magnetic layer here remains the double exchange ferromagnet $La_{0.7}Ca_{0.3}MnO_3$, while the non-magnetic layer consists of $Er_{0.7}Sr_{0.3}MnO_3$, which is a paramagnetic insulator. In the $[(20\ u.c.)\ LCMO/(n\ u.c.)\ ESMO] \times 15$ superlattices with $n \leq 5$ deposited on LAO, the qualitative behavior of resistivity is similar to that of the bulk $LCMO$. However, this behavior is suppressed as the thickness of the spacer layer increases. These samples show large negative MR at low temperature even when the applied magnetic field is small. These samples also show a large quenching of the magnetic moment as the spacer layer thickness increases. We attribute this to random freezing of the spin at the interfaces. The width over which such freezing occurs first increases with the spacer layer thickness and then saturates. The zero-field-cooled hysteresis

loop is symmetric around zero while the field-cooled hysteresis loop shifted towards the negative field. This is a signature of exchange biasing. The exchange coupling between the ferromagnetic and nonmagnetic layers increases with the increasing spacer layer thickness.

8.2 Results

8.2.1 X – ray diffraction
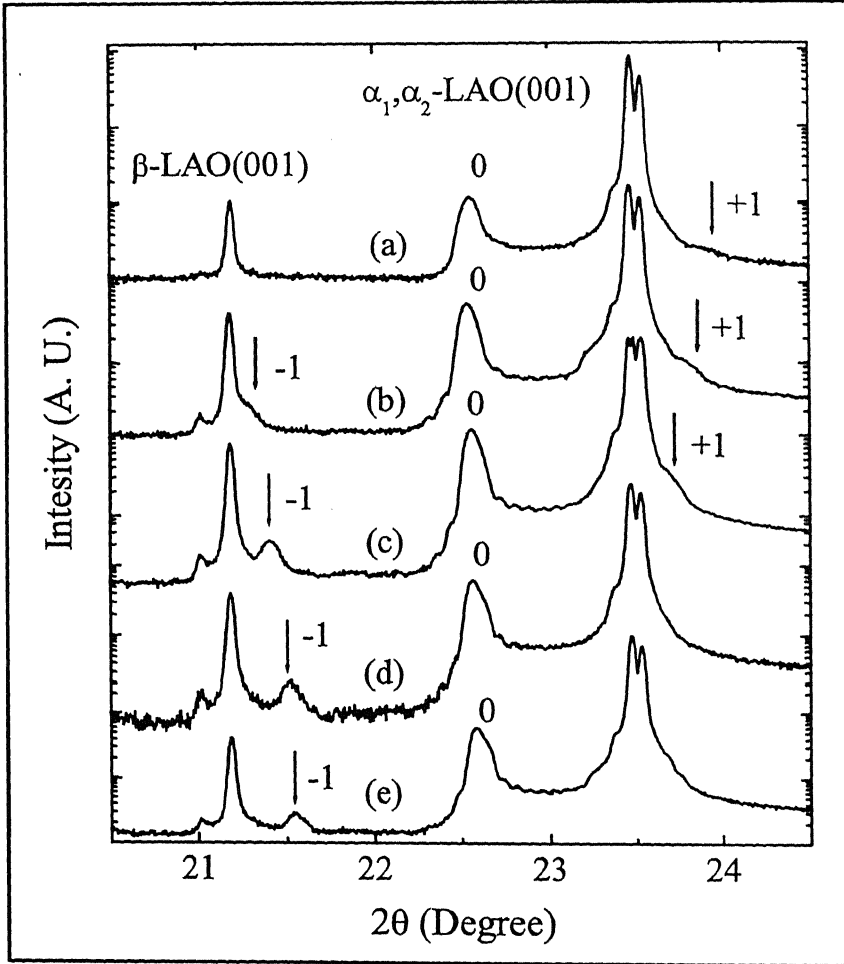
Figure 8.1: X – ray intensity profiles of superlattices with 20 $u.c.$ thick $LCMO$ and various thicknesses (6, 7, 8, 9 and 10 $u.c.$) of $ESMO$ deposited on (001) oriented LAO (curves a, b, c, d and e respectively). The fundamental (001) reflection of the film is marked as '0'. The first order satellites on either side of this reflection are marked as $+ 1$ and $- 1$. The figure also shows (001) reflection of the substrate due to $K\widehat{\alpha}$ and $K\widehat{\beta}$ excitations.

Figure *8.1* shows the X – ray diffraction profiles of five multilayer samples
with *20 u.c.* thick *LCMO* and *6, 7, 8, 9* and *10 u.c.* thick *ESMO* deposited on (001)
oriented *LAO*. The diffraction angle covered here is in the vicinity of (001) Bragg peak
of the substrate. These samples show only first order satellite peaks. One satellite
peak of the sample with *6 u.c.* spacer layer is masked by the $K\widehat{\beta}$ line of the substrate.
Similarly, one satellite peak of the samples with *9 u.c.* and *10 u.c.* spacer layer falls
on the (001) reflection of the substrate due to $K\widehat{\alpha}$. In general, the presence of satellite
peaks on either side of the fundamental (001) diffraction clearly shows the presence
of a modulated structure. The pseudocubic lattice parameter of *LAO* (*3.792 Å*) is
smaller than the lattice parameter of *LCMO* (*3.86 Å*) and *ESMO* (*3.812 Å*). Clearly,
the in-plane lattice parameter of the superlattice is under ~~expansion~~ compression. The c – axis
lattice parameter of the superlattices with various spacer layer thickness is shown in
the Fig. *8.2*. As the spacer layer thickness increases the c – axis lattice parameter
increases up to $n \leq 5$ and remain constant for $n > 5$.
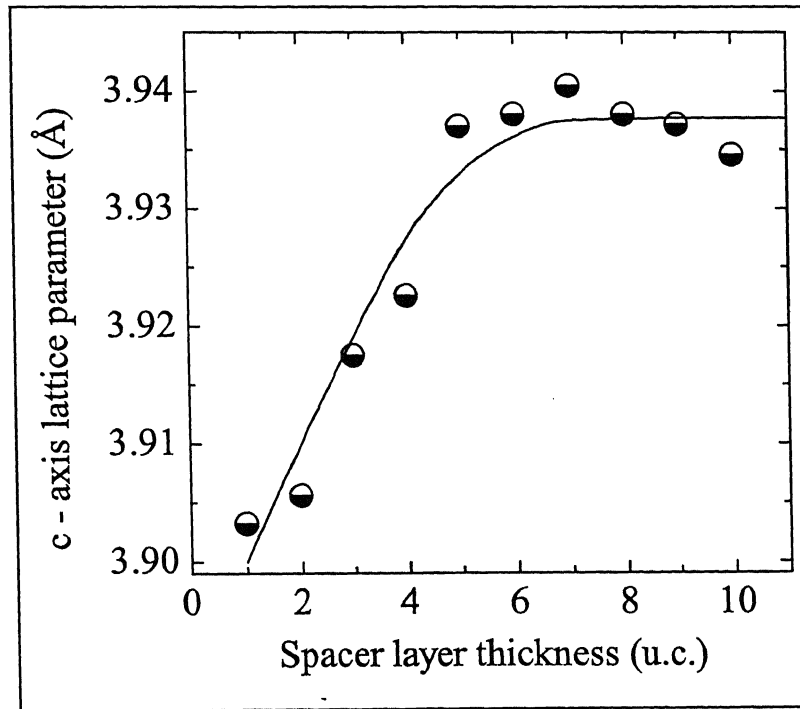
Figure 8.2: c – axis lattice parameter of the (*20 u.c.*) *LCMO*/(*n u.c.*) *ESMO*
superlattices as a function of spacer layer thickness. Sold line in the figure is a guide
to the eye.

8.2.2   Magnetization
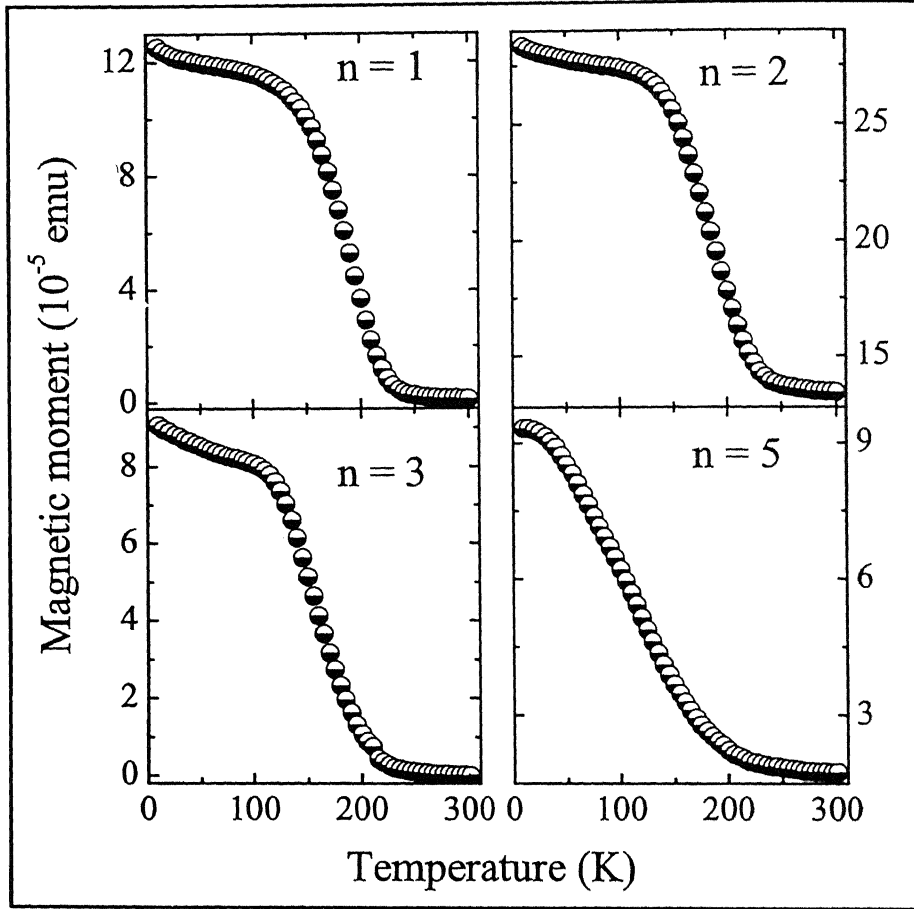
Figure 8.3: Field-cooled magnetization of *20 u.c. LCMO/n u.c. ESMO* superlattices with *n = 1, 2, 3* and *5* in *2000 Gauss* magnetic field aligned along the *(100)* direction of the film.

In Fig. *8.3* we show field-cooled magnetization curves of the samples with $n \leq 5$ measured in $\sim$ *2000 Gauss* field aligned parallel to the plane of the sample. The *FC* magnetization of the sample with *n = 1* on heating above *5 K* first drops slowly and then rapidly. However, above *220 K*, the magnetization remains constant. A qualitatively similar behavior of $M(T)$ is seen in the sample with *n = 2, 3* and *4*. The *FC* magnetization of the sample with *n = 5* in the temperature range *5 K* to *30 K* drops slowly on heating above *5 K*. At temperatures above *30 K*, the magnetization first drops rapidly and then slowly up to *300 K*. The zero-field-cooled and field-cooled magnetization curves of the sample with *n = 1* measured in $\sim$ *100 Gauss* field

aligned parallel to the plane of the sample is shown in the inset of Fig. *8.4*. The large difference in *ZFC* and *FC* magnetizations at low temperatures suggests some kind of freezing/frustration of the moments.
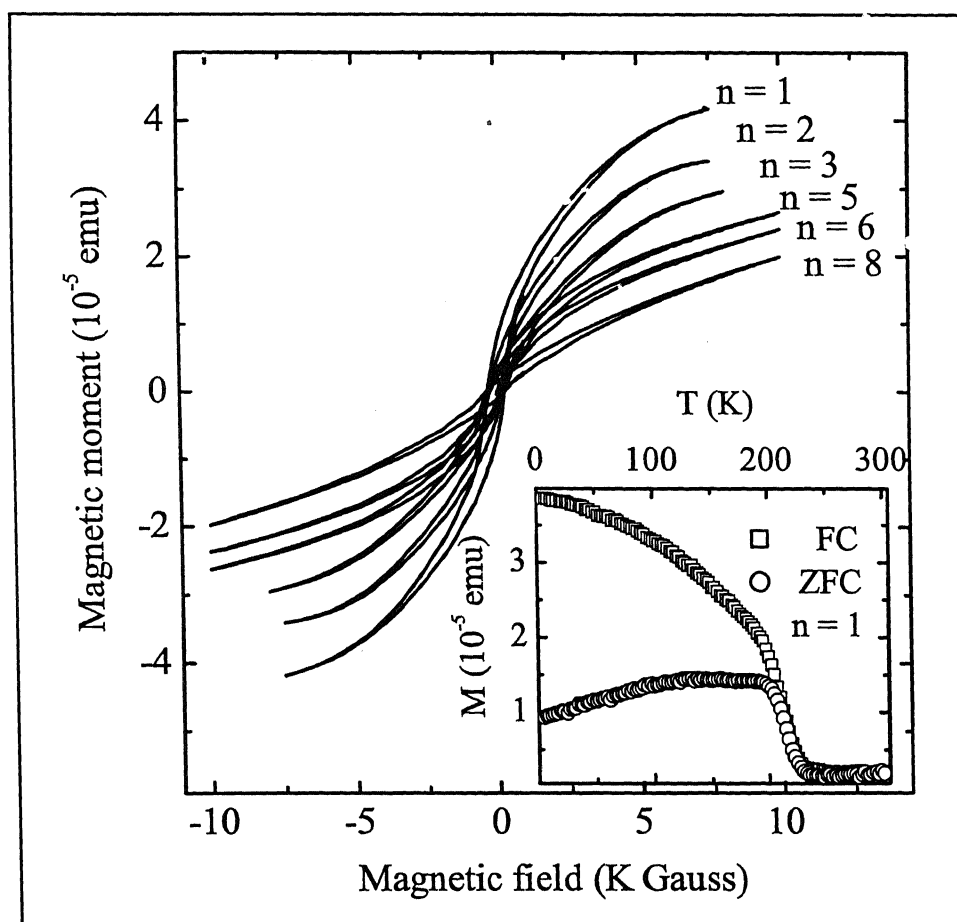
Figure 8.4: Zero-field-cooled hysteresis loops of (*20 u.c.*) *LCMO*/(*n u.c.*) *ESMO* superlattices with various spacer layer thicknesses measured at *10 K*. Inset shows temperature dependent magnetization of the superlattice with $n = 1$ measured at *100 Gauss*.

Figure *8.4* shows the *ZFC* hysteresis loops of some selected samples (with $n \leq 8$) measured at *10 K* with magnetic field aligned parallel to the sample plane. The magnetization is plotted after taking into account the weekly diamagnetic response of the substrate. The magnetization of the sample with $n = 1$ saturates above *0.7 tesla*. Similar saturation in the magnetization is observed in the *ZFC* hysteresis loops for the samples with $n \leq 4$. For the samples with $n > 4$ the magnetization does not saturate even at *1 tesla*. Parts of the *ZFC* and *FC* hysteresis loops of three samples
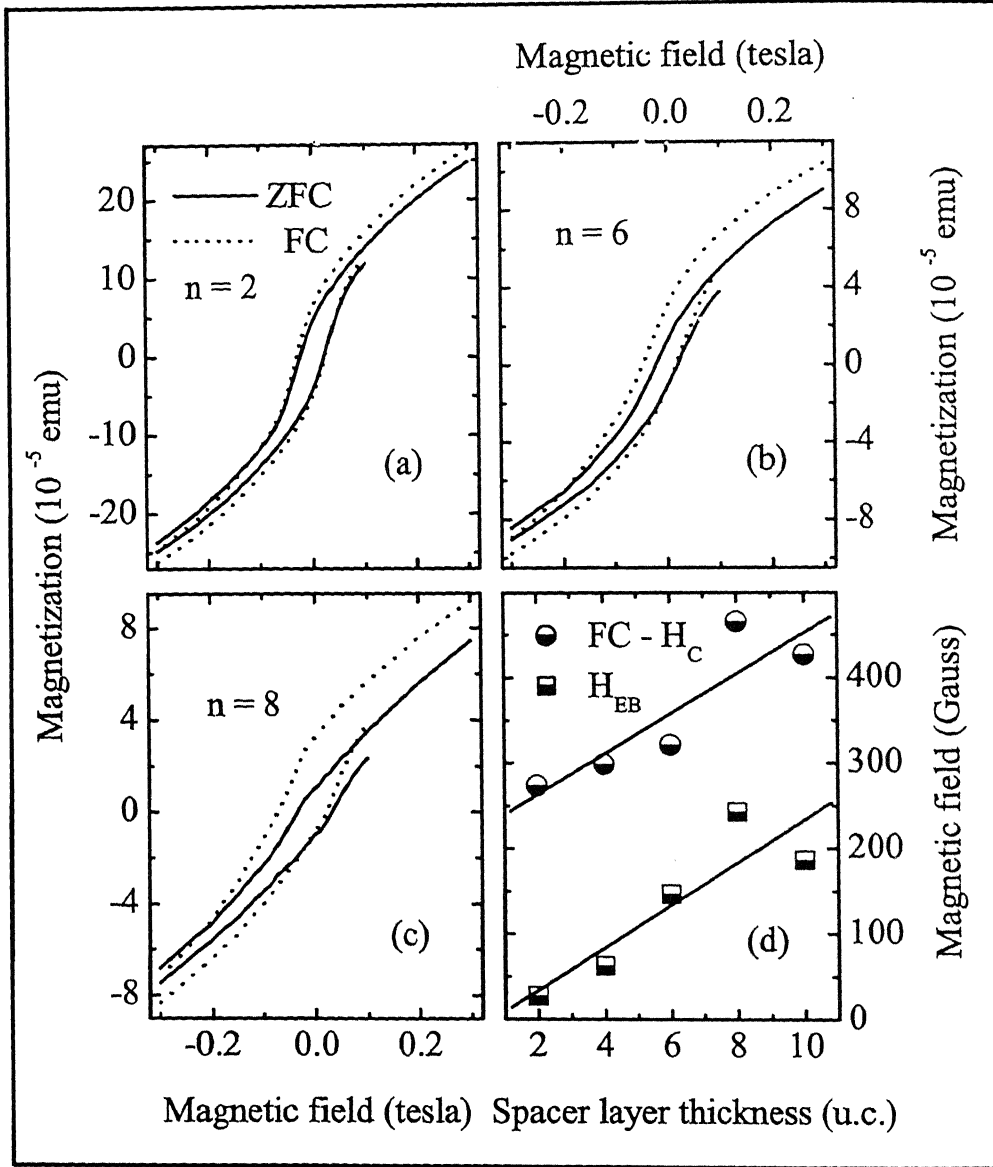
Figure 8.5: Panels (a, b and c) show zero-field-cooled and field-cooled hysteresis loops of *20 u.c. LCMO/n u.c. ESMO* superlattices with $n = 2$, *6* and *8* at *10 K*. The sample were cooled in the presence of *7000 Gauss* field aligned parallel to the film plane. The values of coercive and exchange biasing fields of the superlattices with different spacer layer thicknesses are shown in panel (d). The solid lines are guide to the eye.

with $n = 2$, 6 and 8 are shown in the panel a, b and c respectively of Fig. *8.5*. The *FC*
loops were measured after cooling the sample in *0.7 tesla* to the desired temperature.
We note that the *ZFC* hysteresis loops are symmetric around the zero-field, the *FC*
loops show a shift towards the negative field axis. This is similar to the exchange
biasing effect associated with magnetic disordered at the interfaces. The negative
coercive field H_{C1} and positive coercive field H_{C2} were extracted from the hysteresis
loops after taking into account the diamagnetic response of the substrate. The loop
shifts i.e. the exchange biasing field ($H_{EB} = - (H_{C1} + H_{C2})/2$) and the half width of
the total coercive field ($H_C = - (H_{C1} - H_{C2})/2$) are plotted in panel (d) of Fig. *8.5*
as a function of the spacer layer thickness. The exchange biasing field and coercivity
increase with the increasing spacer layer thickness.
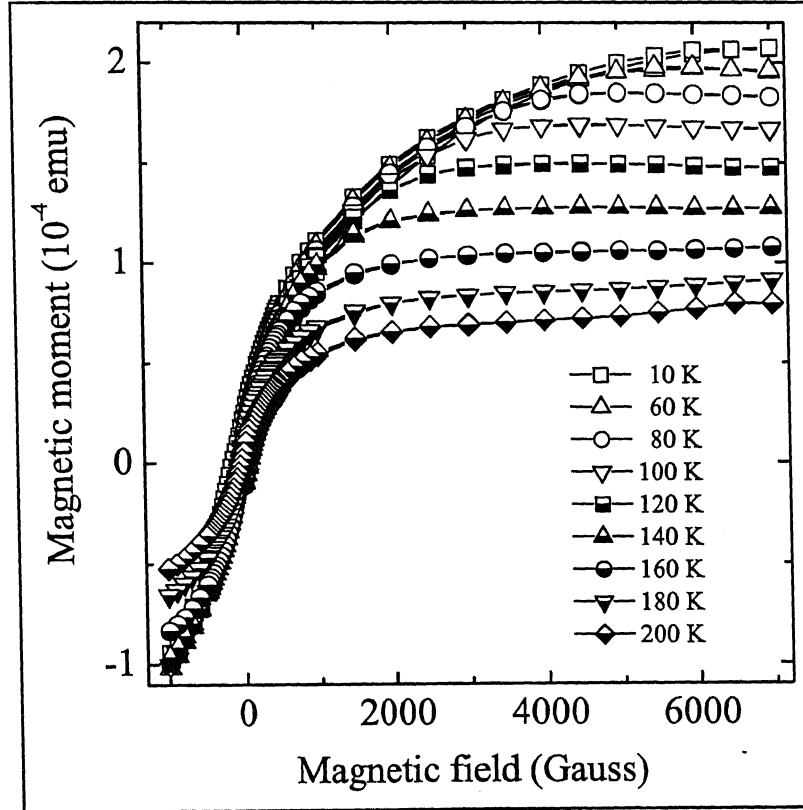
Figure 8.6: A section of zero-field-cooled hysteresis loop of the
20 u.c. LCMO/3 u.c. ESMO superlattice measured at different temperatures.

Figure *8.6* shows part of the *ZFC* hysteresis loop of the sample with $n = 3$ at various temperatures with magnetic field aligned parallel to the sample plane. The shape of the hysteresis loops indicates a lowering in magnetic moment with the increasing temperature of the sample. The H_S, H_C and M_S have been extracted form the hysteresis loops. The antiferromagnetic exchange coupling J_{AF} is directly related to saturation field (H_s) and saturation magnetization (M_S) as $4J_{AF} = H_S M_S t_{FM}$, where t_{FM} is the thickness of the magnetic layer. Since the t_{FM} is constant in the present case, the magnetic coupling between the magnetic layers is proportional to the product of H_S and M_S. The magnetic coupling and coercivity of the sample at various temperatures are shown in panel *a* and *b* respectively of the Fig. *8.7*. Magnetic coupling and coercivity drop with the increasing temperature.
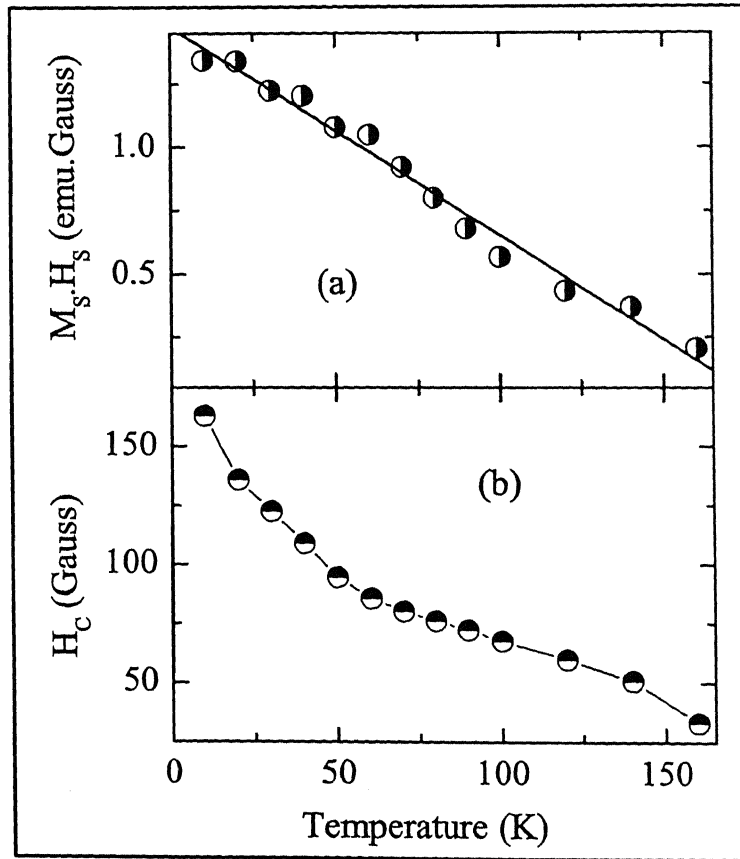
Figure 8.7: Panel (a) shows the magnetic coupling strength of the superlattice with *3 u.c.* spacer layer at different temperatures. Solid line in the figure is a guide to the eye. The coercive field of the same sample at various temperatures is shown in the lower panel (b).

8.2.3 Electrical resistivity and magnetoresistance
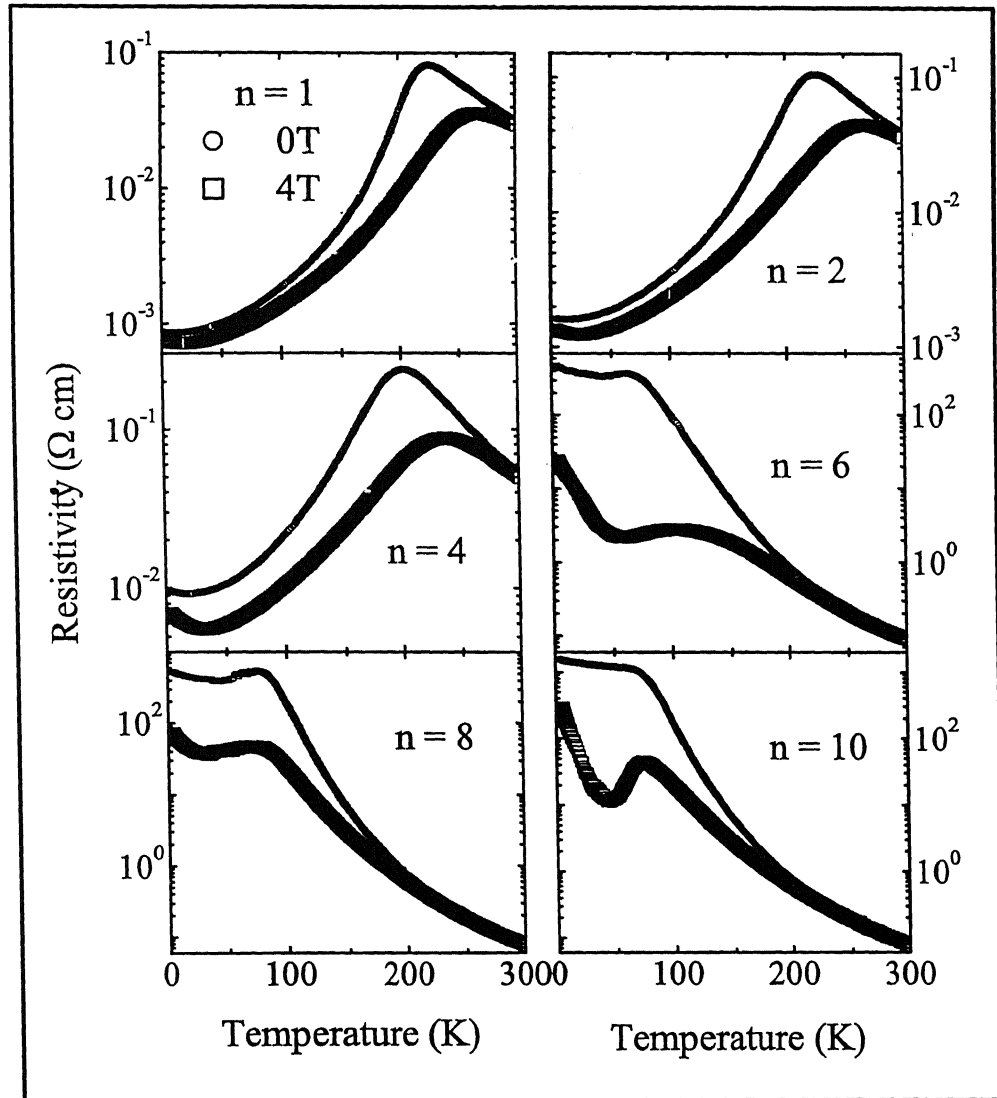
Figure 8.8: The zero-field and in-field (4 *tesla*) temperature dependent resistivity of the superlattices with 20 *u.c.* thick $LCMO$ and different thicknesses of $ESMO$ deposited on (001) oriented LAO.

The zero-field and in-field (4 *tesla*) temperature dependent resistivities for.six samples with 20 *u.c.* thick magnetic layers and different thicknesses of the spacer layer are shown in Fig. *8.8*. The zero-field resistivity of the superlattice with $n = 1$ is thermally activated on cooling below room temperature down to a temperature T_C at which it reaches a peak value. At temperatures below T_C, the resistivity is metal -

like (*positive* $d\rho/dT$) down to *4.2 K*. A qualitatively similar behavior, with a higher

resistivity and lower T_C, is seen in samples with $n = 2$ and *3*. On increasing the spacer

layer thickness to *4 u.c.*, the $\rho(T)$ is thermally activated below room temperature

down to $\sim$ *220 K*, and then becomes metal - like in the temperature window of *25 K*

to *200 K*. Below *25 K* however, resistivity is again thermally activated. A qualitatively

similar behavior with a smaller metal - like window, is seen for sample with $n = 5$. For

the sample with $n = 6$, the resistivity is thermally activated below room temperature

down to $\sim$ *70 K*. Below *70 K* the sample shows metallic behavior down to $\sim$ *40 K*

and then becomes thermally activated. The zero-field resistivity of the samples with

$n = 7$, *8* and *9* is quite similar to that of the sample with $n = 6$. The $\rho(T)$ of the

sample with $n = 10$ on the other hand, remains thermally activated over the entire

temperature range.
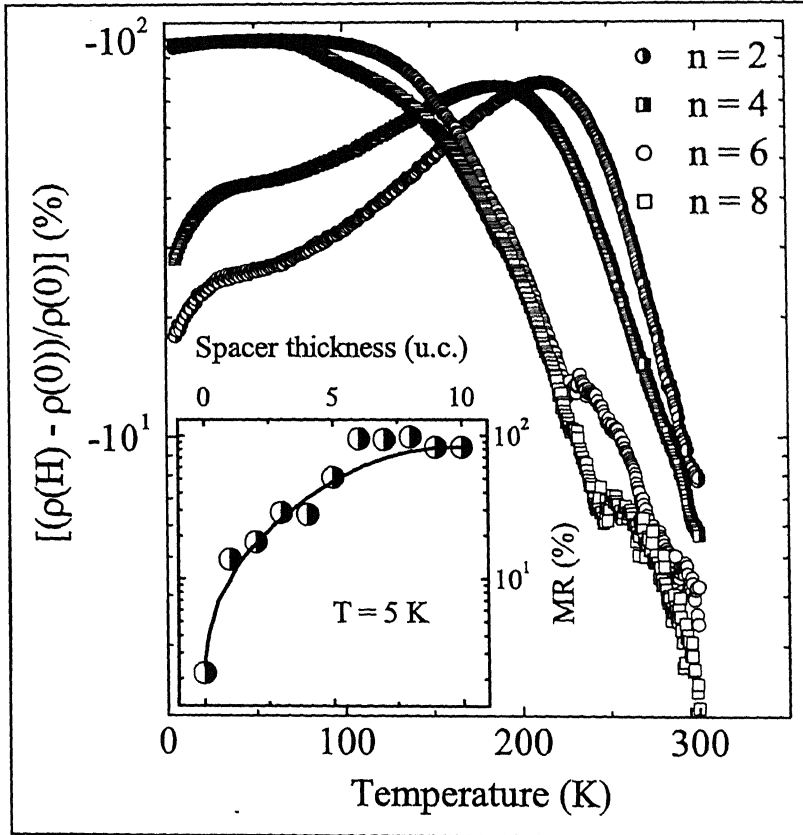
Figure 8.9: Magnetoresistance at *4 tesla* of (*20 u.c.*) *LCMO*/(*n u.c.*) *ESMO* superlattices deposited on (*001*) *LAO*. Inset shows the *MR* at *5 K* as a function of the spacer layer thickness.

The presence of *4 tesla* field affects the $\rho(T)$ of $n = 1$ to *9* samples in three distinct ways. There are (*i*) increase of T_C, (*ii*) increase in the width of the metallic region and (*iii*) large magnetoresistance in the vicinity of the T_C. The resistivity of the sample with $n = 10$ undergoes a remarkable change on application of the field. The $\rho(T)$ curve now develops the metal - like feature over a narrow range of temperature *45 K* to *75 K*.
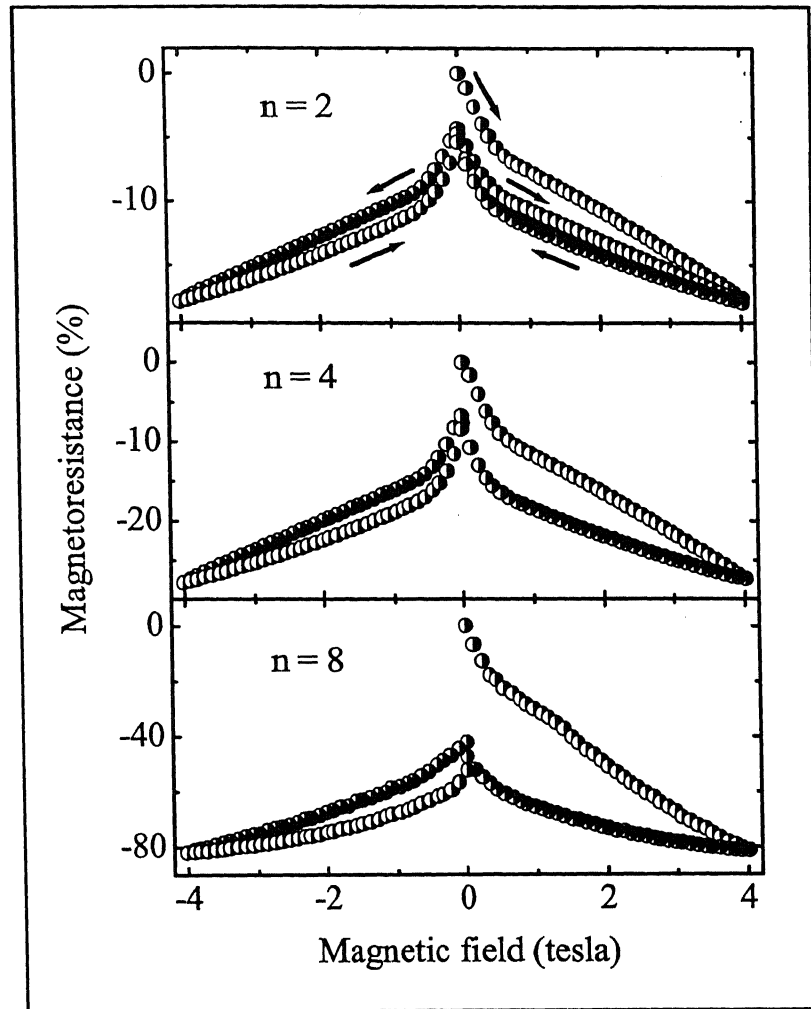
Figure 8.10: Magnetic field dependence of magnetoresistance at *5 K* for superlattices with *20 u.c.* thick *LCMO* and *2, 4* and *8 u.c.* thick *ESMO*. Data for a complete cycle between + *4 tesla* and − *4 tesla* are shown. A field increasing part of the second cycle for the superlattice with *2 u.c.* spacer is also shown. The direction of the magnetic field scan is marked by arrows.

The qualitative behavior of the magnetoresistance of the superlattices with $n \geq 6$ is quite similar to that of the superlattice with $n = 6$. The magnetoresistance of various samples at $5\ K$ is shown in the inset of Fig. 8.9.

The magnetic field dependence of magnetoresistance at $5\ K$ of the superlattices with $n = 2$, 4 and 8 deposited on LAC is shown in the Fig. 8.10. The figure includes the MR data as the magnetic field is scanned between $+ 4\ tesla$ to $- 4\ tesla$. For the superlattice with $n = 2$, we also show the field increasing branch of MR during the second field sweep. The MR during the second sweep cycle does not trace the path taken during the first sweep. As the magnetic field increases, the MR raises rapidly up to a characteristic field (H_S^*). Above H_S^*, the magnetoresistance shows a gradual increase with field and does not saturate even at $4\ tesla$. The change in MR with field is symmetric for $+\ ve$ and $-\ ve$ field sweeps. The magnetoresistance of these samples at $50\ K$ with the similar variation of the magnetic field is shown in the Fig. 8.11. The MR is symmetric and reversible in both the cases.

8.3 Discussion

The $c - axis$ lattice parameter of the superlattice with $n = 1$ is $\sim 3.903\ \mathring{A}$. When compared with the lattice parameter of the substrate and the constituents $LCMO$ and $ESMO$ separately, this shows presence of strain and lattice distortion at the interfaces. A $1\ u.c.$ thick spacer layer of paramagnetic $ESMO$ drastically changes the magnetic properties of $LCMO$ in the superlattice. The Curie temperature and saturation magnetization of the superlattice with $n = 1$ are $224\ K$ and $2.23\ \mu_B$ respectively. In pure $LCMO$ films these are $\sim 247\ K$ and $3.64\ \mu_B$ respectively. This large drop in T_C and M_S of $LCMO$ in the superlattice with $n = 1$ clearly suggests the presence canted or frustrated spins in the vicinity of the interfaces. To identify the effect of spacer layer in Fig. 8.12 we show the variation of T_C, M_S and M_r as a function of spacer layer thickness. The transition temperatures of various superlattices extracted from $\rho(T)$ and $M(T)$ and saturation magnetization extracted from $M(H)$ loops are shown in the panel a and b respectively of Fig. 8.12. Transition temperature decreases linearly with the increasing spacer layer thickness while M_S shows a drop followed by saturation at the higher spacer layer thickness. The M_r extracted from

$M(H)$ loops is shown in the panel (c) in Fig. 8.12. The behavior of M_r is same as that of M_S. The initial decrease in M_S and M_r with the spacer layer thickness suggest an increase in the length of canted spin region in the $LCMO$ layers. The variation of this region in the $LCMO$ layers for various samples is shown in the Fig. 8.13. The region of spin disordered/canting increases with the increasing spacer layer thickness and then saturates. We attribute this spin disorder to deformation of MnO_6 octahedra due to the presence of A – site ions with different size. The disordered spin region seems to posses both structural and magnetic disorder.
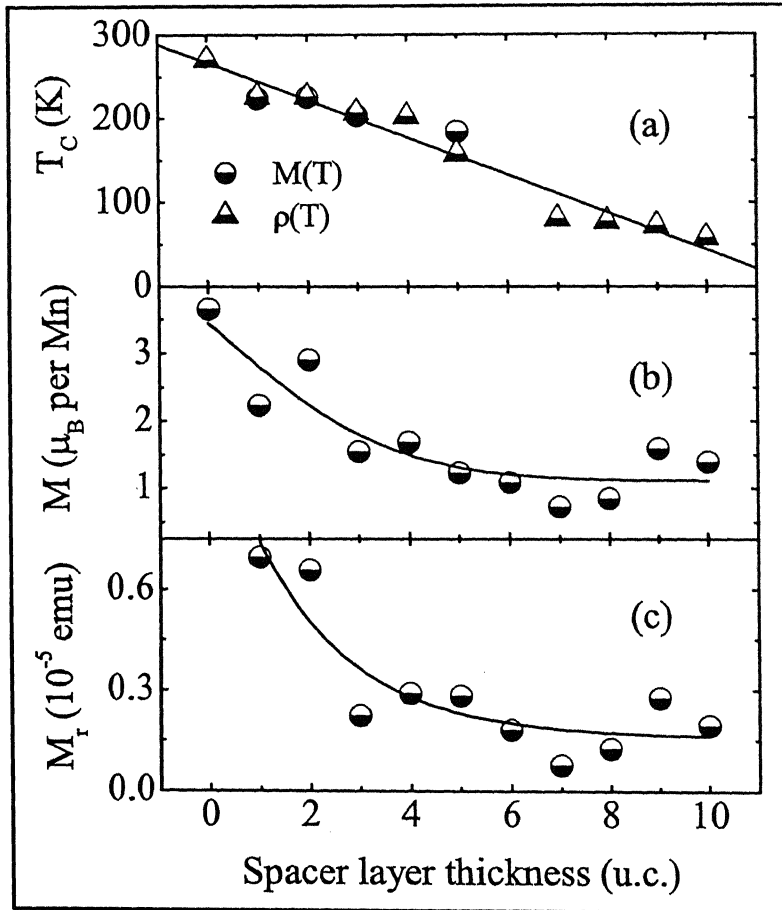
Figure 8.12: Panel (a) shows the transition temperature T_C of the superlattices as function of the spacer layer thickness, the T_C was deduced from resistivity and magnetization measurements. Magnetic moment of the superlattices at 7000 $Gauss$ and 10 K is shown in panel (b) for different spacer layer thicknesses. Remnant moment of superlattices is shown in the lower panel (c). Sold lines in panels a, b and c are guide to the eye.
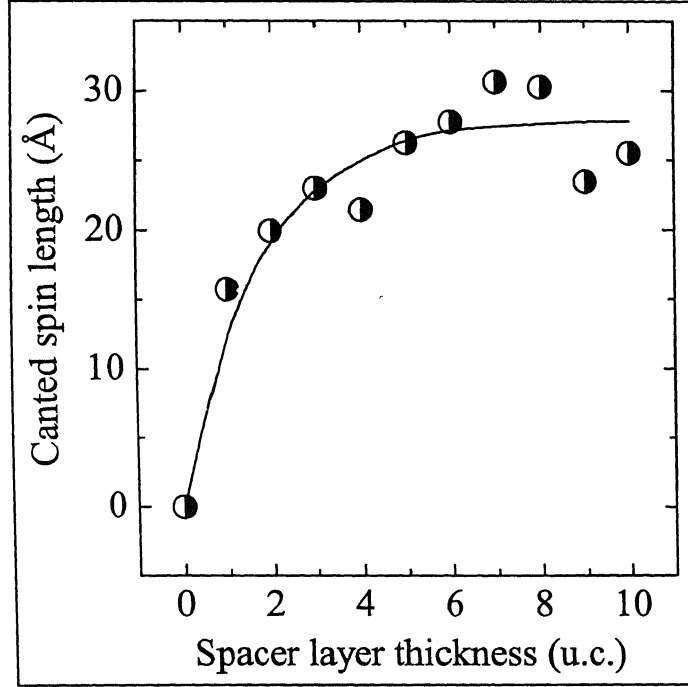
Figure 8.13: Thickness of *LCMO* from the interface over which a significant spin disorder exits is plotted as a function of *n*.

We have observed exchange biasing in the superlattice consisting of ferromagnetic *LCMO* and paramagnetic *ESMO*. The coercivity and high - field magnetization in field-cooled $M(H)$ are larger as compared to the values in the $ZFC - M(H)$ for these samples. The $FC - M(H)$ measurements were performed by cooling the sample down to *10 K* in *0.7 tesla* (the saturation field of *LCMO* is *0.6 tesla*). The interfacial region with structural and magnetic disorder seems to be responsible for the displacement of field-cooled $M(H)$ loop center towards the negative field as seen in the Fig. *8.5*. The magnitude of this shift is equal to the effective field associated with the interlayer exchange coupling. The exchange coupling between the ferromagnetic and antiferromagnetic layers is defined as $J = H_{EB} M_{FM} t_{FM}$, where M_{FM} and t_{FM} are the saturation magnetization and the thickness of the ferromagnetic layer respectively. Since the spins of Mn^{3+} and Mn^{4+} ions in *LCMO* layers in the interface region are frozen, t_{FM} is the effective *LCMO* thickness in which spins are ordered. Using saturation magnetization of a *500 u.c.* thick *LCMO* film and extracted values of H_{EB} and

t_{FM} from the ZFC and FC hysteresis loops we have calculated the value of exchange coupling at the interfaces. The exchange coupling increases monotonically with the spacer layer thickness. Kiwi et al. [171] have proposed the so called frozen interface model for exchange coupling in ferromagnetic - antiferromagnetic magnetic structures. The frozen interfaces possess canted magnetic configurations. Christides et al. [172] have used this model to describe the exchange coupling in superlattices consisting of ferromagnetic $La_{0.66}Ca_{0.33}MnO_3$ and antiferromagnetic $La_{1/3}Ca_{2/3}MnO_3$.

The qualitative behavior of $\rho(T)$ for the superlattices with $n \leq 5$ is similar to that of a thick epitaxial film of $LCMO$, but for a higher resistivity and lower T_C. Below T_C, the transport in the metal - like region can be explained on the basis of the double exchange model by taking into account of the presence of a spin disorder [66]. As the spacer layer thickness increase, the size of the spin disordered region in the $LCMO$ increases leading to the suppression of double exchange transport. The $\rho(T)$ of the samples with $n = 6$ to 10 shows thermally activated behavior down to ~ 100 K. Lu et al. [97] have attributed the reduced T_C and high resistivity of the $La_{2/3}Ba_{1/3}MnO_3/SrTiO_3$ superlattices to the strong biaxial distortion due to lattice mismatch between the constituents. We attribute the increase in the resistivity and lower T_C of these samples to spin and lattice disorders at the interfaces.

The presence of an external magnetic field modifies the magnetic state of the superlattices and hence their transport behavior. The dependence of magnetoresistance on temperature and magnetic field show several interesting features such as; (i) significantly large magnetoresistance below the Curie temperature, (ii) a sharp increase in magnetoresistance at low temperature (< 30 K), (iii) an enhanced low field magnetoresistance, (iv) high remanence MR in samples with thicker spacers, and (v), hysteretic behavior at $T \leq 50$ K. A large MR at low temperatures is also observed in the superlattices where the magnetic layers consisting $La_{2/3}Ba_{1/3}MnO_3$ [43, 97], $La_{0.6}Sr_{0.4}MnO_3$ [92] and $La_{0.7}Ca_{0.3}MnO_3$ [41, 43] and nonmagnetic layer $SrTiO_3$. Izumi et al. [92] suggested that this behavior could be due to spin canting at the interfaces. We believe that the processes such as pinning of the t_{2g} spins at the interfaces, localization of carriers in the spacer layers, and the tunneling of spin - polarized carriers through the spacer layer will also contribute to MR in these systems.

8.4 Conclusions

We have measured electrical and magnetic behaviors of $La_{0.7}Ca_{0.3}MnO_3/Er_{0.7}Sr_{0.3}MnO_3$ superlattices. The magnetoresistance at the lowest temperatures ($T < 150\ K$) rises with the increase in spacer layer thickness, and approaches $\sim 100\ \%$ in the sample with $10\ u.c.$ thick spacer layer. The magnetoresistance at $T < 50\ K$ also shows a steep increase up to a critical field H_S^*, which shifts to the higher values with the increasing spacer layer thickness. These samples also show a giant loss of magnetic moment *per Mn* site in $La_{0.7}Ca_{0.3}MnO_3$ as the spacer layer thickness is increased. This phenomenon strongly suggests spin frustration at the interfaces. The *ZFC* hysteresis loop in these samples is symmetric around the zero-field and *FC* hysteresis loop shifted towards negative fields. This is also indicative of a significant disorder of the magnetic origin at the interfaces.

Chapter 9

Conclusions and scope for further research
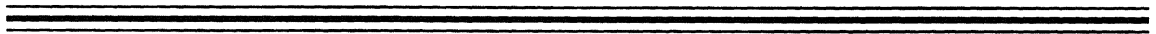
This chapter presents a summary of the main results of this thesis. We have successfully used pulse laser deposition method to synthesize thin films on superlattices of some doped transition metal oxides. The electrical resistivity, magnetoresistance and magnetic properties of the superlattices have been measured. These studies have facilitated understating of interlayer exchange coupling, colossal magnetoresistance in oxide - based superlattices. The chapter ends with identification of some interesting issues for further research.

9.1   Fabrication of thin films and superlattices

Pulsed laser deposition is a powerful method for deposition of thin films and multilayers of multielemental oxides. Using this technique we have synthesized several thin films and superlattices of hole - doped manganites and $LaNiO_3$. We have optimized film properties against variations in deposition parameters such as areal energy density, laser repetition rate, target to substrate distance, substrate temperature and ambient pressure.

The resistivity of these films varies by several orders of magnitudes on changing temperature, composition and magnetic field. We have used both constant voltage as well as constant current methods to measure resistivity. The magnetoresistance has been measured in both current-in-plane and current-perpendicular-to-plane geometries. High T_C thin films were used for CPP measurement. The magnetic behavior of the sample was measured using a $SQUID$ – magnetometer.

9.2   Single layer films of magnetic and
non-magnetic character

The properties of thin films are influenced by the nature of the substrate, which largely controls growth morphology, defect structure and level of stress. However, stress in thin films is gradually relieved with the increase of film thickness. The resistivity of bulk samples changes dramatically when they are prepared in the form of epitaxial film. In the case of $LCMO$ deposited on LAO, the resistivity at small thickness is thermally activated down to the lowest temperature. The hysteretic and history dependent insulating behavior seen in the ferromagnetic state of these films suggests coexistence of ferromagnetic metal - like and non-magnetic insulator - like regions.

In the ultra thin films of LNO deposited on LAO with STO or $LCMO$ buffer layer, the resistivity is mostly metal - like but for an upturn at the lowest temperature. The resistivity of $Er_{0.7}Sr_{0.3}MnO_3$ films is thermally activated over the entire temperature range of $4.2\ K$ to $300\ K$. The magnetoresistance of $LCMO$ films increases

as the film thickness decreases. While the magnetoresistance of *LNO* and *ESMO* is negligible even at *4 tesla* magnetic field.

9.3   Colossal magnetoresistance in LCMO/LNO superlattices

Series of superlattices consisting of *LCMO* and *LNO* have been synthesized. *X* − ray diffraction studies reveal the presence of epitaxy and structural modulation. The angular separation between first order satellite peaks becomes wider as the spacer layer thickness decreases. The variation of *c* − axis lattice parameter of the superlattices with the spacer layer thickness suggests the presence of substrate induced stress. The level of stress depends on whether the film is deposited on $SrTiO_3$ or $LaAlO_3$.

In the case of the superlattices with *10 u.c.* thick *LCMO* layer, the temperature dependent resistivity shows insulator-to-metal-like behavior as the spacer layer thickness increases from *2 u.c.* to *10 u.c.*. We attributed the insulating behavior to the presence of a disordered interfacial phase at *LCMO* − *LNO* interfaces. A parallel resistor model where in the resistance of the disordered interfacial region is considered explicitly, reproduces the broad features of the $\rho(T)$ curve. Our structural and magnetization studies indicate that the disordered *Phase -* at the interface is of magnetic as well as structural origin. We attribute the disordered interfacial region to lattice-mismatch-related strain and truncation of the *3D* − coordination of the magnetic ions.

The insulating sample show enhanced low-field and low-temperature negative *MR*. The magnetoresistance is hysteretic in magnetic field below ∼ *20 K*, and shows weak magnetorelaxor-type behavior.

The saturation field and remnant magnetization show antiferromagnetic interlayer coupling for *n* ≤ *2*, followed by an overdamped oscillatory behavior with a period of ≈ *4 u.c.* with the increasing *n*. A lower value of saturation magnetization of the superlattices with *n* ≤ *5* indicates the presence of spin frustration at the *LCMO* − *LNO* interfaces. All samples show negative magnetoresistance, the effect is

particularly large in samples where the magnetic coupling is antiferromagntic.

The resistance perpendicular-to-plane of the superlattices sandwiched between two thin film $YBCO$ electrodes is measured. The saturation moments and modeling of the perpendicular-to-plane resistance suggest disorder at the ferromagnetic – non-magnetic layer interfaces dominates the MR.

9.4   Magnetoresistance of LCMO – ESMO superlattices

The study of epitaxy and structural modulation in superlattice consisting of $La_{0.7}Ca_{0.3}MnO_3$ and $Er_{0.7}Sr_{0.3}MnO_3$ were performed by using X - diffraction. The c − axis lattice parameter of the superlattices first increases and then saturates as the spacer layer thickness is increased from 1 $u.c.$ to 10 $u.c.$.

The sharp metal-insulator transition seen at the Curie temperature in $LCMO$ films is suppressed in these superlattices as the $ESMO$ spacer layer thickness increases above 1 $u.c.$. The magnetoresistance at low temperature ($T < 150$ K) is significantly large and approaches ~ 100 $\%$ in samples with $n > 8$. The magnetoresistance at $T < 50$ K is also hysteretic and shows a steep increase up to a critical field H_s^*, which shifts to the higher values with the increasing $ESMO$ thickness. At $T \sim 10$ K, these samples also show a weak magnetorelaxor-type behavior.

These samples also show a giant loss of magnetic moment per Mn site in $LCMO$ as the spacer layer thickness is increased. This phenomenon strongly suggests spin frustration at the interfaces of ferromagnetic $LCMO$ and non-magnetic $ESMO$.

9.5   Scope for further research

1. Electron transport in ultra thin films of $LCMO$ is non-linear at low temperature and high electric field. A similar behavior is expected in the superlattices with 10 $u.c.$ $LCMO/n$ $u.c.$ LNO. Careful measurements of non-liner effect need to be carried out in these systems as well. Measurements of frequency dependent conductivity will also be useful in this context.

2. Alternative measurements of oscillatory exchange coupling in the superlattices are desired. Experiments such as Brillouin light scattering and Kerr effect measurements will be useful.

3. The nature of disordered interfacial phase needs to be probed through high resolution cross-sectional electron microscopy in conjunction with electron energy loss spectroscopy. Similarly, using specular and diffuse X – ray scattering, the interface morphology can be extracted and then related to the electron transport. The in-plane lattice structure of these samples can be studied using grazing angle diffraction and reflectivity. The satellite peaks can be verified using structural modeling.

4. The *GMR* in *3d* - transition metal based superlattices has been studied as a function of interface roughness, and interface alloying with magnetic and non-magnetic impurities. Similar studies on oxide - based multilayers are also desired.

References

[1] P. Grunberg, R. Schreiber, Y. Pang, M. B. Brodsky, and H. Sowers, *Phys. Rev. Lett. 57, 2442 (1986)*.

[2] M. B. Salamon, Shantanu Sinha, J. J. Rhyne, J. E. Cunningham, Ross W. Erwin, Julie Borchers, and C. P. Flynn, *Phys. Rev. Lett. 56, 259 (1986)*.

[3] C. F. Majkrzak, J. W. Cable, J. Kwo, M. Hong, D. B. McWhan, Y. Yafet, J. V. Waszczak, and C. Vettier, *Phys. Rev. Lett. 56, 2700 (1986)*.

[4] S. S. P. Parkin, N. More, and K. P. Roche, *Phys. Rev. Lett. 64, 2304 (1990)*.

[5] D. M. Edwards, J. Mathon, R. B. Muniz, and M. S. Phan, *Phys. Rev. Lett. 67, 493 (1991)*.

[6] P. Bruno, and C. Chappert, *Phys. Rev. B 46, 261 (1992)*.

[7] J. Barnas, *J. Magn. Magn. Mat. 111, L215 (1992)*.

[8] J Mathon, M Villeret, and D M Edwards, *J. Phys. Condens. Mat. 4, 9873 (1992)*.

[9] Y. Wang, P. M. Levy, and J. L. Fry, *Phys. Rev. Lett. 65, 2732 (1990)*.

[10] P. Bruno, *J. Magn. Magn. Mat. 116, L13 (1992)*.

[11] M. A. Ruderman, and C. Kittel, *Phys. Rev. 96, 99 (1954)*.

[12] T. Kasuya, *Progr. Theoret. Phys. (Japan) 16, 45 (1956)*; K. Yosida, *Phys. Rev. 106, 893 (1957)*.

[13] P. Bruno, *Phys. Rev. B 52, 411 (1995)*.

[14] P. Bruno, and C. Chappert, *Phys. Rev. Lett. 67, 1602 (1991)*; P. M. Levy, S. Maekawa, and P. Bruno, *Phys. Rev. B 58, 5588 (1998)*.

[15] Y. Yafet, *J. Appl. Phys. 61, 4058 (1987)*.

[16] M. A. M. Gijs, S. K. J. Lenczowski, and J. B. Giesbers, *Phys. Rev. Lett. 70, 3343 (1993)*.

[17] W. P. Pratt Jr., S.-F. Lee, J. M. Slaughter, R. Loloee, P. A. Schroeder, and J. Bass, *Phys. Rev. Lett. 66, 3060 (1991)*; S. F. Lee, W. P. Pratt, Jr., R. Loloee, P. A. Schroeder, and J. Bass, *Phys. Rev. B 46, 548 (1992)*.

[18] T. Valet, and A. Fert, *Phys. Rev. B 48, 7099 (1993)*.

[19] A. Fert, J. Duvail, and T. Valet, *Phys. Rev. B 52, 6513 (1995)*.

[20] N. F. Mott, *Adv. Phys. 13, 325 (1964)*.

[21] K. Fuchs, *Proc. Camb. Philos. Soc. 34, 100 (1938)*.

[22] E. H. Sondheimer, *Adv. Phys. 1, 1 (1952)*.

[23] R. F. Carcia, and A. Suna, *J. Appl. Phys. 54, 2000 (1983)*.

[24] R. E. Camley, and J. Barnas, *Phys. Rev. Lett. 63, 664 (1989)*; J. Barnas, A. Fuss, R. E. Camley, P. Grunberg, and W. Zinn, *Phys. Rev. B 42, 8110 (1990)*.

[25] P. M. Levy, S. Zhang, and A. Fert, *Phys. Rev. Lett. 65, 1643 (1990)*.

[26] L. Xing, and Y. C. Chang, *Phys. Rev. B 48, 4156 (1993)*; L. Xing, Y. C. Chang, M. B. Salamon, D. M. Frenkel, and J. Shi, *Phys. Rev. B 48, 6728 (1993)*.

[27] Mark Johnson, *Phys. Rev. Lett. 67, 3594 (1991)*.

[28] J. Barnas, and A. Fert, *Phys. Rev. B 49, 12835 (1994)*.

[29] S. Zhang, and P. M. Levy, *J. Appl. Phys. 69, 4786 (1991)*.

[30] M. N. Baibich, J. M. Broto, A. Fert, F. Nguyen Van Dau, F. Petroff, P. Etienne, G. Creuzet, A. Friederich, and J. Chazelas, *Phys. Rev. Lett. 61, 2472 (1988)*.

[31] H. Itoh, J. Inoue, and S. Maekawa, *Phys. Rev. B 51, 342 (1995)*.

[32] S. S. P. Parkin, *Phys. Rev. Lett. 71, 1641 (1993)*.

[33] P. Baumgart, Bruce A. Gurney, Dennis R. Wilhoit. Thao Nguyen, Bernard Dieny, and Virgil S. Speriosu, *J. Appl. Phys. 69, 4792 (1991)*.

[34] E. E. Fullerton, D. M. Kelly, J. Guimpel, I. K. Schuller, and Y. Bruynseraede, *Phys. Rev. Lett. 68, 859 (1992)*; J. M. Colino, I. K. Schuller, V. Korenivski, and K. V. Rao, *Phys. Rev. B 54, 13030 (1996)*; M. Velez, and I. K. Schuller, *J. Magn. Mater. 184, 275 (1998)*; J. Santamaria, M. – E. Gomez, M. – C. Cyrile, C. Leighton, Kannan M. Krishnan, and I. K. Schuller, *Phys. Rev. B 65, 012412 (2001)*.

[35] P. Belien, R. Schad, C. D. Potter, G. Verbanck, V. V. Moshchalkov, and Y. Bruynseraede, *Phys. Rev. B 50, 9957 (1994)*.

[36] G. Q. Gong, A. Gupta, Gang Xiao, P. Lecoeur, and T. R. McGuire, *Phys. Rev. B 54, 3742 (1996)*.

[37] A. Orozco, S. B. Ogale, Y. H. Li, P. Fournier, Erch Li, H. Asano, V. Smolyaninova, R. L. Green, R. P. Sharma, R. Ramesh, and T. Venkatesan, *Phys. Rev. Lett. 83, 1680 (1999)*.

[38] K. R. Nikolaev, A. Yu. Dobin, I. N. Krivorotov, W. K. Cooly, A. Bhattacharya, A. L. Kobrinskii, L. I. Glazman, R. M. Wentzovitch, E. Dan Dahlberg, and A. M. Goldman, *Phys. Rev. Lett. 85, 3728 (2000)*; K. R. Nikolaev, A. Bhattacharya, P. A. Kraus, V. A. Vas'ko, W. K. Cooley, and A. M. Goldman, *Appl. Phys. Lett. 75, 118 (1999)*.

[39] G. Jakob, V. V. Moshchalkov, and Y. Bruynseraede, *Appl. Phys. Lett. 66, 2564 (1995)*.

[40] I. Panagiotopoulos, C. Christides, M. Pissas, and D. Niarchos, *Phys. Rev. B 60, 485 (1999)*.

[41] Moon-Ho Jo, Neil D. Mathur, Jan E. Evetts, Mark G. Blamire, Manuel Bibes, and Josep Fontcuberta, *Appl. Phys. Lett. 75, 3689 (1999)*.

[42] M. Izumi, Y. Murakami, Y. Konishi, T. Manako, M. Kawasaki, and Y. Tokura, *Phys. Rev. B 60, 1211 (1999)*.

[43] C. Kwon, K. - C. Kim, M. C. Robson, J. Y. Gu, M. Rajeswari, T. Venkatesan, and R. Ramesh, *J. Appl. Phys. 81, 4950 (1997)*.

[44] H. Li, J. R. Sun, and H. K. Wong, *Appl. Phys. Lett. 80, 628 (2002)*.

[45] R. von Helmolt, J. Wecker, B. Holzapfel, L. Schultz, and K. Samwer, *Phys. Rev. Lett. 71, 2331 (1993)*.

[46] J. B. Goodenough, N. F. Mott, M. Pouchard, G. Demazeau, P. Hagenmüller, *Mat. Res. Bull. 8, 647 (1973)*.

[47] A. Venimadhav, M. S. Hegde, R. Rawat, I. Das, P. L. Paulose, and E. V. Sampathkumaran, *Phys. Rev. B 63, 214404 (2001)*.

[48] *Ultrathin Magnetic Structures II*, edited by B. Heinrich, and J. A. C. Bland (Springer – Verlag, Berlin, *1994*).

[49] G. H. Jonker, and J. H. Van Santen, *Physica 16, 337 (1950)*; J. H. Van Santen, and G. H. Jonker, *Physica 16, 599 (1950)*.

[50] E. O. Wollan, and W. C. Koehler, *Phys. Rev. 100, 545 (1955)*.

[51] C. Zener, *Phys. Rev. 82, 403 (1951)*.

[52] A. J. Millis, *Nature 392, 147 (1998)*.

[53] J. M. De Teresa, M. R. Ibarra, P. A. Algarabel, C. Ritter, C. Marquina, J. Blasco, J. Garcia, A. del Moral, and Z. Arnold, *Nature 386, 256 (1997)*.

[54] J. W. Lynn, R. W. Erwin, J. A. Borchers, Q. Huang, A. Santoro, J. L. Peng, and Z. Y. Li, *Phys. Rev. Lett. 76, 4046 (1996)*.

[55] C. J. Booth, F. Bridges, G. H. Kwei, J. M. Lawrence, A. L. Cornelius, and J. J. Neumeier, *Phys. Rev. Lett. 80, 853 (1998)*.

[56] J. B. Goodenough, *Phys. Rev. 100, 564 (1955)*.

[57] *Colossal magnetoresistance, charge ordering, and related properties of manganese oxides*, edited by C. N. R. Rao, and B. Raveau (World Scientific, Singapore, *1998*).

[58] D. E. Cox, P. G. Radaelli, M. Marezio, and S. -W. Cheong, *Phys. Rev. B 57, 3305 (1998)*.

[59] H. Yoshizawa, R. Kajimoto, H. Kawano, Y. Tomioka, and Y. Tokura, *Phys. Rev. B 55, 2729 (1997)*.

[60] Y. Tomioka, A. Asamitzu, Y. Moritoma, H. Kuwahara, and Y. Tokura, *Phys. Rev. Lett. 74, 5108 (1995)*.

[61] A. Asamitsu, Y. Tomioka, H. Kuwahara, and Y. Tokura, *Nature 388, 50 (1997)*.

[62] K. Miyano, T. Tanaka, Y. Tomioka, and Y. Tokura, *Phys. Rev. Lett. 78, 4257 (1997)*.

[63] J. Zaanen, G. A. Sawatzky, and J. W. Allen, *Phys. Rev. Lett. 55, 418 (1985)*; J. Zaanen, and G. A. Sawatzky, *J. Solid-st. Chem. 88, 8 (1990)*.

[64] J. M. D. Coey, M. Viret, and S. von Molnar *Adv. Phys. 48, 167 (1999)*.

[65] G. A. Gehring, and K. A. Gehring, *Rep. Prog. Phys. 38, 1 (1975)*.

[66] P. W., anderson, and H. Hasegawa. *Phys. Rev. 100, 675 (1955)*.

[67] K. Kubo, and N. Ohata, *J. Phys. Soc. Jpn., 33, 21 (1972)*.

[68] M. Cieplak, *Phys. Rev. B 18, 3470 (1978)*.

[69] P. G. de Gennes, *Phys. Rev. 118, 141 (1960)*.

[70] A. J. Millis, P. B. Littlewood, and B. I. Shraiman, *Phys. Rev. Lett. 74, 5144 (1995)*.

[71] Y. Motome, and N. Furukawa, *J. Phys. Soc. Japan 68, 3853 (1999)*; Y. Motome, and N. Furukawa, *cond-mat/0007408 (2000)*.

[72] A. J. Millis, B. I. Shraiman, and R. Mueller, *Phys. Rev. Lett. 77, 175 (1996)*; A. J. Millis, B. I. Shraiman, and R. Mueller, *Phys. Rev. B 54, 5389 (1996)*; A. J. Millis, *Phys. Rev. Lett. 80, 4358 (1998)*.

[73] H. Roder, R. R. P. Singh, and J. Zang, *Phys. Rev. B 56, 5084 (1997)*.

[74] T. Holstein, *Ann. Phys. (N.Y.) 8, 343 (1959)*.

[75] S. J. L. Billinge, R. G. DiFrancesco, G. H. Kwei, J. J. Neumeier, and J. D. Thompson, *Phys. Rev. Lett. 77, 715 (1996)*.

[76] G. P. Triberis, and L. R. Freidman, *J. Phys. C 18, 2281 (1985)*.

[77] B. I. Shklovskii, and A. L. Efros in *Electronic properties of Doped Semiconductor* (Springer – Verlag, Berlin, *1984*).

[78] P. H. Wagner, V. Metlushko, L. Trappeniers, A. Vantomme, J. Vanacken, G. Kido, V. V. Moshchalkov, and Y. Bruynseraede, *Phys. Rev. B 55, 3699 (1992)*.

[79] Y. Lyanda-Geller, S. H. Chun, M. B. Salamon, P. M. Goldbart, P. D. Han, Y. Tomioka, A. Asamitsu, and Y. Tokura, *Phys. Rev. B 63, 184426 (2001)*.

[80] P. H. Wagner, V. Metlushko, L. Trappeniers, A. Vantomme, J. Vanacken, G. Kido, V. V. Moshchalkov, and Y. Bruynseraede, *Phys. Rev. B 55, 3699 (1997)*; P. Wagner, I. Gordon, L. Trappeniers, J. Vanacken, F. Herlach, V. V. Moshchalkov, and Y. Bruynseraede, *Phys. Rev. Lett. 81, 3980 (1998)*.

[81] B. Abeles, Ping Sheng, M. D. Coutts, and Y. Arie, *Adv. Phys. 24, 407 (1975)*.

[82] Y. Tokura, and Y. Tomioka, *J. Magn. Magn. Mater. 200, 1 (1999)*.

[83] P. G. Radaelli, D. E. Cox, M. Marezio, S.-W. Cheong, P. E. Shiler, A. P. Ramirez, *Phys. Rev. Lett. 75, 4488 (1995)*; P. G. Radaelli, D. E. Cox, M. Marezio, S.-W. Cheong, *Phys.Rev. B 55, 3015 (1997)*.

[84] H. Kuwahara, Y. Tomioka, A. Asamitsu, Y. Moritomo, Y. Tokura, *Science 270, 961 (1995)*.

[85] Y. Tomioka, A. Asamitsu, H. Kuwahara, Y. Moritomo, M. Kasai, R. Kumai, Y. Tokura, *Physica B 237-238, 6 (1997)*.

[86] S. K. Mishra, R. Pandit, and S. Satpathy, *J. Phys.: Condens. Matter. 43, 8561 (1998)*.

[87] B. P. Stojkovic, Z. G. Yu, A. R. Bishop, Neto A. H. Castro, and N. Gronbech-Jensen, *Phys. Rev. Lett. 82, 4679 (1999)*.

[88] E. Dagotto, T. Hotta, and A. Moreo, *Physics Reports 344, 1 (2001)*.

[89] K. R. Nikolaev, A. Yu. Dobin, I. N. Krivorotov, E. Dan Dahlberg, and A. M. Goldman, *Appl. Phys. Lett. 89, 6820 (2001)*.

[90] I. N. Krivorotov, K. R. Nikolaev, A. Yu. Dobin, A. M. Goldman, and E. Dan Dahlberg, *Phys. Rev. Lett. 86, 5779 (2001)*.

[91] M. Izumi, T. Manako, Y. Konishi, M. Kawasaki, and Y. Tokura, *Phys. Rev. B 61, 12187 (2000)*.

[92] M. Izumi, Y. Ogimoto, Y. Okimoto, and T. Manako, P. Ahmet, K. Nakajima, and T. Chikyow, M. Kawasaki, Y. Tokura, *Phys. Rev. B 64, 64429 (2001)*.

[93] A. Venimadhav, M. S. Hegde, V. Prasad, and S. V. Subramanyam, *Phys. Rev. B 63, 214404 (2001)*.

[94] M. Sahana, M. S. Hegde, V. Prasad, and S. V. Subramanyam, *J. Appl. Phys. 85, 1058 (1999)*.

[95] I. Panagiotopoulos, C. Christides, D. Niarchos, and M. Pissas, *J. Appl. Phys. 87, 3926 (2000)*.

[96] D. Magnoux D. Hrabovsky, P. Baules, M. J. Casanove, E. Snoeck, A. R. Fert, and J. F. Boboa, *J. Appl. Phys. 91, 7730 (2002)*.

[97] Y. Lu, J. Klein, C. Hofener, B. Wiedenhorst, J. B. Philipp, F. Herbstritt, A. Marx, L. Alff, and R. Gross, *Phys. Rev. B 62, 15806 (2000)*.

[98] K. Dorr, T. Walter, M. Sahana, K.-H. Muller, K. Nenkov K. Brand, and L. Schultz, *J. Appl. Phys. 89, 6973 (2001)*.

[99] K. Ueda, H. Tabata, and T. Kawai, *Science 280, 1064 (1998)*; K. Ueda, H. Tabata, and T. Kawai *Phys. Rev. B 60, 12561 (1999)*; H. Tanaka, N. Okawa, and T. Kawai, *Solid State Commun. 110, 191 (1999)*; H. Tanaka, and T. Kawai, *J. Appl. Phys. 88, 1559 (2000)*.

[100] M. Kawasaki, K. Takahashi, T. Maeda, R. Tsuchiya, M. Shinohara, O. Ishiyama, T. Yonezawa, M. Yoshimoto, and H. Koinuma, *Science 266, 1540 (1994)*.

[101] L. R. Doolittle, *Nucl. Instrum. Meth. B 5, 344 (1985)*.

[102] E. E. Fullerton, I. K. Schuller, H. Vanderstraeten, and Y. Bruynseraede, *Phys. Rev. B 45, 9292 (1992)*.

[103] G. H. Jonker, *J. Appl. Phys. 37, 1424 (1966)*.

[104] M. F. Hundle, M. Hawley, R. H. Heffner, Q. X. Jia, J. J. Neumeier, and J. Tesmer, *Appl. Phys. Lett. 67, 860 (1995)*.

[105] P. Schiffer, A. P. Ramirez, W. Bao, S.-W. Cheong, *Phys. Rev. Lett. 75, 3336 (1995)*.

[106] H. Y. Hwang, T. Palstra, S. W. Cheong, and B. Batlogg, *Phys. Rev. B 52, 15046 (1995)*.

[107] H. B. Peng, B. R. Zhao, Z. Xie, Y. Lin, B. Y. Zhu, Z. Hao, H. J. Tao, B. Xu, C. Y. Wang, H. Chen, and F. Wu, *Phys.Rev. Lett. 82, 362 (1999)*.

[108] O. I. Lebedev, G. Van Tendeloo, S. Amelinckx, R. Leibold, and H. U. Habermeier, *Phys. Rev. B 58, 8065 (1998)*.

[109] N. C. Yeh, R. P. Vasquez, D. A. Beam, C. C. Fu, J. Huynh, and G. Beach, *J. Phys.: Condens. Matter 9, 3713 (1997)*.

[110] R. A. Rao, D. Lavric, T. K. Nath, C. B. Eom, L. Wu, and F. Tsui, *Appl. Phys. Lett. 73, 3294 (1998)*.

[111] S. Jacob, T. Roch, F. S. Razavia, G. M. Gross, and H.-U. Habermeier, *J. Appl. Phys 91, 2232 (2002)*.

[112] A. Miniotas, A. Vailionis, E. B. Svedberg, and U. O. Karlsson, *J. Appl. Phys. 89, 2134 (2001)*.

[113] M. Ziese, H. C. Semmelhack, K. H. Han, S. P. Sena, and H. J. Blythe, *J. Appl. Phys. 91, 9930 (2002)*.

[114] S. Jin, T. H. Tiefel, M. McCormack, H. M. O'Bryan, L. H. Chen, R. Ramesh, and D. Schuring, *Appl. Phys. Lett. 67, 557 (1995)*.

[115] L. B. Steren, M. Sirena, and J. Guimpel, *J. Appl. Phys. 87, 6755 (2000)*.

[116] J. Aarts, S. Freisem, R. Hendrikx, and H. W. Zandbergen *Appl. Phys. Lett. 72, 2975 (1998)*.

[117] T. Walter, K. Dorr, K.-H. Muller, D. Eckert, K. Nenkov, M. Hecker, M. Lehmann, and L. Schultz, *J. Magn. Magn. Mater. 222, 175 (2000)*.

[118] A. Gupta, G. Q. Gong, G. Xiao, P. R. Duncombe, P. Lecoeur, P. Trouilloud, Y. Y. Wang, V. P. Dravid, and J. Z. Sun, *Phys. Rev. B 54, R15629 (1996)*; X. W. Li, A. Gupta, Gang Xiao, and G. Q. Gong, *Appl. Phys. Lett. 71, 1124 (1997)*.

[119] H. W. Zandbergen, S. Freisem, T. Nojima, and J. Aarts *Phys. Rev. B 60, 10259 (1999)*.

[120] M. Fath, S. Freisem, A. A. Menovsky, Y. Tomioka, J. Aarts, and J. A. Mydosh, *Science 285, 1540 (1999)*.

[121] C. N. R. Rao, A. R. Raju, V. Ponnambalam, S. Parashar, and N. Kumar, *Phys. Rev. B 61, 594 (2000)*.

[122] P. S. Anil Kumar, P. A. Joy, and S. K. Date, *Solid State Commun. 108, 67 (1998)*.

[123] A. Biswas, M. Rajeswari, R. C. Srivastava, Y. H. Li, T. Venkatesan, and R. L. Greene, *Phys. Rev. B 61, 9665 (2000)*.

[124] X. W. Cao, J. Fang, and K. B. Li, *Solid State Commun. 115, 201 (2000)*.

[125] J. J. Neumeier, M. F. Hundley, J. D. Thompson, and R. H. Heffner, *Phys. Rev. B 52, R7006 (1995)*; K. Khazeni, Y. X. Jia, L. Lu, V. H. Crespi, M. L. Cohen, and A. Zettl, *Phys. Rev. Lett. 76, 295 (1996)*.

[126] F. Martin, G. Jakob, W. Westerburg, and H. Adrian, *J. Magn. Magn. Mater. 196-197, 509 (1999)*.

[127] M. Ziese, and C. Srinitiwarawong, *Europhys. Lett. 45, 256 (1999)*.

[128] X. J. Chen, S. Soltan, H. Zhang, and H. - U. Habermeier, *Phys. Rev. B 65, 174402 (2002)*.

[129] Ji-Wen Feng, and Lian-Pin Hwang, *Appl. Phys. Lett. 75, 1592 (1999)*; Yun-Hui Huang, Chun-Hua Yan, Feng Luo, Wei Song, Zhe-Ming Wang, and Chun-Sheng Liao, *Appl. Phys. Lett. 81, 76 (2002)*.

[130] T. Kasuya, and A. Yanase, *Rev. Mod. Phys. 40, 684 (1968)*; J. Tanaka, M. Umehara, S. Tamura, M. Tsukioka, and S. Ehara, *J. Phys. Soc. Jpn. 51, 1236 (1982)*.

[131] J. I. Gittleman, Y. Goldstein, and S. Bozowski, *Phys. Rev. B 5, 3609 (1972)*.

[132] N. A. Babushkina, L. M. Belova, D. I. Khomskii, K. I. Kugel, O. Yu. Gorbenko, and A. R. Kaul, *Phys. Rev. B 59, 6994 (1999)*.

[133] J. Stankiewicz, J. Sese, J. Garcia, J. Blasco, and C. Rillo, *Phys. Rev. B 61, 11236 (2000)*.

[134] M. Medarde, A. Fontaine, J. L. Garcia-Munoz, J. Rodriguez - Carvajal, M. de Santis, M. Sacchi, G. Rossi, and P. Lacorre, *Phys. Rev. B 46, 14975 (1992)*.

[135] S. R. Barman, A. Chainani, and D. D. Sarma, *Phys. Rev. B 49, 8475 (1994)*.

[136] R. D. Sanchez, M. T. Causa, C. Caneiro, A. Butera, M. Vallet-Regi, M.J. Sayagues, J. Gonzalez-Calbet, F. Garcia-Sanz, and J. Rivas, *Phys. Rev. B 54, 16 574 (1996)*.

[137] J. M. Gonzalez - Calbet, M. J. Sayague's, and M. Vallet-Regý', *Solid State Ionics 32 - 33, 721 (1989)*; M. J. Sayague's, M. Vallet-Regý', A. Caneiro, and J. M. Gonza'lez - Calbet, *J. Solid State Chem. 110, 295 (1994)*.

[138] N. Gayathri, A. K. Raychaudhuri, X. Xu, J. L. Peng, and R. Greene, *J. Phys.: Condens. Matter 11, 2901 (1999)*; N. Gayathri, A. K. Raychaudhuri, X. Xu, J. L. Peng, and R. Greene, *J. Phys.: Condens. Matter 10, 1323 (1998)*.

[139] Masayuki Sagoi, Teruyu-ki Kinno, Jiro Yoshida, and Koichi Mizushima, *Appl. Phys. Lett. 62, 1833 (1993)*.

[140] Xiangxin Guo, Chunling Li, Yueliang Zhou, and Zhenghao Chen, *J. Vac. Sci. Technol. A 17, 917 (1999)*.

[141] T. C. Huang, W. Parrish, H. Torya, P. Lacorre, and J. B. Torrance, *Mater. Res. Bull. 25, 1091 (1990)*.

[142] J. L. Garcia-Munoz, J. Rodriguez-Carvajal, P. Lacorre, and J. B. Torrance, *Phys. Rev. B 46, 4414 (1992)*.

[143] J.-S. Zhou, J. B. Goodenough, B. Dabrowski, P. W. Klamut, and Z. Bukowski, *Phys. Rev. lett. 84, 526 (2000)*.

[144] Y. Tomioka, A. Asamitsu, H. Kuwahara, Y. Moritomo, and Y. Tokura, *Phys. Rev. B 53, R1689 (1996)*.

[145] T. Terai, T. Sasaki, T. Kakeshita, T. Fukuda, T. Saburi, H. Kitagawa, K. Kindo, and M. Honda, *Phys. Rev. B 61, 3488 (2001)*.

[146] A. Chainani, H. Kumigashira, T. Takahashi, Y. Tomioka, H. Kuwahara, and Y. Tokura, *Phys. Rev. B 56, R15513 (1997)*.

[147] V. N. Smolyaninova, A. Biswas, X. Zhang, K. H. Kim, B. G. Kim, S.-W. Cheong, and R. L. Greene, *Phys. Rev. B 62, R6093 (2000)*.

[148] Ivan K. Schuller, *Phys. Rev. Lett. 44, 1597 (1980)*.

[149] B. Y. Jin, and J. B. Ketterson, *Adv. in Phys. 38, 189 (1989)*.

[150] Myron B. Salamon, and Marcelo Jaime, *Rev. Mod. Phys. 73, 583 (2001)*.

[151] Y. Ogimoto, M. Izumi, T. Manako, T. Kumar, Y. Tomioka, M. Kawasaki, and Y. Tokura, *Appl. Phys. Lett. 78, 3505 (2002)*.

[152] P. Padhan, N. K. Pandey, S. Srivastava, R. K. Rakshit, V. N. Kulkarni, and R. C. Budhani, *Solid State Commun. 117, 27 (2001)*.

[153] J. - M. Triscone, and Ø. Fischer, *Rep. Prog. Phys. 60, 1673 (1997)*.

[154] C. B. Eom, A. F. Marshall, J. – M. Triscone, B. Wilkens, S. S. Laderman, and T. H. Geballe, *Science 251, 780 (1991)*.

[155] M. Izumi, Y. Konishi, T. Nishihara, S. Hayashi, M. Shinohara, M. Kawasaki, and Y. Tokura, *Appl. Phys. Lett. 73, 2497 (1998)*.

[156] J. B. Torrance, P. Lacorre, A. I. Nazzal, E. J. Ansaldo, and Ch. Niedermayer, *Phys. Rev. B 45, 8209 (1992)*.

[157] S. S. P. Parkin, *Phys. Rev. Lett. 67, 3598 (1991)*.

[158] Prahallad Padhan, and R. C. Budhani *Phys. Rev. B 67, 024414 (2003)*.

[159] J. E. Mattson, C. H. Sowers, A. Berger, and S. D. Bader, *Phys. Rev. Lett. 68, 3252 (1992)*.

[160] R. C. Budhani, N. K. Pandey, P. Padhan, S. Srivastava, and R. P. S. M. Lobo, *Phys. Rev. B 65, 014429 (2002)*.

[161] Amlan Biswas, M. Rajeswari, R. C. Srivastava, T. Venkatesan, R. L. Greene, Q. Lu, A. L. de Lozanne, and A. J. Millis, *Phys. Rev. B 63, 184424 (2001)*.

[162] J. Z. Sun, D. W. Abraham, R. A. Rao, and C. B. Eom, *Appl. Phys. Lett.* **74**, *3017* (*1999*).

[163] Kenji Ueda, Hitoshi Tabata, and Tomoji Kawai, *Phys. Rev. B 60, 12561* (*1999*).

[164] K. Ghosh, S. B. Ogale, S. P. Pai, M. Robson, Eric Li, I. Zin, Zi-wen Dong, R. L. Greene, R. Ramesh, T. Venkatesan, and M. Johnson, *Appl. Phys. Lett.,* **73**, *689* (*1998*).

[165] T. Tamegai, and Y. Iye, *Phys. Rev. B 44, 10167* (*1991*).

[166] Y. Iye, S. Nakamura, and T. Tamegai, *Physica C 159, 616* (*1989*).

[167] V. A. Vas'ko, V. A. Larkin, P. A. Kraus, K. R. Nikolaev, D. E. Grupp, C. A. Nordman, and A. M. Goldman, *Phys. Rev. Lett. 78, 1134* (*1997*).

[168] Z. W. Dong, R. Ramesh, T. Venkatesan, Mark Johnson, Z. Y. Chen, S. P. Pai, V. Talyansky, R. P. Sharma, R. Shreekala, C. J. Lobb, and R. L. Greene, *Appl. Phys. Lett. 71, 689* (*1997*).

[169] Prahallad Padhan, R. S. P. M. Lobo, and R. C. Budhani (Europhys. Lett. in Press).

[170] A. Biswas, M. Rajeswari, R. C. Srivastava, T. Venkatesan, R. L. Greene, Q. Lu, A. L. de Lozanne, and A. J. Millis, *Phys. Rev. B 63, 184424* (*2002*).

[171] M. Kiwi, J. M.-Lopez, R. D. Portugal, and R. Ramirez, *Appl. Phys. Lett.* **75**, *3995* (*1999*); M. Kiwi, *J. Magn. Magn. Mater. 234, 584* (*2001*).

[172] C. Christides, N. Moutis, Ph. Komninou, Th. Kehagias, and G. Nouet, *J. Appl. Phys. 92, 397* (*2002*).